Investigations of Superconductivity and Magnetism in Iron-Based and Cuprate High-Temperature Superconductors

Dissertation

zur
Erlangung der naturwissenschaftlichen Doktorwürde
(Dr. sc. nat.)

vorgelegt der
Mathematisch-naturwissenschaftlichen Fakultät der
Universität Zürich

von

Zurab Guguchia
aus Georgien

Zürich, 2013

Promotionskomitee:

Prof. Dr. Hugo Keller, Universität Zürich (Vorsitz)
Prof. Dr. Alexander Shengelaya, Tbilisi State University (Leitung der Dissertation)
Prof. Dr. Elvezio Morenzoni, Paul Scherrer Institut
Prof. Dr. Boris Kochelaev, Kazan Federal University

Die vorliegende Arbeit wurde von der Mathematisch-naturwissenschaftlichen Fakultät der Universität Zürich auf Antrag von Prof. Dr. Hugo Keller als Dissertation angenommen.

dedicated to the memory of my mother Marina

dedicated to my father Otari

Abstract

High-temperature (high-T_c) superconductivity is a fascinating field in condensed matter physics research, incorporating a tremendous amount of physics within a varity of systems. So far, three classes of high-T_c superconductors (HTSs) are known: cuprates, diborides, and iron-based superconductors. After more than twenty-five years of research, the origin of high-T_c superconductivity is still not clear. To understand the microscopic pairing mechanism and to explain high-T_c superconductivity are for academic and technical reasons of great interest.

In this thesis the superconducting (SC) and magnetic properties and interplay between them were studied in two different classes of HTSs. Namely, in the novel Fe-based compounds $\mathrm{EuFe_{2-x}Co_xAs_2}$, $\mathrm{EuFe_2(As_{1-x}P_x)_2}$, $\mathrm{Ba_{1-x}Rb_xFe_2As_2}$ and in the cuprate $\mathrm{La_{1.875}Ba_{0.125}CuO_4}$. The combination of muon-spin rotation (μSR), nuclear magnetic resonance (NMR), magnetization, and x-ray experiments were used to study structural, magnetic, and SC properties of HTSs on a microscopic and macroscopic level. Magnetization and μSR experiments were carried out at ambient as well as under hydrostatic pressures.

In the first part of this thesis, the results obtained on single crystals of $\mathrm{EuFe_{2-x}Co_xAs_2}$ and pollycrystalline samples of $\mathrm{EuFe_2(As_{1-x}P_x)_2}$ and $\mathrm{Ba_{1-x}Rb_xFe_2As_2}$ are presented. The system $\mathrm{EuFe_2As_2}$ is a particularly interesting member of the iron arsenide $A\mathrm{Fe_2As_2}$ (122) family, since the A site is occupied by magnetic $\mathrm{Eu^{2+}}$ ions. $\mathrm{EuFe_2As_2}$ exhibits both a spin-density wave (SDW) ordering of the itinerant Fe moments and an antiferromagnetic (AFM) ordering of the localized $\mathrm{Eu^{2+}}$ moments below 190 K and 19 K, respectively. It also undergoes a tetragonal-orthorhombic (TO) structural phase transition at the same temperature (190 K) at which the SDW transition of the Fe moments occurs. Hence, this system is an ideal candidate to study the interrelation between superconductivity, structure, and different types of magnetism in Fe-based HTSs (Fe-HTSs).

^{75}As NMR experiments on $\mathrm{EuFe_{1.9}Co_{0.1}As_2}$ revealed a large value of the hyperfine coupling constant between the ^{75}As nuclei and the Eu $4f$ moments, suggesting a strong coupling between the Eu and the conducting $\mathrm{Fe_{1.9}Co_{0.1}As_2}$ layers. The strong interaction between the localized $\mathrm{Eu^{2+}}$ moments and the charge carriers in the $\mathrm{Fe_{2-x}Co_xAs_2}$ layers may cause pair breaking according to the Abrikosov-Gor'kov theory. This may explain why it is difficult to induce superconductivity in $\mathrm{EuFe_{2-x}Co_xAs_2}$, in contrast to the other 122 systems, where the substitution of Fe by Co leads to the appearance of a SC phase. On the other hand, the observed strong interlayer coupling suggests that the magnetic exchange interaction between the localized Eu $4f$ moments is mediated by the itinerant Fe $3d$ electrons, *i.e.*, via a Ruderman-Kittel-Kasuya-Yosida (RKKY) type of mechanism, leading to a high magnetic ordering temperature of the $\mathrm{Eu^{2+}}$ moments in $\mathrm{EuFe_2As_2}$. Magnetization as well as NMR experiments revealed that the SDW state is suppressed as a result of Co doping. Thanks to the extreme sensitivity of NMR to probe the local structure in a solid, we were able to observe the symmetry lowering from the tetragonal to the orthorhombic phase in $\mathrm{EuFe_{1.9}Co_{0.1}As_2}$ at

around 225 K. This is possibly due to the appearance of a electronic nematic phase below 225 K. The presence of this phase was suggested theoretically and recently observed in a few Fe-HTSs by means of measurements of the in-plane anisotropy of the electrical resistivity. The electronic nematic state is interesting, since it could arise from AFM fluctuations, which may play some role for superconductivity. Note that the present NMR results provide the first microscopic evidence for a nematic phase in Fe-HTSs and support the idea that the TO structural transition in Fe-HTSs is of electronic origin.

The phase diagrams for the ordering of the Eu^{2+} magnetic sublattice with respect to temperature, magnetic field, and the angle between the magnetic field and the crystallographic c-axis in single crystals of $EuFe_{2-x}Co_xAs_2$ are determined and discussed. Although at low temperatures typical results for an AFM state in $EuFe_2As_2$ were found, our data strongly indicate the occurrence of a canted AFM (C-AFM) order of the Eu^{2+} moments between 17 K and 19 K, observed even in the lowest studied magnetic fields. By applying a magnetic field within the AFM phase, a transition from AFM order via a canted configuration to a ferromagnetic structure was found. Unlike in the parent compound, no low-field and low-temperature AFM state of the Eu^{2+} moments was detected in doped $EuFe_{1.8}Co_{0.2}As_2$. Only a C-AFM phase is present at low fields and low temperatures, with a reduced magnetic anisotropy as compared to the undoped system. It is likely that the magnetic coupling of the Eu and the Fe sublattices strongly depends on Co doping, having a strong influence on the magnetic phase diagrams as determined in this work. Their impact on the occurrence of superconductivity with higher Co doping is discussed.

The magnetic phase diagrams of the magnetic ordering of the Eu and Fe spins in polycrystalline samples of $EuFe_2(As_{1-x}P_x)_2$ with respect to chemical (isovalent substitution of As by P) and hydrostatic pressure are also presented. It was shown that the properties of $EuFe_2(As_{1-x}P_x)_2$ strongly and similarly depend on both chemical and hydrostatic pressure. One important aspect of the present results is that it confirms the presence of a SC phase in an extremely narrow pressure range in $EuFe_2(As_{1-x}P_x)_2$. This implies that the system $EuFe_2(As_{1-x}P_x)_2$ exhibits an unique SC phase diagram. This is very different from the respective phase diagram of $BaFe_2(As_{1-x}P_x)_2$, where superconductivity is observed over a large pressure range. This might be related to the sophisticated interplay between SDW, Eu-magnetic order, and superconductivity in $EuFe_2(As_{1-x}P_x)_2$.

The temperature and magnetic field dependences of the magnetic penetration depth λ and the resulting SC gap structure were examined in the Fe-HTS $Ba_{1-x}Rb_xFe_2As_2$ ($x = 0.3$, 0.35, 0.4). The system $Ba_{1-x}Rb_xFe_2As_2$ is interesting, since it exhibits the highest SC transition temperature $T_c = 38$ K among the 122 compounds. It was found that in this system two gaps open below T_c, which is in line with the generally accepted view of multi-gap superconductivity in Fe-HTSs. Moreover, the gap to T_c ratio is similar for all the Fe-HTSs. This may give important hints for the pairing mechanism leading to superconductivity in the Fe-HTSs.

In the second part of the thesis, the focus is put on the studies of superconductivity and magnetism in the cuprate superconductor $La_{2-x}Ba_xCuO_4$ with x=1/8 as a function of hydrostatic pressure. This compound is interesting, since near the anomalous hole density of x=1/8 a strong suppression of superconductivity was observed. This is followed by the appearance of a self-organized static charge/spin structure, known as “stripes”. In the framework of the stripe model it is recognized that the charge/spin orders are a manifestation of dynamical spin/charge correlations, and that stabilization of these orders induces an instability of the SC state. Experimental results and theoretical considerations show that the modulations of the charge and spin density appear to be both ubiquitous in the cuprates and intimately tied up with the physics of these materials. However, the role of stripes for superconductivity in cuprates is still unclear at present. Therefore, it is important to find an external control parameter which allows to tune electronic properties of the cuprates and to study the relation between superconductivity and stripe order.

In this work an unusual interplay between static spin order within the stripe phase and superconductivity was revealed in $La_{1.875}Ba_{0.125}CuO_4$. With increasing pressure the spin order temperature and the size of the ordered moment do not change significantly. However, the magnetic volume fraction of the static stripe phase strongly decreases linearly with pressure, while the SC volume fraction increases by the same amount. This demonstrates competition between superconductivity and static magnetic order in the stripe phase of $La_{1.875}Ba_{0.125}CuO_4$ and that these phenomena occur in mutually exclusive spatial regions.

Zusammenfassung

Die Hochtemperatursupraleitung ist ein faszinierendes Gebiet der Festkörperforschung, das einen Grossteil der Physik innerhalb einer Vielzahl von Systemen umfasst. Bis heute sind drei Klassen an Hochtemperatursupraleitern bekannt: Kuprat-, Diborid- und Eisen-basierte Supraleiter. Auch nach mehr als 25 Jahren Forschung ist der Ursprung der Hochtemperatursupraleitung ungeklärt. Das Verständnis des mikroskopischen Paarungsmechanismus der Elektronen sowie der Hochtemperatursupraleitung generell ist aus akademischer und technischer Sicht von grossem Interesse.

In dieser Arbeit wurden die supraleitenden und magnetischen Eigenschaften sowie ihr Zusammenwirken in zwei Hochtemperatursupraleiterklassen untersucht. Es wurden auf der einen Seite die neuartigen Eisen-basierten Verbindungen $\mathrm{EuFe}_{2-x}\mathrm{Co}_x\mathrm{As}_2$, $\mathrm{EuFe}_2(\mathrm{As}_{1-x}\mathrm{P}_x)_2$ und $\mathrm{Ba}_{1-x}\mathrm{Rb}_x\mathrm{Fe}_2\mathrm{As}_2$, und auf der anderen Seite die Kuprat-Verbindung $\mathrm{La}_{1.875}\mathrm{Ba}_{0.125}\mathrm{CuO}_4$ betrachtet. Die Kombination aus Myonen-Spin-Rotation, Kernspinresonanz, Magnetisierungsmessung und Röntgenstreuung ermöglichte die Bestimmung der strukturellen, magnetischen und supraleitenden Eigenschaften dieser Hochtemperatursupraleiter auf mikroskopischem und makroskopischem Niveau. Magnetisierungs- und Myonen-Spin-Rotationsmessungen wurden nicht nur bei Umgebungsdruck sondern auch unter hydrostatischem Druck durchgeführt.

Im ersten Teil werden die Ergebnisse bezüglich dem einkristallinen $\mathrm{EuFe}_{2-x}\mathrm{Co}_x\mathrm{As}_2$ sowie der polykristallinen Systeme $\mathrm{EuFe}_2(\mathrm{As}_{1-x}\mathrm{P}_x)_2$ und $\mathrm{Ba}_{1-x}\mathrm{Rb}_x\mathrm{Fe}_2\mathrm{As}_2$ zusammengefasst. $\mathrm{EuFe}_2\mathrm{As}_2$ ist ein besonders interessanter Vertreter der Klasse der Eisenarsenidfamilie $A\mathrm{Fe}_2\mathrm{As}_2$, auch als (122) Familie bezeichnet, da die Gitterplatzposition A vom magnetischen Eu^{2+} Ion besetzt ist. $\mathrm{EuFe}_2\mathrm{As}_2$ weist ausserdem sowohl eine Spindichtewellenordnung der nichtlokalen Eisenmomente unterhalb 190 K auf sowie eine antiferromagnetische Ordnung der lokalisierten Eu^{2+} Momente unterhalb 19 K. Das System erfährt zudem einen strukturellen Phasenübergang von tetragonal zu orthorhombisch bei der Temperatur bei der auch die Spindichtewellenordnung der Eisenmomente auftritt (190 K). Daher ist dieses System ideal um die wechselseitige Beziehung zwischen Supraleitung, Struktur und verschiedenen Arten von Magnetismus in Eisen-basierten Hochtemperatursupraleiter zu untersuchen.

$^{75}\mathrm{As}$ Kernspinresonanzmessungen an $\mathrm{EuFe}_{1.9}\mathrm{Co}_{0.1}\mathrm{As}_2$ zeigen einen grossen Wert für die Hyperfeinfeldkopplungskonstante zwischen den $^{75}\mathrm{As}$ Kernen und den Eu $4f$ Momenten, was auf eine strake Kopplung zwischen Eu und den leitenden $\mathrm{Fe}_{1.9}\mathrm{Co}_{0.1}\mathrm{As}_2$ Schichten hinweist. Die starke Wechselwirkung zwischen den lokalisierten Eu^{2+} Momenten und den Ladungsträgern der $\mathrm{Fe}_{2-x}\mathrm{Co}_x\mathrm{As}_2$ Schichten könnte gemäss der Abrikosov-Gor'kov Theorie das Aufbrechen von Elektronenpaaren verursachen. Dies könnte erklären, warum es schwierig ist Supraleitung in $\mathrm{EuFe}_{2-x}\mathrm{Co}_x\mathrm{As}_2$ zu induzieren, im Gegensatz zu den anderen Vertretern der (122) Familie, bei denen die Substitution von Fe mit Co zum Auftreten einer supraleitenden Phase führt. Auf der anderen Seite deutet die beobachtete starke Wechselwirkung darauf hin, dass die magnetische Austauschwechselwirkung zwischen den

lokalisierten Eu $4f$ Momenten durch die itineranten Fe $3d$ Elektronen vermittelt wird, z.B. über einen Ruderman-Kittel-Kasuya-Yosida (RKKY) artigen Mechanismus, was zu einer hohen magnetischen Ordnungstemperatur der Eu^{2+} Momente in $EuFe_2As_2$ führen würde. Magnetisierungs- und Kernspinresonanzmessungen zeigten, dass der Spindichtewellenzustand durch Co Dotierung unterdrückt wird. Dank der hohen Sensitivität der Kernspinresonanz bei der Messung der lokalen Struktur in einem Festkörper war es uns möglich die Symmetrieerniedrigung von tetragonal zu orthorhombisch in $EuFe_{1.9}Co_{0.1}As_2$ bei etwa 225 K zu beobachten. Dies ist möglich da eine elektronische nematische Phase unterhalb 225 K auftritt. Diese Phase wurde theoretisch vorhergesagt und kürzlich in einigen Eisen-basierten Hochtemperatursupraleitern mit Hilfe von Messungen der planaren Anisotropie der elektrischen Leitfähigkeit nachgewiesen. Der elektronische nematische Zustand ist interessant, da er womöglich auf antiferromagnetische Fluktuationen zurückgeführt werden kann, welche vielleicht eine Rolle für die Supraleitung spielen. Dabei ist hervorzuheben, dass die vorliegenden Kernspinresonanzdaten den ersten mikroskopischen Nachweis der nematischen Phase in Eisen-basierten Hochtemperatursupraleitern liefern und damit den Ansatz unterstützen, dass der strukturelle Phasenübergang von tetragonal zu orthorhombisch von elektronischem Ursprung ist.

In dieser Arbeit werden zudem die Phasendiagramme bezüglich der Temperatur, des magnetischen Feldes und dem Winkel zwischen Magnetfeld und kristallografischer c-Achse hinsichtlich der Ordnung der magnetischen Eu^{2+} Untergitter untersucht und diskutiert. Obwohl bei niedrigen Temperaturen typische Merkmale für einen antiferromagnetischen Zustand in $EuFe_2As_2$ gefunden wurden, deuten unsere Daten zwischen 17 K und 19 K stark auf das Auftreten eines verkippten antiferromagnetischen Zustands der Eu^{2+} Momente hin. Diese Phase wurde auch in Messungen bei niedrigsten Magnetfeldern beobachtet. Durch Anlegen eines Magnetfeldes innerhalb der antiferromagnetischen Phase ging diese Phase mittels der gekippten Anordnung in eine ferromagnetische Struktur über. Im Gegensatz zur Ausgangsverbindung wurden in dotiertem $EuFe_{1.8}Co_{0.2}As_2$ keine antiferromagnetische Phase bei tiefen Feldern und niedrigen Temperaturen gefunden. Nur eine verkippte antiferromagnetische Phase mit einer reduzierten magnetischen Anisotropie, vergleichbar mit dem undotierten System, war unter den eben genannten Bedingungen nachweisbar. Es ist daher wahrscheinlich, dass die magnetische Kopplung zwischen Eu Momenten und den Fe Untergittern stark von der Kobaltdotierung abhängt, welche wiederum einen starken Einfluss auf das magnetische Phasendiagramm hat, wie in dieser Arbeit gezeigt wird. Der Einfluss der magnetischen Kopplung auf das Auftreten von Supraleitung bei höherer Kobaltdotierung wird ebenfalls diskutiert.

Das magnetische Phasendiagramm in Abhängigkeit von chemischem (isovalente Substitution von As mit P) und hydrostatischem Druck der magnetischen Ordnung der Eu Momente und der Fe Spins in polykristallinen $EuFe_2(As_{1-x}P_x)_2$ Proben wurde untersucht. Es kann gezeigt werden, dass die Eigenschaften von $EuFe_2(As_{1-x}P_x)_2$ stark und auf ähnliche Weise sowohl vom chemischen als auch vom hydrostatischen Druck abhängen. Ein wichtiger Punkte der vorliegenden Ergebnisse ist der Nachweis einer supraleitenden Phase in $EuFe_2(As_{1-x}P_x)_2$ in einem sehr schmalen Druckintervall. Dies zeigt, dass das $EuFe_2(As_{1-x}P_x)_2$ System ein einzigartiges supraleitendes Phasendiagramm aufweist. Es unterscheidet sich damit deutlich vom entsprechendem Phasendiagramm, von $BaFe_2(As_{1-x}P_x)_2$ in dem Supraleitung in einem grossen Druckintervall beobachtet wird. Dies könnte mit dem kompliziertem

Wechselspiel zwischen Spindichtewellen, magnetischer Ordnung der Eu Momente und Supraleitung in $EuFe_2(As_{1-x}P_x)_2$ zusammenhängen.

Die Temperatur- und Magnetfeldabhängigkeit der magnetischen Eindringtiefe λ und der resultierenden Struktur der supraleitenden Bandlücke wurden in optimal dotierten Eisen-basierten Hochtemperatursupraleitern $Ba_{1-x}Rb_xFe_2As_2$ ($x = 0.3$, 0.35, 0.4) untersucht. Das $Ba_{1-x}Rb_xFe_2As_2$ System ist interessant, da es mit $T_c = 38\,K$ die höchste supraleitende Übergangstemperatur innerhalb der (122) Familie aufweist. In diesem System öffnen sich unterhalb von T_c zwei Bandlücken, was im Einklang mit der allgemein anerkannten Sichtweise von Multi-Bandlückensupraleitung in Eisen-basierten Hochtemperatursupraleitern ist. Zudem ist das Verhältnis der Bandlücke zur supraleitenden Übergangstemperatur in allen Eisen-basierten Hochtemperatursupraleitern ähnlich. Dies könnte ein bedeutender Hinweis zur Identifizierung des Paarungsmechanismus sein, welcher der Supraleitung Eisen-basierten Hochtemperatursupraleiter zugrunde liegt.

Im zweiten Teil dieser Arbeit lag der Fokus auf der Untersuchung der Abhängigkeit der Supraleitung und des Magnetismus vom hydrostatischen Druck im Kuprat-Supraleiter $La_{2-x}Ba_xCuO_4$ mit x=1/8. Dieses Material ist von Interesse, da nahe der anormalen Löcherdichte von x=1/8 eine starke Verdrängung der Supraleitung beobachtet wird. Diese wird von der Formation selbstorganisierter statischer Ladungs- oder Spinstrukturen begleitet, bekannt als "‘Streifen"’. Im Rahmen des Streifenmodelles wird davon ausgegangen, dass die Ladungs- bzw. Spinordnung dynamische Ladungs- bzw. Spinkorrelation manifestieren, und dass die Stabilisierung dieser Ordnungen zur Instabilität des supraleitenden Zustandes führt. Experimentelle Ergebnisse sowie theoretische Überlegungen zeigen, dass eine Modulation der Ladungs- und Spindichten in den Kuprat- Supraleitern universell und sehr eng mit der Physik dieser Materialien verknüpft ist. Der Rolle der "‘Streifen"’ in Bezug auf die Supraleitung ist jedoch in den Kuprat-Supraleitern immer noch unklar. Daher ist es wichtig einen externen kontrollparameter zu finden, der es uns erlaubt die elektronischen Eigenschaften der Kuprat-Supraleiter gezielt einzustellen und damit die Beziehung zwischen der Supraleitung und der Streifenordnung zu untersuchen.

Diese Arbeit zeigt das komplizierte Wechselspiel zwischen der statischen Spinordnung innerhalb der Streifenphase und der Supraleitung in $La_{1.875}Ba_{0.125}CuO_4$ auf. Mit steigendem Druck ändern sich die Spinordnungstemperatur und die Grösse der geordneten Momente nicht wesentlich. Der magnetische Volumenanteil der statischen Streifenphase sinkt hingegen deutlich und linear mit steigendem Druck, während der supraleitende Volumenanteil gleichzeitig um denselben Anteil steigt. Dies zeigt die Konkurrenz zwischen supraleitender und statischer magnetischer Ordnung in der Streifenphase des $La_{1.875}Ba_{0.125}CuO_4$ Systems auf und untermauert, dass diese Phänomene nur in gemeinsamen bestimmten räumlichen Bereichen auftreten.

Contents

1 Introduction

One of the most fascinating phenomena in condensed matter physics is superconductivity, discovered by H. Kamerlingh Onnes in Leiden in 1911 [1]. Superconductivity is the ability of a material to lose its electrical resistivity completely below a critical temperature T_c [1, 2, 3, 4], and expel any external magnetic field from the bulk, thus leading to ideal diamagnetism. The latter effect is the so called *Meissner-Ochsenfeld effect*, discovered by Meissner and Ochsenfeld in 1933 [5]. It opened the way towards a deeper understanding of superconductivity.

Since superconductors are defined by the electrodynamic properties, ideal conduction and ideal diamagnetism. It is thus appropriate to ask how these materials can be described within the formal framework of electrodynamics. In 1935 F. and H. London proposed a phenomenological theory for the electrodynamic properties of superconductors [6]. It is based on a *two-fluid picture*. In 1950 the Ginzburg-Landau (GL) theory was developed [7], which extended the London theory. The GL theory is able to describe the thermodynamics of fundamental properties of superconductors as a function of temperature and field without any microscopic implications.

In 1950 E. Maxwell [8] and C.A. Reynolds and coworkers [9] observed an isotope effect on T_c for mercury [8, 9]. This suggested that lattice vibrations might be crucial for the occurence of superconductivity. The isotope effect was an important observation in the process of developing the famous and most elegant theory of Bardeen, Cooper, Schrieffer (BCS) [10, 11, 12]. It gave a definite electronic explanation of superconductivity in terms of Cooper pairs. These pairs are formed in an energy shell $\hbar\omega_\mathrm{D}$ (ω_D denotes the Debye frequency) around the Fermi energy ϵ_F resulting from the electron-phonon interaction. The BCS theory was further completed by the field theoretical approaches of Gor'kov, Abrikosov and Gor'kov, and Eliashberg [13].

A further step was Josephson's tunneling of Cooper pairs through a thin barrier between two superconductors [14]. Very important was also the study of the tunneling density of states by Schrieffer, Scalapino and Wilkens in 1963 explaining the detailed structure observed in the tunneling current and the superconducting (SC) order parameter $\Delta(\omega)(\omega$ denotes the frequency) as due to the electron-phonon coupling [15]. It seemed that the electronic theory for superconductivity, which had replaced the early phenomenological theories was largely completed.

The search for superconductors with higher transition temperatures became increasingly important. In this regard of particular interest was the work by McMillan [16], which attempted to relate T_c to characteristic parameters of the SC metals like electron-phonon coupling, electronic density of states at ϵ_F and other quantities. For a long time one observed only superconductivity due to the electron-phonon coupling and that compounds like $\mathrm{V_3Si}$ and $\mathrm{Nb_3Ge}$ [17, 18] had the highest T_c at about 23 K. The prospects for finding superconductors with higher T_c was affected by the estimates of a maximal T_c given by Anderson, Cohen, and Allen and others [19]. However, one expected that for increasing the electron-phonon coupling strength, the resulting lattice instability limited essentially the occurence of superconductivity. Indeed, until about 1986, superconductivity was limited to rather low temperatures $T_c \approx 23$ K.

Soon after 1980 exciting new superconductors belonging to rather different material classes were discovered. The superconductivity research changed dramatically when the cuprate high-temperature superconductor (HTS) $La_{2-x}Ba_xCuO_4$ was discovered by Bednorz and Müller [20] in 1986. Since this discovery, high-temperature (high-T_c) superconductivity was reported in many other cuprate superconductors with transition temperatures ranging from $T_c \simeq 35$ K to $T_c \simeq 160$ K (under pressure) in the mercury based cuprate system $HgBa_2CaCu_2O_{6+\delta}$ [21, 22, 23].

"High-T_c" has two common definitions in the context of superconductivity:
1) Above the temperature of 30 K that had historically been taken as the upper limit allowed by BCS theory.
2) Having a transition temperature that is a larger fraction of the Fermi temperature than for conventional superconductors such as elemental mercury or lead. This definition encompasses a wider variety of unconventional superconductors and is used in the context of theoretical models.
Note that the mechanism by which these cuprate materials become SC has still remained a mystery after more than 25 years of research. The highly successful BCS theory of superconductivity was designed only for good metals, not for doped insulators. Many ideas have been suggested for how high-temperature superconductors (HTSs) work. Among these theories are those that propose polaronic mechanism, rather than electron-phonon interaction [24, 25, 26]. Thus, instead of a pure s-wave, rather a mixed $d + s$-wave pairing is important [24, 27].

Search for new HTSs resulted in the discovery in 2001, when superconductivity was found at 39 K in the binary compound MgB_2 [28], and again in 2008, when superconductivity at 28 K was observed in the Fe-based system $LaFeAsO_{1-x}F_y$ [29, 30]. Soon after, even higher transition temperatures for Fe-based system up to $T_c \sim 56$ K were found [30]. Iron-based superconductors (Fe-HTSs) are currently the superconductors with the second highest critical temperature, behind the cuprates. Most undoped Fe-HTSs are layered and show a tetragonal-orthorhombic structural phase transition followed at lower temperature by magnetic ordering, similar to the cuprate superconductors. However, they are poor metals rather than Mott insulators. The phase diagram emerging as the iron-arsenide layers are doped is remarkably similar to cuprates, with the SC phase close to or overlapping with the magnetic phase. Strong evidence that T_c varies with the As-Fe-As bond angles has already emerged and shows that the optimal T_c value is obtained with undistorted $FeAs_4$ tetrahedra. Fe-HTSs seem to be multi-gap superconductors with a complicated gap structure. However, the symmetry of the pairing wavefunction is still widely debated. Most probably in the Fe-HTSs the order parameter is $s + s$-wave like [31]. However, some reports point towards an s(+/-), or extended s-wave state [32, 33].

The underlying mechanism of high-T_c superconductivity is still under debate. Many of the properties of HTSs cannot be explained by the BCS theory. Thus, it is fundamentally important to look for alternative theories, or at least a modified version of the BCS theory that can account for high-T_c superconductivity. Therefore, a study of the magnetic, structural and SC properties of HTSs and the interplay between different order parameters in HTSs is necessary. In order to perform these studies on a microscopic and macroscopic level a combination of nuclear magnetic resonance (NMR), muon-spin rotation (μSR), magnetization, and x-ray experiments are used in this work.

The thesis is organized as follows: In Chapter 2 a brief review of the theoretical concepts of magnetism and a summary of the main characteristics of superconductivity are presented. Chapter 3 gives an introduction to the μSR and NMR techniques, demonstrating the power of these methods to study microscopic properties of materials. Chapter 4 focuses on the studies of two members $EuFe_2As_2$ and $Ba_{1-x}Rb_xFe_2As_2$ of the so-called 122 family of Fe-HTSs. The SC and magnetic properties, and the interplay between them in $EuFe_2As_2$ are studied as a function of charge carrier doping, chemical as well as hydrostatic pressure. The structural phase transition from the tetragonal to the orthorombic phase is also studied in high quality single crystals of $EuFe_{2-x}Co_xAs_2$. In addition, measurements of the magnetic penetration depth λ in $Ba_{1-x}Rb_xFe_2As_2$ are reported. Chapter 5 covers recent experimental results focussing on the hydrostatic pressure effect on the static magnetic order and superconductivity within the so called “stripe” phase (one of the most remarkable phases observed in cuprates) in the cuprate system $La_{1.875}Ba_{0.125}CuO_4$. The concluding remarks are presented in Chapter 6.

2 Theoretical concepts

In this chapter the theoretical concepts used to describe the magnetic properties of the samples studied in chapters [4.2.1-4.2.4] are briefly reviewed. In addition, a summary of the main characteristics of superconductivity is given.

2.1 Paramagnetism

Magnetism can be categorized into different magnetic states that depend on the response of the magnetic material to an applied magnetic field, which determines the orientation of the spins of the neighboring atoms. The basic magnetic states of materials are discussed in great details in textbooks [34, 35]. Hence we focus only on aspects relevant to this work.

A basic quantity measured by macroscopic magnetic experimental techniques is the bulk magnetic moment $\vec{\mu}$ of a sample. The volume magnetization is defined by $\vec{M} = \vec{\mu}/\mathrm{V}$, where V is the sample volume. The magnetic susceptibility χ represents the magnetic response of the material to an applied field $\vec{H}$: $\vec{M} = \chi\vec{H}$. We note that, in general, χ is a tensor. Only in special cases, *e.g.* for paramagnetic systems in low fields, a linear relationship between $\vec{M}$ and $\vec{H}$ holds. In most magnetic systems χ is not isotropic, but depends on the direction of the field with respect to the crystal axes.

When a free atom interacts with an external magnetic field $\vec{H}$, the Hamiltonian which represents the coupling between $\vec{H}$ and the atom is given by

$$\hat{H}_{mag} = -\mu_B(\vec{L} + 2\vec{S})\vec{H} + \frac{\mu_B}{2}\sum\left[\frac{e}{2c}\vec{r_i}^2\vec{H}\right]\vec{H}, \tag{2.1}$$

where $\vec{L}$ and $\vec{S}$ are the orbital momentum and the spin of the atom, respectively. μ_B is the Bohr magneton and e is the elementary charge. $\vec{r_i}$ denotes the position of the i^{th} electron in the atom. The second term of Eq. (2.1) is simply a mean shift in energy which gives rise to the diamagnetic contribution. The diamagnetic susceptibility is very small and when atoms carry an intrinsic magnetic moment, it is often negligible.

When the quantum axis z is chosen in the direction of the magnetic field and $\vec{H}$ is small, the Hamiltonian of Eq. (2.1) can be treated by perturbation theory. It can be shown that in first order the perturbed energy levels are given by

$$E_a = E_{M_J} = -g_J\mu_B M_J H, \tag{2.2}$$

where J is the total angular momentum, M_J is the quantum number which characterizes the $2J{+}1$ states of the atom and g_J is the Landé factor

$$g_J = \frac{3}{2} + \frac{S(S+1) - L(L+1)}{2J(J+1)}. \tag{2.3}$$

At high temperatures and in the absence of an applied field, the sample does not exhibit a net magnetization since thermal agitation will ensure a random occupation of the $2J{+}1$ states in the multiplet. The action of a magnetic field will tend to orient the magnetic moments along its direction. It was shown that in the limit of small field and high temperature the mean magnetic moment measured along the field direction is given by

$$\vec{\mu} = \frac{\mu_0 g_J^2 \mu_B^2 J(J+1)}{3k_B T}\vec{H}. \tag{2.4}$$

The susceptibility for a system of N non-interacting ions per unit volume is given by

$$\chi_{para} = \frac{N\mu}{H} = \frac{C}{T}, \tag{2.5}$$

where

$$C = N\frac{\mu_0 g_J^2 \mu_B^2 J(J+1)}{3k_B} \tag{2.6}$$

is the Curie constant. This is the well-known Curie law for the paramagnetic susceptibility.

2.2 Magnetic interactions

The microscopic magnetic moments associated with ions in a solid interact with each other. The ordinary interaction which might be expected to play a role is the magnetic dipolar interaction. However, this interaction is too weak [34] to account for the ordering of most magnetic materials. A much stronger interaction between the magnetic ions occurs through quantum mechanical forces, the so called exchange interaction, which is responsible for the phenomenon of long range magnetic order. Exchange interactions depend on the separation of the magnetic ions as well as on their geometrical arrangement, leading to a variety of magnetic orders in solids. The exchange coupling between the moments is described in different ways, but the basis of all exchange forces is the Pauli exclusion principle (see Fig. 2.1).

2.2.1 Direct exchange

Direct exchange is a coupling between magnetic ions that are close enough to have significant overlap of their wave functions. This coupling decreases rapidly as the ions are separated. The exchange interaction is well described by the Heisenberg model. This model considers a simple model with just two electrons with the spatial coordinates $\vec{r}_1$, $\vec{r}_2$ and the corresponding wave functions $\psi_a(\vec{r}_1)$, $\psi_b(\vec{r}_2)$. It was shown that the effective Hamiltonian of two electronic states is given by [34]

$$\hat{H} = \frac{1}{4}(E_S + 3E_T) - (E_S - E_T)\vec{S}_1\vec{S}_2, \tag{2.7}$$

where $E_S = \int \Psi_S{}^* \hat{H} \Psi_S \mathrm{d}\vec{r}_1 \mathrm{d}\vec{r}_2$ and $E_T = \int \Psi_T{}^* \hat{H} \Psi_T \mathrm{d}\vec{r}_1 \mathrm{d}\vec{r}_2$ denote the energies of spin singlet (S = 0) and spin triplet (S = 1) states, respectively. Here, Ψ_S and Ψ_T represent the wave functions, that obey the particle exchange symmetry, describing the spin singlet and triplet

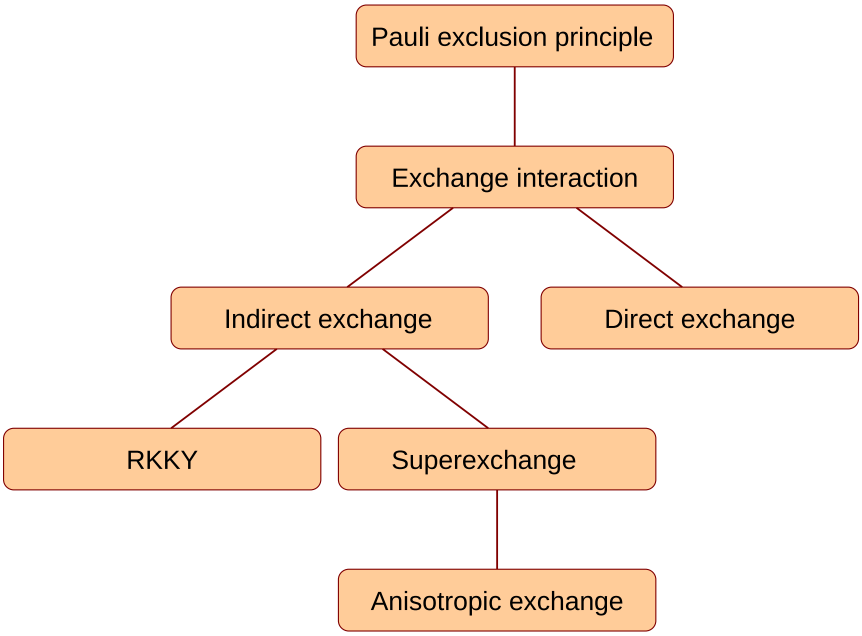

Figure 2.1: Hierarchy of exchange couplings. The Pauli exclusion principle is the basis of all exchange forces. Based on [36, 37].

states, respectively. The first term in the Hamiltonian of Eq. (2.7) is a constant, related to the Coulomb interaction. The second term is spin-dependent and accounts for the interactions between nearest-neighbour magnetic moments. The exchange constant J is defined by

$$J = \frac{E_S - E_T}{2} = \int \psi_a^*(\vec{r}_1)\psi_b^*(\vec{r}_2)\hat{H}\psi_a(\vec{r}_2)\psi_b(\vec{r}_1)d\vec{r}_1 d\vec{r}_2. \tag{2.8}$$

and thus the spin dependent term in the Hamiltonian may be written as

$$\hat{H}^{spin} = -2J\vec{S}_1\vec{S}_2. \tag{2.9}$$

The type of direct exchange interaction depends on the sign of the exchange integral J: For $J > 0$ ($E_S > E_T$), the energy of the high spin state is favored, which leads to ferromagnetic (FM) coupling. For $J < 0$ ($E_T > E_S$), the energy of the singlet spin state is lower, giving rise to antiferromagnetic (AFM) coupling.

2.2.2 Indirect exchange

Often the direct exchange mechanism does not determine the magnetic properties because of insufficient direct overlap of the neighbouring orbitals. For instance, in rare earths the $4f$ electrons have spatially confined wave functions and are strongly localized. Thus, in many magnetic materials it is important to consider some type of indirect exchange interaction. Indirect exchange in insulators is called superexchange and was first introduced by Kramers in 1934 [38]. He pointed out that the ions could cause spin dependent perturbations in the wavefunctions of intervening ions, thereby transmitting the exchange effect over large distances, but no specific mechanisms were discussed. In 1950 Anderson [39] refined

Kramer's approach. The idea can be illustrated by two Mn^{2+} and one O^{2-} ions arranged collinearly. The simplest model requires the consideration of four electrons. The ground state consists of one electron on each Mn^{2+}, and two electrons on the O^{2-} ion in identical p orbitals. The p orbitals have a dumbbell shape that coincides with the axis joining the two Mn^{2+} ions. Because of the overlap of their wavefunctions, one of p electrons from the O^{2-} ion hops over to one of the Mn^{2+} ions. The remaining unpaired p electron on the O^{2-} ion then enters into a direct exchange with one electron of the other Mn^{2+} ion. The superexchange interaction between the Mn^{2+} spins is then AFM.

In 1959 Anderson [40] proposed a new theory of the superexchange interaction from a different view point. He considered molecular orbitals formed of the admixture of the localized $3d$ orbitals and p orbitals of the intervening negative ion. A considerably more satisfactory system of semi-empirical rules was developed over a period of years by Goodenough [41] and Kanamori [42]. These rules have the important feature of taking into account the occupation of the various d levels as dictated by ligand field theory. The main features of the superexchange interactions are usually explained in terms of the so-called Goodenough-Kanamori-Anderson rules. According to these rules, a 180° superexchange (the magnetic ion-ligand-magnetic ion angle is 180°) of two magnetic ions with partially filled d shells is strongly AFM, whereas a 90° superexchange interaction is FM and much weaker.

In metals the exchange interaction can be mediated by the conduction electrons. A localized magnetic moment polarizes the spins of the conduction electrons and this polarization couples to neighbouring localized moments. It is known as the RKKY interaction, named after its principal investigators, Ruderman and Kittel [43], Kasuya [44] and Yoshida [45]. The coupling takes the form of an $\vec{r}$-dependent exchange interaction $J_{RKKY}(\vec{r})$ given by

$$J_{RKKY} = N_F F(2k_F|\vec{r}|), \tag{2.10}$$

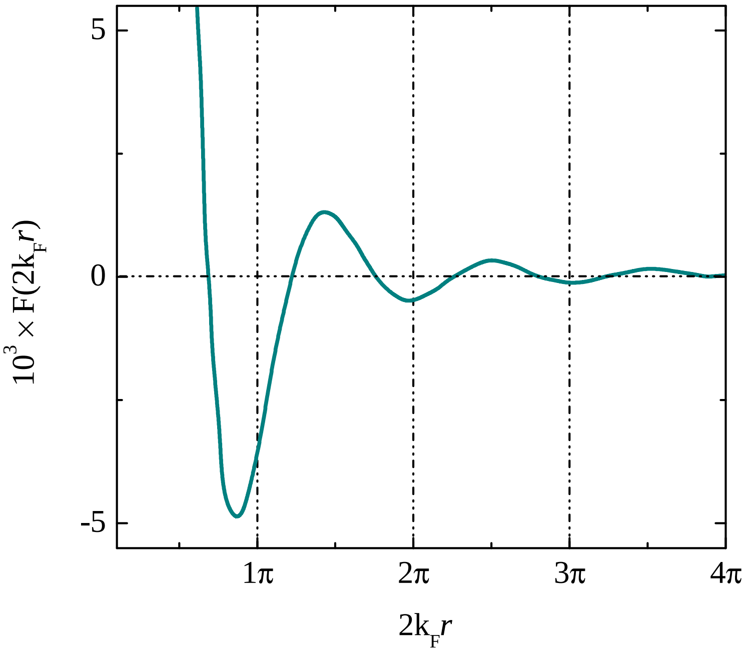

Figure 2.2: The function $F(2k_F r)$ of Eq. (2.11) illustrating the spatial oscillations of the RKKY interaction.

here k_F is the Fermi surface wave number and N_F is the density of states at the Fermi level E_F [46]. The function F is expressed as

$$F(2k_F|\vec{r}|) = \frac{-2k_F|\vec{r}|\cos(2k_F|\vec{r}|) + \sin(2k_F|\vec{r}|)}{(2k_F|\vec{r}|)^4} \tag{2.11}$$

Assuming a spherical Fermi surface with radius k_F (at large distances), the coupling takes the form

$$J_{RKKY} \propto \frac{\cos(2k_F|\vec{r}|)}{|\vec{r}|^3}. \tag{2.12}$$

The RKKY interaction is unique because J_{RKKY} oscillates from positive to negative as the separation between the ions changes (Fig. 2.2). It provides an important mechanism for magnetic coupling between localized moments in metals. One moment produces an oscillatory magnetization of the electron gas which interacts with a second moment. Coupling can be either FM or AFM, depending on the distance between two moments.

2.2.3 Dzyaloshinsky-Moriya interaction

The interactions discussed above do not account for an exchange interaction that is anisotropic. One of the sources of such an anisotropy is spin-orbit coupling. A theory of anisotropic superexchange interaction is developed by extending the Anderson theory of superexchange to include spin-orbit coupling. It is possible that the spin-orbit interaction plays a similar role as the oxygen in the superexchange interaction. In this case the excited state in one of the magnetic ions is produced by the spin-orbit coupling of the anion. There is then an exchange interaction between the excited state of an ion and the ground state of an other ion. For metals the interaction arises, because the spin information carried between the cations by itinerant electrons (that are mediators for RKKY interaction) is upset by the spin-orbit coupling in the anion orbitals. This interaction is known as the anisotropic exchange or the Dzyaloshinsky-Moriya (DM) interaction [47, 48, 49, 50, 51]. The DM interaction leads to an additional term in the Hamiltonian:

$$\hat{H}_{DM} = \vec{D} \cdot \vec{S}_1 \times \vec{S}_2. \tag{2.13}$$

The vector $\vec{D}$ (which is proportional to the strength of the spin-orbit interaction) vanishes when the crystal field has an inversion symmetry with respect to the centre between the two magnetic ions. The form of the interaction is such that it favors the spins to be at right angles to the plane perpendicular to the vector $\vec{D}$. The effect is very often to cant the spins by a small angle (see Fig. 2.3). It was observed in AFM materials, resulting in a small FM component perpendicular to the easy-axis of the antifferomagnet [47, 49].

2.3 Basic quantities characterizing the superconducting state

Many important properties of superconductors follow from an understanding of the difference between the symmetry of the SC and the normal state, *i.e.*, an understanding of

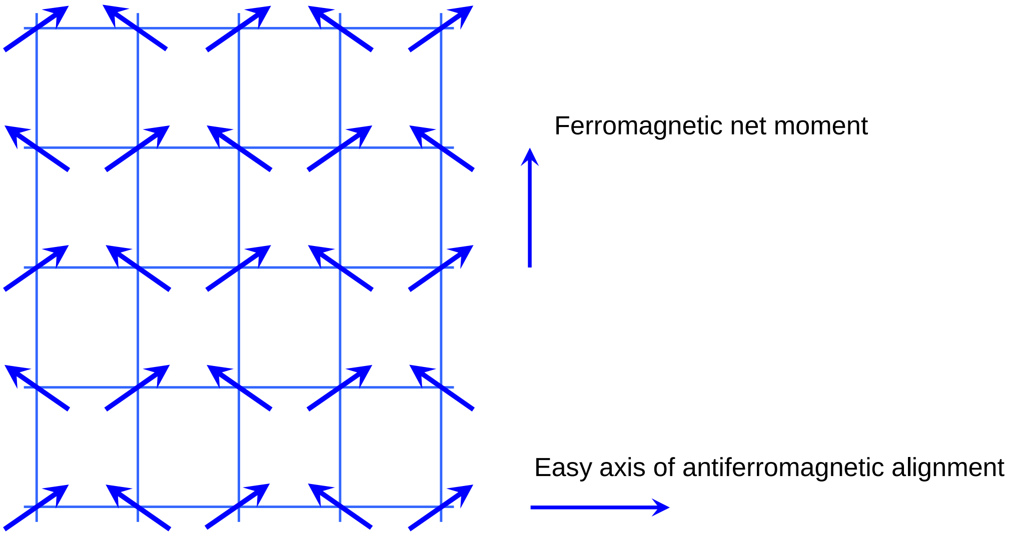

Figure 2.3: Illustration of the spin canting due to the Dzyaloshinsky-Moriya interaction. This interaction gives rise to a FM component perpendicular to the easy-axis in initially antiferromagnetically ordered materials.

the nature of the order parameter arising from the phase transition between these states. A quantitative description of superconductors near the transition point was given by Ginzburg and Landau in 1950 [7]. The Ginzburg-Landau (GL) theory is based on general ideas associated with the Landau theory [52] of second-order phase transitions. It was proposed that the free energy F of a superconductor near T_c can be expressed in terms of a complex, macrosopic order parameter $\psi = |\psi|\mathrm{e}^{i\phi}$ of the SC phase. Assuming that the order parameter is small near T_c and changes slowly in space, the free energy may be written in the form [7]:

$$F = F_\mathrm{n} + \alpha|\psi|^2 + \frac{\beta}{2}|\psi|^4 + \frac{1}{2m_e^*}\left|\left(\frac{\hbar}{i}\vec{\nabla} - e^*\vec{A}\right)\psi\right|^2 + \frac{\mu_0\vec{H}^2}{2}, \tag{2.14}$$

where $m_e{}^*$ denotes the effective mass, e* the charge of the SC carriers, F_n the free energy at $\psi = 0$ (*i.e.* free energy of the normal state), and α, β are expansion coefficients. $\vec{A}$ is the magnetic vector potential, μ_0 is the magnetic constant, and $\vec{H} = \frac{1}{\mu_0}(\vec{\nabla} \times \vec{A})$ is the applied magnetic field.

Using the variational principle one derives the two Ginzburg-Landau equations:

$$0 = \alpha|\psi| + \beta|\psi|^2\psi + \frac{1}{2m_e^*}\left(\frac{\hbar}{i}\vec{\nabla} - e^*\vec{A}\right)^2\psi, \tag{2.15}$$

$$\vec{j}_\mathrm{s} = \frac{e^*}{m_e^*}|\psi|^2\left(\hbar\vec{\nabla}\phi - e^*\vec{A}\right). \tag{2.16}$$

Here $|\psi|^2 = n_\mathrm{s}^*$ is the density of the SC carriers and $\vec{j}_\mathrm{s}$ the density of the SC currents.

The presence of the gradient term in Eq. (2.16) means that the GL theory contains a characteristic parameter, with the dimensions of a length, called the *coherence length* ξ. It is given by

$$\xi = \sqrt{\frac{\hbar^2}{2m_e^*\,|\alpha|}}. \tag{2.17}$$

ξ defines the scale of the spatial change of the wave function $\psi(\vec{r})$. If the gradient of the phase is neglected, then Eq. (2.16) is equivalent to the London equation [6]

$$\vec{j}_{\mathrm{s}} = -\frac{\vec{A}}{\mu_0 \lambda^2}, \tag{2.18}$$

where the quantity λ is given by

$$\lambda = \sqrt{\frac{m_e^*}{\mu_0 n_{\mathrm{s}}^* e^{*2}}}. \tag{2.19}$$

It is called the London magnetic penetration depth. λ controls the ability of a superconductor to screen magnetic fields over a distance λ. λ and ξ are two of the most important length scales characterizing a superconductor.

The ratio of the two characteristic lengths defines the GL parameter [53, 54]

$$\kappa = \frac{\lambda}{\xi} \tag{2.20}$$

λ has the same temperature dependence as ξ. Hence, the dimensionless parameter κ does not depend on temperature. κ depends on the properties of the material and characterizes the superconductor. The values of κ differ widely among superconductors. The majority of pure metals have a relatively small $\kappa \sim 0.01$ to 0.2. For SC alloys large values of κ are typical. The HTSs are very anisotropic and correspondingly the values of κ range from 50 to 500 depending on direction. The behavior of superconductors in a magnetic field with small and large values of κ is completely different. It allows to identify different types of superconductors: type I and type II. Superconductors with $\kappa < 1/\sqrt{2}$ are of I type [55, 56]. In this case the surface energy associated with a boundary between a normal and SC material is positive. Positive surface energy leads to a sharp boundary between two phases. Application of a magnetic field on a type I supercondutor induces perfect diamagnetism up to the critical field H_{c} where superconductivity is fully suppressed. This ideal diamagnetism

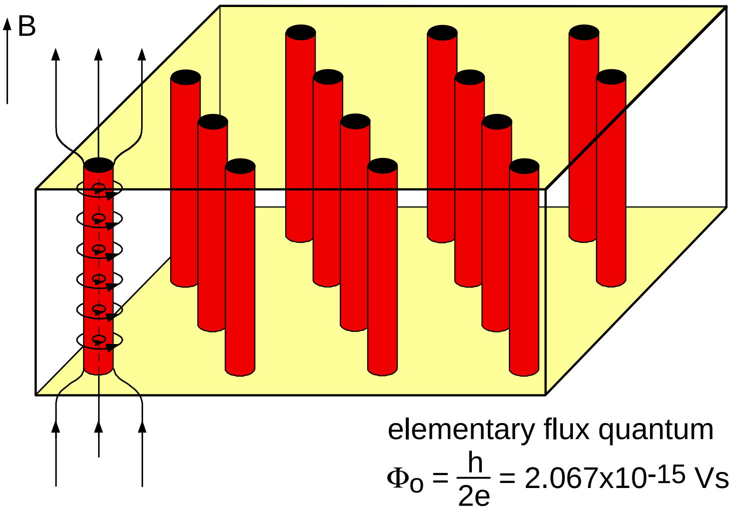

Figure 2.4: A lattice of flux lines in a type-II superconductor in the presence of an applied external field $\vec{B}$.

is called *Meissner-Ochsenfeld effect*. Materials with $\kappa > 1/\sqrt{2}$ are of II type. For type II superconductors the surface energy is negative. Instead of a discontinuous breakdown of superconductivity at H_c, it is energetically favorable to have a mixture of normal and SC regions for magnetic fields around H_c. A continuous increase in field penetration was observed starting at a lower critical field H_c1. The magnetic field penetrates the sample in the form of quantized flux lines (vortices), each containing an elementary flux quantum $\Phi_0 = \mathrm{h}/2\mathrm{e} \simeq 2.068 \times 10^{-15}$ Vs [56] (see Fig. 2.4). Note that the vortices are arranged in a regular lattice. This lattice is reffered to as a flux-line lattice (FLL) and typically has a hexagonal or square geometry [56]. Superconductivity is destroyed at a second critical field H_c2 which is much higher than H_c in type I superconductors. For fields H between H_c1 and H_c2 the superconductor is in the so-called *mixed state*, while the state for $H < H_\mathrm{c1}$ is called the *Meissner phase*.

3 Experimental techniques

3.1 Muon spin rotation (μSR)

The acronym μSR stands for muon spin rotation, or relaxation, or resonance, depending respectively on whether the muon spin motion is predominantly a rotation (more precisely a precession around a magnetic field), or a relaxation towards an equilibrium direction, or a more complex dynamics dictated by the addition of short radio frequency pulses. High sensitivity (because of the large magnetic moment of the muon) to extremely small magnetic moments (down to 10^{-3}-10^{-4} μ_{B}) and the broad time window of 10^{-4} s to 10^{-11} s makes μSR a powerfull tool to investigate magnetism in solid state physics. Moreover, the μSR technique has a unique time window for the study of magnetic fluctuations in materials, which is complementary to other experimental techniques such as neutron scattering, NMR or magnetic susceptibility. In addition to magnetism, this technique allows to study interesting problems related to superconductivity, chemical kinetics, diffusion, molecular dynamics, and semiconductor physics. In this chapter a brief introduction to the μSR technique and its applications to the study of magnetic and SC materials are presented. A detailed description of the μSR technique can be found in textbooks [57, 58] or in review articles [59, 60, 61, 62].

3.1.1 Production of spin polarized muon beams and parity violating decay

The muon is an elementary particle similar to the electron or positron, with a unitary positive or negative electric charge (± 1) and a spin of 1/2 [63]. The muon is a particle belonging to the family of the leptons with an average lifetime of $\tau_\mu = 2.2$ μs. The muon mass is about $1/9^{th}$ of the proton mass or, alternatively, about 200 times the electron mass [63]. Note that for experiments in condensed matter physics mainly the positive muon is used. Beams of positive muons are artificially produced using proton accelarators. High energy proton beams are fired onto a target (usually graphite) to produce pions via the following process:

$$p + p \rightarrow \pi^+ + p + n, \tag{3.1}$$

where p denotes the proton and n is a neutron. The pions π^+ decay with a lifetime of $\tau_\pi =$ 26 ns into muons:

$$\pi^+ \rightarrow \mu^+ + \nu_\mu, \tag{3.2}$$

where ν_μ is a muon neutrino. Lets consider pions which are produced at rest in the laboratory frame. According to the momentum conservation law, the muon μ^+ and the neutrino ν_μ must have equal and opposite momentum. Since the pion π^+ has zero spin the muon spin must be opposite to the neutrino spin. An interesting property of the neutrino is that its spin is aligned antiparallel to its momentum (it has negative helicity). This implies that the muon also has negative helicity. Thus by selecting pions which stop in the target a beam of 100 % spin-polarized muons is produced. This is the method most commonly used for producing muon beams for condensed matter physics research [59]. Note that the muons poduced by the above mentioned way are called surface muons [64], and have a well defined kinetic energy of 4.1 Mev and a corresponding momentum of 29.8 MeV/c.

When a beam of the spin polarized muons is implanted into a specimen of interest [65], the muons thermalize in the sample within typically 1 ns. Muons with positive charge stop at interstitial positions away from positively charged ions. In the presence of a magnetic field, the spin of the implanted muon precesses around the direction of the local magnetic field B with the Larmor frequency:

$$\omega_\mu = \gamma_\mu B, \tag{3.3}$$

where $\gamma_\mu = 2\pi\cdot$ 135.5MHz/T is the gyromagnetic ratio of the muon. An implanted μ^+ in the sample will decay after a mean life time of $\tau_\mu = 2.2$ μs. The muon decay is a three body process:

$$\mu^+ \rightarrow e^+ + \nu_e + \bar{\nu}_\mu, \tag{3.4}$$

where e^+ denotes the positron, ν_e the electron neutrino, and $\bar{\nu}_\mu$ the muon antineutrino. The kinetic energy of the emitted positron may vary continuously between zero and $E_{\mathrm{max}} = 52.3$ MeV. Because of the parity violating decay of the muon (the decay involves the weak interaction) the decay positrons are emitted preferentially along the direction of muon spin. By measuring the anisotropy of the decay positrons from a bunch of muons, the statistical average direction of the spin polarization of the muon ensemble is determined. This in turn reflects the spatial and temporal distribution of magnetic fields at the muon site.

The μSR technique is made possible by the unique properties of the pion and the muon: (i) Due to parity violation in the decay of pions, surface muons are 100 % spin polarized, (ii) the positron is preferentially emitted along the direction of the muon spin at decay time, and (iii) the muon has a magnetic moment and its spin precesses around a magnetic field with the Larmor frequency.

3.1.2 Principle of a μSR experiment

In the following the principle of a μSR experiment will be explained. The μSR method is based on the observation of the time evolution of the spin polarization $\vec{P}(\mathrm{t})$ of the muon ensemble. A schematic layout of a μSR experiment is shown in Fig. 3.1a. The muons implanted in the sample will decay after a mean life time of $\tau_\mu = 2.2$ μs, emitting a fast positron preferentially along its spin direction [see Eq. (3.4)]. Various detectors placed around the sample track the incoming μ^+ and the outgoing e^+. Namely, as soon as the μ^+ detector records the arrival of a μ^+ in the specimen, the electronic clock starts. The clock is stopped when the decay positron e^+ is observed in one of the e^+ detectors, and the measured time is stored in a histogramming memory. In this way a positron-count versus time histogrm is formed. A muon decay event requires that within a certain time interval after a μ^+ has stopped in the sample, the corresponding decay e^+ is detected. This time interval extends usually over several muon lifetimes (*e.g.* 10 μs) [57]. An electronic trigger

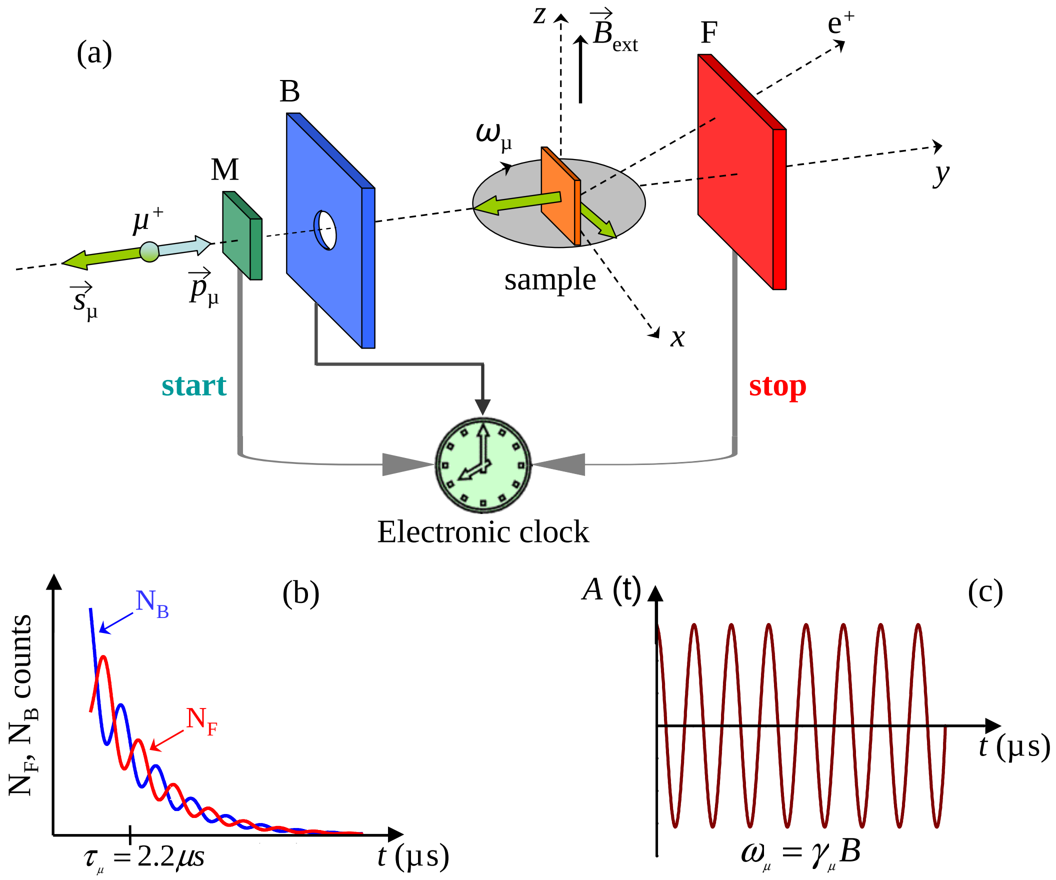

Figure 3.1: Principle of a μSR experiment. (a) overview of the experimental setup. Spin polarized muons with spin $\vec{S}_\mu$ antiparallel to the momentum $\vec{p}_\mu$ are implanted in the sample placed between the forward (F) and the backward (B) positron detectors. A clock is started at the time the muon enters the muon detector (M) and stopped as soon as the decay positron is detected in detector F or B. (b) The number of detected positrons N_F and N_B as a function of time for the forward and backward detector, respectively. (c) The asymmetry signal calculated according to Eq. (3.6).

logic ensures that only those events are accepted where a single muon was inside the sample during the observation period, so that the start and the stop signals originate from the same muon event. After a bunch of muons stopped in the sample, one obtains histograms for the forward $N_{\mathrm{e^+F}}$ and the backward $N_{\mathrm{e^+B}}$ detectors as shown in Fig. 3.1b, which in the ideal case has the following form:

$$N_{e^+F(B)}(t) = N_0 e^{-\frac{t}{\tau_\mu}}(1 + A_0 \vec{P}(t)\hat{n}_{F(B)}) + N_{bgr}. \tag{3.5}$$

Here, $\vec{P}$(t) is the muon-spin polarization function with the unit vector $\hat{n}_{F(B)}$ with respect to the incoming muon spin polarization. The exponential factor $N_0 e^{-\frac{t}{\tau_\mu}}$ accounts for the radioactive muon decay. N_{bgr} is a background contribution due to uncorrelated starts and stops. A_0 is the initial asymmetry. It depends on different experimental factors, such as the detector solid angle, efficiency, absorption, and scattering of positrons in the material. Typical values of A_0 are between 0.2 and 0.3. Note that Eq. (3.5) is given for the ideal case, when the two detectors (F and B) are identical, so that the quantities N_0, N_{bgr}, and A_0 are

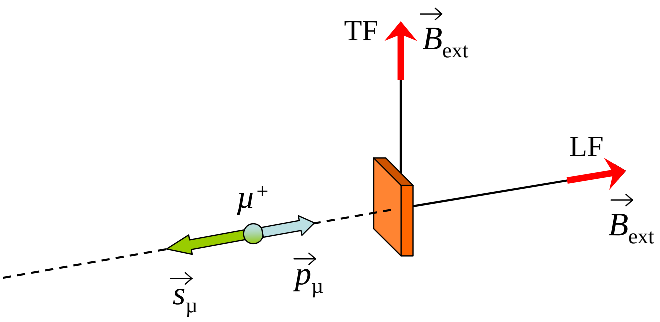

Figure 3.2: Schematics of a TF and a LF μSR configurations (see text for an explanation).

the same in both detectors. In this idealistic situation the histograms recorded by the two detectors differ only by the phase. If the detectors are aligned precisely opposite to each other, the difference between the phases of the histograms is 180°.

Since the positrons are emitted predominantly in the direction of the muon spin which precesses with ω_μ, the forward and backward detectors will detect a signal oscillating with the same frequency. In order to remove the exponential decay due to the finite life time of the muon, the so-called asymmetry signal $A(\mathrm{t})$ is calculated (see Fig. 3.1c) [66]:

$$A(t) = \frac{N_{e^+F}(t) - N_{e^+B}(t)}{N_{e^+F}(t) + N_{e^+B}(t)} = A_0 P(t), \tag{3.6}$$

where, $N_{e^+F}(\mathrm{t})$ and $N_{e^+F}(\mathrm{t})$ are the number of positrons detected in the forward and backward detectors, respectively. The quantities $A(\mathrm{t})$ and $P(\mathrm{t})$ depend sensitively on the spatial distribution and dynamical fluctuations of the magnetic environment of the muons. Hence, these functions allow to study interesting physics of the investigated system.

In μSR experiments two different magnetic field configurations are used: (i) Transverse field (TF) μSR involves the application of an external field perpendicular to the initial direction of the muon spin polarization (see Fig. 3.2). The muon spin precesses around the transverse field, with a frequency that is proportional to the size of the field at the muon site in the material. (ii) In the longitudinal field (LF) configuration the magnetic field is applied parallel to the initial direction of the muon spin polarization (see Fig. 3.2). The time evolution of the muon spin polarization along its initial direction is measured in this configuration. Measurements can be also carried out in the absence of external magnetic field, a configuration called zero-field (ZF) μSR. In this configuration the frequency of an obtained μSR signal is proportional to the internal magnetic field, from which the size of the ordered moment and thus the magnetic order parameter is calculated. The capability of studying materials in zero external field is a big advantage over other magnetic resonance techniques.

All μSR experiments related to this thesis were performed at the Paul Scherrer Institute.

3.1.3 Applications of μSR in magnetism and superconductivity

μSR has been widely applied to magnetic materials due to the high sensitivity of the muon to small fields and its capability to probe both static and dynamic local field distributions. ZF μSR is used to investigate microscopic magnetic properties of solids. If the local magnetic field $\vec{B}(\vec{r})$ at the muon site is pointing under an angle θ with respect to the initial muon spin polarization, the decay positron asymmetry is given by [66]:

$$A(t) = A_0[\cos^2(\theta) + \sin^2(\theta)\cos(\gamma_\mu Bt)], \tag{3.7}$$

where A_0 is the maximal value of the asymmetry. Further assuming that the random fields are isotropic and each component can be represented by a Gaussian distribution of width Δ/γ, then a statistical average of this distribution yields:

$$A(t) = A_0\Big[\frac{1}{3} + \frac{2}{3}e^{-\Delta^2 t^2/2}(1 - \Delta^2 t^2)\Big], \tag{3.8}$$

This function was first obtained in a general stochastic treatment of Kubo and Toyabe [67]. The form of the distribution of internal magnetic fields influences the form of the μSR signal [67, 68, 69]. Thus, by analysing the observed muon-spin time evolution, the magnetic field distribution inside the sample can be obtained. If there is an inhomogeneous static internal field in the sample, different muons will precess at slightly different frequencies. This leads to a progressive dephasing of the μSR signal, and the oscillations in the μSR time spectra will be damped. In some cases the signal is strongly damped, so that the oscillation will not be observed, and the resulting muon spin polarization will be averaged out to zero. Then, at a magnetic phase transition, if no wiggles are observed in the μSR signal, one expects a drop in the effective initial asymmetry from A_0 in the paramagnetic state to $A_0 = 1/3$ in the ordered state [62]. However, this effect could also be due to fluctuations of the internal field. μSR is capable to distinguish between these two possibilities by performing a LF-μSR experiment (see Sec. 3.1.2). In a longitudinal field inhomogeneous line broadening and fluctuations lead to different μSR time spectra.

μSR is also valuable for studying materials in which magnetic order is random or of short range. Moreover, μSR is very helpfull to study samples containing multiple phases or samples which are partially magnetically ordered. This is because muons stop uniformly throughout a sample, and the amplitudes of the μSR signals arising from the different regions of the sample are proportional to the volume of the sample occupied by a particular phase. Thus, μSR provides quantitative information on coexisting and competing phases in a material.

The rapid development of the μSR technique was trigerred by the discovery of the cuprate HTSs in 1986. In a sizeable applied magnetic field (above the first critical field) a type II superconductor is characterized by a large internal field inhomogeneity due to the penetration of quantized flux lines, called vortices (see Fig. 2.4) [55]. These vortices have a core of radius $\approx \xi$ (coherence length), and they carry a flux tube of radius λ (magnetic field penetration depth). λ and ξ are introduced in chapter 2.3 [53]. μSR studies of vortex matter usually involve TF μSR (see Sec. 3.1.2) [60], *i.e.* the measurements give access to the field distribution characterising this mixed phase. The field distribution $P(B)$ in the vortex state is the probability that at a randomly chosen point in the sample the magnetic field has a value B. This is shown in Fig. 3.3 for an ideal vortex lattice. $P(B)$ is highly asymmetric, the high field "tail" corresponding to regions of the lattice close to the vortex cores. The maximum of the distribution occurs below the mean field $\langle \mathrm{B} \rangle$. Implanted muons in a superconductor in the vortex state will sit at certain crystallographic sites and the muon spin precesses around the transverse field. The muons implanted close to the vortex core

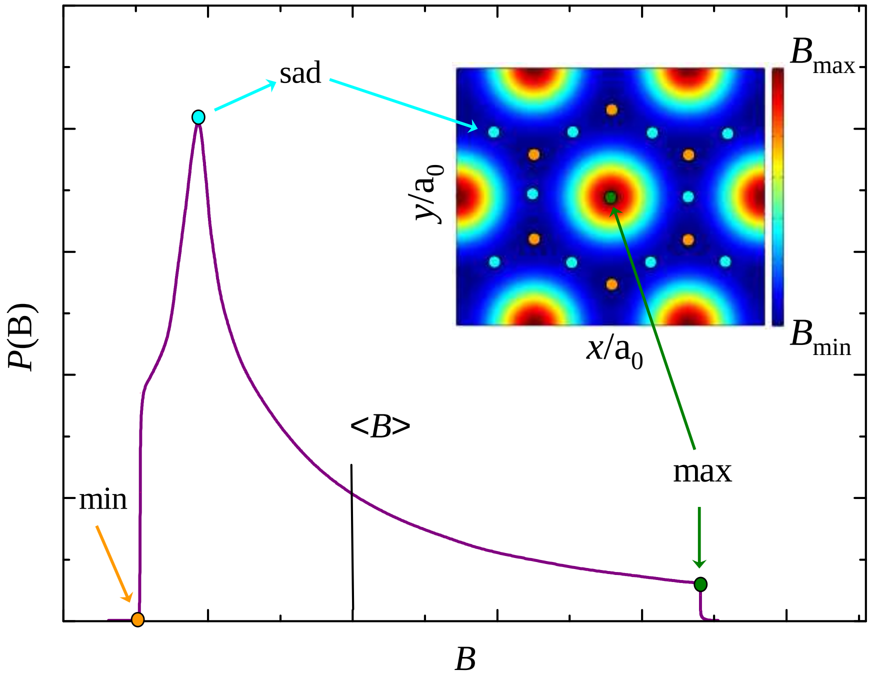

Figure 3.3: The field distribution $P(B)$ in the vortex lattice. Contours of B are shown in the inset.

experience a larger magnetic field than those implanted between vortices. Consequently, there is a spread in precession frequencies, which results in a dephasing of the observed precession signal. By this random sampling of the field in the vortex state by the muon, the field distribution $P(B)$ in the vortex lattice is probed leading to the following asymmetry function:

$$A(t) = A_0 \int P(B) \cos(\gamma_\mu B t + \varphi) dB, \tag{3.9}$$

where A_0 denotes the initial asymmetry and φ is the initial phase of the muon-spin ensemble. Since the muon is a local probe, the μSR relaxation function is given by the weighted sum of all oscillations. By performing a Fourier transformation of the μSR time spectra $P(B)$ profiles are obtained. For an isotropic extreme type II superconductor ($\lambda \gg \xi$) in the vortex state (ideal FLL) it was shown that λ is directly related to the second moment $\langle \Delta \mathrm{B}^2 \rangle$ of $P(B)$ [70, 71, 72]:

$$\langle \Delta B^2 \rangle \approx 7.5 \times 10^{-4} (1-b)^2 [1 + 3.9(1-b)^2] \phi_0^2 \lambda^{-4}, \tag{3.10}$$

where b=$\langle \mathrm{B} \rangle / B_{c2}$ is the reduced magnetic field. $\langle \mathrm{B} \rangle$ denotes the first moment of $P(B)$ and B_{c2} is the second critical field of a type II superconductor. For estimating $\langle \Delta \mathrm{B}^2 \rangle$ from the measured $P(B)$ a sum of N Gaussian distributions was found to be a reasonable approximation for $P(B)$ [73, 74, 75]:

$$P(B) = \frac{\gamma_\mu}{\sqrt{2\pi}(A_1 + ... + A_N)} \sum_{i=1}^{N} (A_i/\sigma_i) \exp[(B - B_i)^2 / 2(\sigma_i/\gamma_\mu)^2], \tag{3.11}$$

where B_i, A_i, and σ_i are the first moment, the weighting factor and the standard deviation of the i-th Gaussian component, respectively. The first and the second moment of $P(B)$ are given by:

$$\langle B\rangle = \sum_{i=1}^{N} \frac{A_i B_i}{A_1 + ... + A_N}, \tag{3.12}$$

and

$$\langle \Delta B^2\rangle = \sum_{i=1}^{N} \frac{A_i}{A_1 + ... + A_N}[(\sigma_i/\gamma_\mu)^2 + (B_i - \langle B\rangle)^2]. \tag{3.13}$$

According to Eq. (3.13) the relaxation rate σ of the observed precession signal can be used to directly determine λ and its temperature dependence. According to London theory $1/\lambda^2$ is proportional to the carrier density n_s of the superconductor [53]:

$$\frac{1}{\lambda^2} = \frac{\mu_0 e^2 n_s}{m^*}, \tag{3.14}$$

where μ_0, e, and m^* are the magnetic permeability of the vacuum, the elementary charge, and the effective mass of a electron, respectively. $n_s(T)$ contains information on the SC gap $\Delta(T)$. Therefore, $\lambda(T)$ gives access to the symmetry of the SC gap and hence the symmetry of the pairing wave function. It was shown that the second-moment method often used to analyse μSR data yields reliable values of λ in the applied field range $H_{c1} \ll H \lesssim H_{c2}$ [75]. More advanced approaches which allow to determine not only λ but also ξ require a theoretical model for the spatial internal field distribution $\vec{B}(\vec{r})$ [75, 76, 77].

In addition to studies of the ideal periodic array of vortices in clean samples, μSR has been shown to be a unique microscopic probe of vortex fluctuations, pinning, flux-lattice melting, and the decomposition of flux lines into two-dimensional “pancake” vortices [78, 79, 80, 81]. With μSR it was possible to access regions of the field-temperature $(B-T)$ phase diagram well below the irreversibility line [78, 80, 81], not accessible by transport measurements. One can also probe vortices at the surface of a superconductor using ultra-low energy muons [82].

3.2 Nuclear magnetic resonance (NMR)

Nuclear magnetic resonance was discovered in 1945 by F. Bloch and E.M. Purcell, who received the Nobel prize in physics for this discovery. This method has proven to be a versatile tool for the elucidation of key properties of condensed matter. It has also remarkable applications in many other scientific areas, for instance in chemistry, biology, geology, medicine, and archeology.

In this chapter we will introduce some basics of NMR, and briefly describe the nuclear spin Hamiltonian, the magnetic shift, and the relaxation behavior of nuclear spins. For further details we refer to the excellent textbooks of Abragam [83] and Slichter [84].

3.2.1 Principle of NMR

To perform a NMR experiment a nucleus with a non-zero spin $(I \neq 0)$ is needed. Many atomic nuclei have a non-zero spin angular momentum $\vec{I}\hbar$ and a dipolar magnetic

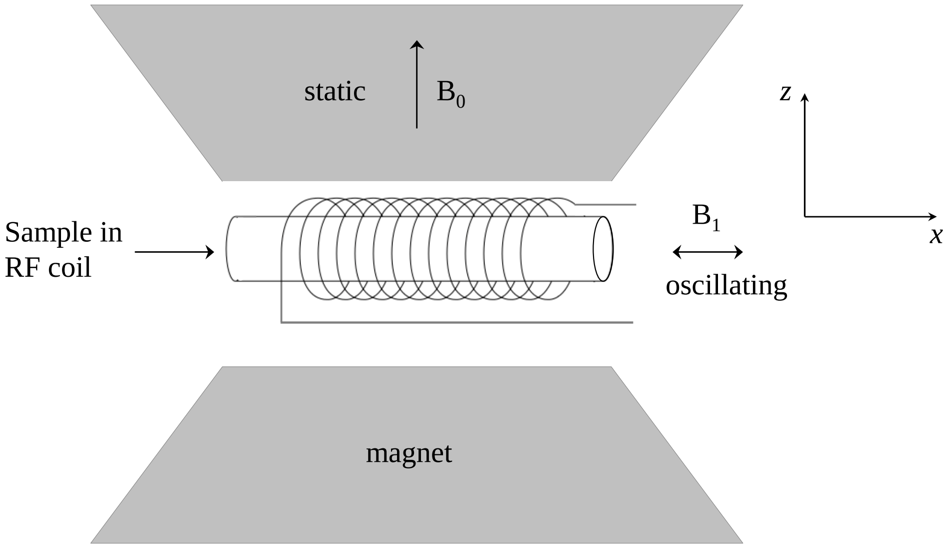

Figure 3.4: Schematic diagram of a NMR experiment. The sample sits inside a RF coil which produces an oscillating RF field. The static field $\vec{B}_0$ and the oscillating field $\vec{B}_1$ are perpendicular to each other.

moment $\vec{\mu} = \gamma\hbar\vec{I}$ collinear with it. Here γ denotes the nuclear gyromagnetic constant. In a NMR experiment a sample is placed inside a coil and a magnetic field $\vec{B}_0$ is applied along a particular direction, say the z-direction (see Fig. 3.4). The energy of a nucleus with a magnetic moment $\vec{\mu}$ in $\vec{B}_0$ is given by

$$E_m = -\mu B_0 = -\hbar\gamma m_I B_0 \tag{3.15}$$

Here, γ is the gyromagnetic ratio, and m_I is the z component of the angular momentum of the nucleus which can only take integral values between I and -I. Thus, the energy E_m corresponds to $2I$+1 equally spaced levels. Exciting transitions between different energy levels with a radiofrequency (RF) field is the basis of nuclear magnetic resonance. The RF field $\vec{B}_1$ ($\vec{B}_1 \ll \vec{B}_0$) is applied perpendicular to the external field $\vec{B}_0$, *i.e.*, in the x-direction (see Fig. 3.4). The selection rules for dipole transitions allow only $\Delta m_I = \pm\, 1$, implying that only transitions between adjacent levels may occur. From Eq. (3.15) the resonance condition becomes

$$\omega_L = \gamma B_0, \tag{3.16}$$

where ω_L is called Larmor frequency. The RF coil not only produces the excitation, but is itself part of a tuned circuit with a large quality factor. As transitions are excited in the nuclei, energy is transferred between the RF circuit and the sample. This results in small changes of the quality factor of the circuit.

In the absence of resonance, the nuclear spins are in thermal equilibrium with their surroundings or “lattice”. According to the fundamental Boltzmann law, the populations P_{m} of the energy levels E_{m} in equilibrium are proportional to exp(-E_m/k_BT) = exp($\gamma\hbar m_I B_0/k_BT$), where k_B is the Boltzmann constant. The nuclear magnetization of a sample containing N spins obeys the well-known Curie law [83, 84]:

$$M = \frac{N\gamma^2\hbar^2 I(I+1)}{3k_BT}B_0 = \frac{1}{\mu_0}\chi_0 B_0, \tag{3.17}$$

where χ_0 is the static nuclear susceptibility. The static nuclear susceptibility is much smaller than the electronic paramagnetic susceptibility (by a factor of the order of 10^{-6} to 10^{-8}). Thus, it is difficult to observe it by conventional magnetostatic methods.

3.2.2 Spin Hamiltonian for nuclei with a quadrupole moment

An important nuclear property is the nuclear quadrupole moment Q, which is a measure of the lack of spherical symmetry of the electric charge distribution inside the nucleus. The quadrupolar moment interacts with the local electric field gradient (EFG) in the specimen and induces electric quadrupole transitions between the energy levels of the nuclear spins. When a magnetic field is applied to a sample containing nuclei with quadrupole moments, the nuclear spin Hamiltonian describing the interactions of the investigated nucleus with the external magnetic field and the crystal electric field gradient at the nuclear site is given by the sum of the Zeeman and quadrupolar terms [83, 84]:

$$\hat{H} = \hat{H}_Z + \hat{H}_Q = \gamma\hbar(1+K_\alpha)I_\alpha B_0 + \frac{\hbar\omega_Q}{6[(3I_z^2-1)+\eta(I_x^2-I_y^2)]}. \tag{3.18}$$

Here K_α ($\alpha = x,\, y,\, z$) is the relative magnetic shift in the α direction, I_α ($\alpha = x,\, y,\, z$) are the nuclear spin components, B_0 is the external magnetic field, γ is the gyromagnetic ratio, and the quadrupole frequency ν_Q is defined as:

$$\omega_Q = \frac{3eQV_{zz}}{2I(2I-1)\hbar}, \tag{3.19}$$

where V_zz denotes the major principal axis of the EFG tensor, and η the EFG asymmetry parameter defined as $\eta = (V_\mathrm{xx}\text{-}V_\mathrm{yy})/V_\mathrm{zz}$ $(0 \leq \eta \leq 1)$. We use the standard convention $V_\mathrm{xx} \leq V_\mathrm{yy} \leq V_\mathrm{zz}$. Since the principal axis of the EFG tensor as well as the magnetic shift tensor are defined by the symmetry of the nuclear site, the resonance frequency of a particular nuclear transition depends on the field direction relative to the crystalline axes.

Fig. 3.5 illustrates the effect of the Zeeman and the quadrupole interaction for a nucleus with spin $I = 3/2$. In the absence of a static magnetic field, the remaining term gives rise to double degenerate energy levels, between which nuclear quadrupole resonance (NQR) transitions can be induced. A nucleus with spin $I = \frac{3}{2}$ has two double degenerate energy levels ($\pm\frac{1}{2}$ and $\pm\frac{3}{2}$). In the presence of a large external magnetic field B_0 a splitting of the NMR spectrum into a central line, arising from the central transition ($+\frac{1}{2}$,$-\frac{1}{2}$) and two satellite lines due to the ($\pm\frac{1}{2}$,$\pm\frac{3}{2}$) transitions occurs.

3.2.3 NMR frequency shifts

The signal frequency that is detected in NMR would be a pure Larmor frequency ω_L if the only magnetic field acting on the nucleus is the external magnetic field. Since the nuclei are surrounded by electrons, an interaction between them is present. The magnetic coupling of the nucleus to the electrons arises from internal magnetic fields originating either from the motion of the electrical charges or from the magnetic moment associated with the electron

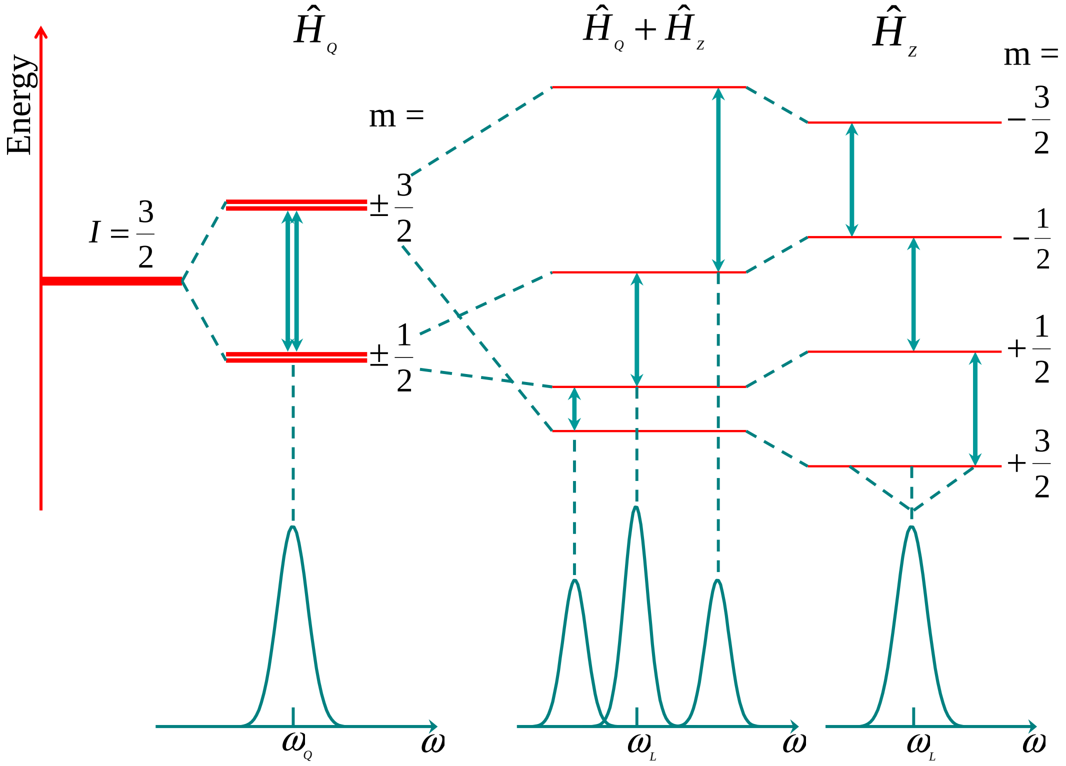

Figure 3.5: Result of the combination of the Zeeman ($\hat{H}_Z$) and the quadrupole ($\hat{H}_Q$) interaction for a spin $I = 3/2$ nucleus in an external magnetic field.

spin. The nuclear spin $\vec{I}$ sees an internal field superimposed to the applied field. This change of the local field at the nucleus causes a shift in resonance frequency. The resulting shift in metals is called Knight shift, which is qualitatively defined as [83, 84]:

$$K = \frac{\Delta B}{B_0} = \frac{\Delta\omega}{\omega_0}, \tag{3.20}$$

where B_0 is the applied field, ΔB is the additional field due to the hyperfine coupling, and $\Delta\omega$ is the corresponding shift in frequency. The origin of the Knight shift is the presence of conduction electrons in metals. In the applied magnetic field, the conduction electrons will be polarized, leading to the Pauli spin susceptibility:

$$\chi_P = \frac{3n\mu_0\mu_B^2}{2E_F}. \tag{3.21}$$

Here μ_0 is the permeability of the vacuum, n is the electron density, μ_B is the Bohr magneton, and E_F is the Fermi energy. The coupling of a given nuclear spin $\vec{I}$ with the electrons is obtained by summing the expectation values of the hyperfine couplings of this spin with all the conduction electrons. This results in the following expression for the isotropic Knight shift (K_{iso}):

$$K_{iso} = \frac{\Delta\omega_{iso}}{\omega_0} = \frac{8\pi}{3}\langle|\psi_k(0)|^2\rangle_F\chi_P = \frac{A}{g\mu_B}\chi, \tag{3.22}$$

$\langle|\psi_k(0)|^2\rangle_F$ is the probability of finding the electron at the nucleus and A is the hyperfine coupling constant. The symbol $\langle\ \rangle_F$ means that an average is made over all orbits at the top of the Fermi distribution. Eq. (3.22) implies that the Knight shift conveys information on the static spin susceptibility and the hyperfine interactions.

Note that Eq. (3.22) is valid when the symmetry of the elctronic environment of the nuclear spin is not lower than cubic. In this case the tensor describing the elctron-nucleus interaction has only non-zero scalar parts. When the symmetry is lower than cubic, the Knight shift will depend on the direction of the applied field with respect to the crystalline axes. The anisotropic part of the Knight shift (K_{anis}) is given by

$$K_{anis} = \frac{\Delta\omega_{anis}}{\omega_0} = \frac{1}{3}(K_{\parallel} - K_{\perp})(3\cos^2\theta - 1), \tag{3.23}$$

where θ is the angle between the crystal symmetry axis and the direction of the applied field. $K_{\parallel}$ and $K_{\perp}$ are the shifts corresponding to $\theta = 0°$ and $\theta = 90°$, respectively.

Similar shifts in non-metallic compounds are called "chemical shifts". The presence of an applied field modifies the occupied energy levels of the system, mixing in higher unoccupied states having a net orbital magnetic moment in the direction of the field. This electron orbital paramagnetism is responsible for the chemical shifts. For simple metals the chemical shift is much smaller than the Knight shift.

3.2.4 Spin-spin and spin-lattice relaxation times

The spin-spin relaxation time T_2 is the time the magnetic moments of the nuclear spins need to get out of phase in the plane perpendicular to the external magnetic field, causing a decay of the transverse components (M_x and M_y) of the magnetization. The components M_x and M_y relax to zero in a time T_2 such that:

$$\frac{dM_x}{dt} = -\frac{M_x}{T_2}, \qquad \frac{dM_y}{dt} = -\frac{M_y}{T_2}. \tag{3.24}$$

There are two ways of determining T_2. One way is to measure it directly from the free induction decay (FID) that develops after a short RF pulse. The problem that occurs in this case is that this method also measures relaxation due to the inhomogeneity of the magnet because this will cause a spread in precession frequencies. One shoud use the method which separates the real spin-spin relaxation from the relaxation mentioned above. One way to achieve this is the spin-echo technique. The discovery of spin echoes using pulsed NMR techniques was made by E. Hahn, which led to the invention of a plethora of pulse sequences to measure magnetic properties of atoms. To generate a spin echo one applies two short RF pulses of amplitude B_1, fixed widths and delay time τ, near the Larmor resonance $\omega \approx \omega_L$. This is known as a $\pi/2$,τ,π pulse sequence. A $\pi/2$-pulse refers to a pulse that lasts a time $\mathrm{t}_{\pi/2}$ such that $\omega \mathrm{t}_{\pi/2} = \gamma B_1 \mathrm{t}_{\pi/2} = \pi/2$ and a π-pulse has double duration.

The spin echo effect is schematically shown in Fig. 3.6. This effect is better understood by breaking a $\pi/2$,τ,π echo pulse sequence down into different steps and looking at the evolution of the magnetization vector of the specimen of interest. Each step in the sequence is denoted by a black circle, as presented in Figs. 3.6a-f. The vertical red arrow in Fig. 3.6a is the equilibrium magnetization vector of the sample, initially pointing in the z-direction, parallel to B_0. First, a $\pi/2$-pulse is used (*i.e.*, transverse field B_1, in the x-direction is applied for a time $t_{\pi/2}$) that rotates the magnetization vector of the sample down into the xy plane, say along the y-direction (Fig. 3.6b). By waiting a small time τ, the magnetization precesses around the static field, staying in the transverse plane. Due to local magnetic field inhomogeneities (variations in the magnetic field at different parts of the sample that are constant in time), as the net moment precesses, some spins slow down due to lower local field strength (and so begin to progressively trail behind) while some speed up due to higher field strength and start getting ahead of the others. This means they progressively dephase with respect to each other (Fig. 3.6c), becoming more separated in angle as they precess round (Fig. 3.6d).

A π-pulse applied at time τ (B_1 again in the x-direction) reverses the phases of the magnetization of individual nuclei (Fig. 3.6e) so that the slower spins lead ahead of the main moment and the fast ones trail behind. Progressively, the fast spins catch up with the main moment and the slow moments drift back toward the main one. After a time τ, the spins will have completely recovered, restoring the state that occured directly following

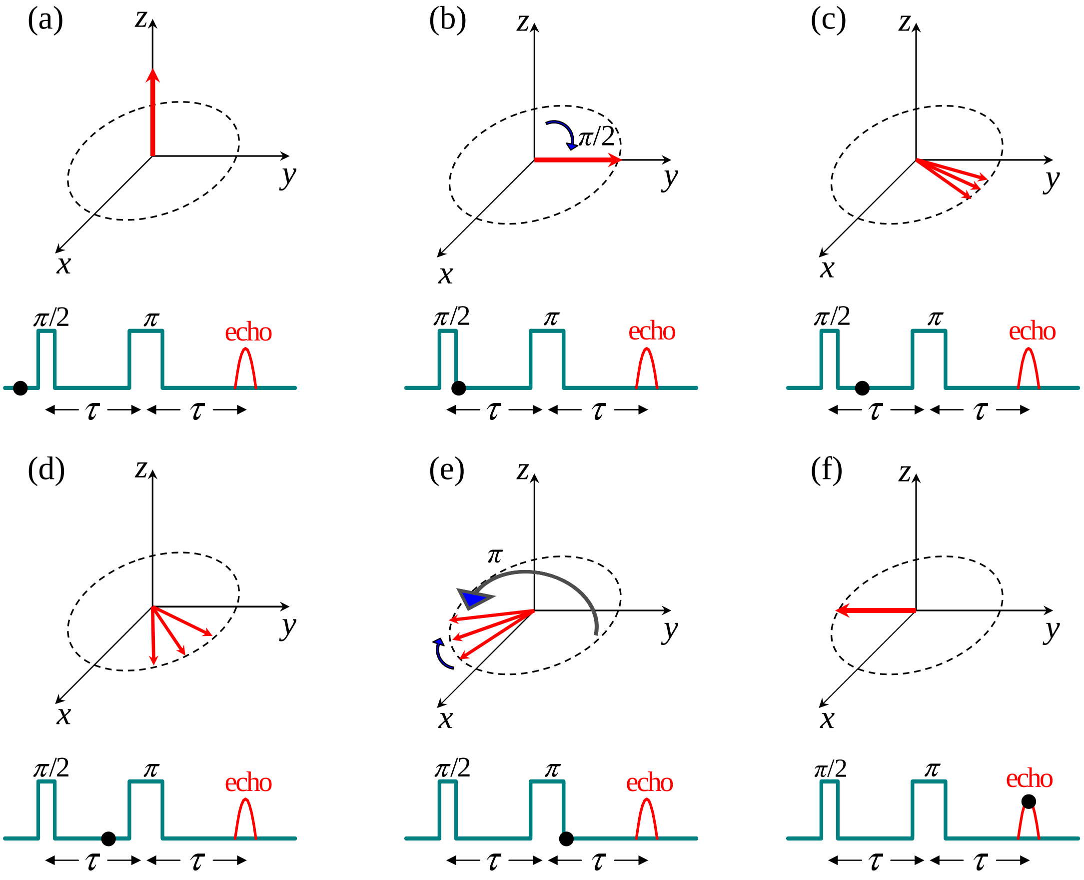

Figure 3.6: The spin echo effect. For clarity the exho pulse sequence $\pi/2$,τ,π is splited into different steps. Each step in the sequence is denoted by black circle. (a) The equilibrium magnetization along the z-direction. (b) Rotation of the spins into the xy plane by application of the $\pi/2$ pulse along the x-axis. (c),(d) The spins progressively dephase with respect to each other, becoming more separated in angle as they precess around. (e) At time $t = \tau$, a π-pulse along the x-axis rotates the spins by 180° around the x-axis. (f) The spins will get together at time 2τ, producing the spin echo signal. The figure is drawn for the case of a short delay between the $\pi/2$ pulse and the π. The figure is adopted from [34].

the first $\pi/2$-pulse, except the magnetization is in the -y direction (Fig. 3.6f). This means that at time 2τ after the first pulse a spin echo signal is produced. Because of the spin-spin interaction, which is due to time-dependent fluctuating random magnetic fields due to neighbouring nuclei, the echo signal intensity will be reduced by increasing pulse spacing time τ. The time evolution of the spin-echo amplitude A can be expressed as [84]:

$$A(2\tau) = A_0 e^{-2\tau/T_2}. \tag{3.25}$$

According to Eq. (3.25) measuring the echo signal intensity as a function of τ allows to obtain T_2. Beside the transverse relaxation, there is also spin lattice or longitudinal relaxation present. The spin-lattice relaxation time T_1 is associated with the approach to thermal equilibrium. In other words, it is the characteristic decay time for the return to the Boltzmann distribution. It is also a measure of how quickly the longitudinal magnetization returns to equilibrium. A measurement of T_1 can be also performed using a spin-echo method.

4 Superconducting and magnetic properties of the 122-family of Fe-based high-temperature superconductors

This chapter focusses on results obtained on several members of the so-called 122 family of the novel Fe-HTSs. In the first section the discovery of Fe-HTSs is briefly summarized. Next the SC and magnetic properties of the iron arsenide system $\mathrm{EuFe_2As_2}$ as a function of charge carrier doping and chemical as well as hydrostatic pressure are presented. Then the temperature and field dependences of the magnetic penetration depth λ of optimally doped $\mathrm{Ba}_{1-x}\mathrm{Rb}_x\mathrm{Fe_2As_2}$ are reported.

4.1 High-temperature superconductivity in Fe-based compounds

The term "HTS" was first coined for a family of cuprate perovskite ceramic materials, discovered by Bednorz and Müller in 1986 [20]. As the transition temperatures are much higher than the boiling point of liquid nitrogen, these materials have a tremendous potential for applications.

Although the synthesis and structural analysis of iron-based systems was presented already at the end of the last century [85, 86, 87], no electronic and magnetic properties were reported. Research on Fe-based systems was taken up seriously only after the discovery of superconductivity at 4 K in LaOFeP in 2006 [29]. In 2008 Hideo Hosono and co-workers reported the discovery of 26 K superconductivity in fluorine-doped LaFeAsO [30], marking the beginning of worldwide efforts to investigate this new class of HTSs. Because elemental iron is strongly magnetic, the discovery of Fe-HTSs with high transition temperature was completely unexpected. These superconductors have triggered extensive interest in their physical properties and the underlying mechanism of high-T_c superconductivity.

The Fe-HTSs that have been found so far can be categorized into five classes according to their structure. An overview of the crystal structures for some of the families is presented in Fig. 4.1. One of these is LFeAsO (L1111) known as 1111 type (L represents lanthanides). LFeAsO has a ZrCuSiAs type structure belonging to the tetragonal $P4/nmm$ space group (see Fig. 4.1a). It is a stack of alternating positively charged LO layers and negatively charged FeAs layers along the c-axis. The $L_2\mathrm{O}_2$ layer is an insulating charge reservoir layer, while the $\mathrm{Fe_2As_2}$ layer acts as the conducting active block. The structure of LFeAsO comprises sheets of Fe^{2+} ions in between ionic blocks of $L\mathrm{OAs}^{2-}$. The L atoms

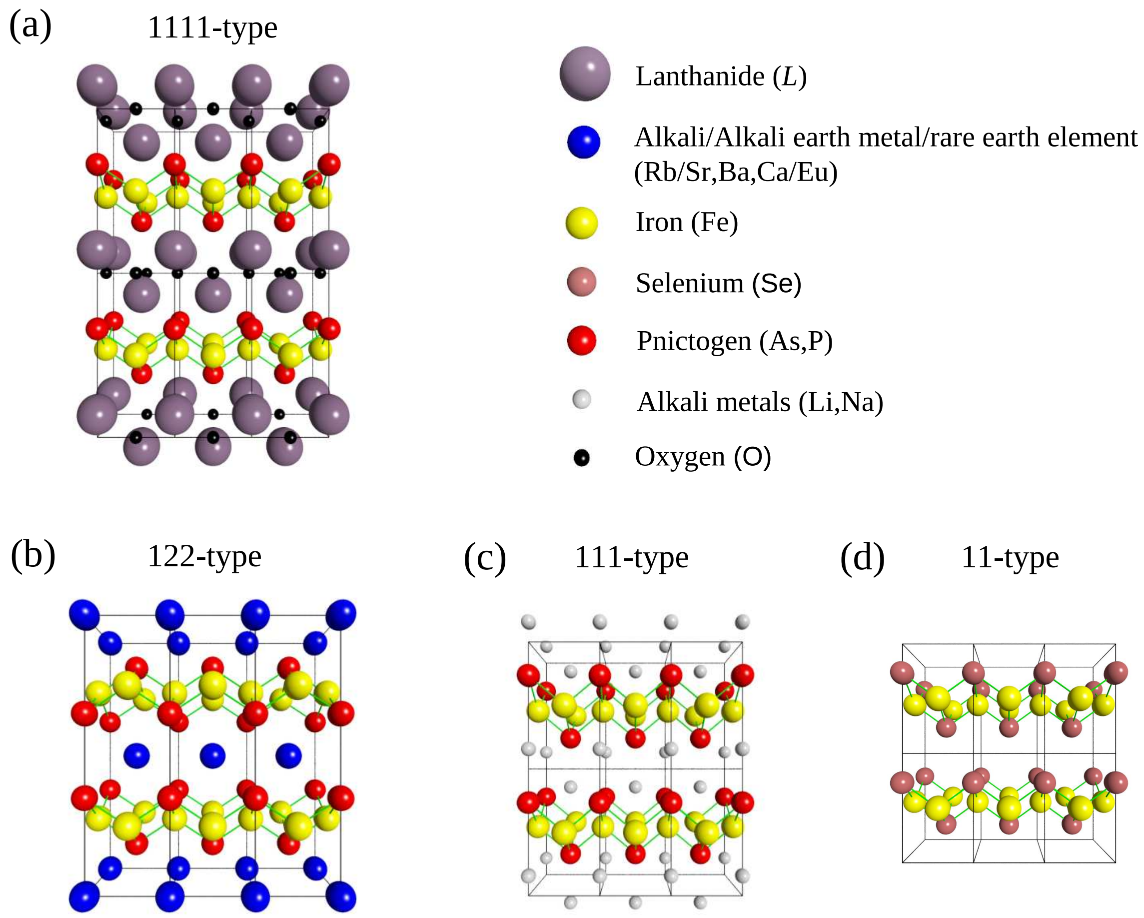

Figure 4.1: (Color online) Crystal structure of four different families of iron-based superconductors: (a) the 1111-type, (b) the 122-type, (c) the 111-type, and (d) the 11-type. Superconductivity in these Fe-based materials takes place in a corrugated layer made up of Fe and one of two pnictogens (phosphorus, arsenic). Note that these structural families incorporate the layer with a characteristically different interlayer. The figure is adopted from [88].

(having $4mm$ site symmetry) are coordinated by four As atoms and four O atoms forming distorted square antiprisms. The parent compound LFeAsO is not SC and shows an AFM transition at 150 K. Superconductivity is induced upon doping the lanthanide oxide layers or by applying pressure [29, 30, 89]. Directly related to the compound discovered by Kamihara *et al.* [29, 30, 90, 91] are the Fe-HTSs belonging to the 1111-family with the general formula $L\mathrm{Fe}Pn\mathrm{O}_{1-x}\mathrm{F}_x$ (Pn = P, As; L = La, Ce, Pr, Nd, Sm, Gd, Tb, Dy, Ho, and Y) [30, 89, 92, 93, 94, 95, 96, 97, 98, 99, 100, 101, 102, 103, 104, 105, 106].

The second category, $A\mathrm{Fe}_2\mathrm{As}_2$, has a $\mathrm{ThCr}_2\mathrm{Si}_2$ structure abbreviated as 122 type. Here the A site corresponds to a divalent ion (A = Ba, Sr, Ca, Eu) (Fig. 4.1b). The $A\mathrm{Fe}_2\mathrm{As}_2$ structure was first reported in $\mathrm{BaFe}_2\mathrm{As}_2$, which shows AFM ordering similar to 1111 type [107]. In this family the first superconductor discovered was $\mathrm{Ba}_{1-x}\mathrm{K}_x\mathrm{Fe}_2\mathrm{As}_2$ with $T_c \simeq 38$ K [107]. Later on, superconductivity was found in various related compounds. Mainly in hole-doped $\mathrm{Sr}_{1-x}\mathrm{K}_x\mathrm{Fe}_2\mathrm{As}_2$ and $\mathrm{Sr}_{1-x}\mathrm{Cs}_x\mathrm{Fe}_2\mathrm{As}_2$ [108], $\mathrm{Ca}_{1-x}\mathrm{Na}_x\mathrm{Fe}_2\mathrm{As}_2$ [109], $\mathrm{Eu}_{1-x}\mathrm{K}_x\mathrm{Fe}_2\mathrm{As}_2$ [110], $\mathrm{Eu}_{1-x}\mathrm{Na}_x\mathrm{Fe}_2\mathrm{As}_2$ [111], and $\mathrm{Ba}_{1-x}\mathrm{Rb}_x\mathrm{Fe}_2\mathrm{As}_2$ [112, 113] as well as in electron-doped $\mathrm{BaFe}_{2-x}\mathrm{Co}_x\mathrm{As}_2$ [114], $\mathrm{SrFe}_{2-x}\mathrm{Co}_x\mathrm{As}_2$ [115], and $\mathrm{BaFe}_{2-x}\mathrm{Ni}_x\mathrm{As}_2$ [116].

The third one has the $\mathrm{Cu}_2\mathrm{Sb}$ type structure (111 type) as shown in Fig. 4.1c and was realized in SC LiFeAs and NaFeAs [117, 118]. Other compounds which belong to the class of Fe-HTSs are the dichalogenide 11-family $Fe_{1+x}Se_{1-y}Te_z$ (see Fig. 4.1d) [119, 120] and the 21311-family E_2MO_3FeAs (E = Ca, Sr, Ba; M = Sc, Ti, V, Cr, Co) [121, 122, 123].

Fe-HTSs are the first non-cuprate materials exhibiting superconductivity at relatively high temperatures upon electron or hole doping of non-SC AFM parent compounds. They have very high upper critical fields, making these superconductors very interesting for applications. The phase diagram of the Fe-HTSs is in fact strikingly similar to the cuprates. They have a layered crystal structure and exhibit multiband features along with an unconventional pairing symmetry similar to cuprates [124, 125, 126]. Although significant progress in our understanding of Fe-HTSs was made, many important questions still remain unanswered. In particular, the symmetry of the order parameter remains uncertain. Some reports point towards an $s(+/-)$, or extended s-wave state [32, 33, 127]. AFM fluctuations, which originate from the nesting between the hole and electron Fermi surfaces, are thought to play an important role in the Fe-HTSs and could be embedded into the fully gapped s(+/-)-pairing state [128]. However, it appears that the suggested nodal states may be impurity or 'accidental' effects rather than intrinsic features of the Fe-HTSs [129]. An important hint to the pairing mechanism came from isotope exchange experiments. They showed that T_c depends on the Fe-isotope mass, which strongly indicates that lattice effects play an important role in the microscopic mechanism of high-T_c superconductivity [130, 131, 132, 133, 134]. Moreover, a polaronic two-band model, involving s-wave order parameters, was proposed for the Fe-HTSs [31], similar to the one for the cuprates [25, 26], where multi-gap superconductivity was suggested to occur [135, 136, 137, 138]. The resemblance of interpenetrating ground states in cuprates and Fe-HTSs has to be considered in a generalized theory of unconventional superconductivity.

4.2 The $EuFe_2As_2$ system

$EuFe_2As_2$ is a particularly interesting member of the iron arsenide AFe_2As_2 family, since the A site is occupied by a Eu^{2+} S-state (orbital moment $L = 0$) rare-earth ion. It has a $4f^7$ electronic configuration with a total electron spin $S = 7/2$, corresponding to a theoretical effective magnetic moment of 7.94 μ_B. It is the only known member of the 122 family containing $4f$ electrons. $EuFe_2As_2$ exhibits both a SDW ordering of the Fe moments and AFM ordering of the localized Eu^{2+} moments below $T_{SDW} = 190$ K and $T_{Eu} = 19$ K, respectively. The presence of magnetic phase transitions at $T_{Eu} = 19$ K and $T_{SDW} = 190$ K in $EuFe_2As_2$ was first reported by Mössbauer and susceptibility measurements [139, 140]. Recently, neutron diffraction and resonant x-ray scattering measurements were performed on $EuFe_2As_2$ and the magnetic structure illustrated in Fig. 4.2 was established [141, 142]. It is built up by $[FeAs]^{2-}$ layers, seperated by layers of magnetic Eu^{2+} ions. This material exhibits an A-type AFM order of the Eu^{2+} moments, *e.g.*, the Eu^{2+} spins align ferromagnetically in the planes, while the planes are coupled antiferromagnetically [34, 141, 142].

In contrast to the other 122 systems, where the substitution of Fe by Co leads to superconductivity [143, 144], the compounds containing Eu^{2+} exhibit an onset of a SC transition, but do not show zero resistivity at ambient pressure [145]. For clarity, the temperature dependence of the electrical resistivity for two different systems $\mathrm{BaFe}_{2-x}\mathrm{Co}_x\mathrm{As}_2$ and $\mathrm{EuFe}_{2-x}\mathrm{Co}_x\mathrm{As}_2$ is shown in Figs. 4.3a and b, respectively. Reentrant SC behavior was also observed in a $\mathrm{EuFe}_2\mathrm{As}_2$ crystal under applied pressure up to 2.5 GPa [146, 147]. Only above 2.8 GPa, where a valence change of the Eu ions from a divalent magnetic state ($4f^7$, $J = 7/2$) to a trivalent nonmagnetic state ($4f^6$, $J = 0$) was suggested to occur [148], a sharp transition to a zero-resistivity state was observed [147]. Bulk superconductivity is also observed in $\mathrm{EuFe}_2\mathrm{As}_{2-x}\mathrm{P}_x$ [148, 149], where isovalent P-substitution of the As-site acts as chemical pressure in $\mathrm{EuFe}_2\mathrm{As}_2$. No superconductivity was detected in $\mathrm{EuFe}_{2-x}\mathrm{Ni}_x\mathrm{As}_2$ [150], while superconductivity with a maximum $T_\mathrm{c} \simeq 20$ K was reported for $\mathrm{BaFe}_{2-x}\mathrm{Ni}_x\mathrm{As}_2$ [151]. It was suggested from different experiments [150, 152, 153, 154] that there is a strong coupling between the localized Eu^{2+} spins and the conduction electrons of the two-dimensional (2D) $\mathrm{Fe}_2\mathrm{As}_2$ layers. This may lead to a sophisticated interplay between the magnetism of localised Eu and itinerant Fe moments and superconductivity in $\mathrm{EuFe}_2\mathrm{As}_2$. Hence, this system is an ideal candidate to study the interrelation between superconductivity and different kinds of magnetism in Fe-HTSs.

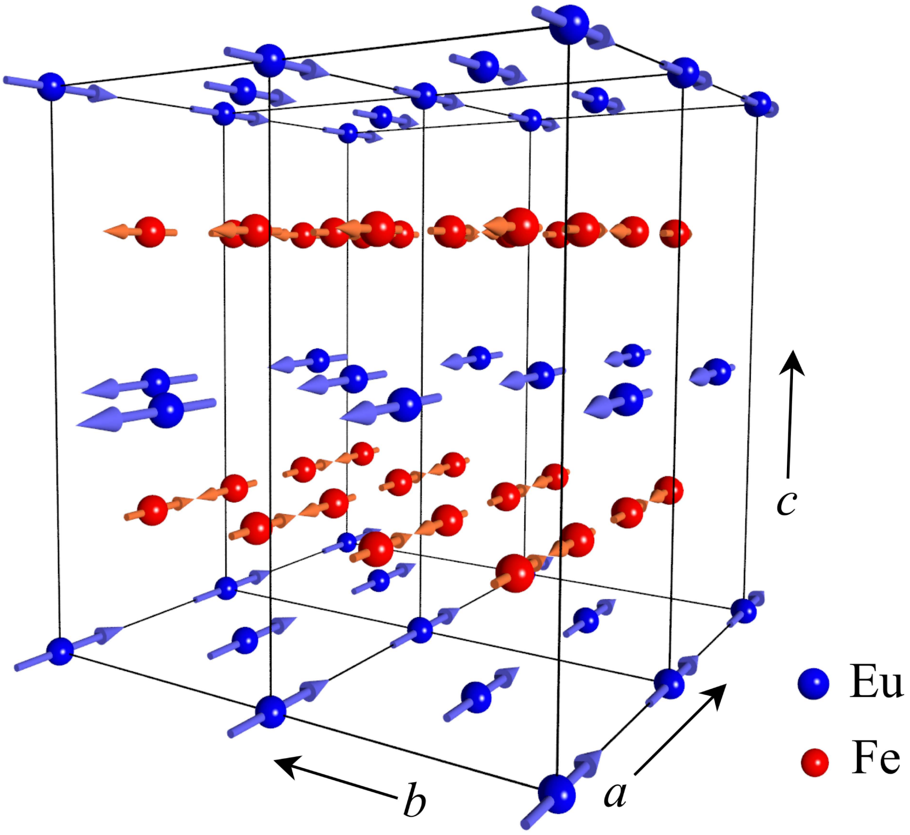

Figure 4.2: Schematic illustration of the magnetic structure of $\mathrm{EuFe}_2\mathrm{As}_2$. The Fe moments (red) form a SDW state, whereas the Eu moments (blue) order ferromagnetically in the *ab*-plane and align antiferromagnetically along the *c*-axis. After [155].

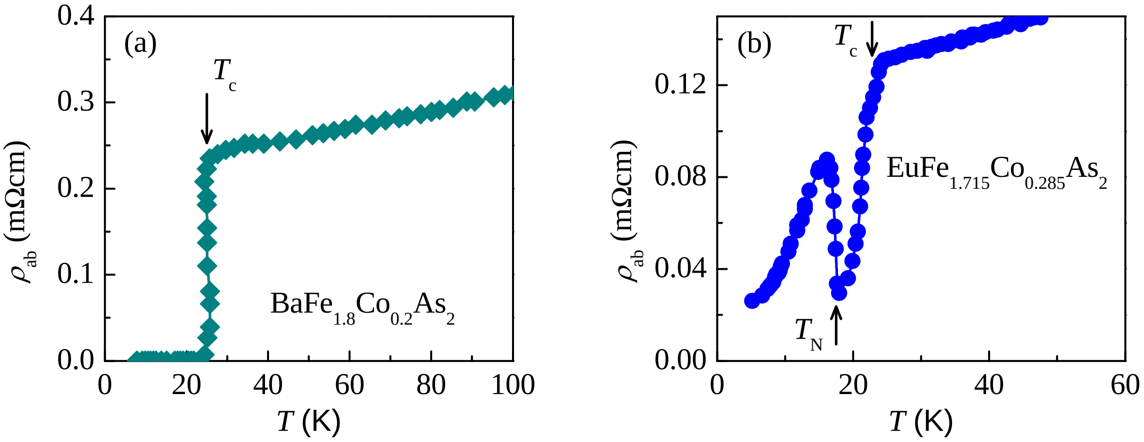

Figure 4.3: In-plane electrical resisitivity of $BaFe_{1.8}Co_{0.2}As_2$ (a) and $EuFe_{1.715}Co_{0.285}As_2$ (b) as a function of temperature. The solid lines are guides to the eyes. After [145, 156].

4.2.1 Coupling between the Eu^{2+} spins and the Fe_2As_2 layers in single crystals of Co-doped $EuFe_{1.9}Co_{0.1}As_2$ studied with NMR

The study of the interaction between the rare-earth Eu^{2+} magnetic moment and the conducting Fe_2As_2 layers is crucial to understand why it is difficult to induce superconductivity in the Co-doped $EuFe_{2-x}Co_xAs_2$ system. In order to investigate this coupling as well as to study the magnetic phases in Co-doped $EuFe_{1.9}Co_{0.1}As_2$, a combination of x-ray diffraction, magnetization, and ^{75}As nuclear magnetic resonance (NMR) experiments were performed on single crystals [157].

Single crystals of $EuFe_{1.9}Co_{0.1}As_2$ were grown out of Sn flux. The chemical composition of the single crystals was determined on freshly cleaved samples using wavelength-dispersive x-ray spectroscopy (WDS). The obtained composition corresponds to the formula $EuFe_{1.9}Co_{0.1}As_2$ within experimental error (± 5 %). X-ray diffraction experiments at room temperature, performed on a single crystal (approximate size: 0.2 x 0.1 x 0.008 mm^3) revealed that the crystal is of good quality. The lattice constants for the tetragonal unit cell based upon the refinement of 689 reflections were found to be $a = b = 3.9104(1)$ Å, $c = 11.9434(3)$ Å, $V = 182.629(8)$ Å^3 [157]. It was observed that in the Co-substituted crystal the room-temperature lattice parameter c is reduced and the lattice parameter a is increased relative to the parent compound $EuFe_2As_2$ ($a = b = 3.898(1)$ Å, $c = 12.085(5)$ Å) which was also grown out of Sn flux. Note that no additional phases (impurities, twins, or intergrowing crystals) were detected by examination of the reconstructed reciprocal space sections measured at room temperature, shown in Fig. 4.4 [157].

The susceptibility measurements of the $EuFe_{1.9}Co_{0.1}As_2$ crystals were carried out with a SQUID magnetometer (*Quantum Design*) in the temperature range from 5 to 300 K. As an example, the temperature dependence of the magnetic susceptibility χ in an applied field of $\mu_0 H = 0.3$ T parallel ($H \parallel c$) and perpendicular ($H \perp c$) to the crystallographic c-axis for the $EuFe_{1.9}Co_{0.1}As_2$ crystal is shown in Fig. 4.5a. The inverse susceptibility for $H \perp c$ measured as a function of temperature is also shown. These measurements reveal a transition to the AFM state of the Eu^{2+} moments below 15 K [157]. It was found that the Eu^{2+} moments align in the ab-plane [152], similar as for $EuFe_2As_2$ [141]. From 50 K to 120

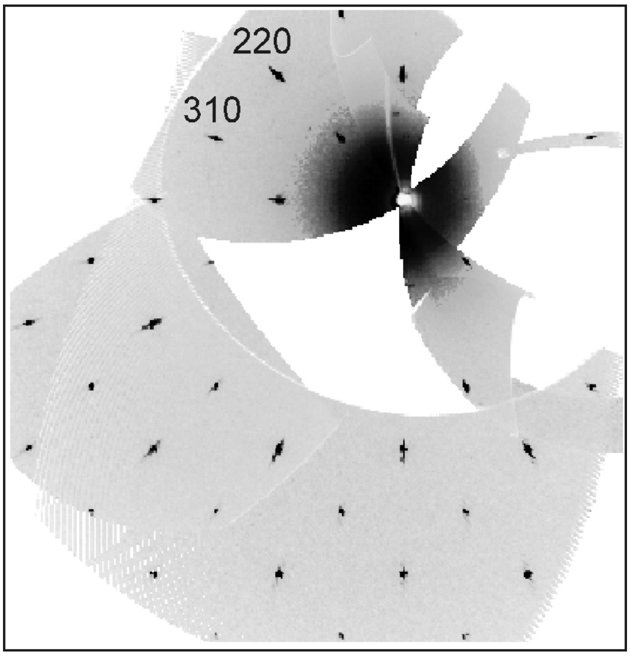

Figure 4.4: (Color online) The reconstructed *hk0* reciprocal space section of the single crystal $EuFe_{1.9}Co_{0.1}As_2$ used in this work. After [157].

K the susceptibility $\chi_\perp$ ($H \perp c$) is well described by the Curie-Weiss law:

$$\chi_{\perp CW}(T) = \frac{C}{T - \theta_{CW}}. \tag{4.1}$$

Here C denotes the Curie-Weiss constant, and θ_{CW} the Curie-Weiss temperature. Analyzing the data with Eq. (4.1) in the temperature range from 30 K to 120 K yields: $C = 2.43(5)\times10^{-4}$ m^3 K/mol and θ_{CW} = -21.34(7) K. The calculated effective magnetic moment $\mu_{eff} = 8.7\ \mu_B$ is close to the theoretical value of the magnetic moment of a free ion ($\mu_{free} = 7.94\ \mu_B$). Note that, after subtracting the Curie-Weiss contribution $\chi_{\perp CW}(T)$ from $\chi_\perp(T)$, a small anomaly in $\chi_{\perp res}(T) = \chi_\perp(T)$ - $\chi_{\perp CW}(T)$ is visible at around 120 K (see Fig. 4.5b). This behavior resembles that observed in $BaFe_2As_2$ [158] which was ascribed to the SDW transition of the Fe moments. However, in the case of $EuFe_{1.9}Co_{0.1}As_2$ the large signal from the Eu^{2+} moments does not allow a direct observation of the SDW anomaly (without subtracting the Curie-Weiss term).

The microscopic magnetic properties of $EuFe_{1.9}Co_{0.1}As_2$ were investigated using ^{75}As nuclear magnetic resonance (NMR) [see Sec. 3.2]. The ^{75}As NMR experiments on a single crystal (dimensions: 4 x 4 x 0.2 mm^3) from the same batch as the crystals used for magnetization and x-ray experiments were performed in an external magnetic field of 9 T using a standard pulse spectrometer. NMR is a powerful and extremely sensitive microscopic tool to probe magnetism in a solid. ^{75}As has a nuclear spin I = 3/2 and a large quadrupolar moment (Q = 0.3b) that interacts with the local electric field gradient (EFG) in the crystal. Hence, it gives rise to an additional term in the nuclear-spin Hamiltonian describing the interaction of the investigated nucleus with the crystal electric field gradient. Note that the details of the different contributions to the nuclear-spin Hamiltonian are given in Sec. 3.2.2. ^{75}As ($I=\frac{3}{2}$) has two double degenerate $\pm\frac{1}{2}$ and $\pm\frac{3}{2}$ energy levels in the absence of a static magnetic field.

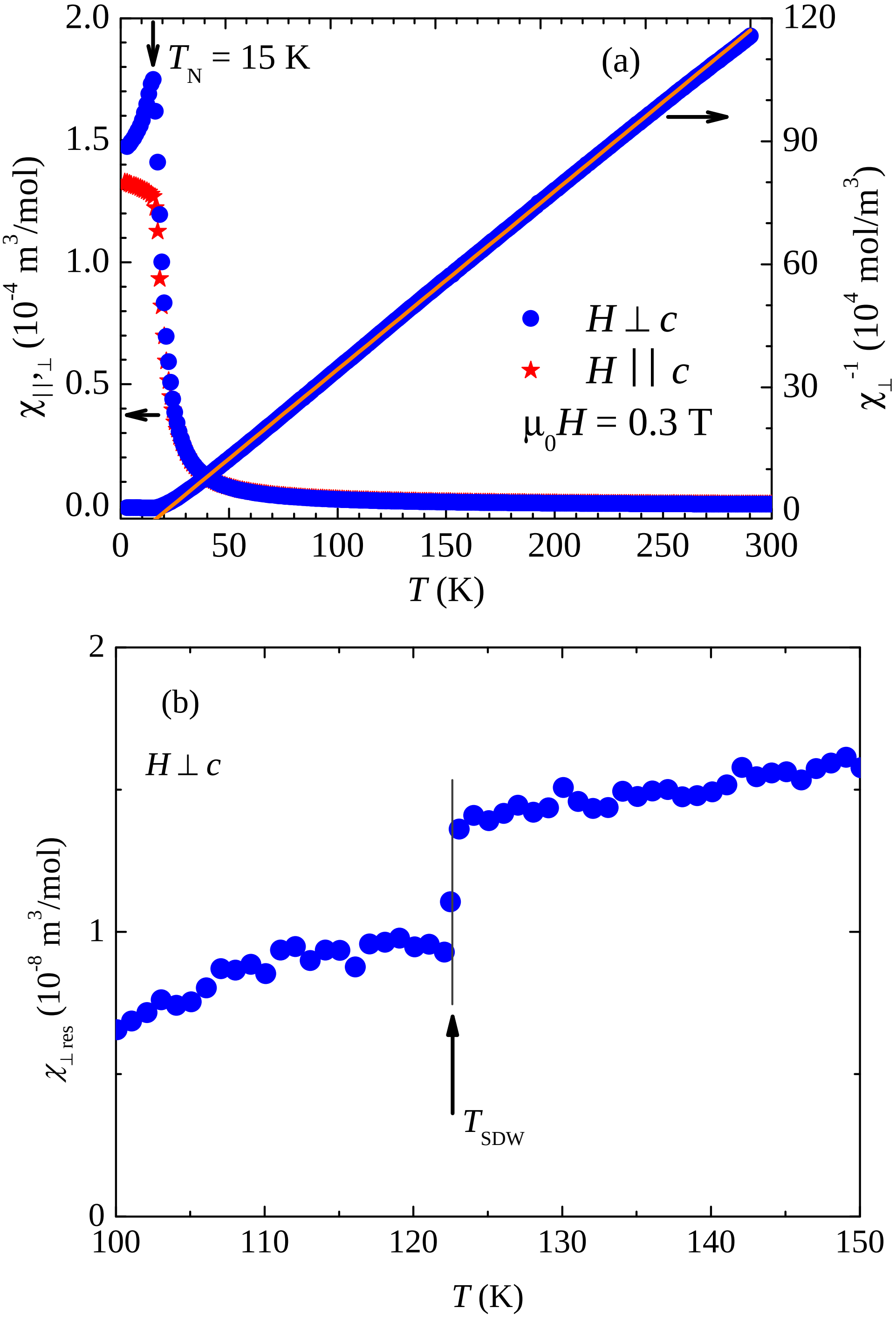

Figure 4.5: (Color online) (a) Temperature dependence of the magnetic susceptibility measured in a field of $\mu_0 H = 0.3$ T applied parallel ($H \parallel c$) and perpendicular ($H \perp c$) to the crystallographic c-axis of single crystal EuFe$_{1.9}$Co$_{0.1}$As$_2$. The measurements were performed in the zero-field cooling mode. In addition, for $H \perp c$ the temperature dependence of the inverse susceptibility $1/\chi_\perp$ is plotted. The solid line represents a fit to the data with the Curie-Weiss law given in Eq. (4.1). (b) Temperature dependence of $\chi_{\perp res}(T)$=$\chi_\perp(T)$-$\chi_{\perp CW}(T)$ (see text for an explanation) for single crystal EuFe$_{1.9}$Co$_{0.1}$As$_2$. The solid line is the guide to the eye. After [157].

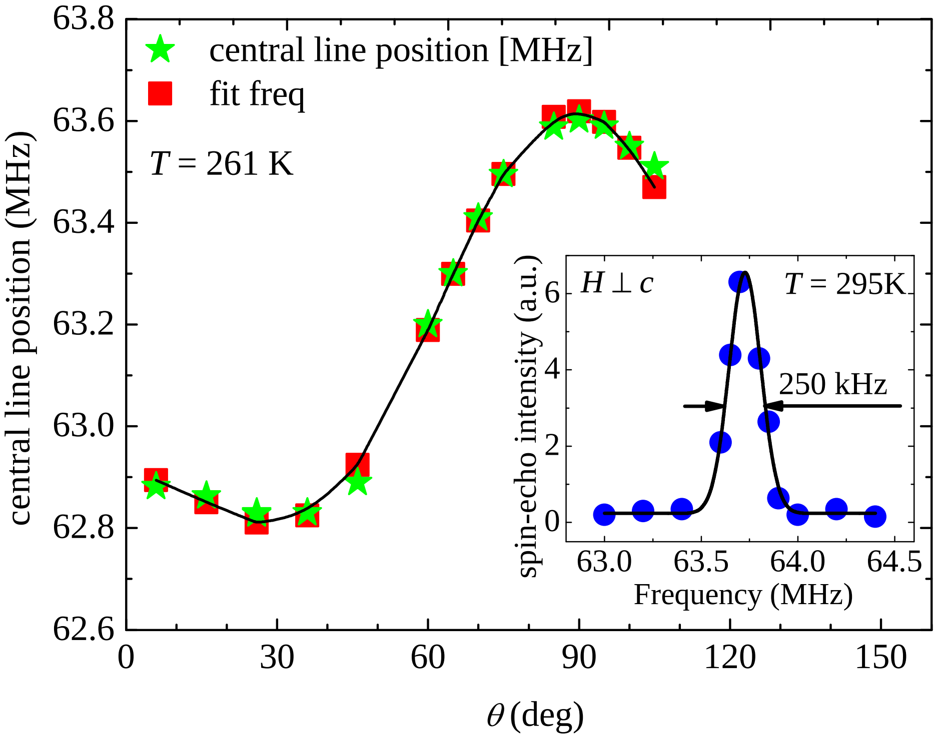

Figure 4.6: (Color online) Dependence of the ^{75}As NMR central line frequency at 261 K on the angle θ between the external magnetic field and the crystallographic c-axis of single crystal $\mathrm{EuFe_{1.9}Co_{0.1}As_2}$. The solid line is a guide to the eye. Solid squares represent the fitting results as described in the text. The inset illustrates the ^{75}As NMR central line shape at 295 K. The solid line represents a Gaussian fit. After [157].

In the presence of a large external magnetic field H_0 a splitting of the ^{75}As spectrum into a central line, arising from the central transition ($+\frac{1}{2}$,$-\frac{1}{2}$), and two satellite lines due to the ($\pm\frac{1}{2}$,$\pm\frac{3}{2}$) transitions occurs (see Fig. 3.5 in Sec. 3.2.2). As an example, a ^{75}As NMR spectrum of the central transition at 295 K is shown in the inset of Fig. 4.6. In the paramagnetic state ($T > T_{\mathrm{SDW}}$) NMR lines with a full width at half maximum (FWHH) of about 250 kHz (central line) and 500 kHz (satellite lines) are observed. The dependence of the ^{75}As NMR central line position on the angle θ between the magnetic field orientation and the c-axis at 261 K (tetragonal phase) was measured and is presented in Fig. 4.6. For all orientations the resonance frequencies show a strong negative shift relative to the corresponding ^{75}As Larmor frequency of 65.9 MHz at 9 T. The angular dependence of the frequency of the central line was analyzed using the diagonalization of the Hamiltonian (Eq. (3.18) in Sec. 3.2.2) and yields K_{ab} = -0.0372(2), K_{c} = -0.0456(3), and ν_{Q} = 7.39(24) MHz. In the analysis η is assumed to be zero, since the tetragonal site symmetry of ^{75}As requires a uniaxial symmetry along the c-axis for the EFG tensor ($\eta = 0$) and the magnetic shift K tensor.

To determine the spin-spin relaxation rate $1/T_2$ of the central line of the ^{75}As NMR spectrum for $H \parallel c$ the spin-echo intensity was measured as a function of delay time between the exciting and the refocusing pulse (see Sec. 3.2.4). The measured temperature dependence of $1/T_2$ is shown in Fig. 4.7. $1/T_2$ exhibits a Curie-Weiss-like temperature dependence down to 120 K. A reduction of $1/T_2$ is observed below 120 K, which reflects the slowing down of the Fe spin fluctuations due to the SDW ordering of the Fe moments. A similar behavior across

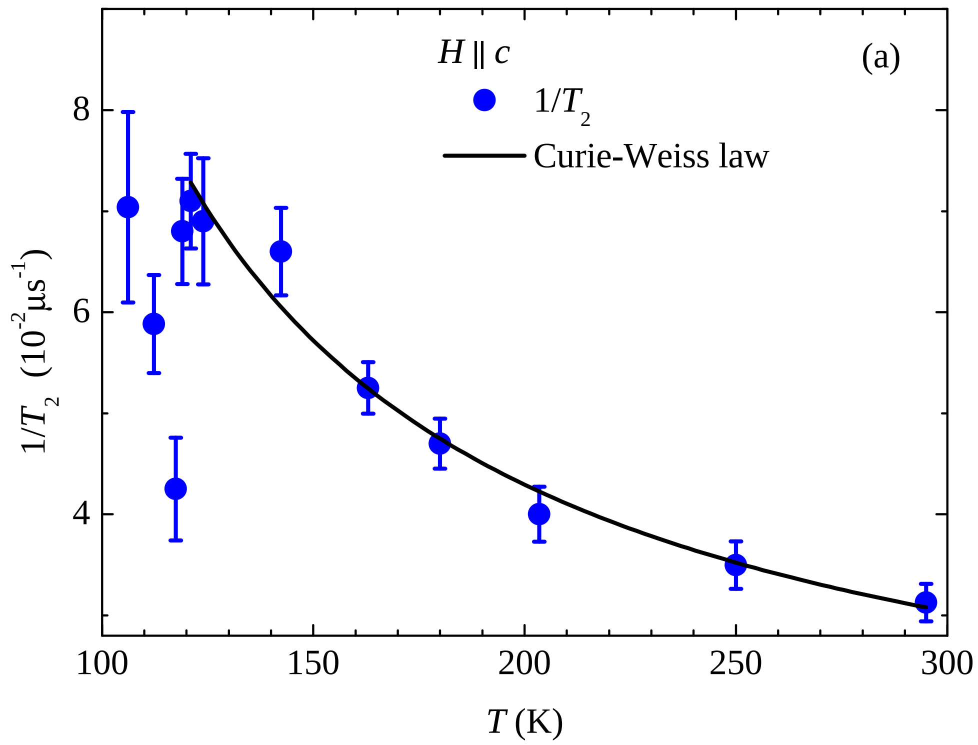

Figure 4.7: (Color online) Temperature dependence of the spin-spin relaxation rate $1/T_2$ of the ^{75}As central line of single crystal $EuFe_{1.9}Co_{0.1}As_2$ for $H \parallel c$. The solid line represents the Curie-Weiss law, and the dashed line is to guide to the eye. After [157].

the SDW transition was also reported for spin-lattice relaxation measurements in AFe$_2$As$_2$ (A = Ba, Ca, Sr) [159, 160, 161, 162]. This finding is consistent with the presence of the SDW phase below 120 K found by magnetization measurements and reveals a decrease of the SDW transition temperature from T_{SDW} = 190 K to T_{SDW} = 120 K as a result of Co-doping.

As presented in Fig. 4.7 $1/T_2$ exhibits a Curie-Weiss-like temperature dependence down to 120 K, showing that the ^{75}As nuclei interact with the localized Eu-4f moments. The hyperfine coupling strength between the ^{75}As nuclei and Eu^{2+} 4f moments was quantitatively determined by measuring the temperature dependence of the magnetic shift K of the ^{75}As NMR central line. A brief description of the shift of the NMR frequency is given in Sec. 3.2.3. The temperature dependence of the shift in the temperature range 100-300 K for $H \parallel c$ ($K_{\parallel}$ = K_{c}) and $H \perp c$ ($K_{\perp}$ = K_{ab}) is shown in Fig. 4.8a. Compared to the magnetic shift data for AFe$_2$As$_2$ (A = Ba, Ca, Sr) [159, 160, 161, 162], the observed shifts in $EuFe_{1.9}Co_{0.1}As_2$ are significantly larger, negative, and show a completely different temperature dependence. The relative magnetic shift K above T_{SDW} = 120 K exhibits a Curie-Weiss like temperature dependence for both directions of the magnetic field H:

$$K(T) = K_0 + \frac{C_K}{T + \Theta}. \tag{4.2}$$

Here K_0 is the constant part of the shift. C_{K} and Θ are phenomenogical quantities. Analysing the data for $H \perp c$ using Eq. (4.2) yields: Θ = -18.9(9) K. The value of Θ is in good agreement with the value Θ_{CW} = -21.34(7) K determined from the magnetic susceptibility measurements. This suggests that the temperature dependent part of the shift arises from

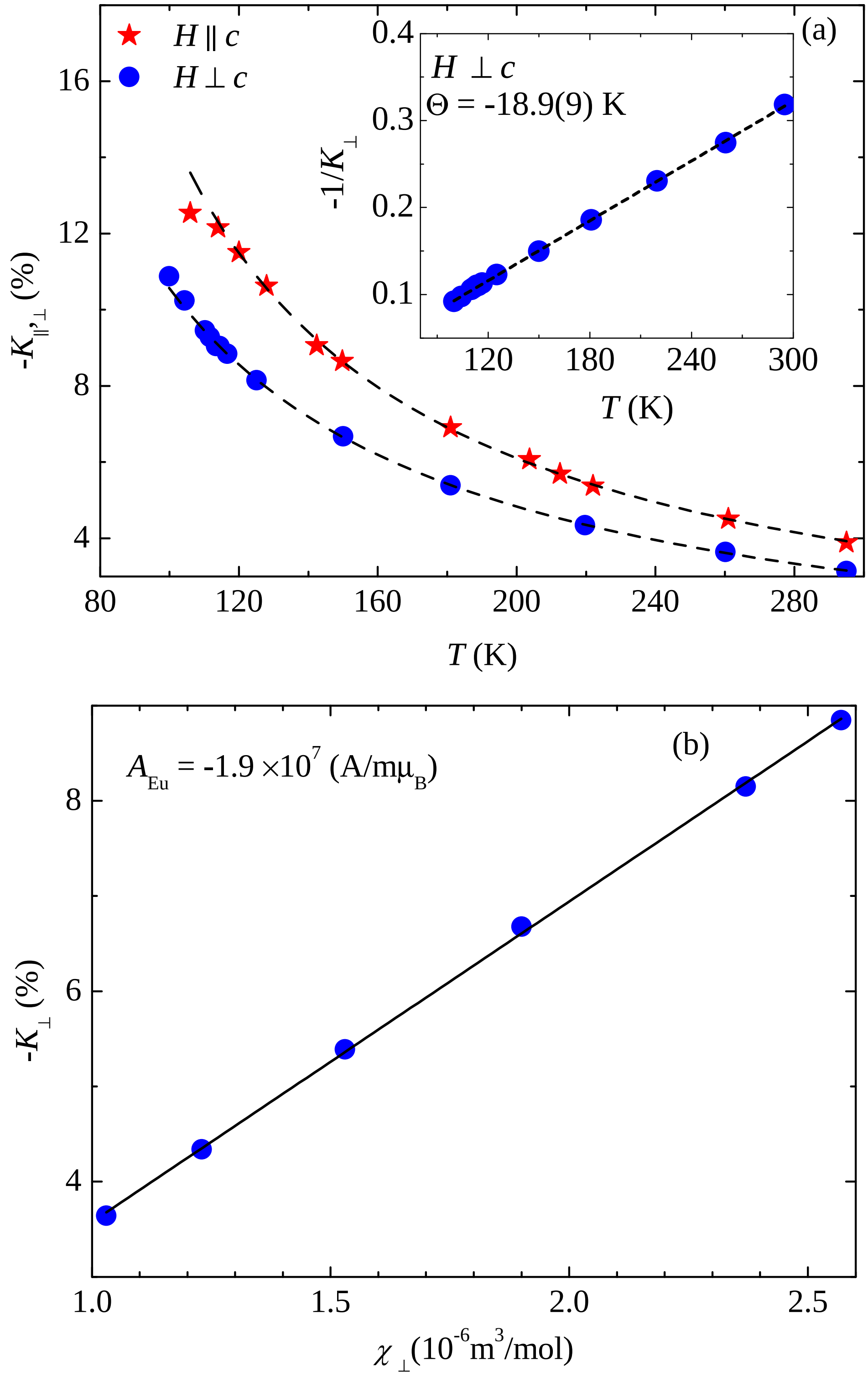

Figure 4.8: (Color online) (a) Temperature dependence of the ^{75}As magnetic shift in single crystal $EuFe_{1.9}Co_{0.1}As_2$ for $H \parallel c$ and $H \perp c$. The inset shows the inverse of the temperature dependent part of the shift $-1/K_{\perp}$ as a function of T. The dashed lines represent the Curie-Weiss behavior. (b) Plot of $-K_{\perp}$ vs. $\chi_{\perp}$ as obtained from the susceptibility measurements. The solid line is a linear fit. After [157].

the hyperfine coupling between the ^{75}As nuclei and the Eu^{2+} $4f$ moments. In addition, we obtained $K_0 = 0.17(25)$ %, which could be related to the coupling of ^{75}As with the itinerant $3d$ electrons in the Fe$_2$As$_2$ layer. The Curie-Weiss part of the magnetic shift K_{Eu} $= C_{\mathrm{K}}/(T+\Theta)$ can be related to the susceptibility χ_{Eu} of the localized Eu $4f$ moments as follows:

$$K_{\mathrm{Eu}} = \frac{A_{Eu}}{gN_A\mu_B}\chi_{\mathrm{Eu}} \tag{4.3}$$

where A_{Eu} is the hyperfine coupling of the ^{75}As nuclear spins with the $4f$ moments, g is the Land$\acute{e}$ factor, N_{A} and μ_{B} are the Avogadro number and the Bohr magneton, respectively. From the linear fit of $K_\perp(T)$ versus $\chi_\perp(T)$ (the temperature is an implicit parameter) (see Fig. 4.8b) the hyperfine coupling constant is estimated to be A_{Eu} = -1.9×10^7 A/m per μ_{B}. This value of A is almost 60 times larger than the one reported for NdFeAsO$_{0.85}$F$_{0.15}$ [163]. The reason for the much stronger hyperfine coupling in the 122 compound may be the smaller interlayer distance $d = 5.9713(3)$ Å in the 122 compounds as compared to the 1111 system ($d = 8.577$ Å) and the more isotropic band structure [164]. The large value of the hyperfine coupling constant, quantitatively determined from the present NMR data, provides direct experimental evidence for a strong coupling between the Eu^{2+} localized moments and the Fe$_{1.9}$Co$_{0.1}$As$_2$ layers. This suggests that the magnetic exchange interaction between the localized Eu $4f$ moments is mediated by a RKKY type of mechanism (see Sec. 2.2.2) [139, 150], leading to a high magnetic ordering temperature of the Eu^{2+} moments in EuFe$_2$As$_2$. On the other hand, the strong interaction between the localized Eu^{2+} moments and charge carriers in the Fe$_{2-x}$Co$_x$As$_2$ layers may cause pair breaking according to the Abrikosov-Gor'kov theory [165], which may explain why it is difficult to obtain superconductivity in EuFe$_{2-x}$Co$_x$As$_2$.

4.2.2 Microscopic evidence for a possible electronic nematic phase in EuFe$_{1.9}$Co$_{0.1}$As$_2$

EuFe$_2$As$_2$ undergoes a tetragonal-orthorhombic (TO) ($I4/mmm \rightarrow Fmmm$) structural transition at the same temperature (190 K) as the SDW transition temperature of the Fe moments occurs. While magnetism in the AFe$_2$As$_2$ (A = Ba, Sr, Ca, Eu) compounds has already been observed by Mössbauer spectroscopy more than 15 years ago [139], the structural phase transition was observed only recently [158, 166, 167, 168, 169, 170, 171, 172, 173, 174, 175, 176]. The structural transition in BaFe$_2$As$_2$ [158, 166, 167, 168, 169, 170], SrFe$_2$As$_2$ [171, 172, 173, 174, 175], CaFe$_2$As$_2$ [176], and EuFe$_2$As$_2$ [173] was studied by several groups, demonstrating that in the AFe$_2$As$_2$ (A = Ba, Sr, Eu) systems the SDW order is accompanied by a structural phase transition. This suggests that the formation of the SDW state and the lattice distortion are strongly coupled [177], in contrast to the undoped 1111 system, in which the SDW transition is preceded by a TO phase transition [158]. This first-order character of the structural phase transition was revealed by measurements of transmission electron microscopy (TEM) [178]. In general, doping in iron-arsenides leads to a suppression of the TO structural and SDW transition temperatures and the appearance of superconductivity [179, 180, 181, 182]. However, the manner how these transitions occur appears to vary between systems. In CeFeAsO$_{1-x}$F$_x$ the magnetic order is suppressed before superconductivity develops and superconductivity exists in the orthorhombic as well as in tetragonal phase [181], whereas in $LaFeAsO_{1-x}F_x$ the orthorhombicity and magnetic order disappear abruptly [180, 182] just as superconductivity develops. In addition, for $BaFe_{2-x}Co_xAs_2$ the orthorhombic transition and magnetic order persist to higher dopings and coexist with superconductivity [168]. Hence, a detailed knowledge of the magnetic and structural phase transitions and their interrelation is important to get a deeper understanding of the origin of the SC state in the iron-arsenides.

It has been proposed that this structural distortion is driven by an electron nematic state [183, 184, 185, 186] which could arise from AFM fluctuations [183, 184] or orbital ordering [185, 186, 187, 188, 189]. While the structural anisotropy (the ratio of the in-plane lattice parameters a/b) is very small, the electronic structure in the AFM phase is highly anisotropic, as manifested in first principles calculations [190, 191, 192, 193] and observed in experiments [194]. A strong intrinsic anisotropy is considered to be a key component of a nematic AFM state [195] and may play an important role for superconductivity [183, 188, 195]. Recently, electrical resistivity measurements of detwinned undoped AFe$_2$As$_2$ (A=Ba, Ca) [196] and Co-doped $BaFe_{2-x}Co_xAs_2$ [197] single crystals revealed a dramatic in-plane anisotropy below the structural phase transition temperature. This observation confirms that the orthorombic structural transition is of electronic origin.

The structural properties of single crystal $EuFe_{1.9}Co_{0.1}As_2$ was studied by measuring the rocking curves of the tetragonal (220) reflection at different temperatures using X-ray diffraction. The reflection was measured as a function of angle ω with steps of 0.05° from room temperature down to 140 K. At room temperature the full width at half maximum $\Delta\omega$ is 0.49° (Fig. 4.9). All measured (220) reflections were normalized to maximum intensity. As illustrated in Fig. 4.9 the angle ω at which the (220) reflection occurs increases with decreasing temperature, and the width $\Delta\omega$ increases. Below 235 K the reflection starts to

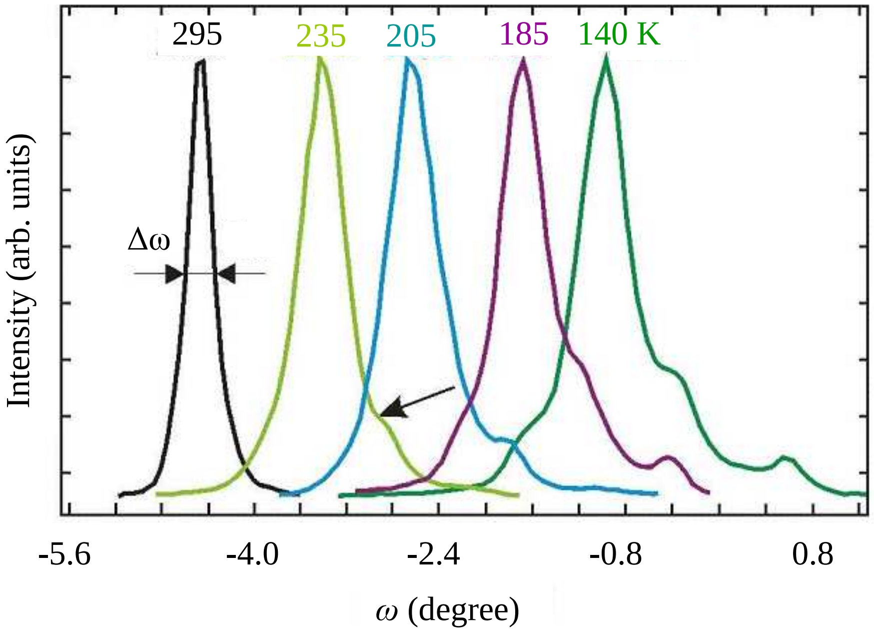

Figure 4.9: (Color online) Rocking curves of the tetragonal (220) reflection for single crystal $EuFe_{1.9}Co_{0.1}As_2$ at different temperatures. $\Delta\omega$ represents the the full width at half maximum. The arrow indicates the splitting as a consequence of formation of twinned orthorhombic domains.

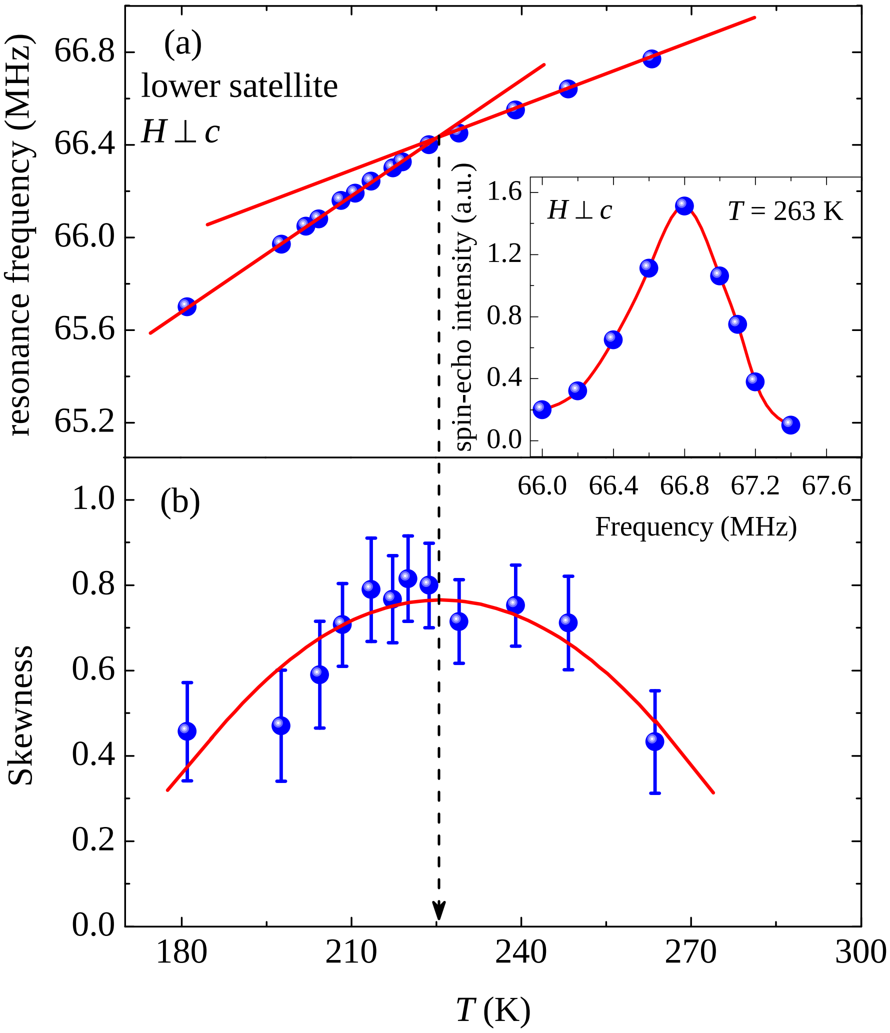

Figure 4.10: (Color online) Temperature dependence of the frequency (a) and the skewness (b) of the ^{75}As lower-satellite line for $H \perp c$ of single crystal $EuFe_{1.9}Co_{0.1}As_2$. Solid and dashed lines are guides to the eye. The inset illustrates the ^{75}As NMR lower-satellite line shape at 263 K for $H \perp c$. After [157].

split, indicating the formation of orthorhombic domains as observed in other members of the 122 system [171, 176]. The mechanism of the phase transition and the accompanying twinning in the 122 systems is described in detail elsewhere [170, 178].

Since NMR is a very sensitive tool to study the local structure in a solid, it was also used to study microscopically a structural phase transition in $EuFe_{1.9}Co_{0.1}As_2$. For this reason the temperature dependence of the frequency and the skewness (defined as the third standartised moment) of the ^{75}As lower-satellite line for $H \perp c$ is presented in Fig. 4.10. The inset of Fig. 4.10a illustrates a typical ^{75}As-NMR spectrum of the low-frequency satellite at 263 K. The spectra exhibit an asymmetric lineshape in the investigated temperature range. A change in the slope of the temperature dependence of the satellite line frequency can be seen at 225 K as shown in Fig. 4.10a. In addition, with decreasing temperature the skewness exhibits an increase down to 225 K, where it starts to decrease again (Fig. 4.10b). The slope change in the temperature dependence of the frequency of the ^{75}As lower-satellite line, the maximum in the temperature evolution of the skewness as well as the splitting of the (220) reflection may be related to the appearence of a electronic nematic phase below $T_n = 225$ K in $\mathrm{EuFe_{1.9}Co_{0.1}As_2}$.

In order to obtain more quantitative NMR results for a possible nematic phase, the angular dependence of the full ^{75}As NMR spectrum (central line and both satellite lines) was measured at 181 K. The analysis of the angular dependence of the full NMR spectrum using the diagonalization of the Hamiltonian [Eq. (3.18) in Sec. 3.2.2] yields the asymmetry parameter $\eta = 0.04(3)$. The slight increase of η suggests the lower symmetry of the As site in a possible nematic phase. Note that this observation is the first evidence of a nematic phase in $\mathrm{EuFe_{2-x}Co_xAs_2}$ using any microscopic tool.

As mentioned above, the parent compound $\mathrm{EuFe_2As_2}$ undergoes a structural phase transition at 190 K lowering the symmetry from tetragonal to orthorombic, followed by an AFM ordering of the Fe moments [139, 141]. According to the above NMR and single crystal x-ray experiments, $\mathrm{EuFe_{1.9}Co_{0.1}As_2}$ exhibits a SDW transition at $T_{SDW} = 120$ K. While the nematic phase appears at 225 K, *i.e.* at much higher temperature. In other members of the 122 family such as $A\mathrm{Fe_2As_2}$ (A = Ba, Sr, Ca) [168, 169, 175] the difference between T_n and T_{SDW} is not more than about 20 K. We note that the distinctive property of $\mathrm{EuFe_2As_2}$ compared to it's isostructural compounds $A\mathrm{Fe_2As_2}$ (A = Ba, Sr, Ca) is the fact that the $\mathrm{Eu^{2+}}$ ions carry large local magnetic moments. Thus, the observed difference may be related to the magnetic moment of $\mathrm{Eu^{2+}}$ and its strong coupling with the $\mathrm{Fe_{1.9}Co_{0.1}As_2}$ layers.

4.2.3 Anisotropic magnetic order of the Eu sublattice and its field dependence in $\mathrm{EuFe_{2-x}Co_xAs_2}$ (x = 0, 0.2)

It is well established that the SDW state of the Fe moments is suppressed as a result of Co doping. However, so far there was no clear picture how the ordering of the Eu spins develops with increasing Co concentration. Generally, it was assumed that in the 122 systems the direction of the sublattice magnetization of the $\mathrm{Eu^{2+}}$ magnetic moments is strongly affected by the magnetic behavior of the Fe atoms [141, 198, 199, 200, 201, 202]. Thus, it is important to compare the magnetic properties of the Eu sublattice in $\mathrm{EuFe_{2-x}Co_xAs_2}$ without and with Co doping in order to study the correlation between the ordering of the $\mathrm{Eu^{2+}}$ moments and the magnetism of the Fe sublattice. This in turn is important to understand the interplay between magnetism of localized moments and supercondcutivity in $\mathrm{EuFe_{2-x}Co_xAs_2}$.

We performed magnetic susceptibility and magnetization experiments on single crystals of $\mathrm{EuFe_{2-x}Co_xAs_2}$ ($x = 0, 0.2$) to investigate the macroscopic magnetic properties of the Eu sublattice [155]. These investigations provide information on the magnetic structure of a single-crystal sample in magnetic fields applied along the principal axes. In addition, the evolution of the magnetic structure as a function of the tilting angle between the magnetic field and the crystallographic axes was studied by magnetic torque [203] measurements.

In Fig. 4.11 the results of the susceptibility and magnetization experiments are summarized. They are discussed in terms of the phase diagram of the $\mathrm{Eu^{2+}}$ magnetic sublattice of $\mathrm{EuFe_2As_2}$ and $\mathrm{EuFe_{1.8}Co_{0.2}As_2}$ for $H \perp c$ and $H \parallel c$.

For the parent compound $\mathrm{EuFe_2As_2}$ four different magnetic phases were identified (see Fig. 4.11a and b): paramagnetic (PM), antiferromagnetic (AFM), canted antiferromagnetic (C-AFM), and ferromagnetic (FM). The determination of the corresponding transition tem-

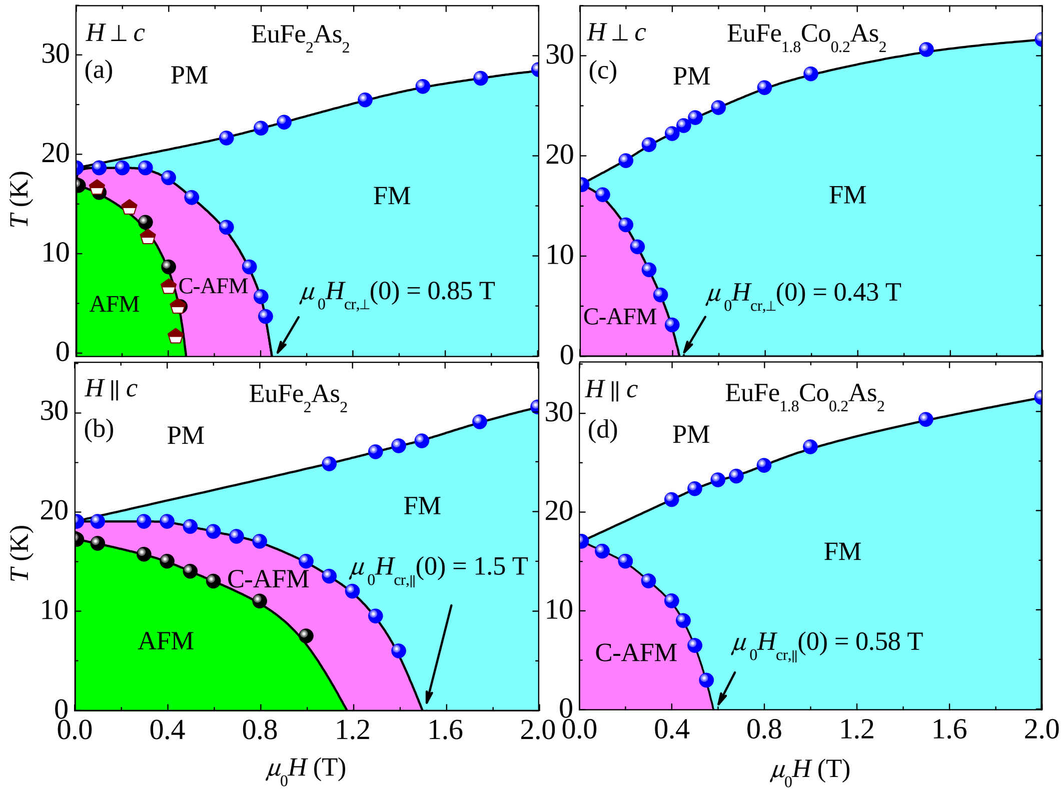

Figure 4.11: (Color online) Magnetic phase diagrams of single-crystal EuFe$_2$As$_2$ (a and b) and single-crystal EuFe$_{1.8}$Co$_{0.2}$As$_2$ (c and d) for $H \perp c$ and for $H \parallel c$. The various phases in the phase diagrams are denoted as follows: paramagnetic (PM), antiferromagnetic (AFM), canted antiferromagnetic (C-AFM), ferromagnetic (FM). The solid lines are guides to the eyes. After [155].

peratures and fields is described in Sec. III of Ref. [155]. The present experiments suggest a C-AFM order of the Eu^{2+} spins in EuFe$_2$As$_2$ in the temperature range between 17 K and 19 K, while below 17 K an AFM structure is proposed. We suggest that at low temperatures the system can be well described with a uniaxial model with easy plane and A-type AFM order. By applying a magnetic field within the AFM phase, a transition from AFM order via a canted configuration to a FM structure is observed. The critical magnetic field $H_{\rm cr}(T)$ at which the magnetic moment in the Eu sublattice saturates was determined at different temperatures. The values of $H_{\rm cr}$ extrapolated to zero temperature were found to be $\mu_0 H_{{\rm cr},\perp}(0) \simeq 0.85$ T and $\mu_0 H_{{\rm cr},\parallel}(0) \simeq 1.5$ T for $H \perp c$ and $H \parallel c$, respectively. The magnetic ordering of the Eu^{2+} moments at low temperatures is consistent with the magnetic structure established by neutron diffraction at 2.5 K [141]. Note that in previous reports [150, 152] a possible C-AFM state in the temperature range 17 K $\leq T \leq$ 19 K was not discussed. To our knowledge no neutron data for the magnetic configuration of the Eu sublattice in this temperature range are available.

The corresponding magnetic phase diagrams for Co-doped EuFe$_{1.8}$Co$_{0.2}$As$_2$ are shown in Figs. 4.11c and d. The magnetic ordering temperature of $\simeq$ 17 K is only about 2 K lower as compared to the parent compound. However, in the Co-doped EuFe$_{1.8}$Co$_{0.2}$As$_2$, no signatures of a low-field and low-temperature AFM state of the Eu^{2+} moments was found.

Only a C-AFM phase (with a dominant FM component in the *ab*-plane) is present at low fields and low temperatures. The tilt angle from *c*-axis was estimated using the relation $\theta = \arctan(\chi_\perp/\chi_\parallel)$, where $\chi_\perp$ and $\chi_\parallel$ denote the susceptibilities for the field applied perpendicular and parallel to the *c*-axis [155]. The experimental value is $\theta \approx 60°$. The ordering

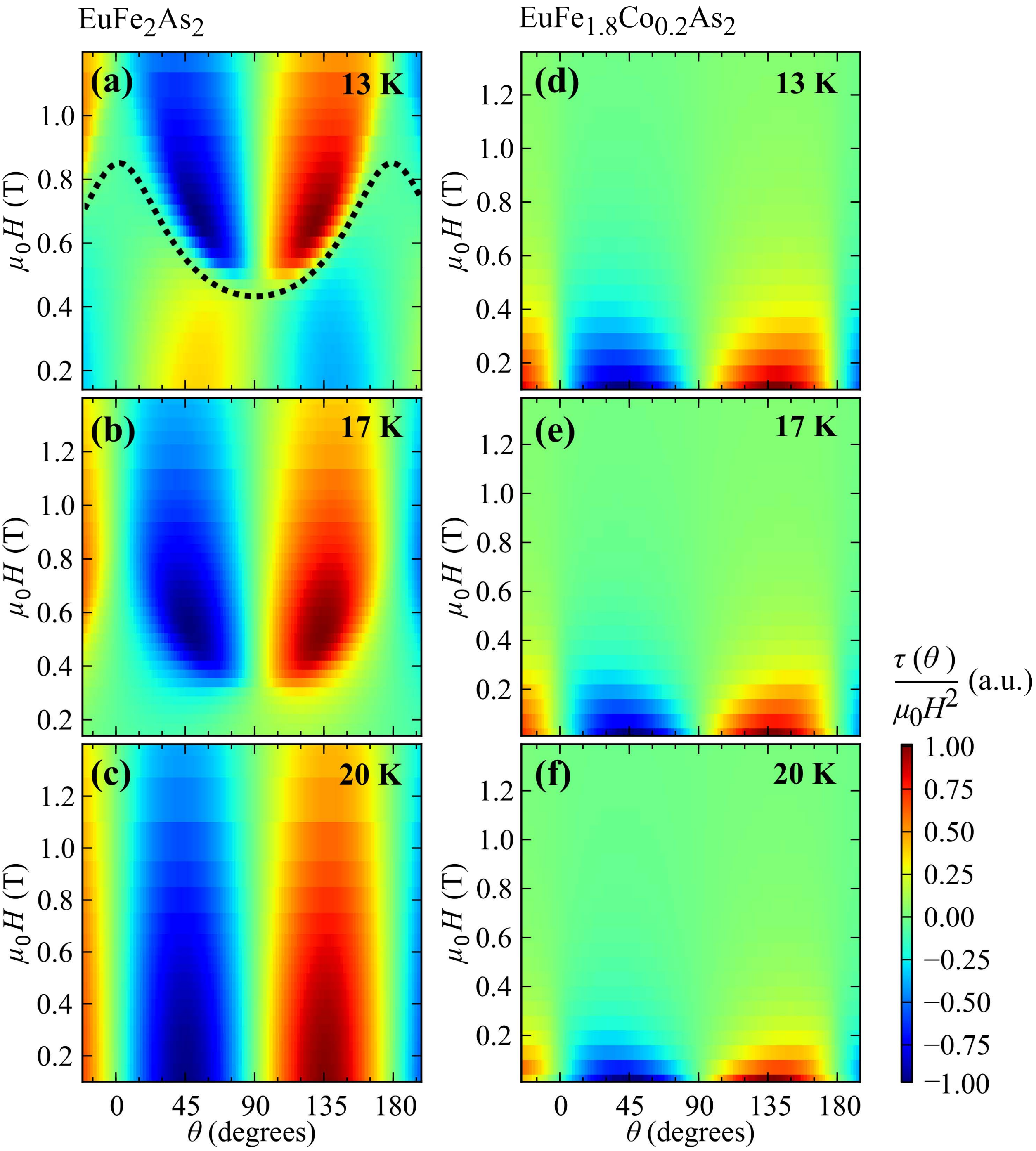

Figure 4.12: (Color online) Color map of $\tau/(\mu_0 H^2)$ (in a.u.) for single crystal $EuFe_2As_2$ and single crystal $EuFe_{1.8}Co_{0.2}As_2$ as a function of angle θ and field H for T = 13 K, 17 K, and 20 K. The dotted line in (a) is a fit according to Eq. (8) of Ref. [155]. Panels (a), (b), and (c) are the data for $EuFe_2As_2$ at 13 K, 17 K, and 20 K, respectively, whereas (d), (e), and (f) are the data for $EuFe_{1.8}Co_{0.2}As_2$ at 13 K, 17 K, and 20 K, respectively. After [155].

temperature $T_{\mathrm{C-AFM}}$ decreases with increasing magnetic field (see Figs. 4.11c and d), similar to the parent compound. $\mu_0 H_{\mathrm{cr}}$ was determined for different temperatures, and the extrapolated zero-temperature values were found to be: $\mu_0 H_{\mathrm{cr},\perp}(0) \simeq 0.43$ T and $\mu_0 H_{\mathrm{cr},\parallel}(0) \simeq 0.58$ T for $H \perp c$ and $H \parallel c$, respectively. These values of $\mu_0 H_{\mathrm{cr}}$ are much smaller than those obtained for the parent compound. Moreover, the magnetic anisotropy $\gamma_{\mathrm{cr}} = H_{\mathrm{cr},\parallel}(0)/H_{\mathrm{cr},\perp}(0) \simeq 1.35$ of Co-doped EuFe$_{1.8}$Co$_{0.2}$As$_2$ is also smaller than $\gamma_{\mathrm{cr}} \simeq 1.76$ of the parent compound.

The different magnetic phases for EuFe$_2$As$_2$ and EuFe$_{1.8}$Co$_{0.2}$As$_2$ discussed above were confirmed by magnetic torque experiments, where the anisotropy of the susceptibility was directly probed. In Fig. 4.12 the scaled magnetic torque $\tau/(\mu_0 H^2)$ for EuFe$_2$As$_2$ and EuFe$_{1.8}$Co$_{0.2}$As$_2$ is shown in a color map for the representative temperatures of 13 K, 17 K, and 20 K as a function of angle θ and field H. As seen in Fig. 4.12 the transition between the different magnetic phases induced by the magnetic field appears abruptly along a clearly angular dependent boundary line, demonstrating the anisotropy of this magnetically ordered system. The shape of the angular dependence of the transition between the AFM and C-AFM phase in the (H, θ) diagram was analyzed by Eq. (8) of Ref. [155] and represented by the dashed line in Fig. 4.12a. It describes the experimental data rather well and is consistent with the above magnetization data.

In order to explain long-range AFM ordering in EuFe$_2$As$_2$ one has to take into account the conduction-electron-mediated RKKY interaction. However, the RKKY interaction alone is not sufficient to explain the spin-canting in EuFe$_{1.8}$Co$_{0.2}$As$_2$. Recently, the C-AFM structure was also observed in Eu(Fe$_{0.81}$Co$_{0.19}$)$_2$As$_2$ [204, 205]. In order to interprete the spin canting, the model developed by Fert and Levy [50] was invoked. According to this model, the enhancement of the anisotropy field may arise from an additional term in the RKKY interaction, which is of the Dzyaloshinskii-Moriya (DM) type (see Sec. 2.2.3). It is due to spin-orbit scattering of the conduction electrons by the non-magnetic impurities. However, in the case of EuFe$_{2-x}$Co$_x$As$_2$ it is not clear whether Co atoms introduce such a spin-orbit scattering. Hence, at present not enough arguments exist to apply the Fert-Levy interaction to explain the spin canting in Co-doped EuFe$_{2-x}$Co$_x$As$_2$ [155, 204, 205].

Note that the present results for EuFe$_{1.8}$Co$_{0.2}$As$_2$, which exhibits a SDW ground state below 80 K, reveal a C-AFM structure of the Eu spins with a FM component in the ab-plane. This finding confirms previous assumptions that for materials in which the Fe ions are in the SDW ground state (such as EuFe$_2$As$_2$) the direction of the Eu magnetic moments is in the ab-plane [141, 198]. On the other hand, in the case of no magnetism in the Fe sublattice, like in SC EuFe$_{2-x}$Co$_x$As$_2$ compounds, where the SDW state is totally suppressed, the direction of the Eu magnetic moments is parallel to the c-axis [199, 200, 201, 202]. These observations imply that the magnetic configuration of the Eu moments is strongly influenced by the magnetic moments of the Fe-sublattice.

We note that recently in the system Eu(Fe$_{0.81}$Co$_{0.19}$)$_2$As$_2$ field-induced (FI) superconductivity was observed when the magnetic field is applied parallel to the ab-plane [204]. Interestingly, FI superconductivity appears at the field where the field induced reorientation of the Eu magnetic moments takes place [205]. This indicates a strong correlation between superconductivity and Eu magnetism in EuFe$_{2-x}$Co$_x$As$_2$. Different possible mechanisms for FI superconductivity are discussed in the literature [204, 205].

4.2.4 Chemical and hydrostatic pressure effects in $EuFe_2(As_{1-x}P_x)_2$

Isovalent P substitution on the As site in $EuFe_2As_2$ without introducing holes or electrons simulates a condition generally referred to as "chemical pressure". Interestingly, in contrast to the Co-doped system $EuFe_{2-x}Co_xAs_2$, in P substituted $EuFe_2(As_{1-x}P_x)_2$ bulk superconductivity was observed by resistivity, magnetization, and specific heat measurements [149]. This might be related to the findings of ARPES experiments [206] that in p- and n-type doped and chemically pressurized Fe-HTSs there are different ways in which the nesting conditions can be reduced causing the destabilization of AFM order and the appearance of the SC state. One of the important and controversially discussed issues in $EuFe_2(As_{1-x}P_x)_2$ is the interplay between superconductivity and Eu FM ordering. A coexistence of bulk superconductivity and FM ordering of the Eu magnetic moments below 20 K in polycrystalline samples of $EuFe_2(As_{0.7}P_{0.3})_2$ was discussed by Ren *et. al.* [207]. Subsequent magnetic Compton scattering experiments on similar polycrystalline material indicated competition between the two phenomena [208]. Recently, Jeevan *et al.* [149] reported the phase diagram for single crystalline $EuFe_2(As_{1-x}P_x)_2$. According to this report superconductivity was only found in a very narrow range of P content x ($0.16 \leq x \leq 0.22$), where the SDW state is suppressed. Superconductivity with a zero resistivity state was also observed for $EuFe_2As_2$ under an applied pressure p [147, 209]. Similar to the case of P substitution, superconductivity covers only a narrow pressure range of 2.5-3.0 GPa.

Since this issue is still under debate we decided to perform chemical and hydrostatic pressure experiments on well characterized $EuFe_2(As_{1-x}P_x)_2$ samples. For this reason detailed magnetization and μSR experiments in $EuFe_2As_{2-x}P_x$ ($x = 0$, 0.12, 0.2, and 1) were performed. One P substituted sample $EuFe_2(As_{0.88}P_{0.12})_2$ was also studied under hydrostatic pressure p. μSR experiments provide reliable measurements of T_c, T_{SDW}, T_{Eu} (magnetic ordering temperature of Eu), and the size of the ordered moment as a function of p and x. Consequently, the SC and magnetic phase diagrams with respect to x and p are determined from these experiments. The present results are compared with previous high pressure studies on the parent compound $EuFe_2As_2$ [146, 147]. The combined results are discussed in terms to the relation of x and p.

Among the studied samples, the one with $x = 0$ is single crystalline, and all the P substituted compounds are pollycrystalline [157, 210]. The crystal structure for all the samples $EuFe_2(As_{1-x}P_x)_2$ ($x = 0$, 0.12, 0.2, and 1) at room temperature was refined with the tetragonal $ThCr_2Si_2$ structure [210, 211]. Importantly, no obvious secondary phase could be detected [210].

The temperature dependence of the zero-field-cooled (ZFC) and field-cooled (FC) magnetic susceptibility ($\chi = M/H$) for $EuFe_2(As_{1-x}P_x)_2$ ($x = 0.12$, 0.2 and 1) in a magnetic field of $\mu_0H = 2$ mT, measured with a commercial SQUID magnetometer (*Quantum Design* MPMS-XL), is shown in Fig. 4.13. For all the P substituted samples an obvious divergence between χ_{ZFC} and χ_{FC} is seen at low temperatures, which is not the case for $x = 0$ [140, 157], for which AFM order of Eu^{2+} was reported. These results are consistent with previous magnetizaton studies [212], suggesting that the coupled Eu^{2+} spins form canted AFM (C-AFM) state (*i.e.*, AFM with a net FM component along the c-axis) in $EuFe_2(As_{1-x}P_x)_2$ ($x = 0.12$, 0.2) and a FM state in $EuFe_2P_2$. The C-AFM and FM structure of the Eu-sublattice in $EuFe_2(As_{1-x}P_x)_2$ ($x = 0.12$, 0.2, 1) is different from the planar antiferromagnetism seen in the parent compound $EuFe_2As_2$ [140, 157], suggesting a delicate interplay between the Eu $4f$ and transition metal $3d$ electrons. Notice that no indication of superconductivity was seen for $x = 0.2$ from the present magnetization measurements. This is in contrast to a previous report revealling superconductivity in $EuFe_2(As_{1-x}P_x)_2$ [149] for $0.16 \leq x \leq 0.22$, where the SDW transition is suppressed. Absence of superconductivity in the present case might be due to the fact that in our sample with $x = 0.2$ the SDW state is still not completely suppressed as seen from μSR experiments [210].

Magnetization measurements were performed also under hydrostatic pressures up to $p = 5.6$ GPa by using a diamond anvil cell (DAC) filled with Daphne oil which served as a pressure-transmitting medium [213, 214]. Hydrostatic pressure was used to tune physical properties of one of the P substituted sample $EuFe_2(As_{0.88}P_{0.12})_2$. The sample with $x = 0.12$ was chosen for the following reason: According to the SC phase diagram reported for $EuFe_2As_2$ as a function of chemical pressure the sample with $x = 0.12$ is close to the region of the phase diagram where superconductivity appears. By applying hydrostatic pressure the SC phase might be reachable.

Furthermore, the system $EuFe_2(As_{1-x}P_x)_2$ at ambient and at applied pressures was also studied by means of ZF-μSR experiments. The maximum pressures reached was 2.0 GPa, using a double wall piston-cylinder type of cell made of MP35N material, especially designed to perform μSR experiments under pressure [215]. As an example, ZF-μSR time spectra for the single crystal sample $EuFe_2As_2$ and for the polycrystalline samples $EuFe_2(As_{1-x}P_x)_2$ (x

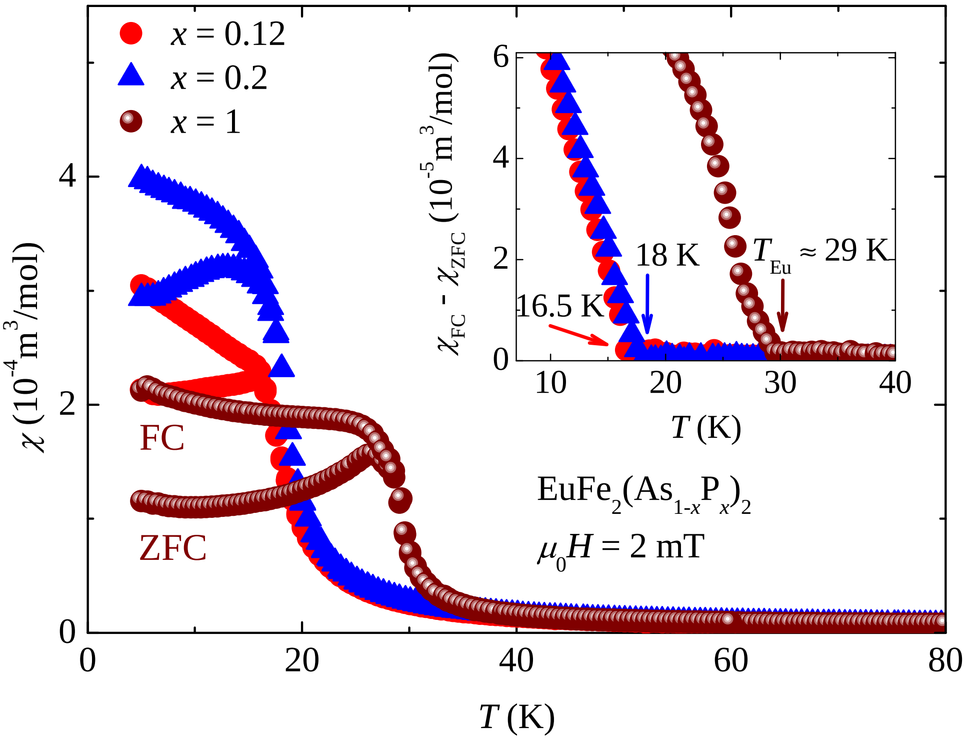

Figure 4.13: (Color online) Temperature dependence of the ZFC and FC magnetic susceptibility for the samples $EuFe_2(As_{1-x}P_x)_2$ ($x = 0.12$, 0.2, 1) measured in a magnetic field of $\mu_0 H = 2$ mT. The inset illustrates the temperature dependence of the difference of both susceptibilities (χ_{FC}-χ_{ZFC}). The arrows mark the magnetic ordering temperatures of the Eu^{2+} moments. After [210].

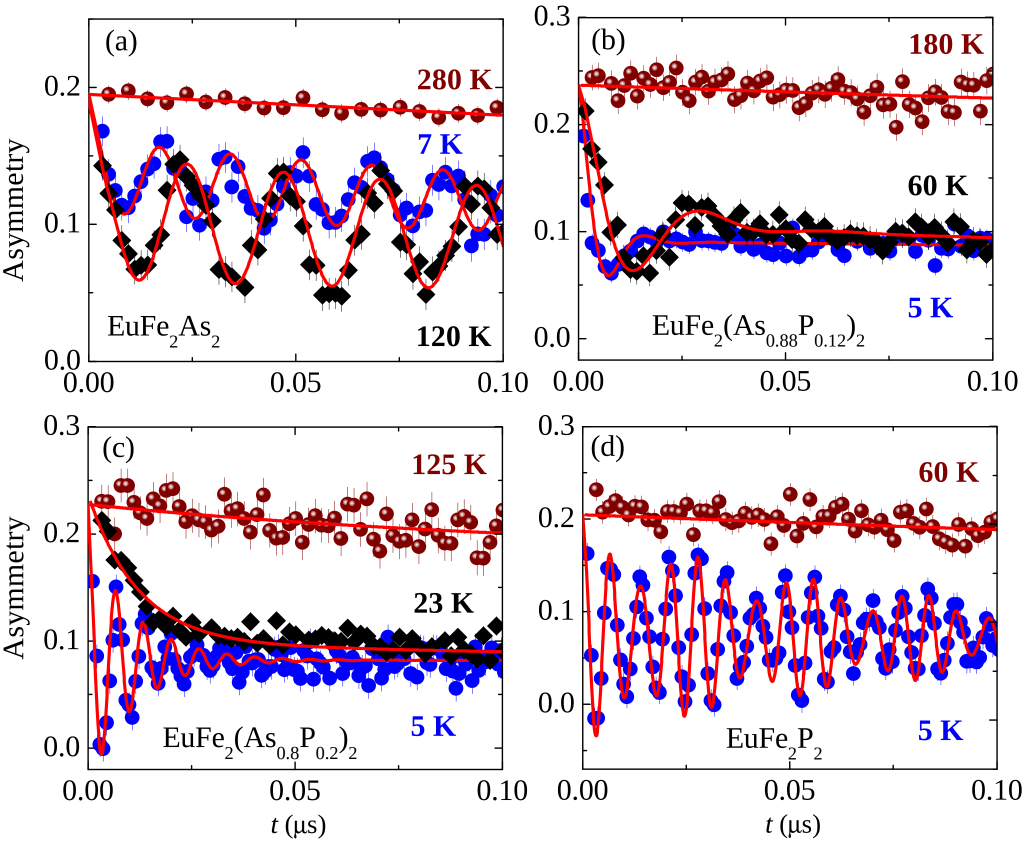

Figure 4.14: (Color online) ZF-μSR spectra for EuFe$_2$(As$_{1-x}$P$_x$)$_2$ (x = 0, 0.12, 0.2, 1) recorded for three different temperatures: $T < T_{\rm Eu}$, $T_{\rm Eu} < T < T_{\rm SDW}$, and $T > T_{\rm SDW}$. The solid lines represent fits to the data, as described in [210]. After [210].

= 0.12, 0.2, 1) are shown in Fig. 4.14, recorded at ambient pressure for three different temperatures: $T < T_{\rm Eu}$, $T_{\rm Eu} < T < T_{\rm SDW}$, and $T > T_{\rm SDW}$. The slowly relaxing non-oscillating signal for $T > T_{\rm SDW}$ signifies the paramagnetic state of the samples. The observation of well-defined spontaneous muon spin precession at low temperatures indicates the magnetic order of Eu and Fe moments. Note that for the compounds with x = 0, 0.12, and 0.2 only one μSR frequency is visible. However, for x = 1 the μSR signal reveals two distinct components with well defined local magnetic fields at the muon sites. One with $B_\mu^1 \simeq 1.08$ T corresponding to $\simeq$ 70% of the signal and other one with $B_\mu^2 \simeq 1.37$ T corresponding to $\simeq$ 30% of the signal. The details of the ZF-μSR data analysis at ambient and applied pressures are described in Ref. [210]. From the analysis of the μSR signal the following important parameters are extracted:

a) The internal magnetic field at the muon site B_μ. It is proportional to the magnitude of the ordered moment and thus to the magnetic order parameter.

b) The relative weights of the magnetic fractions in the sample.

c) The depolarization rates $\lambda_{\rm T}$ and $\lambda_{\rm L}$, characterizing the damping of the oscillating and nonoscillating part of the μSR signal, respectively.

The SDW ordering of the Fe moments was observed by the appearance of B_μ below $T_{\rm SDW}$. The magnetic ordering of Eu was manifested as an additional increase of B_μ below $T_{\rm Eu}$ [210]. The magnetic ordering temperatures of Eu and Fe are also clearly visible in the transverse and longitudinal relaxation rates $\lambda_{\rm T}$ and $\lambda_{\rm L}$, which show a clear maximum at $T_{\rm Eu}$ and $T_{\rm SDW}$ [210].

In Figs. 4.15 and 4.16 the results of the magnetization and μSR experiments are summarized. Fig. 4.15a shows the (x-T) phase diagram for the system $EuFe_2(As_{1-x}P_x)_2$. The (p-T) phase diagram of $EuFe_2(As_{0.88}P_{0.12})_2$ is plotted in Fig. 4.15b. In Fig. 4.16 the internal magnetic fields $B^1_{\mu,\rm Eu}$ and $B_{\mu,\rm SDW}$ probed by the muons in the Eu ordered and in the SDW state and the low temperature value of the magnetic susceptibility $\chi_{\rm ZFC}$(7 K) are plotted as a function of x and applied pressure p.

By combining the above phase diagrams one obtains a coherent physical picture of the system $EuFe_2As_2$ upon P substitution and on $EuFe_2(As_{0.88}P_{0.12})_2$ under hydrostatic pressure. An important finding is the observation of pressure-induced superconductivity in $EuFe_2(As_{0.88}P_{0.12})_2$, which coexists with AFM order of the Eu and SDW order of the Fe moments. Superconductivity appears only in the narrow pressure region of 0.36-0.5 GPa. The presented phase diagrams in combination with the results obtained for the parent compound under pressure [147, 209] allow us to draw the following conclusion on the relation between chemical and hydrostatic pressure in $EuFe_2As_2$:

1) Both chemical and hydrostatic pressure suppress $T_{\rm SDW}$ and $B_{\mu,\rm SDW}(0)$ (zero-temperature value of $B_{\mu,\rm SDW}$). However, the SDW ground state is differently affected by x and p. At all applied pressures below $p = 1.1$ GPa long-range SDW order was observed, while in the case of chemical pressure for $x = 0.2$ a disordered SDW phase exists. This may be related to the fact that by chemical pressure considerably more disorder is introduced.

2) As evident in Fig. 4.15a, the ordering temperature $T_{\rm Eu}$ first decreases as a function of x, reaches a shallow minimum at $x = 0.12$, and then increases. For a fixed P content of $x = 0.12$ the ordering temperature $T_{\rm Eu}$ increases with pressures up to $p = 5.6$ GPa. Above $p = 5.6$ GPa, however, $T_{\rm Eu}(p)$ decreases, accompanied by a possible valence change of the Eu moments [216, 217]. In the parent compound $EuFe_2As_2$ a valence change was found at a higher pressure $p = 8$ GPa.

3) The internal magnetic field $B^1_{\mu,\rm Eu}(0)$ in the Eu ordered state increases with increasing x as well as by applying hydrostatic pressure (see Figs. 4.16a and b). Interestingly, a drastic increase of $B^1_{\mu,\rm Eu}(0)$ was observed at $x \simeq 0.2$, where SDW is suppressed. Considering the magnetization results, the increase of $B^1_{\mu,\rm Eu}(0)$ may be ascribed to the appearance/growth of the ferromagnetic component as a result of P substitution.

4) The low temperature value of the magnetic susceptibility $\chi_{\rm ZFC}$ (7 K) first increases with increasing x and p. Above $x = 0.2$ and $p = 1.1$ GPa, at which the SDW state is suppressed, it decreases (see Figs. 4.16a and b). This strongly suggests that the Eu magnetic order is influenced by the moments of the Fe sublattice.

5) Pressure-induced superconductivity in P substituted $EuFe_2(As_{0.88}P_{0.12})_2$ is observed in the pressure range 0.36-0.5 GPa. This pressure range is narrower than $p = 2.5$-3.0 GPa for the parent compound (see inset of Fig. 4.15b) [147, 209].

By considering the findings listed above the qualitative statement can be made that the properties of $EuFe_2(As_{1-x}P_x)_2$ are similarly tuned by chemical and hydrostatic pressure. These investigations reveal that the magnetic coupling between the Eu and the Fe sublattices strongly depends on both chemical and hydrostatic pressure. One of the important aspects of the present results is that it confirms the presence of superconductivity in the extremely narrow pressure range in $EuFe_2(As_{1-x}P_x)_2$ (see inset of Fig. 4.15b). After our data had been

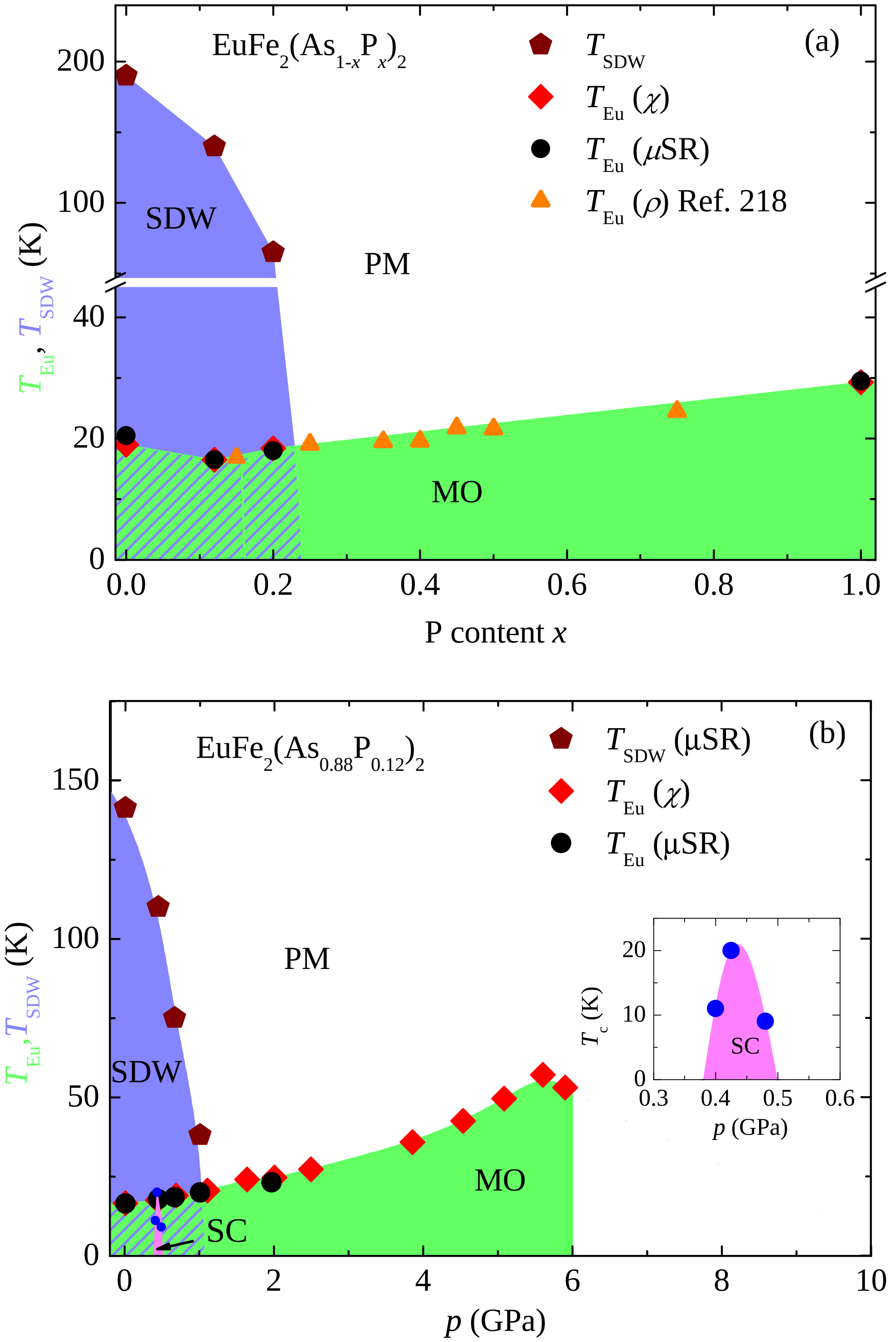

Figure 4.15: (Color online) (a) (x-T) phase diagram of $\mathrm{EuFe_2(As_{1-x}P_x)_2}$. (b) ($p$-$T$) phase diagram of $\mathrm{EuFe_2(As_{0.88}P_{0.12})_2}$. The various phases in the phase diagrams and the corresponding transition temperatures are denoted as follows: paramagnetic (PM), spin-density wave (SDW) and T_{SDW}, magnetic ordering of Eu (MO) and T_{Eu}, SC phase and T_c. For clarity the inset in (b) shows the SC phase present in a very narrow pressure range. After [210].

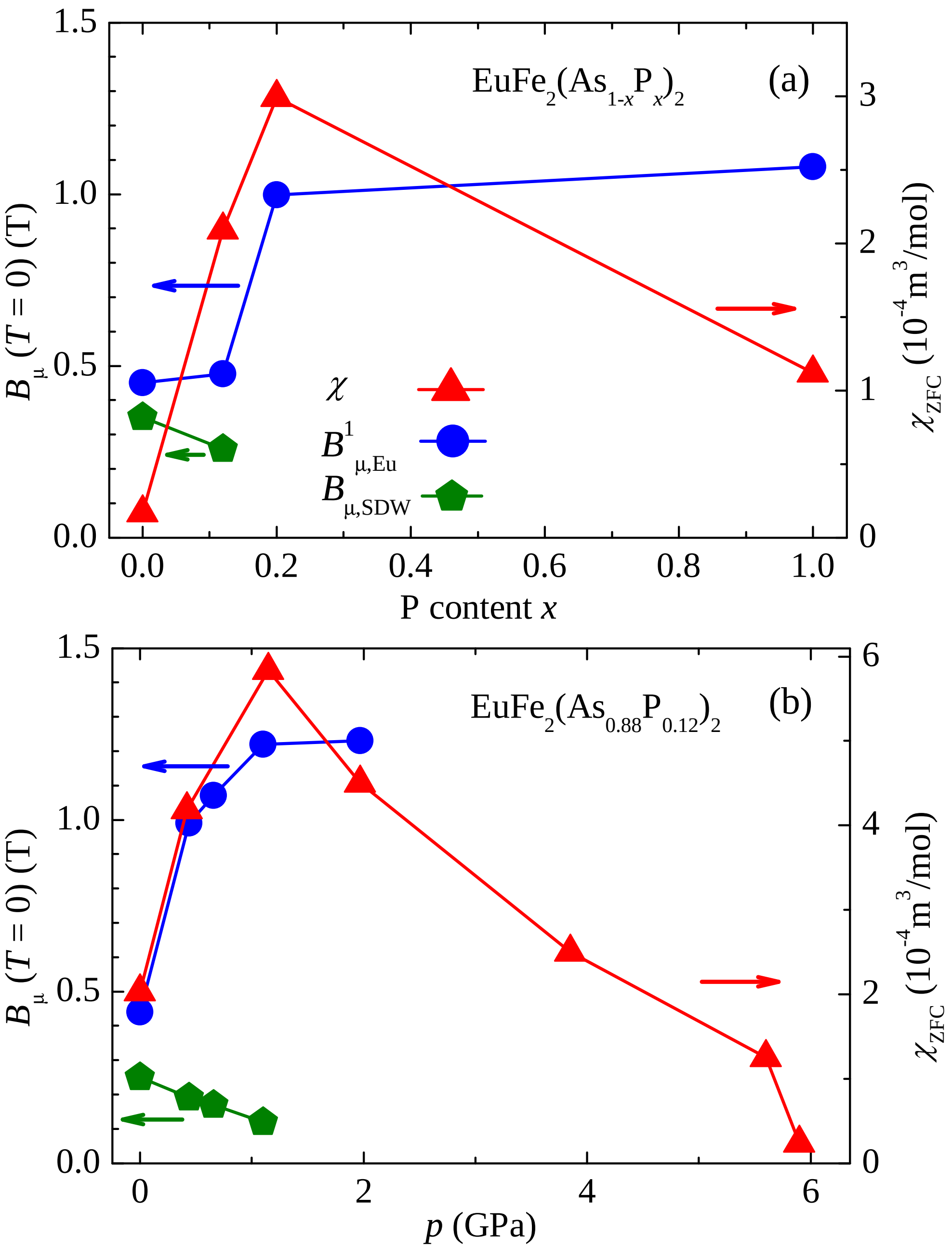

Figure 4.16: (Color online) Zero-temperature values of the internal magnetic fields $B^1_{\mu,\mathrm{Eu}}$ and $B_{\mu,\mathrm{SDW}}$ (see text for an explanation) and the low-temperature value of the magnetic susceptibility χ_{ZFC}(7 K) as a function of the P content x for $\mathrm{EuFe_2(As_{1-x}P_x)_2}$ (a) and as a function of applied pressure for $\mathrm{EuFe_2(As_{0.88}P_{0.12})_2}$ (b). After [210].

reported, the pressure experiments were also performed for $x = 0.18$ by another group [219]. Again superconductivity confined to a narrow pressure range was found. This implies that the system $\mathrm{EuFe_2(As_{1-x}P_x)_2}$ has an unique superconducting phase diagram. This is very different than the respective phase diagram for $\mathrm{BaFe_2(As_{1-x}P_x)_2}$, where superconductivity is observed over a large pressure range. This might be related to the sophisticated interplay between SDW, Eu magnetic order, and superconductivity in $\mathrm{EuFe_2(As_{1-x}P_x)_2}$.

Note, that according to the obtained phase diagram (see Fig. 4.15a), suppression of the

SDW state appears near $x \simeq 0.23$ at which the change of Eu magnetic order is observed (see Fig. 4.16) [149, 210, 212]. Interestingly, at $x \simeq 0.23$ angular-resolved photoemission spectroscopy (ARPES) has detected a change of the Fermi surface nesting properties with chemical pressure [206]. Namely, the inner hole-like Fermi surface near the Γ point shrinks to zero at $x \simeq 0.23$. On the other hand, by using a minimal multiband model, it has recently been shown that the Fermi surface nesting has strong influence on the RKKY interaction [220]. Hence, the change of the electronic structure most likely modifies the Eu RKKY interaction such that the Eu magnetism switches from AFM to FM ordering. Since FM ordering is incompatible with superconductivity, this explains the fact that in $\mathrm{EuFe_2(As_{1-x}P_x)_2}$ the SC phase only exists in a very narrow range of P content ($0.16 \leq x \leq 0.22$) and hydrostatic pressure.

4.3 The temperature and field dependence of the magnetic penetration depth λ in optimally doped $\mathrm{Ba_{1-x}Rb_xFe_2As_2}$

We also performed measurements of the magnetic penetration depth λ in the Fe-HTS $\mathrm{Ba_{1-x}Rb_xFe_2As_2}$ ($x = 0.3$, 0.35, 0.4) by using the μSR technique [221]. In this system the spacer layer is provided by an alkali earth element Ba, forming non-magnetic layers, in contrast to the Eu based compounds discussed in the previous sections. Hence, only the SDW ordering of the Fe moments is present in the parent compound $\mathrm{BaFe_2As_2}$ [222]. By replacing Ba with an alkali metal, such as K, Cs or Rb, the SDW state is suppressed and superconductivity appears [223]. This system allows to study the SC properties without influence of magnetism and it has the highest $T_\mathrm{c} = 38$ K among the 122 compounds. Moreover, several disconnected Fermi-surface sheets contribute to superconductivity as revealed by ARPES [224, 225, 226]. In addition, indications of multi-gap superconductivity in the related system $\mathrm{Ba_{1-x}K_xFe_2As_2}$ were obtained from the temperature dependence of λ by means of μSR [227] and ARPES [224]. The temperature dependence of λ (see Sec. 2.3) reflects the topology of the SC gap. The μSR technique provides a powerful tool to measure λ in type II superconductors [228].

Polycrystalline samples of $\mathrm{Ba_{1-x}Rb_xFe_2As_2}$ were prepared in evacuated quartz ampoules by a solid state reaction method [221]. Powder x-ray diffraction analysis revealed that the synthesized samples are single phase materials. The μSR experiments were performed at the πM3 beamline of the Paul Scherrer Institute (Villigen, Switzerland), using the general purpose instrument (GPS).

Figures 4.17a and b show the TF-μSR time spectra for $\mathrm{Ba_{1-x}Rb_xFe_2As_2}$ ($x = 0.3$, 0.4) measured in an applied magnetic field of $\mu_0 H = 0.04$ T above (45 K) and below (1.7 K) the SC transition temperature T_c. Above T_c the oscillations show a small relaxation due to the random local fields from the nuclear magnetic moments. Below T_c the relaxation rate strongly increases due to the presence of a nonuniform local field distribution as a result of the formation of a flux-line lattice (FLL) in the SC state. Magnetism, if present in the sample, may enhance the muon depolarization rate and falsify the interpretation of the TF-

μSR results. ZF-μSR experiments performed above and below T_c revealed no sign of either static or fluctuating magnetism down to 1.7 K [221]. Moreover, no field induced magnetism [229, 230, 231] was observed in the system $Ba_{1-x}Rb_xFe_2As_2$ down to 1.7 K [221]. The absence of magnetism in $Ba_{1-x}Rb_xFe_2As_2$ implies that the increase of the TF relaxation rate below T_c is attributed entirely to the vortex lattice.

TF μSR data were analyzed by using the functional form [232]

$$P(t) = A\exp\Big[-\frac{(\sigma_{sc}^2+\sigma_{nm}^2)t^2}{2}\Big]\cos(\gamma_\mu B_\mu t+\varphi), \tag{4.4}$$

where A denotes the initial assymmetry, $\sigma_{\rm sc}$ is the relaxation rate, characterizing the damping due to the formation of the FLL in the SC state. $\sigma_{\rm nm}$ is the nuclear magnetic dipolar contribution to the relaxation, which was assumed to be constant over the entire temperature range in the analysis. B_μ denotes the internal field at the muon site, and φ is the initial phase of the muon-spin ensemble. The temperature dependence of $\sigma_{\rm sc}$ for $Ba_{1-x}Rb_xFe_2As_2$ ($x = 0.3$, 0.35, and 0.4) at $\mu_0H = 0.04$ T is shown in Fig. 4.18. Below T_c the relaxation rate $\sigma_{\rm sc}$ starts to increase from zero due to the formation of the FLL.

For polycrystalline samples the temperature dependence of the London magnetic penetration depth $\lambda(T)$ is related to the SC part of the Gaussian muon spin depolarization rate $\sigma_{\rm sc}(T)$ by the equation [233, 234]:

$$\frac{\sigma_{sc}^2(T)}{\gamma_\mu^2} = 0.00371\frac{\Phi_0^2}{\lambda^4(T)}, \tag{4.5}$$

where $\gamma_\mu = 2\pi\cdot$ 135.5MHz/T is the gyromagnetic ratio of the muon and $\Phi_0 = \mathrm{h}/2\mathrm{e} \simeq 2.068 \times 10^{-15}$ Vs is the elementary flux quantum.

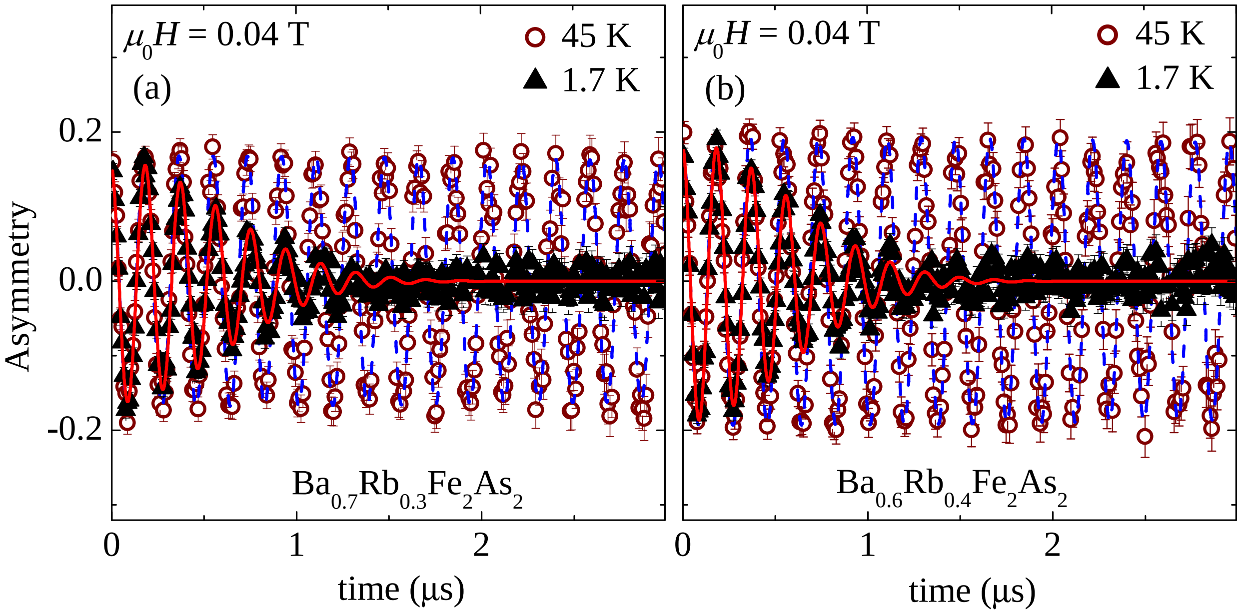

Figure 4.17: (Color online) Transverse-field μSR time spectra obtained at $\mu_0H = 0.04$ T above and below T_c (after field cooling the sample from above T_c): (a) $Ba_{0.7}Rb_{0.3}Fe_2As_2$ and (b) $Ba_{0.6}Rb_{0.4}Fe_2As_2$. The solid lines represent fits to the data by means of Eq. (4.4). After [221].

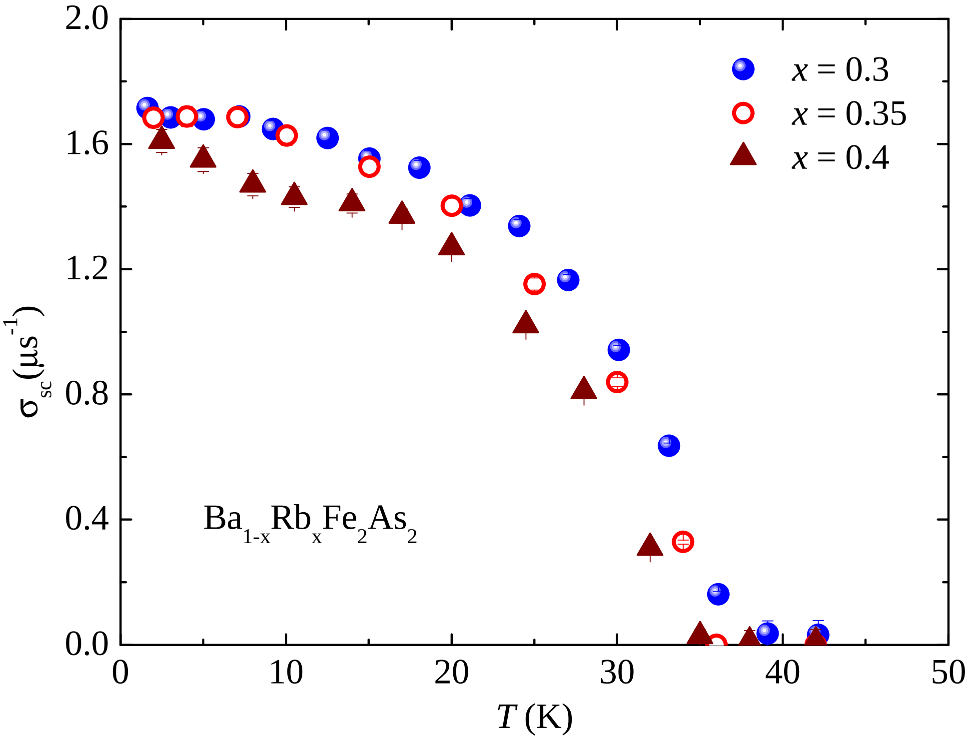

Figure 4.18: (Color online) Temperature dependence of the SC muon spin depolarization rate σ_{sc} measured in an applied magnetic field of $\mu_0 H = 0.04$ T for $\mathrm{Ba}_{1-x}\mathrm{Rb}_x\mathrm{Fe}_2\mathrm{As}_2$ ($x = 0.3$, 0.35, 0.4). After [221].

$\lambda(T)$ was calculated within the local (London) approximation ($\lambda \gg \xi$) by the following expression [53, 221, 232]:

$$\frac{\lambda^{-2}(T,\Delta_{0,i})}{\lambda^{-2}(0,\Delta_{0,i})} = 1 + \frac{1}{\pi}\int_0^{2\pi}\int_{\Delta(T,\Phi)}^{\infty}\left(\frac{\partial f}{\partial E}\right)\frac{EdEd\Phi}{\sqrt{E^2-\Delta_i(T,\Phi)^2}}, \tag{4.6}$$

where $f = [1+\exp(E/k_{\mathrm{B}}T)]^{-1}$ is the Fermi function, Φ is the angle along the Fermi surface, and $\Delta_i(T,\Phi) = \Delta_{0,i}\delta(T/T_{\mathrm{c}})g(\Phi)$ ($\Delta_{0,i}$ is the maximum gap value at $T = 0$). The temperature dependence of the gap is approximated by the expression $\delta(T/T_{\mathrm{c}}) = \tanh\{1.82[1.018(T_{\mathrm{c}}/T-1)]^{0.51}\}$ [235], while $g(\Phi)$ describes the angular dependence of the gap and it is replaced by 1 for both an s-wave and an s+s-wave gap, and $|\cos(2\Phi)|$ for a d-wave gap [236].

The temperature dependence of the penetration depth was analyzed using either a single gap or a two-gap model which is based on the so-called α model [221, 235, 237, 238]. The results of the analysis for $\mathrm{Ba}_{1-x}\mathrm{Rb}_x\mathrm{Fe}_2\mathrm{As}_2$ ($x = 0.3$, 0.35, 0.4) are presented in Fig. 4.19. The dashed and the solid lines represent fits to the data using a s-wave and a $s+s$-wave model, respectively. The two-gap $s+s$-wave scenario with a small gap $\Delta_1 \simeq 2$ meV and a large gap $\Delta_2 \simeq 6$ meV, describes the experimental data remarkably well. A two-gap scenario is in line with the generally accepted view of multi-gap superconductivity in Fe-HTSs [224, 225, 227, 239, 240, 241]. Moreover, the gap to T_{c} ratio [$2\Delta_1(0)/k_B T_{\mathrm{c}}$=2.0(5) and $2\Delta_2(0)/k_B T_{\mathrm{c}}$=5.8(6)] is similar in all the Fe-HTSs. This may give important hints for the pairing mechanism leading to superconductivity in the Fe-HTSs.

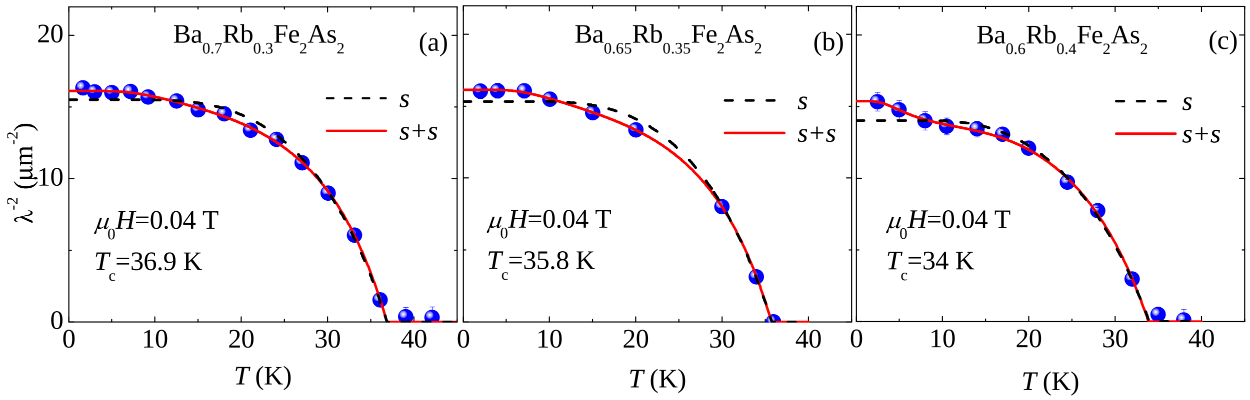

Figure 4.19: (Color online) The temperature dependence of λ^{-2} for $\mathrm{Ba}_{1-x}\mathrm{Rb}_x\mathrm{Fe}_2\mathrm{As}_2$, measured in an applied field of $\mu_0 H = 0.04$ T: (a) $x = 0.3$, (b) $x = 0.35$, and (c) $x = 0.4$. The dashed lines correspond to a single gap BCS s-wave model, whereas the solid ones represent a fit using a two-gap $(s+s)$-wave model. After [221].

4.4 Publications related to Chapter 4

- *Strong coupling between Eu^{2+} spins and Fe$_2$As$_2$ layers in EuFe$_{1.9}$Co$_{0.1}$As$_2$ observed with NMR*
  Z. Guguchia, J. Roos, A. Shengelaya, S. Katrych, Z. Bukowski, S. Weyeneth, F. Murányi, S. Strässle, A. Maisuradze, J. Karpinski, and H. Keller
  Phys. Rev. B **83**, 144516 (2011).

- *Anisotropic magnetic order of the Eu sublattice in single crystals of EuFe$_{2-x}$Co$_x$As$_2$ (x = 0, 0.2) studied by means of magnetization and magnetic torque*
  Z. Guguchia, S. Bosma, S. Weyeneth, A. Shengelaya, R. Puzniak, Z. Bukowski, J. Karpinski, and H. Keller
  Phys. Rev. B **84**, 144506 (2011).

- *Muon-spin rotation and magnetization studies of chemical and hydrostatic pressure effects in EuFe$_2$(As$_{1-x}$P$_x$)$_2$*
  Z. Guguchia, A. Shengelaya, A. Maisuradze, L. Howald, Z. Bukowski, M. Chikovani, H. Luetkens, S. Katrych, J. Karpinski, and H. Keller
  J. Supercond. Nov. Magn. **26**, 285 (2013).

- *Muon-spin rotation measurements of the magnetic penetration depth in the iron-based superconductor Ba$_{1-x}$Rb$_x$Fe$_2$As$_2$*
  Z. Guguchia, Z. Shermadini, A. Amato, A. Maisuradze, A. Shengelaya, Z. Bukowski, H. Luetkens, R. Khasanov, J. Karpinski, and H. Keller
  Phys. Rev. B **84**, 094513 (2011).

4.4.1 Publication I: Strong coupling between Eu^{2+} spins and Fe_2As_2 layers in $EuFe_{1.9}Co_{0.1}As_2$ observed with NMR

Z. Guguchia, J. Roos, A. Shengelaya, S. Katrych, Z. Bukowski, S. Weyeneth, F. Murányi, S. Strässle, A. Maisuradze, J. Karpinski, and H. Keller
Phys. Rev. B **83**, 144516 (2011).

Abstract

A combination of X-ray diffraction, magnetization, and ^{75}As nuclear magnetic resonance (NMR) experiments were performed on single-crystal $EuFe_{1.9}Co_{0.1}As_2$. The strength of the hyperfine interaction between the ^{75}As nuclei and the Eu^{2+} $4f$ states suggests a strong coupling between the Eu^{2+} moments and the $Fe_{1.9}Co_{0.1}As_2$ layers. Such a strong interlayer coupling may be due to an indirect exchange interaction between the localized Eu^{2+} $4f$ moments, mediated by the Fe $3d$ conduction electrons. Magnetic susceptibility as well as ^{75}As-NMR measurements reveal a decrease of the SDW transition temperature to $T_{\mathrm{SDW}} =$ 120 K as a result of Co-doping. A change of the slope in the temperature dependence of the NMR frequency of the ^{75}As lower-satellite line was observed at 225 K. At the same temperature also a change of the satellite line shape was found. These changes of the NMR spectra may be caused by the formation of a nematic phase below 225 K in $EuFe_{1.9}Co_{0.1}As_2$.

DOI: 10.1103/PhysRevB.83.144516

PACS numbers: 74.70.-b, 76.60.-k, 75.30.Fv, 61.50.Ks

The original publication is electronically available at:
http://prb.aps.org/abstract/PRB/v83/i14/e144516

PHYSICAL REVIEW B **83**, 144516 (2011)

Strong coupling between Eu^{2+} spins and Fe_2As_2 layers in $EuFe_{1.9}Co_{0.1}As_2$ observed with NMR

Z. Guguchia,[1,*] J. Roos,[1] A. Shengelaya,[2] S. Katrych,[3] Z. Bukowski,[3] S. Weyeneth,[1] F. Murányi,[1] S. Strässle,[1]
A. Maisuradze,[1,4] J. Karpinski,[3] and H. Keller[1]
[1]*Physik-Institut der Universität Zürich, Winterthurerstrasse 190, CH-8057 Zürich, Switzerland*
[2]*Department of Physics, Tbilisi State University, Chavchavadze 3, GE-0128 Tbilisi, Georgia*
[3]*Laboratory for Solid State Physics, ETH Zürich, CH-8093 Zürich, Switzerland*
[4]*Laboratory for Muon Spin Spectroscopy, Paul Scherrer Institute, CH-5232 Villigen PSI, Switzerland*

(Received 20 October 2010; revised manuscript received 14 February 2011; published 19 April 2011)

A combination of x-ray diffraction, magnetization, and ^{75}As nuclear magnetic resonance (NMR) experiments were performed on single-crystal $EuFe_{1.9}Co_{0.1}As_2$. The strength of the hyperfine interaction between the ^{75}As nuclei and the Eu^{2+} $4f$ states suggests a strong coupling between the Eu^{2+} moments and the $Fe_{1.9}Co_{0.1}As_2$ layers. Such a strong interlayer coupling may be due to an indirect exchange interaction between the localized Eu^{2+} $4f$ moments, mediated by the Fe $3d$ conduction electrons. Magnetic susceptibility as well as ^{75}As-NMR measurements reveal a decrease of the SDW transition temperature to $T_{SDW} = 120$ K as a result of Co doping. A change of the slope in the temperature dependence of the NMR frequency of the ^{75}As lower-satellite line was observed at 225 K. At the same temperature also a change of the satellite line shape was found. These changes of the NMR spectra may be caused by the formation of a nematic phase below 225 K in $EuFe_{1.9}Co_{0.1}As_2$.

DOI: 10.1103/PhysRevB.83.144516 PACS number(s): 74.70.−b, 76.60.−k, 75.30.Fv, 61.50.Ks

I. INTRODUCTION

The discovery of superconductivity in iron-based arsenides at temperatures up to 56 K[1–7] has triggered extensive interest in their physical properties and the underlying mechanism of high-temperature superconductivity. The undoped parent compounds adopt a tetragonal structure at room temperature, which consists of $[Fe_2As_2]^{2-}$ layers separated by $[Ln_2O_2]^{2+}$ ($Ln =$ lanthanoide) layers[8,9] or A^{2+} ($A =$ Ca, Sr, Ba, Eu) layers.[10–13] At low temperatures, the parent compounds undergo a structural phase transition from a tetragonal to an orthorhombic phase, accompanied[14] or followed[15] by a spin density wave (SDW) transition of the itinerant Fe moments. The superconducting (SC) state can be achieved either by electron or by hole doping of the parent compounds, leading to a suppression of the SDW formation.[6,16–18] The suppression of the magnetic transition in connection with the simultaneous formation of a SC state is reminiscent of cuprates and heavy fermion systems, therefore suggesting that the SC state in these systems is unconventional as well.

$EuFe_2As_2$ is a particularly interesting member of the iron arsenide AFe_2As_2 ('122') family, since the A site is occupied by a Eu^{2+} S-state (orbital moment $L = 0$) rare-earth ion with a $4f^7$ electronic configuration with a total electron spin $S = 7/2$, corresponding to a theoretical effective magnetic moment of 7.94 μ_B. Figure 1 shows the crystal structure of $EuFe_2As_2$. This compound is built up by $[FeAs]^{2-}$ layers, separated by layers of magnetic Eu^{2+} ions. $EuFe_2As_2$ exhibits both a SDW ordering of the Fe moments and an antiferromagnetic ordering of the localized Eu^{2+} moments below 190 K and 19 K, respectively. The presence of magnetic phase transitions at 19 K and 190 K in $EuFe_2As_2$ was seen by Mössbauer spectroscopy[19] and is confirmed by neutron diffraction.[20] In contrast to the other '122' systems, where the substitution of Fe by Co leads to superconductivity,[21,22] the compounds containing Eu^{2+} exhibit the onset of a superconducting transition but seem to be hindered to reach zero resistivity at ambient pressure.[23] Reentrant superconducting behavior was also observed in a $EuFe_2As_2$ crystal under applied pressure up to 2.5 GPa.[24,25] Only above 2.8 GPa a sharp resistive transition to a zero-resistivity state is achieved.[25] Bulk superconductivity is also observed in $EuFe_2As_{2-x}P_x$,[26,27] where isovalent P substitution of the As site acts as chemical pressure on $EuFe_2As_2$. No superconductivity was detected in $EuFe_{2-x}Ni_xAs_2$,[28] while superconductivity with a maximum $T_c \simeq 20$ K was reported for $BaFe_{2-x}Ni_xAs_2$.[29] It was suggested from different experiments[28,30–32] that there is a strong coupling between the localized Eu^{2+} spins and the conduction electrons of the two-dimensional (2D) Fe_2As_2 layers. The study of the interaction between the rare-earth Eu^{2+} magnetic moments and the conducting Fe_2As_2 layers is important in order to understand why it is difficult to induce superconductivity in Co-doped $EuFe_{2-x}Co_xAs_2$.

In order to investigate the coupling between the Eu and $Fe_{1.9}Co_{0.1}As_2$ layers as well as to study the magnetic transitions in $EuFe_{1.9}Co_{0.1}As_2$, a combination of x-ray diffraction, magnetization, and ^{75}As nuclear magnetic resonance (NMR) experiments were performed on single crystals. Magnetic susceptibility as well as ^{75}As-NMR measurements reveal a decrease of the SDW transition temperature to $T_{SDW} = 120$ K for $EuFe_{1.9}Co_{0.1}As_2$. It was found that the ^{75}As NMR spectra are characterized by a negative frequency shift with respect to the ^{75}As-NMR Larmor frequency. This shift is significantly larger than the one observed in $BaFe_2As_2$, $CaFe_2As_2$, and $SrFe_2As_2$.[33–36] The temperature dependence of the shift follows a Curie-Weiss type behavior with a Curie-Weiss temperature close to the one determined from the magnetization data. The estimate of the hyperfine coupling constant between the ^{75}As nuclei and the Eu $4f$ states suggests a strong coupling between the Eu^{2+} magnetic moments and the $Fe_{1.9}Co_{0.1}As_2$ layers.

II. EXPERIMENTAL DETAILS

Single crystals of $EuFe_{1.9}Co_{0.1}As_2$ were grown out of Sn flux. The chemical composition of the single crystals was determined on freshly cleaved samples using

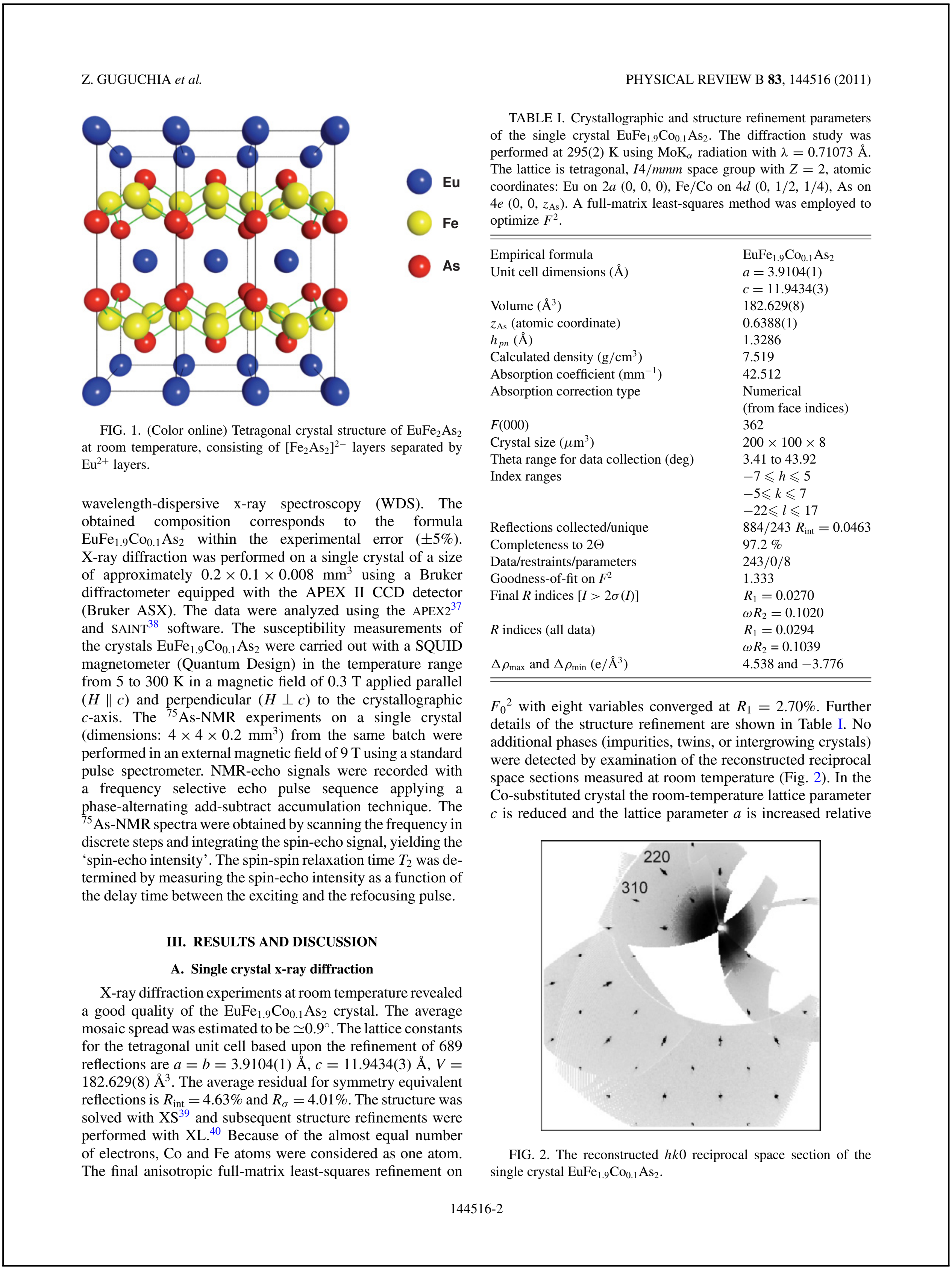

Z. GUGUCHIA *et al.* PHYSICAL REVIEW B **83**, 144516 (2011)

FIG. 1. (Color online) Tetragonal crystal structure of $EuFe_2As_2$ at room temperature, consisting of $[Fe_2As_2]^{2-}$ layers separated by Eu^{2+} layers.

wavelength-dispersive x-ray spectroscopy (WDS). The obtained composition corresponds to the formula $EuFe_{1.9}Co_{0.1}As_2$ within the experimental error (±5%). X-ray diffraction was performed on a single crystal of a size of approximately $0.2 \times 0.1 \times 0.008$ mm^3 using a Bruker diffractometer equipped with the APEX II CCD detector (Bruker ASX). The data were analyzed using the APEX2[37] and SAINT[38] software. The susceptibility measurements of the crystals $EuFe_{1.9}Co_{0.1}As_2$ were carried out with a SQUID magnetometer (Quantum Design) in the temperature range from 5 to 300 K in a magnetic field of 0.3 T applied parallel ($H \parallel c$) and perpendicular ($H \perp c$) to the crystallographic c-axis. The ^{75}As-NMR experiments on a single crystal (dimensions: $4 \times 4 \times 0.2$ mm^3) from the same batch were performed in an external magnetic field of 9 T using a standard pulse spectrometer. NMR-echo signals were recorded with a frequency selective echo pulse sequence applying a phase-alternating add-subtract accumulation technique. The ^{75}As-NMR spectra were obtained by scanning the frequency in discrete steps and integrating the spin-echo signal, yielding the 'spin-echo intensity'. The spin-spin relaxation time T_2 was determined by measuring the spin-echo intensity as a function of the delay time between the exciting and the refocusing pulse.

III. RESULTS AND DISCUSSION

A. Single crystal x-ray diffraction

X-ray diffraction experiments at room temperature revealed a good quality of the $EuFe_{1.9}Co_{0.1}As_2$ crystal. The average mosaic spread was estimated to be $\simeq 0.9^\circ$. The lattice constants for the tetragonal unit cell based upon the refinement of 689 reflections are $a = b = 3.9104(1)$ Å, $c = 11.9434(3)$ Å, $V = 182.629(8)$ Å^3. The average residual for symmetry equivalent reflections is $R_{\text{int}} = 4.63\%$ and $R_\sigma = 4.01\%$. The structure was solved with XS[39] and subsequent structure refinements were performed with XL.[40] Because of the almost equal number of electrons, Co and Fe atoms were considered as one atom. The final anisotropic full-matrix least-squares refinement on $F_0{}^2$ with eight variables converged at $R_1 = 2.70\%$. Further details of the structure refinement are shown in Table I. No additional phases (impurities, twins, or intergrowing crystals) were detected by examination of the reconstructed reciprocal space sections measured at room temperature (Fig. 2). In the Co-substituted crystal the room-temperature lattice parameter c is reduced and the lattice parameter a is increased relative

TABLE I. Crystallographic and structure refinement parameters of the single crystal $EuFe_{1.9}Co_{0.1}As_2$. The diffraction study was performed at 295(2) K using MoK$_\alpha$ radiation with $\lambda = 0.71073$ Å. The lattice is tetragonal, $I4/mmm$ space group with $Z = 2$, atomic coordinates: Eu on $2a$ (0, 0, 0), Fe/Co on $4d$ (0, 1/2, 1/4), As on $4e$ (0, 0, z_{As}). A full-matrix least-squares method was employed to optimize F^2.

Empirical formula	$EuFe_{1.9}Co_{0.1}As_2$
Unit cell dimensions (Å)	$a = 3.9104(1)$ $c = 11.9434(3)$
Volume (Å^3)	182.629(8)
z_{As} (atomic coordinate)	0.6388(1)
h_{pn} (Å)	1.3286
Calculated density (g/cm^3)	7.519
Absorption coefficient (mm^{-1})	42.512
Absorption correction type	Numerical (from face indices)
$F(000)$	362
Crystal size (μm^3)	$200 \times 100 \times 8$
Theta range for data collection (deg)	3.41 to 43.92
Index ranges	$-7 \leqslant h \leqslant 5$ $-5 \leqslant k \leqslant 7$ $-22 \leqslant l \leqslant 17$
Reflections collected/unique	884/243 $R_{\text{int}} = 0.0463$
Completeness to 2Θ	97.2 %
Data/restraints/parameters	243/0/8
Goodness-of-fit on F^2	1.333
Final R indices [$I > 2\sigma(I)$]	$R_1 = 0.0270$ $\omega R_2 = 0.1020$
R indices (all data)	$R_1 = 0.0294$ $\omega R_2 = 0.1039$
$\Delta\rho_{\text{max}}$ and $\Delta\rho_{\text{min}}$ (e/Å^3)	4.538 and −3.776

FIG. 2. The reconstructed $hk0$ reciprocal space section of the single crystal $EuFe_{1.9}Co_{0.1}As_2$.

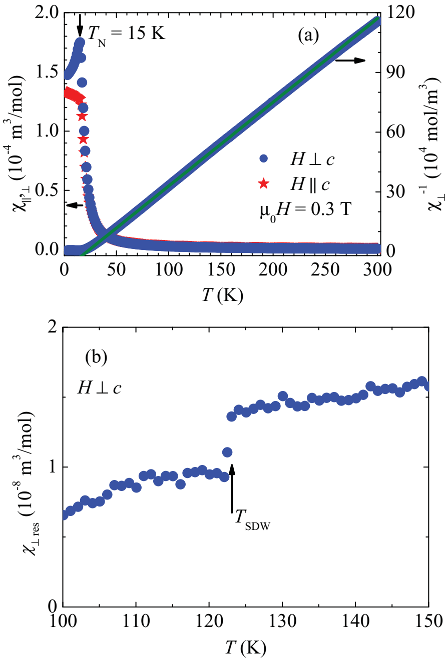

FIG. 3. (Color online) (a) Temperature dependence of the magnetic susceptibility measured in a field of $\mu_0 H = 0.3$ T applied parallel ($H \parallel c$) and perpendicular ($H \perp c$) to the crystallographic c-axis of the single crystal $EuFe_{1.9}Co_{0.1}As_2$. The measurements were performed in the zero-field cooling mode. In addition, for $H \perp c$ the temperature dependence of the inverse susceptibility $1/\chi_\perp$ is plotted. The solid line represents a fit to the data with the Curie-Weiss law given in Eq. (1). (b) Temperature dependence of $\chi_{\perp \mathrm{res}}(T) = \chi_\perp(T)$-$\chi_{\perp CW}(T)$ (see text for an explanation) in the single crystal $EuFe_{1.9}Co_{0.1}As_2$.

to the parent compound $EuFe_2As_2$ ($a = b = 3.898(1)$ Å, $c = 12.085(5)$ Å) which was also grown out of Sn flux.

B. Magnetic properties

Figure 3(a) shows the temperature dependence of the magnetic susceptibility χ for the $EuFe_{1.9}Co_{0.1}As_2$ crystal in an applied field of $\mu_0 H = 0.3$ T parallel ($H \parallel c$) and perpendicular ($H \perp c$) to the crystallographic c-axis. The temperature dependence of the inverse susceptibility for $H \perp c$ is also shown. Below 30 K, χ increases sharply, indicating ferromagnetic coupling between the Eu^{2+} moments. Below 15 K, a sudden decrease in the magnetic susceptibility for $H \perp c$ ($\chi_\perp$) can be seen, indicative for a transition to the antiferromagnetic state of the Eu^{2+} moments. On the other hand, the magnetic susceptibility for $H \parallel c$ ($\chi_\parallel$) remains almost constant below 15 K. This suggests that the Eu^{2+} moments align in the *ab* plane,[41] similar as in the case of $EuFe_2As_2$.[20] From 50 K to 120 K, $\chi_\perp$ is well described by the Curie-Weiss law:

$$\chi_{\perp CW}(T) = \frac{C}{T + \Theta}. \qquad (1)$$

Here C denotes the Curie-Weiss constant, and Θ the Weiss temperature. Analyzing the data with Eq. (1) in the temperature range from 30 K to 120 K yields $C = 2.43(5) \times 10^{-4}$ m^3 K/mol and $\Theta = -21.34(7)$ K. The Curie-Weiss C constant corresponds to an effective magnetic moment of $\mu_{\mathrm{eff}} = 8.7\ \mu_B$, which is slightly larger than the theoretical value of the magnetic moment of a free Eu^{2+} ion ($\mu_{\mathrm{free}} = 7.94\ \mu_B$). The negative value of Θ infers that the interaction between the Eu^{2+} moments is ferromagnetic. Therefore, one can expect that the intralayer arrangement of the Eu^{2+} spins is ferromagnetic as in the parent compound $EuFe_2As_2$. A clear drop in the susceptibility at the SDW transition temperature was observed in $BaFe_2As_2$.[14] In the case of $EuFe_2As_2$ the large signal from the Eu^{2+} spins makes it impossible to directly observe the SDW anomaly. However, after subtracting the Curie-Weiss contribution $\chi_{\perp CW}(T)$ from $\chi_\perp(T)$, a small anomaly in $\chi_{\perp \mathrm{res}}(T) = \chi_\perp(T)$-$\chi_{\perp CW}(T)$ is visible at around 120 K (Fig. 3(b)). This behavior resembles that observed in $EuFe_2As_2$[42] and $BaFe_2As_2$[14] which was ascribed to the SDW transition of the Fe moments.

C. Nuclear magnetic resonance

In this section we present ^{75}As nuclear magnetic resonance (NMR) studies in single crystal $EuFe_{1.9}Co_{0.1}As_2$. NMR is a powerful and extremely sensitive microscopic tool to probe both, magnetism and the local structure in a solid. ^{75}As has a large quadrupolar moment ($Q = 0.3$ b) that interacts with the local electric field gradient (EFG) in the crystal. The nuclear spin Hamiltonian describing the interactions of the investigated nucleus with the external magnetic field and the crystal electric field gradient at the nuclear site is given by the expression

$$H = \gamma\hbar(1 + K_\alpha)I_\alpha H_0 + \frac{h\nu_Q}{6\left[\left(3I_z^2 - 1\right) + \eta\left(I_x^2 - I_y^2\right)\right]}. \qquad (2)$$

Here K_α ($\alpha = x, y, z$) is the relative magnetic shift in the α direction, I_α are the nuclear spin components, H_0 is the external magnetic field, γ is the gyromagnetic ratio, and ν_Q is defined as

$$\nu_Q = \frac{3eQV_{zz}}{2I(2I-1)h}, \qquad (3)$$

where V_{zz} denotes the major principal axis of the EFG tensor, and η the EFG asymmetry parameter defined as $\eta = (V_{xx}$-$V_{yy})/V_{zz}$ ($0 \leqslant \eta \leqslant 1$). We use the standard convention $V_{xx} \leqslant V_{yy} \leqslant V_{zz}$. Since the principal axis of the EFG tensor as well as the magnetic shift tensor are defined by the symmetry of the nuclear site, the resonance frequency of a particular nuclear transition depends on the field direction relative to the crystalline axes.

In the absence of a static magnetic field, the remaining term gives rise to double degenerate energy levels, between which nuclear quadrupole resonance (NQR) transitions can be induced. ^{75}As has a nuclear spin $I = \frac{3}{2}$ and thus two double degenerate $\pm\frac{1}{2}$ and $\pm\frac{3}{2}$ energy levels. In the presence of a large external magnetic field H_0 a splitting of the ^{75}As spectrum into a central line, arising from the central transition ($+\frac{1}{2}$,$-\frac{1}{2}$) and two satellite lines due to the ($\pm\frac{1}{2}$,$\pm\frac{3}{2}$) transitions occurs. A representative ^{75}As NMR spectrum of the central transition at 295 K is shown in the inset of Fig. 4. In the paramagnetic state

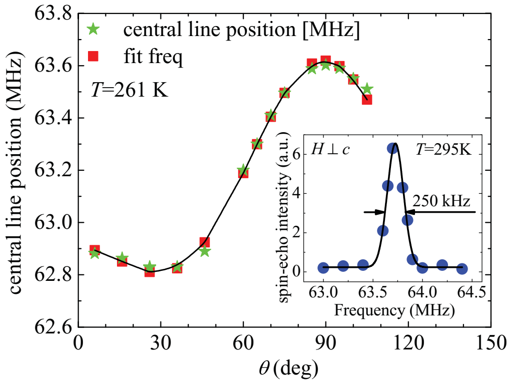

FIG. 4. (Color online) Solid stars represent the dependence of the ^{75}As NMR central line frequency at 261 K on the angle θ between the external magnetic field and the crystallographic c-axis of single crystal $EuFe_{1.9}Co_{0.1}As_2$. The solid line is a guide to the eye. Solid squares represent the calculated frequencies as described in the text. The inset illustrates the ^{75}As NMR central line shape at 295 K. The solid line represents a Gaussian fit.

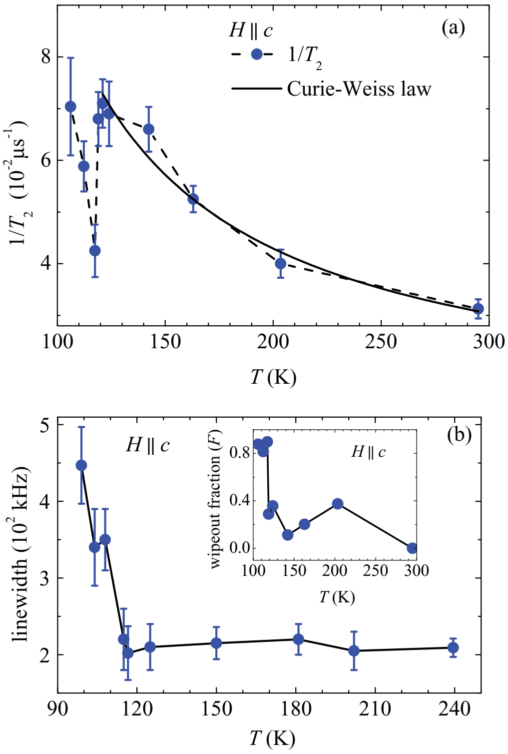

FIG. 5. (Color online) (a) Temperature dependence of the spin-spin relaxation rate $1/T_2$ of the ^{75}As central line of the single crystal $EuFe_{1.9}Co_{0.1}As_2$ for $H \parallel c$. The solid line represents the Curie-Weiss law, and the dashed line is to guide to the eye. (b) Temperature dependence of the linewidth (FWHM) and the wipeout fraction F (inset) for $H \parallel c$. Solid lines are guides to the eye.

($T > T_{SDW}$) lines with a full-width at half-maximum (FWHH) of about 250 kHz (central line) and 500 kHz (satellite lines) are observed.

Figure 4 presents the dependence of the ^{75}As-NMR central line position on the angle θ between the magnetic field orientation and the c-axis at 261 K (tetragonal phase). For all orientations of the magnetic field with respect to the c-axis the line positions show a strong negative shift relative to the corresponding ^{75}As Larmor frequency of 65.9 MHz at 9 T. ^{75}As has four nearest-neighbor Fe atoms, and lies just above or below the Fe plane (see Fig. 1). In the tetragonal phase its site symmetry requires uniaxial symmetry along the c axis for the EFG tensor ($\eta = 0$) and the K tensor. The analysis of the angular dependence of the frequency of the central line using the diagonalization of the Hamiltonian [Eq. (2)] yields $K_{ab} = -0.0372(2)$, $K_c = -0.0456(3)$, and $\nu_Q = 7.39(24)$ MHz with η set to be zero.

Figure 5(a) shows the temperature dependence of the spin-spin relaxation rate $1/T_2$ of the central line of the ^{75}As NMR spectrum for $H \parallel c$. $1/T_2$ exhibits a Curie-Weiss–like temperature dependence down to 120 K. This shows that the ^{75}As nuclei interact with the localized Eu-4f moments. A reduction of $1/T_2$ is observed at 120 K, which reflects the slowing down of the Fe spin fluctuations due to the SDW ordering of the Fe moments. A similar behavior across the SDW transition was also reported for spin-lattice relaxation measurements in AFe_2As_2 (A = Ba, Ca, Sr).[33–35] However, in contrast to these findings, in our case $1/T_2$ increases again upon further cooling. This increase reflects the dominant Eu^{2+} contribution in the spin-spin relaxation process. The SDW transition below 120 K is also reflected in the temperature dependence of the NMR linewidth as shown in Fig. 5(b). In addition, we observed a so-called wipeout phenomenon of the central line intensity with decreasing the temperature across the SDW transition. The temperature dependence of the wipeout fraction, defined as $F = [A_1(295\text{ K}) - A_1(T)]/A_1(295\text{ K})$ is displayed in the inset of Fig. 5(b). The wipeout fraction is a measure for an unobserved signal intensity,[43,44] $A_1 = I \cdot T$, where I represents the NMR echo intensity, corrected for the T_2 echo decay and integrated over the full central line. A sudden increase in the wipeout fraction and a pronounced broadening (Fig. 5(b)) of the ^{75}As central line can be clearly seen below 120 K. The decrease of $1/T_2$, the pronounced broadening of the ^{75}As central line, and the sudden jump of the wipeout fraction are caused by the appearance of inhomogeneous internal magnetic fields in the SDW phase.

Next we describe the determination of the hyperfine coupling strength between the ^{75}As nuclei and Eu^{2+} 4f moments. For this reason we measured the temperature dependence of the magnetic shift K of the central line of the ^{75}As NMR spectrum. Since for this temperature range ν_Q is almost constant, as it will be shown below and η is very close to zero, the observed temperature dependence of the central line frequency is fully determined by the temperature behavior of K. In Fig. 6(a)

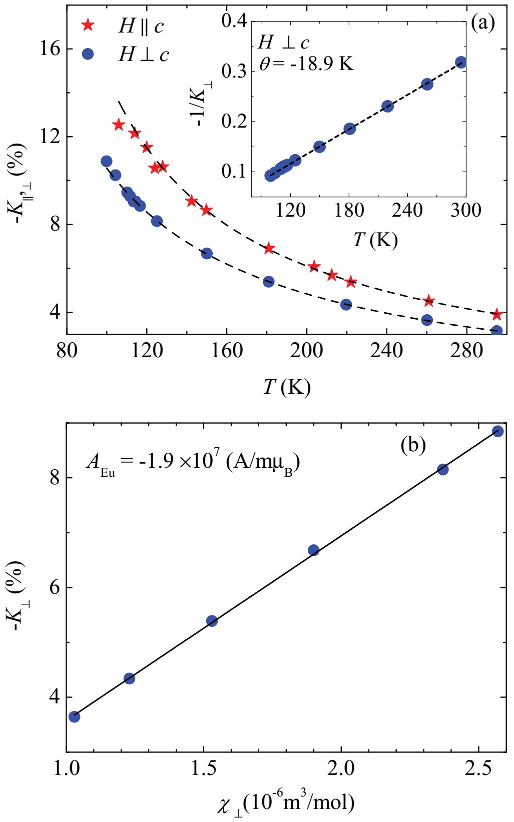

FIG. 6. (Color online) (a) Temperature dependence of the ^{75}As magnetic shift in a single crystal $EuFe_{1.9}Co_{0.1}As_2$ for $H \parallel c$ and $H \perp c$. The inset shows the inverse of the temperature dependent part of the shift $-1/K_{\perp}$ as a function of T. The dashed lines represent the Curie-Weiss behavior. (b) Plot of $-K_{\perp}$ vs. $\chi_{\perp}$ as obtained from the susceptibility measurements. The solid line is a linear fit.

we present the temperature dependence of the shift K in the temperature range from 100 and 300 K for $H \parallel c$ ($K_{\parallel} = K_c$) and $H \perp c$ ($K_{\perp} = K_{ab}$). Compared to the magnetic shift data for AFe_2As_2 (A = Ba, Ca, Sr),[33–36] our observed shifts are significantly larger, negative, and show a completely different temperature dependence. The temperature dependence of the relative magnetic shift K above 117 K is well described by a Curie-Weiss–like behavior for both directions of the magnetic field H:

$$K(T) = K_0 + \frac{C_K}{T + \Theta}. \tag{4}$$

The inset of Fig. 6(a) presents the inverse of the temperature dependent part of the shift for $H \perp c$ as a function of temperature. Below the SDW transition T_{SDW} = 120 K the data deviates from the Curie-Weiss behavior. This deviation can be understood when considering that above T_{SDW} both the Eu and Fe sublattices are in the paramagnetic state, and both contribute to the shift, while below T_{SDW} only the Eu^{2+} moments contribute. An analysis of the data for $H \perp c$ using Eq. (4) yields $\Theta = -18.9(9)$ K, $K_0 = 0.17(25)\%$. The value of Θ is in fair agreement with the value $\Theta = -21.34(7)$ K determined from the magnetic susceptibility measurements. This suggests that the Curie-Weiss part of the shift arises from the hyperfine coupling between the ^{75}As nuclei and the Eu^{2+} 4f moments. The remaining constant part of the shift K_0 could be related to the coupling of ^{75}As with the itinerant 3d electrons in the Fe_2As_2 layer, including an orbital shift. However, the value of K_0 is a factor two smaller than the total ^{75}As magnetic shift reported for $BaFe_{1.8}Co_{0.2}As_2$.[36] The contribution of Eu to the magnetic shift K_{Eu} can be related to the susceptibility χ_{Eu} of the localized Eu 4f moments as follows:

$$K_{Eu} = \frac{A_{Eu}}{g N_A \mu_B} \chi_{Eu}, \tag{5}$$

where A_{Eu} is the ^{75}As hyperfine coupling with the 4f moments, N_A and μ_B are the Avogadro number and Bohr magneton, respectively. Figure 6(b) shows $K_{\perp}$ versus $\chi_{\perp}$ with the temperature as an implicit parameter. From the linear fit of this data we can estimate a hyperfine coupling constant $A_{Eu} = -1.9\times10^7$ A/m per μ_B. This value of A is almost 60 times larger than the one reported for $NdFeAsO_{0.85}F_{0.15}$.[45] It is known that the '1111' compounds are more anisotropic than the '122' compounds.[46] Therefore, the '1111' systems are treated as quasi-two-dimensional, while the '122' systems are regarded as three-dimensional systems. Moreover, the distance between the rare-earth ion Eu^{2+} and the conduction layers in $EuFe_{1.9}Co_{0.1}As_2$ is $d = c/2 = 5.9713(3)$ Å, which is much smaller than in $NdFeAsO_{0.85}F_{0.15}$ (d = 8.577 Å).[45] The smaller interlayer distance in the '122' compounds as compared to the '1111' system and the more isotropic band structure may be the reason for the much stronger hyperfine coupling in the '122' compound. The large value of hyperfine coupling constant, quantitatively determined from the present NMR experiment, provides direct experimental evidence for a strong coupling between the Eu^{2+} localized moments and the $Fe_{1.9}Co_{0.1}As_2$ layers. This suggests that the magnetic exchange interaction between the localized Eu 4f moments is mediated by the itinerant Fe 3d electrons, i.e., via a Ruderman-Kittel-Kasuya-Yosida (RKKY) type of mechanism[19,28] leading to a high magnetic ordering temperature of the Eu^{2+} moments in $EuFe_2As_2$. It was shown that Co substitution induces superconductivity in $EuFe_{2-x}Co_xAs_2$ with a reentrant behavior of resistivity due to the antiferromagnetic ordering of the Eu^{2+} spins.[23] Reentrant superconducting behavior was also observed in a $EuFe_2As_2$ crystal under an applied pressure up to 2.5 GPa.[24,25] Moreover, while superconductivity with a maximum T_c = 20 K has been reported for $BaFe_{2-x}Ni_xAs_2$,[29] no superconductivity was observed in $EuFe_{2-x}Ni_xAs_2$.[28] The strong interaction between the localized Eu^{2+} moments and charge carriers in the $Fe_{2-x}Co_xAs_2$ layers may cause pair breaking according to the Abrikosov-Gorkov theory,[47] which may be the reason why it is difficult to get superconductivity in $EuFe_{2-x}Co_xAs_2$.

Finally, we would like to discuss the temperature dependence of the resonance frequency and the skewness of a ^{75}As lower-satellite line for $H \perp c$ (see Fig. 7). A change in the slope

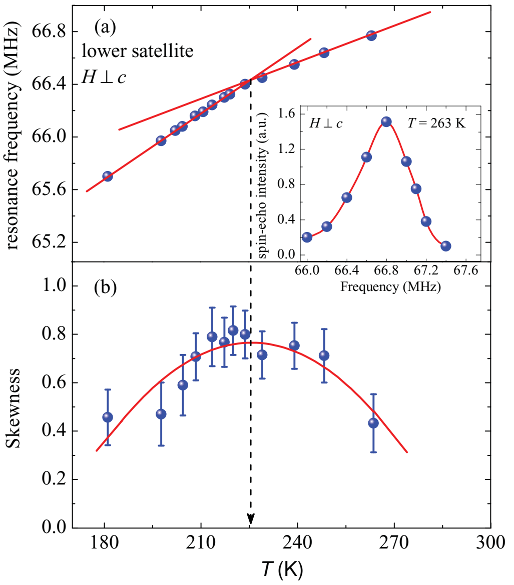

FIG. 7. (Color online) Temperature dependence of the frequency (a) and the skewness (b) of the ^{75}As lower-satellite line for $H \perp c$. The inset illustrates the ^{75}As NMR lower-satellite line shape at 263 K for $H \perp c$. Solid and dashed lines are guides to the eye.

of the temperature dependence of the satellite line frequency can be seen at 225 K as shown in Fig. 7(a). The inset of Fig. 7(a) illustrates a typical ^{75}As-NMR spectrum of the low-frequency satellite at 263 K. The spectra exhibit an asymmetric lineshape in the investigated temperature range. We analyzed the asymmetry of the satellite line shape at different temperatures by calculating its skewness (see Fig. 7(b)), defined as the third standardized moment. With decreasing temperature the skewness exhibits an increase down to 225 K, where it starts to reduce again. The slope change in the temperature dependence of the frequency of the ^{75}As lower-satellite line as well as the maximum in the temperature evolution of the skewness may be related to the appearance of a electronic nematic phase below 225 K in $\mathrm{EuFe_{1.9}Co_{0.1}As_2}$. Note that evidence for an electron nematic phase transition was recently established in undoped $A\mathrm{Fe_2As_2}$ (A = Ba, Ca)[48] and Co-doped $\mathrm{BaFe_{2-x}Co_xAs_2}$[49] single crystals by means of in-plane anisotropy measurements of the electrical resistivity.

In order to get more quantitative NMR results for a possible nematic phase, the angular dependence of the full ^{75}As NMR spectrum (central line and both satellite lines) was measured at 181 K. The dominant contribution to the magnetic shift stems from the Eu^{2+} $4f$ moments (see above), and it is acceptable to assume that this contribution does not have a strong *ab* anisotropy. Therefore, we reduced the parameter set to $K_\mathrm{a} = K_\mathrm{b} = K_\mathrm{ab}$, K_c, ν_Q, and η. Analysis of the angular dependence of the full spectrum using the diagonalization of the Hamiltonian [Eq. (2)] yields $K_\mathrm{ab} = -0.059(1)$, $K_\mathrm{c} = 0.069(2)$, $\nu_\mathrm{Q} = 7.51(17)$ MHz, and $\eta = 0.04(3)$. The change in ν_Q compared to the value $\nu_\mathrm{Q} = 7.39(24)$ MHz obtained at 261 K in the tetragonal phase is small. The slight increase of η may reflect the lower symmetry of the As site in a possible nematic phase. However, further experiments are needed to clarify the presence of a nematic phase in $\mathrm{EuFe_{1.9}Co_{0.1}As_2}$. Resistivity measurements on detwinned[50] single crystals could provide more information by probing the in-plane electronic anisotropy.

IV. SUMMARY AND CONCLUSIONS

In summary, the magnetic properties of a $\mathrm{EuFe_{1.9}Co_{0.1}As_2}$ single crystal were investigated by x-ray diffraction, magnetization, and ^{75}As NMR experiments. It was found that the temperature dependence of the ^{75}As magnetic shift as well as the spin-spin relaxation rate follow a Curie-Weiss type behavior, implying that the ^{75}As nuclei interact with the localized Eu $4f$ moments in the Eu layer. A large value of the hyperfine coupling constant between the ^{75}As nuclei and the Eu $4f$ moments suggests a strong coupling between the Eu and $\mathrm{Fe_{1.9}Co_{0.1}As_2}$ layers. Due to such a strong interlayer coupling the antiferromagnetic interaction between the localized Eu^{2+} $4f$ moments is probably mediated by a Ruderman-Kittel-Kasuya-Yosida (RKKY) type interaction. Evidence for a SDW transition at 120 K was obtained from magnetic susceptibility as well as from ^{75}As-NMR measurements. A change of the slope in the temperature dependence of the frequency of the ^{75}As lower-satellite line is observed at 225 K. In addition, at the same temperature also a maximum in the temperature behavior of the skewness is detected. These findings may indicate a phase transition to an electron nematic state below 225 K.

ACKNOWLEDGMENTS

This work was supported by the Swiss National Science Foundation, SCOPES Grant No. IZ73Z0_128242, the NCCR Project MaNEP, the EU Project CoMePhS, and the Georgian National Science Foundation Grant No. GNSF/ST08/4-416.

---

[*] zurabgug@physik.uzh.ch

[1] Y. Kamihara, T. Watanabe, M. Hirano, and H. Hosono, J. Am. Chem. Soc. **130**, 3296 (2008).
[2] X. H. Chen, T. Wu, G. Wu, R. H. Liu, H. Chen, and D. F. Fang, Nature (London) **453**, 761 (2008).
[3] G. F. Chen, Z. Li, D. Wu, G. Li, W. Z. Hu, J. Dong, P. Zheng, J. L. Luo, and N. L. Wang, Phys. Rev. Lett. **100**, 247002 (2008).
[4] Z. A. Ren, J. Yang, W. Lu, W. Yi, G. C. Che, X. L. Dong, L. L. Sun, and Z. X. Zhao, Mater. Res. Innovations **12**, 105 (2008).
[5] Z. A. Ren, J. Yang, W. Lu, W. Yi, X. L. Shen, Z. C. Li, G. C. Che, X. L. Dong, L. L. Sun, F. Zhou, and Z. X. Zhao, Europhys. Lett. **82**, 57002 (2008).
[6] H. H. Wen, G. Mu, L. Fang, H. Yang, and X. Y. Zhu, Europhys. Lett. **82**, 17009 (2008).

[7] C. Wang, L. J. Li, S. Chi, Z. W. Zhu, Z. Ren, Y. K. Li, Y. T. Wang, X. Lin, Y. K. Luo, S. Jiang, X. F. Xu, G. H. Cao, and Z. A. Xu, Europhys. Lett. **83**, 67006 (2008).

[8] V. Johnson and W. Jeitschko, J. Solid State Chem. **11**, 161 (1974).

[9] P. Quebe, L. J. Terbüchte, and W. Jeitschko, J. Alloys Compd. **302**, 70 (2000).

[10] M. Pfisterer and G. Nagorsen, Z. Naturforsch. B **35**, 703 (1980).

[11] M. Pfisterer and G. Nagorsen, Z. Naturforsch. B **38**, 811 (1983).

[12] R. Marchand and W. Jeitschko, J. Solid State Chem. **24**, 351 (1978).

[13] G. Wu, H. Chen, T. Wu, Y. L. Xie, Y. J. Yan, R. H. Liu, X. F. Wang, J. J. Ying, and X. H. Chen, J. Phys. Condens. Matter **20**, 422201 (2008).

[14] M. Rotter, M. Tegel, D. Johrendt, I. Schellenberg, W. Hermes, and R. Pöttgen, Phys. Rev. B **78**, 020503(R) (2008).

[15] C. de la Cruz, Q. Huang, J. W. Lynn, J. Li, W. Ratcliff II, J. L. Zarestky, H. A. Mook, G. F. Chen, J. L. Luo, N. L. Wang, and Pengcheng Dai, Nature (London) **453**, 899 (2008).

[16] Z. A. Ren, W. Lu, J. Yang, W. Yi, X. L. Shen, Z. C. Li, G. C. Che, X. L. Dong, L. L. Sun, F. Zhou, and Z. X. Zhao, Chin. Phys. Lett. **25**, 2215 (2008).

[17] S. Matsuishi, Y. Inoue, T. Nomura, M. Hirano, and H. Hosono, J. Phys. Soc. Jpn. **77**, 113709 (2008).

[18] J. Zhao, Q. Huang, C. de la Cruz, S. Li, J. W. Lynn, Y. Chen, M. A. Green, G. F. Chen, G. Li, Z. Li, J. L. Luo, N. L. Wang, and P. Dai, Nat. Mater. **7**, 953 (2008).

[19] H. Raffius, M. Mörsen, B. D. Mosel, W. Müller-Warmuth, W. Jeitschko, L. Terbüchte, and T. Vomhof, J. Phys. Chem. Solids **54**, 135 (1993).

[20] Y. Xiao, Y. Su, M. Meven, R. Mittal, C. M. N. Kumar, T. Chatterji, S. Price, J. Persson, N. Kumar, S. K. Dhar, A. Thamizhavel, and Th. Brueckel, Phys. Rev. B **80**, 174424 (2009).

[21] A. S. Sefat, R. Jin, M. A. McGuire, B. C. Sales, D. J. Singh, and D. Mandrus, Phys. Rev. Lett. **101**, 117004 (2008).

[22] A. Leithe-Jasper, W. Schnelle, C. Geibel, and H. Rosner, Phys. Rev. Lett. **101**, 207004 (2008).

[23] Y. He, T. Wu, G. Wu, Q. J. Zheng, Y. Z. Liu, H. Chen, J. J. Ying, R. H. Liu, X. F. Wang, Y. L. Xie, Y. J. Yan, J. K. Dong, S. Y. Li, and X. H. Chen, J. Phys. Condens. Matter **22**, 235701 (2010).

[24] C. F. Miclea, M. Nicklas, H. S. Jeevan, D. Kasinathan, Z. Hossain, H. Rosner, P. Gegenwart, C. Geibel, and F. Steglich, Phys. Rev. B **79**, 212509 (2009).

[25] T. Terashima, M. Kimata, H. Satsukawa, A. Harada, K. Hazama, S. Uji, H. S. Suzuki, T. Matsumoto, and K. Murata, J. Phys. Soc. Jpn. **78**, 083701 (2009).

[26] Liling Sun, Jing Guo, Genfu Chen, Xianhui Chen, Xiaoli Dong, Wei Lu, Chao Zhang, Zheng Jiang, Yang Zou, Suo Zhang, Yuying Huang, Qi Wu, Xi Dai, Yuanchun Li, Jing Liu, and Zhongxian Zhao, Phys. Rev. B **82**, 134509 (2010).

[27] H. S. Jeevan, Deepa Kasinathan, H. Rosner, and P. Gegenwart, Phys. Rev. B **83**, 054511 (2011).

[28] Zhi Ren, Xiao Lin, Qian Tao, Shuai Jiang, Zengwei Zhu, Cao Wang, Guanghan Cao, and Zhuan Xu, Phys. Rev. B **79**, 094426 (2009).

[29] L. J. Li, Y. K. Luo, Q. B. Wang, H. Chen, Z. Ren, Q. Tao, Y. K. Li, X. Lin, M. He, Z. W. Zhu, G. H. Cao, and Z. A. Xu, New J. Phys. **11**, 025008 (2009).

[30] S. Jiang, Y. K. Luo, Z. Ren, Z. W. Zhu, C. Wang, X. F. Xu, Q. Tao, G. H. Cao, and Z. A. Xu, New J. Phys. **11**, 025007 (2009).

[31] E. Dengler, J. Deisenhofer, H. A. Krug von Nidda, Seunghyun Khim, J. S. Kim, Kee Hoon Kim, F. Casper, C. Felser, and A. Loidl, Phys. Rev. B **81**, 024406 (2010).

[32] J. J. Ying, T. Wu, Q. J. Zheng, Y. He, G. Wu, Q. J. Li, Y. J. Yan, Y. L. Xie, R. H. Liu, X. F. Wang, and X. H. Chen, Phys. Rev. B **81**, 052503 (2010).

[33] Kentaro Kitagawa, Naoyuki Katayama, Kenya Ohgushi, Makoto Yoshida, and Masashi Takigawa, J. Phys. Soc. Jpn. **77**, 114709 (2008).

[34] Kentaro Kitagawa, Naoyuki Katayama, Kenya Ohgushi, and Masashi Takigawa, J. Phys. Soc. Jpn. **78**, 063706 (2009).

[35] Fanlong Ning, Kanagasingham Ahilan, Takashi Imai, Athena S. Sefat, Ronying Jin, Michael A. McGuire, Brian C. Sales, and David Mandrus, J. Phys. Soc. Jpn. **77**, 103705 (2008).

[36] S.-H. Baek, N. J. Curro, T. Klimczuk, E. D. Bauer, F. Ronning, and J. D. Thompson, Phys. Rev. B **79**, 052504 (2009).

[37] APEX2 version 2009.9 (Bruker AXS Inc., 2009).

[38] SAINT version 7.68A (Bruker AXS Inc., 2009).

[39] XS version 2008/1 [George M. Sheldrick, Acta Crystallogr. Sect. A **64**, 112 (2008)].

[40] XL version 2008/4 [George M. Sheldrick, Acta Crystallogr. Sect. A **64**, 112 (2008)].

[41] Shuai Jiang, Hui Xing, Guofang Xuan, Zhi Ren, Cao Wang, Zhu-an Xu, and Guanghan Cao, Phys. Rev. B **80**, 184514 (2009).

[42] Z. Ren, Z. W. Zhu, S. Jiang, X. F. Xu, Q. Tao, C. Wang, C. M. Feng, G. H. Cao, and Z.-A. Xu, Phys. Rev. B **78**, 052501 (2008).

[43] N. Bloembergen and T. J. Rowland, Acta Metall. **1**, 731 (1953).

[44] J. Winter, *Magnetic Resonance in Metals* (Oxford University Press, Oxford, 1971).

[45] P. Jeglič, J.-W. G. Bos, A. Zorko, M. Brunelli, K. Koch, H. Rosner, S. Margadonna, and D. Arčon, Phys. Rev. B **79**, 094515 (2009).

[46] Fengjie Ma, Zhong-Yi Lu, and Tao Xiang, Front. Phys. China **5**, 150 (2010).

[47] A. A. Abrikosov and L. P. Gor'kov, Zh. Eksp. Teor. Fiz. **39**, 1781 (1960) [Sov. Phys. JETP **12**, 1243 (1961)].

[48] M. A. Tanatar, E. C. Blomberg, A. Kreyssig, M. G. Kim, N. Ni, A. Thaler, S. L. Bud'ko, P. C. Canfield, A. I. Goldman, I. I. Mazin, and R. Prozorov, Phys. Rev. B **81**, 184508 (2010).

[49] Jiun-Haw Chu, James G. Analytis, Kristiaan De Greve, Peter L. McMahon, Zahirul Islam, Yoshihisa Yamamoto, and Ian R. Fisher, Science **329**, 824 (2010).

[50] M. A. Tanatar, A. Kreyssig, S. Nandi, N. Ni, S. L. Bud'ko, P. C. Canfield, A. I. Goldman, and R. Prozorov, Phys. Rev. B **79**, 180508(R) (2009).

4.4.2 Publication II: Anisotropic magnetic order of the Eu sublattice in single crystals of $EuFe_{2-x}Co_xAs_2$ ($x = 0, 0.2$) studied by means of magnetization and magnetic torque

Z. Guguchia, S. Bosma, S. Weyeneth, A. Shengelaya, R. Puzniak, Z. Bukowski, J. Karpinski, and H. Keller
Phys. Rev. B **84**, 144506 (2011).

Abstract

We present a combination of magnetization and magnetic torque experiments to investigate the magnetic orders in undoped $EuFe_2As_2$ and Co doped $EuFe_{1.8}Co_{0.2}As_2$ single crystals. Although at low temperatures typical results for an antiferromagnetic (AFM) state in $EuFe_2As_2$ were found, our data strongly indicate the occurrence of a canted antiferromagnetic (C-AFM) order of the Eu^{2+} moments between 17 K and 19 K, observed even in the lowest studied magnetic fields. However, unlike in the parent compound, no low-field and low-temperature AFM state of the Eu^{2+} moments was observed in the doped $EuFe_{1.8}Co_{0.2}As_2$. Only a C-AFM phase is present at low fields and low temperatures, with a reduced magnetic anisotropy as compared to the undoped system. We present and discuss for both, $EuFe_2As_2$ and $EuFe_{1.8}Co_{0.2}As_2$, the experimentally deduced magnetic phase diagrams of the magnetic ordering of the Eu^{2+} sublattice with respect to the temperature, the applied magnetic field, and its orientation to the crystallographic axes. It is likely that the magnetic coupling of the Eu and the Fe sublattice is strongly depending on Co doping, having detrimental influence on the magnetic phase diagrams as determined in this work. Their impact on the occurrence of superconductivity with higher Co doping is discussed.

DOI: 10.1103/PhysRevB.84.144506
PACS numbers: 74.70.Xa, 75.30.Gw, 75.30.Kz, 75.50.Ee

The original publication is electronically available at:
http://prb.aps.org/abstract/PRB/v84/i14/e144506

PHYSICAL REVIEW B **84**, 144506 (2011)

Anisotropic magnetic order of the Eu sublattice in single crystals of $\mathrm{EuFe}_{2-x}\mathrm{Co}_x\mathrm{As}_2$ ($x = 0,0.2$) studied by means of magnetization and magnetic torque

Z. Guguchia,[*] S. Bosma, and S. Weyeneth
Physik-Institut der Universität Zürich, Winterthurerstrasse 190, CH-8057 Zürich, Switzerland

A. Shengelaya
Department of Physics, Tbilisi State University, Chavchavadze 3, GE-0128 Tbilisi, Georgia

R. Puzniak
Institute of Physics, Polish Academy of Sciences, Aleja Lotników 32/46, PL-02-668 Warsaw, Poland

Z. Bukowski[†] and J. Karpinski
Laboratory for Solid State Physics, ETH Zürich, CH-8093 Zürich, Switzerland

H. Keller
Physik-Institut der Universität Zürich, Winterthurerstrasse 190, CH-8057 Zürich, Switzerland

(Received 11 July 2011; published 4 October 2011)

We present a combination of magnetization and magnetic torque experiments to investigate the magnetic orders in undoped $\mathrm{EuFe_2As_2}$ and Co-doped $\mathrm{EuFe_{1.8}Co_{0.2}As_2}$ single crystals. Although at low temperatures typical results for an antiferromagnetic (AFM) state in $\mathrm{EuFe_2As_2}$ were found, our data strongly indicate the occurrence of a canted antiferromagnetic (C-AFM) order of the Eu^{2+} moments between 17 and 19 K, observed even in the lowest studied magnetic fields. However, unlike in the parent compound, no low-field and low-temperature AFM state of the Eu^{2+} moments was observed in the doped $\mathrm{EuFe_{1.8}Co_{0.2}As_2}$. Only a C-AFM phase is present at low fields and low temperatures, with a reduced magnetic anisotropy as compared to the undoped system. We discuss for both $\mathrm{EuFe_2As_2}$ and $\mathrm{EuFe_{1.8}Co_{0.2}As_2}$ the experimentally deduced magnetic phase diagrams of the magnetic ordering of the Eu^{2+} sublattice with respect to the temperature, the applied magnetic field, and its orientation to the crystallographic axes. It is likely that the magnetic coupling of the Eu and the Fe sublattice is strongly dependent on Co doping, having detrimental influence on the magnetic phase diagrams as determined in this work. Their impact on the occurrence of superconductivity with higher Co doping is discussed.

DOI: 10.1103/PhysRevB.84.144506 PACS number(s): 74.70.Xa, 75.30.Gw, 75.30.Kz, 75.50.Ee

I. INTRODUCTION

The discovery of superconductivity in the iron-based pnictides[1] provided a new class of compounds to the high-temperature-superconductor (HTS) family. Three main groups of these iron-based superconductors are intensively studied: the $R\mathrm{FeAsO}$ compounds with R = La-Gd (1111),[1,2] the ternary arsenides $A\mathrm{Fe_2As_2}$ with A = Ba, Sr, Ca, Eu (122),[3] and the binary chalcogenides such as FeSe_{1-x} (11).[4] Similar to the cuprate HTS's, the undoped iron pnictides are not superconducting (SC) at ambient pressure and undergo a spin-density wave (SDW) transition at high temperatures.[5] The SC state in iron-based compounds can be achieved either under pressure (chemical and hydrostatic)[6–15] or by appropriate charge-carrier doping of the parent compounds,[16–18] both accompanied by a suppression of the SDW state.

Here, we focus on $\mathrm{EuFe_2As_2}$, which is a particularly interesting member of the ternary system $A\mathrm{Fe_2As_2}$, since the A site is occupied by a rare-earth Eu^{2+} S-state (orbital moment $L = 0$) ion with a $4f^7$ electronic configuration. Eu^{2+} has a total electron spin $S = 7/2$, corresponding to a theoretical effective magnetic moment of 7.94 μ_B. It is the only known member of the 122 family containing $4f$ electrons. In addition to the SDW ordering of the Fe moments at $T_\mathrm{SDW} \simeq 190$ K, an antiferromagnetic (AFM) order of the Eu^{2+} spins at $T_\mathrm{AFM} \simeq 19$ K was reported by Mössbauer and susceptibility measurements.[19–21] Recently, neutron diffraction measurements were performed on $\mathrm{EuFe_2As_2}$ and the magnetic structure illustrated in Fig. 1 was established.[5] This material exhibits an A-type AFM order of the Eu^{2+} moments, e.g., the Eu^{2+} spins align ferromagnetically in the planes, while the planes are coupled antiferromagnetically.[5,22] It was demonstrated that, by applying a high enough magnetic field, the Eu^{2+} moments can be realigned ferromagnetically in both the parent compound $\mathrm{EuFe_2As_2}$ (Refs. 21 and 23) as well as in the Co-doped system $\mathrm{EuFe}_{2-x}\mathrm{Co}_x\mathrm{As}_2$ ($x = 0.22$).[24] In addition, neutron diffraction measurements[23] suggested a canted AFM (C-AFM) structure of the Eu^{2+} moments in $\mathrm{EuFe_2As_2}$ at intermediate magnetic fields.

Co-substitution induces superconductivity in $\mathrm{EuFe}_{2-x}\mathrm{Co}_x\mathrm{As}_2$ with a reentrant behavior of resistivity due to the AFM ordering of the Eu^{2+} spins.[25] Reentrant superconducting behavior was also observed in resistivity experiments on $\mathrm{EuFe_2As_2}$ under an applied pressure up to 2.5 GPa.[14,15] However, only above 2.8 GPa, where a valence change of the Eu ions from a divalent magnetic state ($4f^7$, $J = 7/2$) to a trivalent nonmagnetic state ($4f^6$, $J = 0$) was suggested to occur,[7] a sharp transition to a zero-resistivity state was observed.[14] Bulk superconductivity was also achieved in $\mathrm{EuFe_2As}_{2-x}\mathrm{P}_x$,[7,26] where isovalent P substitution of the As site induces chemical pressure in $\mathrm{EuFe_2As_2}$. No

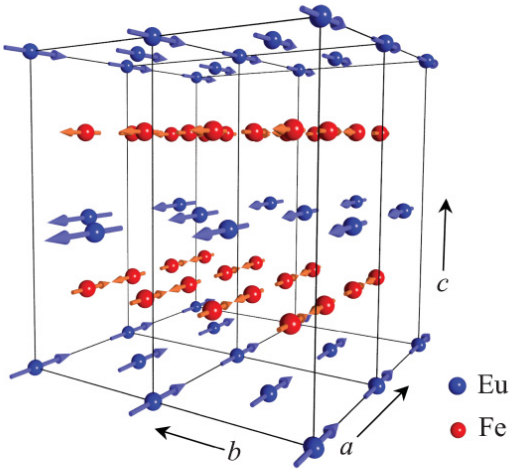

FIG. 1. (Color online) Schematic illustration of the magnetic structure of $EuFe_2As_2$. The Fe moments (red) form a SDW state, whereas the Eu moments (blue) order ferromagnetically in the *ab* plane and align antiferromagnetically along the *c* axis.

superconductivity was detected in $EuFe_{2-x}Ni_xAs_2$,[27] while superconductivity with a maximum $T_c \simeq 20$ K was reported for $BaFe_{2-x}Ni_xAs_2$.[28] It was suggested in various reports[21,27,29,30] that there is a strong coupling between the localized Eu^{2+} spins and the conduction electrons of the Fe_2As_2 layers. Recently, the hyperfine coupling constant A_{Eu} between the ^{75}As nuclei and the Eu $4f$ states in $EuFe_{1.9}Co_{0.1}As_2$ was quantitatively determined from ^{75}As nuclear magnetic resonance (NMR) to be $A_{\mathrm{Eu}} = -1.9 \times 10^7$ A/mμ_B.[31] This large value of A_{Eu} indicates a strong coupling between the Eu^{2+} localized moments and the charge carriers in the Fe_2As_2 layers, and points to a strong correlation between the ordering of the localized magnetic moments and superconductivity in $EuFe_{2-x}Co_xAs_2$.

It is well established that the SDW state of the Fe moments is suppressed as a result of Co doping. However, at present, there is no clear picture as to how the ordering of the Eu spins develops with increasing Co concentration. Generally, it was assumed that, in the 122 systems, the direction of the sublattice magnetization of the Eu^{2+} magnetic moments is strongly affected by the magnetic behavior of the Fe atoms.[5,32–36] Thus, it is important to compare the magnetic properties of the Eu sublattice in $EuFe_{2-x}Co_xAs_2$ without and with Co doping in order to study the correlation between ordering of Eu^{2+} moments and the magnetism of the Fe sublattice. This, in turn, is crucial to understand the interplay between magnetism of localized moments and superconductivity in $EuFe_{2-x}Co_xAs_2$.

In this paper, we present magnetic susceptibility, magnetization, and magnetic torque experiments performed on single crystals of $EuFe_{2-x}Co_xAs_2$ ($x = 0$, 0.2). The goal of this study is to investigate the macroscopic magnetic properties of the Eu sublattice. Magnetic susceptibility and magnetization investigations provide information on the magnetic structure of a single-crystal sample in magnetic fields applied along the principal axes. In addition, the evolution of the magnetic structure as a function of the tilting angle of the magnetic field and the crystallographic axis can be studied by magnetic torque. This paper is organized as follows: Experimental details are described in Sec. II. The results of the magnetic susceptibility, the magnetization, and the magnetic torque measurements are presented and discussed in Sec. III. In Sec. IV, the magnetic phase diagrams of the Eu^{2+} sublattice ordering with respect to magnetic field and temperature in single crystals of $EuFe_{2-x}Co_xAs_2$ ($x = 0$, 0.2) are discussed. The conclusions follow in Sec. V.

II. EXPERIMENTAL DETAILS

Single crystals of $EuFe_{2-x}Co_xAs_2$ ($x = 0$, 0.2) were grown out of Sn flux.[31] The magnetization measurements of the $EuFe_{2-x}Co_xAs_2$ ($x = 0$, 0.2) samples were performed with a commercial SQUID magnetometer (*Quantum Design* MPMS-XL) with the magnetic field H applied parallel ($H \parallel c$) or perpendicular ($H \perp c$) to the crystallographic c axis. The magnetic torque measurements were carried out using a homemade torque sensor.[37] The sample is mounted on a platform hanging on piezoresistive legs. A magnetic field $\vec{H}$ applied to the sample having magnetic moment $\vec{m}$ results in a mechanical torque $\vec{\tau} = \mu_0 \vec{m} \times \vec{H}$. This torque bends the legs, and thus creates a measurable electric signal proportional to the torque amplitude. The temperature is controlled by an *Oxford* flow cryostat, and the magnetic field is provided by a rotatable resistive *Bruker* magnet with a maximum magnetic field of 1.4 T.

III. RESULTS

A. Magnetization measurements

1. Temperature dependence

The temperature dependence of the magnetic susceptibility $\chi = M/H$ (here M is the magnetization determined as magnetic moment per mol) for the crystal of $EuFe_2As_2$ in a field of $\mu_0 H = 0.01$ T for $H \perp c$ and for $H \parallel c$ is shown in Fig. 2(a). In agreement with previous reports,[20,21] the magnetic susceptibility for $H \perp c$ ($\chi_\perp$) and for $H \parallel c$ ($\chi_\parallel$), determined in the temperature range from 30 to 190 K (i.e., far above $T_{\mathrm{AFM}} \simeq 19$ K of the Eu moments up to $T_{\mathrm{SDW}} \simeq 190$ K of the Fe moments) is well described by the Curie-Weiss law

$$\chi(T) = \frac{C}{T - \theta_{\mathrm{CW}}}. \qquad (1)$$

Here, C denotes the Curie constant and θ_{CW} the Curie-Weiss temperature. Analyzing the data in Fig. 2(a) with Eq. (1) yields $C = 1853(15)\times 10^{-7}$ m^3 K/mol, $\theta_{\mathrm{CW}} = 19.74(8)$ K for $H \parallel c$ and $C = 2127(23)\times 10^{-7}$ m^3 K/mol, $\theta_{\mathrm{CW}} = 20.69(4)$ K for $H \perp c$. The calculated effective magnetic moment is $\mu_{\mathrm{eff}} \simeq 7.6\ \mu_B$ for $H \parallel c$ and $\mu_{\mathrm{eff}} \simeq 8.3\ \mu_B$ for $H \perp c$. These estimates of μ_{eff} are close to the theoretical value of the magnetic moment of a free Eu^{2+} ion ($\mu_{Eu^{2+}} = 7.94\ \mu_B$). The positive value of θ_{CW} for both $H \parallel c$ and $H \perp c$ is consistent with previous magnetization measurements,[20,21] indicating that the direct interaction between the Eu^{2+} moments is ferromagnetic (FM). This is in agreement with the magnetic structure of $EuFe_2As_2$ suggested by zero-field neutron diffraction measurements,[5]

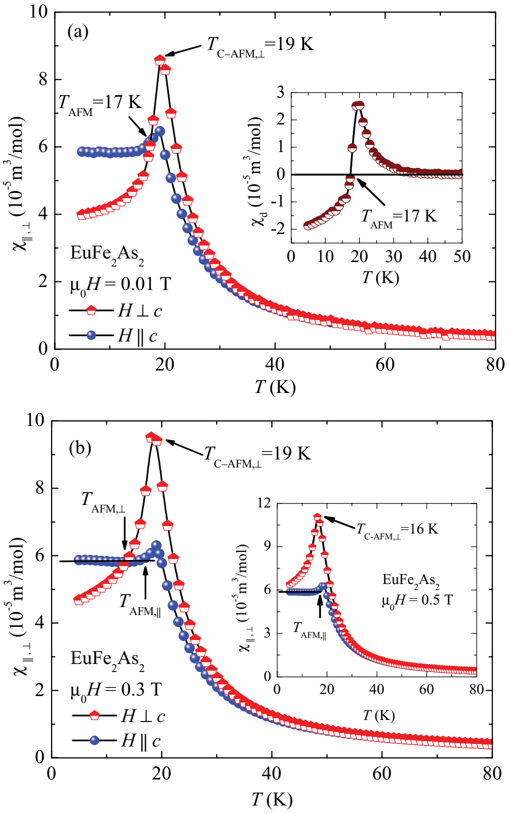

FIG. 2. (Color online) Temperature dependence of the magnetic susceptibility measured at fixed magnetic fields applied perpendicular ($H \perp c$) and parallel ($H \parallel c$) to the crystallographic c axis of single-crystal EuFe$_2$As$_2$: (a) $\mu_0 H = 0.01$ T; (b) $\mu_0 H = 0.3$ T and $\mu_0 H = 0.5$ T (inset). The inset of panel (a) illustrates the temperature dependence of the difference between both susceptibilities ($\chi_d = \chi_\perp - \chi_\parallel$). The arrows mark the AFM and C-AFM ordering temperatures of the Eu^{2+} moments, and $T_{\text{AFM},\perp}$ and $T_{\text{AFM},\parallel}$ refer to the AFM ordering temperatures for $H \perp c$ and $H \parallel c$, respectively. The canted-AFM ordering temperature for $H \perp c$ is denoted by $T_{\text{C-AFM},\perp}$.

revealing that the intralayer arrangement of the Eu^{2+} spins is FM. The sharp increase of χ with decreasing temperature below 30 K also indicates a FM coupling between the Eu^{2+} moments. The Eu moments align with respect to the Fe moments along the a axis[5] as illustrated in Fig. 1.

With decreasing temperature from 19 to 17 K, the susceptibility $\chi_\perp$ of single-crystal EuFe$_2$As$_2$ decreases rapidly, and below 17 K, the decrease of $\chi_\perp$ is less pronounced. On the other hand, $\chi_\parallel$ decreases with decreasing temperature from 19 to 17 K and remains constant below 17 K. Moreover, the values of $\chi_\perp$ and $\chi_\parallel$ at 19 K are substantially different ($\chi_\perp/\chi_\parallel \simeq 1.33$), already in a rather low magnetic field $\mu_0 H = 0.01$ T [see Fig. 2(a)]. Note that within the classical picture of an ideal antiferromagnet, the magnetic susceptibility χ in a magnetic field perpendicular to the easy axis is constant, and χ in a field parallel to the easy plane decreases linearly with decreasing temperature. In addition, for an antiferromagnet, the values of χ at the antiferromagnetic (AFM) transition temperature are the same for both $H \perp c$ and $H \parallel c$.[22] The inset of Fig. 2(a) illustrates the temperature dependence of the difference between both susceptibilities $\chi_d = \chi_\perp - \chi_\parallel$. Note that, below 19 K, the quantity χ_d decreases with decreasing temperature and reaches zero at around 17 K. This behavior of $\chi_d(T)$ can be explained by invoking a transition from the high-temperature paramagnetic state to a FM state or to a C-AFM state at about 19 K. The transition from a FM or a C-AFM to an AFM state of the Eu^{2+} spins occurs only below 17 K. The pronounced increase of $\chi_\parallel$ above 17 K indicates the appearance of a magnetic moment along the c axis. Since $\chi_\parallel$ is smaller than $\chi_\perp$ in the FM/C-AFM state, it is suggested that the ab plane is the easy plane of this ordered state. In Fig. 2(b), the temperature dependences of $\chi_\perp$ and $\chi_\parallel$ of single-crystal EuFe$_2$As$_2$ in a magnetic field of 0.3 and 0.5 T (inset) are shown. Obviously, the AFM transition temperatures for $H \perp c$ (crossing point of $\chi_\perp$ and $\chi_\parallel$) and for $H \parallel c$ (temperature at which $\chi_\parallel$ starts to increase) are shifted to lower temperature with higher magnetic field [see Fig. 2(a) for comparison]. However, at $\mu_0 H = 0.5$ T, the curves $\chi_\perp$ and $\chi_\parallel$ do not cross in the investigated temperature range, indicating that the AFM state of the Eu^{2+} ions is suppressed in EuFe$_2$As$_2$ in magnetic fields $H \perp c$ exceeding $\mu_0 H \simeq 0.5$ T. For $H \parallel c$, the suppression of the AFM state occurs in fields higher than $\mu_0 H \simeq 1.2$ T since, above this field, the susceptibility for $H \parallel c$ is temperature dependent even at temperature as low as 2 K [see Fig. 3(b)]. Importantly, the magnetic field at which the magnetic moments of the Eu sublattice saturate (i.e., the field at which the FM state is reached) is much higher than the field of suppression of the AFM state. This implies that a FM state appears in a magnetic field higher than the field of suppression of antiferromagnetism and that those two transitions are distinguishable. The peak in the magnetic susceptibility at about 19 K in low fields (see Fig. 2) can be associated with the transition from a PM to a C-AFM state. This peak is shifted to lower temperatures with applied magnetic field above $\mu_0 H \simeq 0.3$ T for $H \perp c$ and above $\mu_0 H \simeq 0.5$ T for $H \parallel c$ [see Figs. 2(b) and 3(b)]. Finally, we may conclude that a field-induced magnetic phase transition from an AFM via a C-AFM configuration to a FM state takes place below 17 K. Such a transition is visible even at the lowest temperature of 2 K reached in our experiment.

The magnetization $M(T)$ in the FM state in the vicinity of the Curie temperature T_C can be described by the power law

$$M(T) = M_0 \left(1 - \frac{T}{T_C}\right)^{\tilde{\beta}}. \tag{2}$$

Here, $\tilde{\beta}$ and M_0 are empirical constants. Analyzing the data at 1.5 T with Eq. (2) yields $T_C = 27.2(1)$ K and $\tilde{\beta} = 0.39(1)$ for both directions of the magnetic field [solid lines in the insets of Figs. 3(a) and 3(b)]. It was found that T_C increases gradually with increasing applied magnetic field for $H \perp c$ and $H \parallel c$. By extrapolating $T_C(H)$ to low fields, the zero-field value of

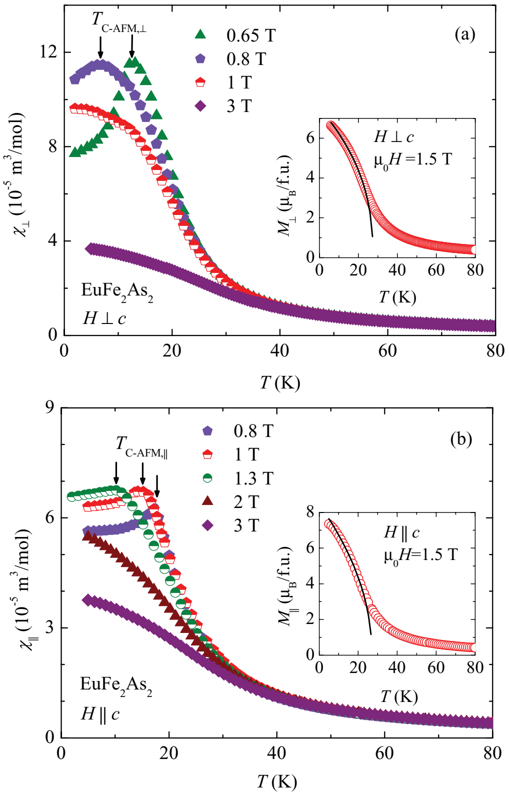

FIG. 3. (Color online) Temperature dependence of the magnetic susceptibility measured at fixed magnetic fields of single-crystal EuFe$_2$As$_2$ for $H \perp c$ (a) and $H \parallel c$ (b). The arrows mark the canted antiferromagnetic ordering temperature $T_{\text{C-AFM}}$ of the Eu^{2+} moments in low fields. $T_{\text{C-AFM},\perp}$ and $T_{\text{C-AFM},\parallel}$ refer to the C-AFM ordering temperatures for $H \perp c$ and $H \parallel c$, respectively. The insets illustrate the determination of T_{C} using the power law given in Eq. (2).

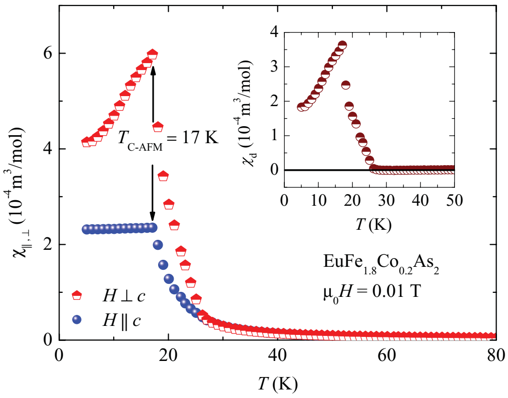

FIG. 4. (Color online) Temperature dependence of the magnetic susceptibility measured in a field of $\mu_0H = 0.01$ T of single-crystal EuFe$_{1.8}$Co$_{0.2}$As$_2$ for $H \perp c$ and $H \parallel c$. The arrows mark the canted antiferromagnetic ordering temperature $T_{\text{C-AFM}} \simeq 17$ K of the Eu^{2+} moments. In the inset, the difference between the susceptibilities for the two different field configurations ($\chi_d = \chi_\perp - \chi_\parallel$) is plotted as a function of temperature.

T_{C} was found to be $\simeq$19 K. The present values of $T_{\mathrm{C}}(H)$ are in agreement with those reported by Xiao *et al.*[23]

The temperature dependence of the magnetic susceptibility for the Co-doped crystal of EuFe$_{1.8}$Co$_{0.2}$As$_2$ in an applied field of $\mu_0H = 0.01$ T for $H \perp c$ and $H \parallel c$ is presented in Fig. 4. In the inset, the temperature dependence of the difference between the susceptibilities for two field configurations $\chi_d = \chi_\perp - \chi_\parallel$ is shown. Analyzing the susceptibility data above 30 K with Eq. (1) yields $C = 2108(32)\times10^{-7}$ m^3 K/mol, $\theta_{\mathrm{CW}} = 21.86(6)$ K for $H \perp c$ and $C = 1915(34)\times10^{-7}$ m^3 K/mol, $\theta_{\mathrm{CW}} = 20.67(7)$ K for $H \parallel c$. Again, θ_{CW} turns out to be positive. Like in the parent compound, a sharp increase of χ below 30 K is observed, which is attributed to the in-plane FM coupling between the Eu^{2+} moments. Below 17 K, the susceptibility $\chi_\perp$ starts to decrease with decreasing temperature, indicating the onset of an AFM transition of the Eu^{2+} spins. On the other hand, $\chi_\parallel$ remains almost constant below 17 K. This suggests that the Eu^{2+} moments align along the *ab* plane, similar to undoped EuFe$_2$As$_2$. However, for EuFe$_2$As$_2$, the AFM ordering temperature of the Eu^{2+} spins is about 2 K higher. Below 17 K, $\chi_\perp$ is significantly larger than $\chi_\parallel$, even in magnetic fields as low as $\mu_0H = 0.01$ T (see Fig. 4). Thus, no crossing between $\chi_\perp$ and $\chi_\parallel$ is observed (inset of Fig. 4), in contrast to the parent compound EuFe$_2$As$_2$ (see Fig. 2). Furthermore, $\chi_\perp$ is temperature dependent even at the lowest applied magnetic field. This is inconsistent with an AFM state with an easy *c* axis. Hence, we suggest that, for all temperatures below 17 K, the ground state of the coupled Eu^{2+} spins in EuFe$_{1.8}$Co$_{0.2}$As$_2$ is a C-AFM state with a FM component in the *ab* plane. This implies that the magnetic configuration of the Eu moments is strongly influenced by the magnetization of the Fe sublattice. This is consistent with previous NMR studies, revealing a strong coupling between the Eu and Fe$_{2-x}$Co$_x$As$_2$ layers.[31]

The temperature dependences of $\chi_\perp$ and $\chi_\parallel$ at different magnetic fields of single-crystal EuFe$_{1.8}$Co$_{0.2}$As$_2$ are shown in Fig. 5. Zero-field cooling (ZFC) and field cooling (FC) susceptibilities $\chi_\perp(T)$ measured in an applied field of $\mu_0H = 0.001$ T are shown in the inset of Fig. 5(a). Below 17 K, the ZFC and FC curves deviate from each other, indicating the presence of a C-AFM state of the Eu^{2+} moments. The data reveal a decrease of the C-AFM ordering temperature $T_{\text{C-AFM}}$ with increasing magnetic field for both field orientations, similar as for the parent compound EuFe$_2$As$_2$. However, the values for $T_{\text{C-AFM}}$ for EuFe$_{1.8}$Co$_{0.2}$As$_2$ are substantially smaller than those for EuFe$_2$As$_2$.

2. *Field dependence*

The susceptibility investigations of the preceding section clearly demonstrate that the system EuFe$_{2-x}$Co$_x$As$_2$

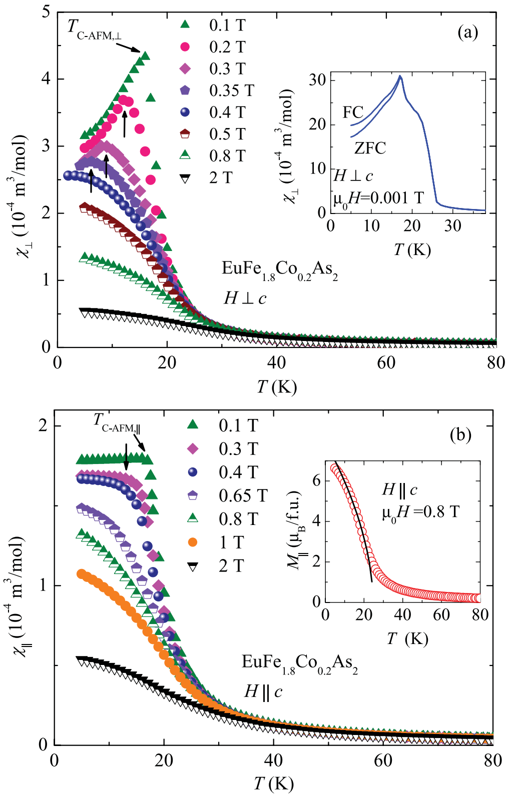

FIG. 5. (Color online) Temperature dependence of the ZFC magnetic susceptibility measured at various fixed magnetic fields of single-crystal $EuFe_{1.8}Co_{0.2}As_2$ for $H \perp c$ (a) and $H \parallel c$ (b). The arrows mark the canted antiferromagnetic ordering temperature $T_{\text{C-AFM}}$ of the Eu^{2+} moments in low magnetic fields. $T_{\text{C-AFM},\perp}$ and $T_{\text{C-AFM},\parallel}$ refer to the C-AFM ordering temperatures for $H \perp c$ and $H \parallel c$, respectively. In the inset of (a), $\chi_\perp(T)$ for FC and ZFC in an applied field of $\mu_0 H = 0.001$ T is plotted. The inset of (b) shows the approximation of $M_\parallel(T)$ in $\mu_0 H = 0.8$ T by the power law (solid curve) given in Eq. (2).

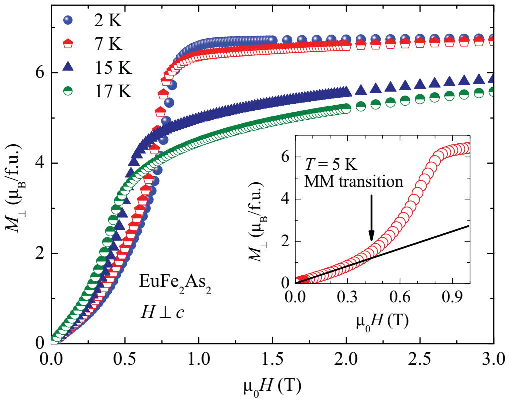

FIG. 6. (Color online) Field dependence of the magnetization at various temperatures of single-crystal $EuFe_2As_2$ for $H \perp c$. The inset shows the low-field $M_\perp$ data at 5 K, illustrating the metamagnetic (MM) transition marked by the arrow.

($x = 0$, 0.2) shows a rich variety of magnetic phases. In order to explore in detail the various magnetic field-induced phases, magnetization experiments were also performed as a function of the applied magnetic field at different temperatures.

The field dependence of the magnetization of single-crystal $EuFe_2As_2$ at different temperatures for $H \perp c$ is shown in Fig. 6. In the inset, the low-field magnetization $M_\perp$ at 5 K is shown. $M_\perp$ increases almost linearly with increasing magnetic field H up to $\mu_0 H \simeq 0.45$ T, where a sudden increase of $M_\perp$ appears. Then, $M_\perp$ further increases with increasing H, and finally saturates for $\mu_0 H \geqslant 0.8$ T. The value of the saturation magnetization corresponds to an effective magnetic moment of 6.8 μ_B/f.u., which is close to $g\mu_B S = 7\ \mu_B$/f.u. expected for Eu^{2+} moments. This result suggests that there is a metamagnetic[38,39] (MM) transition at $\mu_0 H_{\text{MM}} \simeq 0.45$ T at 5 K in $EuFe_2As_2$, consistent with previous observations.[20,21] Such a metamagnetic transition is characteristic for A-type antiferromagnetism in layered systems as, e.g., $Na_{0.85}CoO_2$ (Ref. 38) and $La_{2-x}Sr_{1+x}Mn_2O_7$.[40] Figure 6 shows that the MM transition shifts toward lower fields with increasing temperature. The values of the magnetic field at which the MM transition occurs is in agreement with the results obtained from the susceptibility measurements for the AFM to C-AFM transition. Thus, we propose that the MM transition corresponds to the onset of a spin-flop transition[22] from an AFM to a C-AFM state in $EuFe_2As_2$. However, no MM transition for $H \perp c$ is detected in $EuFe_{1.8}Co_{0.2}As_2$ [Fig. 7(a)]. Both $M_\perp$ and $M_\parallel$ first increase almost linearly with increasing H and then saturate at higher fields (Fig. 7). The absence of a MM transition in $EuFe_{1.8}Co_{0.2}As_2$ is consistent with the susceptibility measurements presented above, suggesting that the Eu^{2+} moments exhibit a C-AFM ground state even at very low H. This conclusion is also supported by magnetic hysteresis measurements at 5 K performed in magnetic fields up to 0.5 T. As demonstrated in the inset of Fig. 7(a), the field dependence of $M_\perp$ at 5 K shows a well-developed hysteresis for $EuFe_{1.8}Co_{0.2}As_2$, in contrast to the parent compound $EuFe_2As_2$ where no hysteresis is observed.

Obviously, the presented susceptibility and magnetization measurements reveal a complex and rather sophisticated interplay of magnetic phases in the $EuFe_{2-x}Co_xAs_2$ system. Additional information on the complex magnetic phases in $EuFe_{2-x}Co_xAs_2$ is obtained from angular-dependent magnetic torque studies presented in the next section.

B. Magnetic torque

In low magnetic fields, the Eu^{2+} magnetic moments prefer to order antiferromagnetically in $EuFe_2As_2$. High magnetic fields reorient the magnetic moments, leading to various

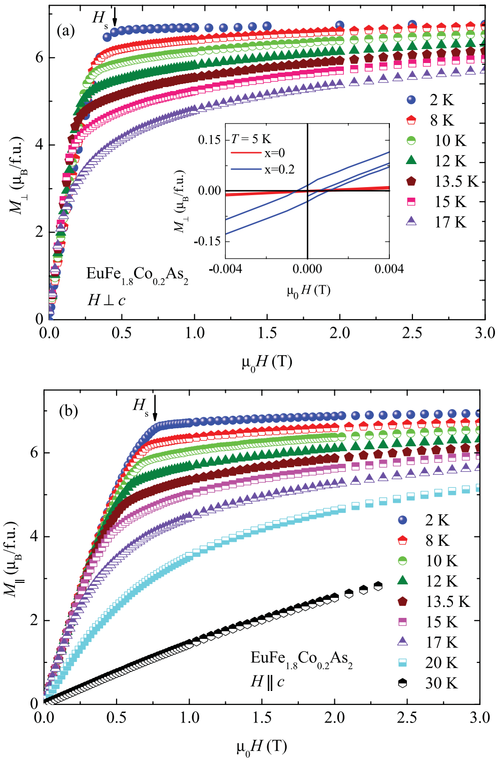

FIG. 7. (Color online) Field dependence of the magnetization at low temperatures of single-crystal EuFe$_{1.8}$Co$_{0.2}$As$_2$ for $H \perp c$ (a) and $H \parallel c$ (b). The saturation field H_s at 2 K is marked by arrows. The inset of (a) shows the field dependence of $M_\perp$ for EuFe$_2$As$_2$ and EuFe$_{1.8}$Co$_{0.2}$As$_2$ at 5 K.

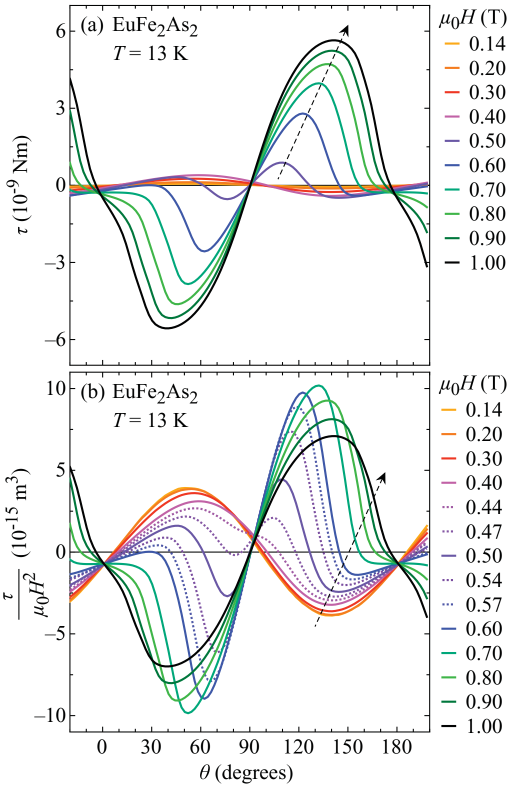

FIG. 8. (Color online) (a) Angular-dependent magnetic torque τ of single-crystal EuFe$_2$As$_2$ at 13 K in various magnetic fields. For clarity, not all measured data are shown. (b) Angular dependence of the quantity $\tau/(\mu_0 H^2)$. The dashed arrows denote the direction of increasing magnetic field.

magnetic field-induced phases. Magnetic torque allows us to investigate multiple aspects of magnetic order as a function of the magnetic field with respect to the principal axes. Whereas magnetization provides direct information on the magnetic moment oriented along the field, magnetic torque directly probes the anisotropy of the susceptibility in magnetic systems.

The angular dependence of the magnetic torque τ of single-crystal EuFe$_2$As$_2$ measured at 13 K in various magnetic fields is presented in Fig. 8(a). In Fig. 8(b), the same data are plotted in terms of $\tau/(\mu_0 H^2)$. The torque data below 0.3 T are of sinusoidal shape, following the simple angular dependence for a uniaxial antiferromagnet[41]:

$$\tau(\theta) = -V\frac{(\chi_\perp - \chi_\parallel)}{2}\mu_0 H^2 \sin(2\theta). \tag{3}$$

Here, θ denotes the angle between the field H and the crystallographic c axis, V is the volume of the sample, and $\chi_\perp$ and $\chi_\parallel$ are the magnetic susceptibilities for $H \perp c$ and for $H \parallel c$, respectively. Above 0.3 T, the shape of the torque signal changes drastically (see Fig. 8). For $\theta \simeq 90^\circ$(H almost parallel to the ab plane), an additional torque signal appears, with an opposite sign relative to the AFM torque. Upon increasing the magnetic field, this additional signal rises steeply and leads to a sign change of the torque signal for all angles θ. A similar behavior was observed in RbVBr$_3$ (Ref. 42) and was interpreted as the appearance of a weak field-induced magnetic moment. This additional contribution to the torque signal observed here is substantially larger than the AFM torque signal. This is consistent with the magnetization data (see Sec. III A), from which the presence of a C-AFM phase was concluded above 0.3 T at 13 K. The sign change of the torque signal is in agreement with the sign change of the quantity $\chi_d = \chi_\perp - \chi_\parallel$, which was interpreted as a signature of a transition to a C-AFM state of the Eu^{2+} magnetic moments. It was shown previously[29] that EuFe$_2$As$_2$ exhibits a weak in-plane anisotropy. Since the in-plane anisotropy is much weaker than the out-of-plane anisotropy, this system can be treated approximately

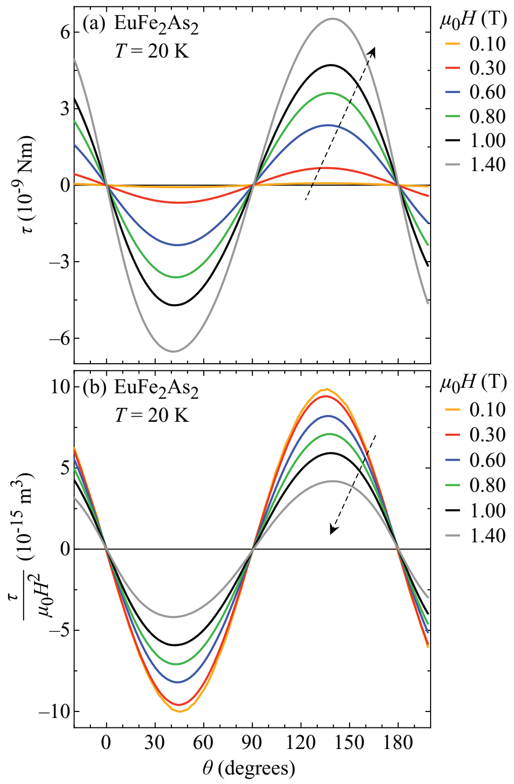

FIG. 9. (Color online) Magnetic torque τ (a) and the quantity $\tau/(\mu_0 H^2)$ (b) as a function of the angle θ of single-crystal EuFe$_2$As$_2$ in various magnetic fields at 20 K. The dashed arrows denote the direction of increasing magnetic field.

as a uniaxial anisotropic antiferromagnet. However, even a small in-plane anisotropy may lead to discrepancies between experimental results and theoretical predictions for a uniaxial anisotropic ferromagnet. Particularly, the torque signal of the AFM state shown in Fig. 8(a) is shifted by $\Delta\theta \sim 10^\circ$ with respect to one of the C-AFM state [see Fig. 8(b)]. A similar phase shift $\Delta\theta$ was observed in λ-(BETS)$_2$FeCl$_4$ (Ref. 43) and interpreted as a change of the easy axis. However, here the phase shift appears to indicate a crystallographic multidomain state due to a twinning of the crystal in the AFM state.

Figure 9(a) shows the measured magnetic torque for the same EuFe$_2$As$_2$ single crystal at 20 K, where, according to the magnetization results, the AFM regime has disappeared. Consistently, no AFM torque signal is observed. Instead, the magnetic torque amplitude increases like H^2 and saturates at higher H. Such a behavior is characteristic for a paramagnet. Consistently, the quantity $\tau/(\mu_0 H^2)$ plotted in in Fig. 9(b) decreases with increasing field.

In Fig. 10, the scaled magnetic torque $\tau/(\mu_0 H^2)$ for EuFe$_2$As$_2$ and EuFe$_{1.8}$Co$_{0.2}$As$_2$ is shown in a color map for the representative temperatures of 13, 17, and 20 K as a function of angle θ and field H. Note that $\tau/(\mu_0 H^2)$ is scaling according to the magnetic susceptibility. As seen in Fig. 10(a), the low-field regime of undoped EuFe$_2$As$_2$ at 13 K is dominated by the AFM state, whereas for higher fields, the C-AFM state appears abruptly along a clearly angular-dependent boundary line (dotted line), demonstrating the anisotropy of this magnetically ordered system. At 17 K [Fig. 10(b)], the AFM phase is not present, consistent with the conclusions from the above susceptibility measurements. At 20 K [Fig. 10(c)], the signal is clearly sinusoidal, consistent with FM behavior. In order to induce a canting of a planar antiferromagnetically ordered subsystem, the in-plane component of the magnetic field $H_\perp$ must overcome the in-plane magnetization $\mathcal{M}_\perp$ in one of the two magnetic sublattices

$$H_\perp \geqslant A\cdot\mathcal{M}_\perp = A\cdot\sqrt{\mathcal{M}^2-\mathcal{M}_\parallel^2}. \tag{4}$$

Here, $\mathcal{M}$ is the saturation magnetization of the magnetic sublattice, $\mathcal{M}_\parallel$ its out-of-plane component, and A is a constant. Taking into account

$$\begin{aligned} H_\perp &= H\sin(\theta), \\ \mathcal{M}_\parallel &= \tfrac{1}{2}\chi_\parallel H\cos(\theta), \end{aligned} \tag{5}$$

where $\chi_\parallel$ is the susceptibility of the total Eu^{2+} magnetic sublattice, we obtain for the boundary condition

$$H^2\sin^2(\theta) = A^2\left(\mathcal{M}^2 - \tfrac{1}{4}\chi_\parallel^2 H^2\cos^2(\theta)\right). \tag{6}$$

Solving this equality for H yields the angle-dependent canting field

$$H_{\mathrm{cant}}(\theta) = \frac{A\cdot\mathcal{M}}{\sqrt{\sin^2(\theta)+\frac{1}{4}\chi_\parallel^2 A^2\cos^2(\theta)}}. \tag{7}$$

Interestingly, the resulting $H_{\mathrm{cant}}(\theta)$ is analog to the expression for the angular dependence of the upper critical field $H_{c2}(\theta)$ in a type-II superconductor.[44] Hence, Eq. (7) can be simplified according to

$$H_{\mathrm{cant}}(\theta) = \frac{H_{\mathrm{cant},\perp}}{\sqrt{\sin^2(\theta)+\gamma_{\mathrm{cant}}^{-2}\cos^2(\theta)}}, \tag{8}$$

where $H_{\mathrm{cant},\perp} = H_{\mathrm{cant}}(90^\circ)$ is the in-plane canting field, $\gamma_{\mathrm{cant}} = H_{\mathrm{cant},\parallel}/H_{\mathrm{cant},\perp}$ its anisotropy parameter, and $H_{\mathrm{cant},\parallel} = H_{\mathrm{cant}}(0^\circ)$ the out-of-plane canting field. This shape of the angular dependence of the transition between the AFM and C-AFM phases in the (H,θ) diagram is represented by the dashed line in Fig. 10(a). It describes the experimental torque data rather well, with the parameters $H_{\mathrm{cant},\perp}(13\text{ K}) \simeq 0.42(2)$ T and $\gamma_{\mathrm{cant}} \simeq 2.0(2)$. This yields an estimate of the canting field parallel to the c axis $H_{\mathrm{cant},\parallel}(13\text{ K}) \simeq 0.84(6)$ T.

The low-field torque signal of EuFe$_{1.8}$Co$_{0.2}$As$_2$ at 20 K [Fig. 10(f)] shows a shape typical for an anisotropic paramagnet. However, the anisotropy of the system is quite quickly suppressed with increasing magnetic field, which may indicate a transformation of the paramagnetic state to a short-range ordered state at relatively low field. It might be caused by large fluctuations of the magnetic moments in the vicinity of the transition from a disordered PM state to an ordered

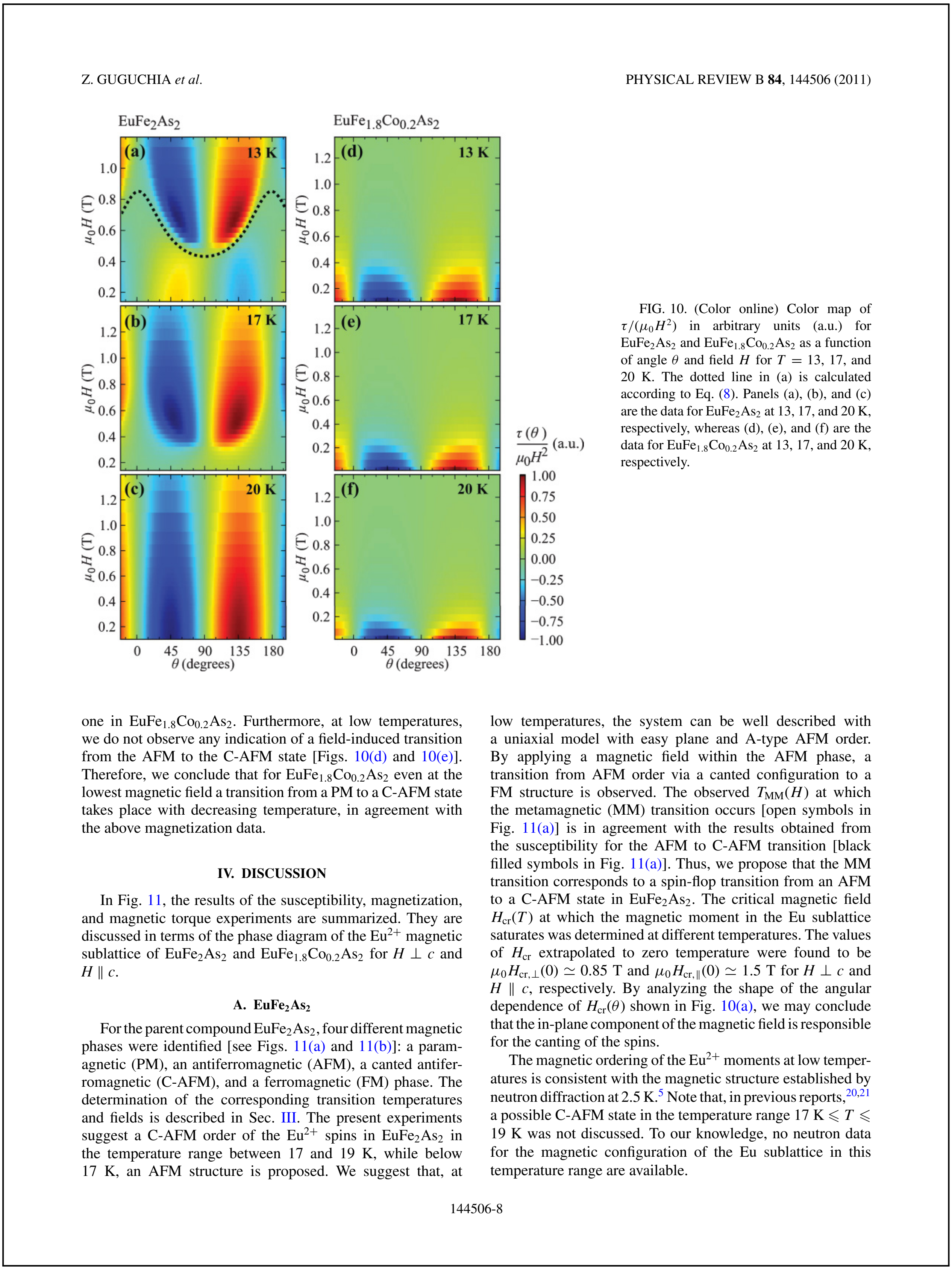

FIG. 10. (Color online) Color map of $\tau/(\mu_0 H^2)$ in arbitrary units (a.u.) for $EuFe_2As_2$ and $EuFe_{1.8}Co_{0.2}As_2$ as a function of angle θ and field H for $T = 13$, 17, and 20 K. The dotted line in (a) is calculated according to Eq. (8). Panels (a), (b), and (c) are the data for $EuFe_2As_2$ at 13, 17, and 20 K, respectively, whereas (d), (e), and (f) are the data for $EuFe_{1.8}Co_{0.2}As_2$ at 13, 17, and 20 K, respectively.

one in $EuFe_{1.8}Co_{0.2}As_2$. Furthermore, at low temperatures, we do not observe any indication of a field-induced transition from the AFM to the C-AFM state [Figs. 10(d) and 10(e)]. Therefore, we conclude that for $EuFe_{1.8}Co_{0.2}As_2$ even at the lowest magnetic field a transition from a PM to a C-AFM state takes place with decreasing temperature, in agreement with the above magnetization data.

IV. DISCUSSION

In Fig. 11, the results of the susceptibility, magnetization, and magnetic torque experiments are summarized. They are discussed in terms of the phase diagram of the Eu^{2+} magnetic sublattice of $EuFe_2As_2$ and $EuFe_{1.8}Co_{0.2}As_2$ for $H \perp c$ and $H \parallel c$.

A. $EuFe_2As_2$

For the parent compound $EuFe_2As_2$, four different magnetic phases were identified [see Figs. 11(a) and 11(b)]: a paramagnetic (PM), an antiferromagnetic (AFM), a canted antiferromagnetic (C-AFM), and a ferromagnetic (FM) phase. The determination of the corresponding transition temperatures and fields is described in Sec. III. The present experiments suggest a C-AFM order of the Eu^{2+} spins in $EuFe_2As_2$ in the temperature range between 17 and 19 K, while below 17 K, an AFM structure is proposed. We suggest that, at low temperatures, the system can be well described with a uniaxial model with easy plane and A-type AFM order. By applying a magnetic field within the AFM phase, a transition from AFM order via a canted configuration to a FM structure is observed. The observed $T_{MM}(H)$ at which the metamagnetic (MM) transition occurs [open symbols in Fig. 11(a)] is in agreement with the results obtained from the susceptibility for the AFM to C-AFM transition [black filled symbols in Fig. 11(a)]. Thus, we propose that the MM transition corresponds to a spin-flop transition from an AFM to a C-AFM state in $EuFe_2As_2$. The critical magnetic field $H_{cr}(T)$ at which the magnetic moment in the Eu sublattice saturates was determined at different temperatures. The values of H_{cr} extrapolated to zero temperature were found to be $\mu_0 H_{cr,\perp}(0) \simeq 0.85$ T and $\mu_0 H_{cr,\parallel}(0) \simeq 1.5$ T for $H \perp c$ and $H \parallel c$, respectively. By analyzing the shape of the angular dependence of $H_{cr}(\theta)$ shown in Fig. 10(a), we may conclude that the in-plane component of the magnetic field is responsible for the canting of the spins.

The magnetic ordering of the Eu^{2+} moments at low temperatures is consistent with the magnetic structure established by neutron diffraction at 2.5 K.[5] Note that, in previous reports,[20,21] a possible C-AFM state in the temperature range 17 K $\leqslant T \leqslant$ 19 K was not discussed. To our knowledge, no neutron data for the magnetic configuration of the Eu sublattice in this temperature range are available.

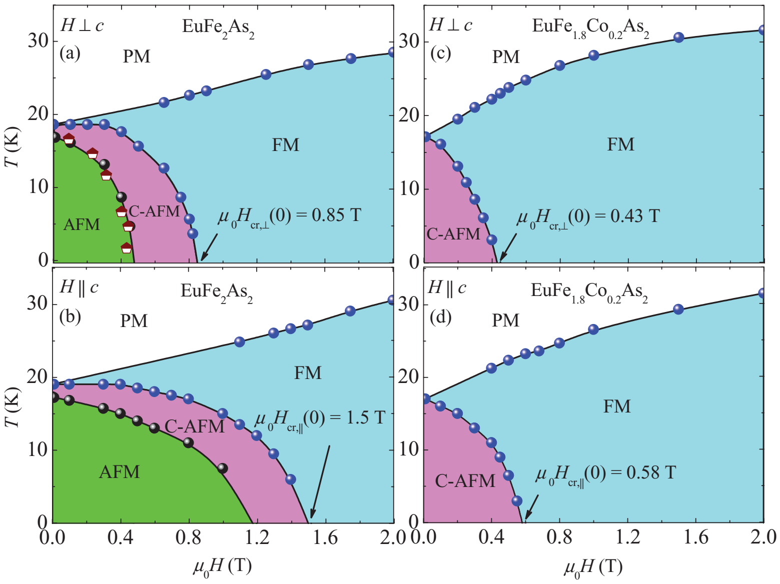

FIG. 11. (Color online) Magnetic phase diagrams of single-crystal EuFe$_2$As$_2$ [(a) and (b)] and single-crystal EuFe$_{1.8}$Co$_{0.2}$As$_2$ [(c)and (d)] for $H \perp c$ and for $H \parallel c$. The various phases in the phase diagrams are denoted as follows: paramagnetic (PM), antiferromagnetic (AFM), canted antiferromagnetic (C-AFM), and ferromagnetic (FM). The filled and open symbols are from the susceptibility and field-dependent magnetization measurements, respectively. The solid lines are guides to the eyes.

B. EuFe$_{1.8}$Co$_{0.2}$As$_2$

The corresponding magnetic phase diagrams for Co-doped EuFe$_{1.8}$Co$_{0.2}$As$_2$ are shown in Figs. 11(c) and 11(d). The magnetic ordering temperature of $\simeq$17 K is only about 2 K lower as compared to the parent compound. However, in the Co-doped EuFe$_{1.8}$Co$_{0.2}$As$_2$, no signatures of a low-field and low-temperature AFM state of the Eu^{2+} moments were found. Only a C-AFM phase (with a FM component in the *ab* plane) is present at low fields and low temperatures. The ordering temperature $T_{\text{C-AFM}}$ decreases with increasing magnetic field, similar to the parent compound [see Figs. 11(a) and 11(b)]. The critical magnetic field H_{cr} at which the Eu magnetic ordering is saturated was determined for different temperatures, and the extrapolated zero-temperature values were found to be $\mu_0 H_{\text{cr},\perp}(0) \simeq 0.43$ T and $\mu_0 H_{\text{cr},\parallel}(0) \simeq 0.58$ T for $H \perp c$ and $H \parallel c$, respectively. These values of $\mu_0 H_{\text{cr}}$ are much smaller than those obtained for the parent compound. Moreover, the magnetic anisotropy $\gamma_{\text{cr}} = H_{\text{cr},\parallel}(0)/H_{\text{cr},\perp}(0) \simeq 1.35$ of Co-doped EuFe$_{1.8}$Co$_{0.2}$As$_2$ is also smaller than $\gamma_{\text{cr}} \simeq 1.76$ of the parent compound.

It was concluded from different experiments[21,27,29–31] that there is a strong coupling between the localized Eu^{2+} spins and the conduction electrons of the two-dimensional (2D) Fe$_2$As$_2$ layers. Recently, direct experimental evidence for a strong interlayer coupling was obtained by means of ^{75}As NMR,[31] revealing a magnetic exchange interaction between the localized Eu 4f moments, which is mediated by the itinerant Fe 3d electrons. However, the direct interaction of the Eu moments and the magnetic moments in Fe sublattice can not be neglected. Only a combination of both interactions can further elucidate the C-AFM ground state observed in the parent compound EuFe$_2$As$_2$ as well as in the Co-doped system EuFe$_{1.8}$Co$_{0.2}$As$_2$ (see Fig. 11).

Note that the present results for EuFe$_{1.8}$Co$_{0.2}$As$_2$, exhibiting a SDW ground state below 60 K,[30] reveal a C-AFM structure of the Eu spins with a FM component in the *ab* plane. This finding confirms previous assumptions that, for materials in which the Fe ions are in the SDW ground state (such as EuFe$_2$As$_2$), the direction of the Eu magnetic moments is in the *ab* plane.[5,32] On the other hand, in the case of nonmagnetic Fe ground states, like in superconducting EuFe$_{2-x}$Co$_x$As$_2$ compounds, where the SDW magnetic state is totally suppressed, the direction of the Eu magnetic moments is parallel to the *c* axis.[33–36]

V. CONCLUSIONS

The magnetic properties of single crystals of EuFe$_2$As$_2$ and EuFe$_{1.8}$Co$_{0.2}$As$_2$ were studied by means of susceptibility, magnetization, and magnetic torque investigations. The susceptibility and magnetization experiments performed for various temperatures and magnetic fields along the crystallographic axes provided information on the magnetic structure of the studied crystals. In addition, the evolution of the magnetic structure as a function of the tilting angle of the field and the crystallographic axes is studied by magnetic torque experiments. The phase diagrams for the ordering of the Eu^{2+} magnetic sublattice with respect to temperature, magnetic field, and the angle between the magnetic field

and the crystallographic c axis in $\mathrm{EuFe}_{2-x}\mathrm{Co}_x\mathrm{As}_2$ are determined and discussed. The present investigations reveal a complex and sophisticated interplay of magnetic phases in $\mathrm{EuFe}_{2-x}\mathrm{Co}_x\mathrm{As}_2$. The magnetic ordering temperature of the Eu^{2+} moments remains nearly unchanged upon Co doping. However, unlike the parent compound, in which the Eu^{2+} moments order antiferromagnetically at low temperatures, the Co-doped system $\mathrm{EuFe}_{1.8}\mathrm{Co}_{0.2}\mathrm{As}_2$ exhibits a C-AFM state with a FM component in the ab plane. The magnetic anisotropy γ_{cr} becomes smaller as a result of Co doping. This implies that the magnetic configuration of the Eu moments is strongly influenced by the magnetic moments of the Fe sublattice, where superconductivity takes place for a certain range of Co doping. A detailed knowledge of the interplay between the Eu^{2+} moments and magnetism of the Fe sublattice is important to understand the role of magnetism of the localized Eu^{2+} moments for the occurrence of superconductivity in $\mathrm{EuFe}_{2-x}\mathrm{Co}_x\mathrm{As}_2$.

ACKNOWLEDGMENT

This work was supported by the Swiss National Science Foundation, the SCOPES Grant No. IZ73Z0_128242, the NCCR Project MaNEP, the EU Project CoMePhS, and the Georgian National Science Foundation Grant No. GNSF/ST08/4-416.

---

[*] zurabgug@physik.uzh.ch

[†] Current address: Institute of Low Temperature and Structure Research, Polish Academy of Sciences, 50-422 Wroclaw, Poland.

[1] Y. Kamihara, T. Watanabe, M. Hirano, and H. Hosono, J. Am. Chem. Soc. **130**, 3296 (2008).

[2] X. H. Chen, T. Wu, G. Wu, R. H. Liu, H. Chen, and D. F. Fang, Nature (London) **453**, 761 (2008).

[3] M. Rotter, M. Tegel, and D. Johrendt, Phys. Rev. Lett. **101**, 107006 (2008).

[4] F.-C. Hsu, J.-Y. Luo, K.-W. Yeh, T.-K. Chen, T.-W. Huang, P. M. Wu, Y.-C. Lee, Y.-L. Huang, Y.-Y. Chu, D.-C. Yan, and M.-K. Wu, Proc. Natl. Acad. Sci. USA **105**, 14262 (2008).

[5] Y. Xiao, Y. Su, M. Meven, R. Mittal, C. M. N. Kumar, T. Chatterji, S. Price, J. Persson, N. Kumar, S. K. Dhar, A. Thamizhavel, and Th. Brueckel, Phys. Rev. B **80**, 174424 (2009).

[6] M. S. Torikachvili, S. L. Bud'ko, N. Ni, and P. C. Canfield, Phys. Rev. Lett. **101**, 057006 (2008).

[7] Liling Sun, Jing Guo, Genfu Chen, Xianhui Chen, Xiaoli Dong, Wei Lu, Chao Zhang, Zheng Jiang, Yang Zou, Suo Zhang, Yuying Huang, Qi Wu, Xi Dai, Yuanchun Li, Jing Liu, and Zhongxian Zhao, Phys. Rev. B **82**, 134509 (2010).

[8] H. Lee, E. Park, T. Park, V. A. Sidorov, F. Ronning, E. D. Bauer, and J. D. Thompson, Phys. Rev. B **80**, 024519 (2009).

[9] P. L. Alireza, Y. T. C. Ko, J. Gillett, C. M. Petrone, J. M. Cole, G. G. Lonzarich, and S. E. Sebastian, J. Phys. Condens. Matter **21**, 012208 (2009).

[10] K. Igawa, H. Okada, H. Takahashi, S. Matsuishi, Y. Kamihara, M. Hirano, H. Hosono, K. Matsubayashi, and Y. Uwatoko, J. Phys. Soc. Jpn. **78**, 025001 (2009).

[11] H. Fukazawa, N. Takeshita, T. Yamazaki, K. Kondo, K. Hirayama, Y. Kohori, K. Miyazawa, H. Kito, H. Eisaki, and A. Iyo, J. Phys. Soc. Jpn. **77**, 105004 (2008).

[12] W. J. Duncan, O. P. Welzel, C. Harrison, X. F. Wang, X. H. Chen, F. M. Grosche, and P. G. Niklowitz, J. Phys. Condens. Matter **22**, 052201 (2010).

[13] A. Mani, N. Ghosh, S. Paulraj, A. Bharathi, and C. S. Sundar, Europhys. Lett. **87**, 17004 (2009).

[14] T. Terashima, M. Kimata, H. Satsukawa, A. Harada, K. Hazama, S. Uji, H. S. Suzuki, T. Matsumoto, and K. Murata, J. Phys. Soc. Jpn. **78**, 083701 (2009).

[15] C. F. Miclea, M. Nicklas, H. S. Jeevan, D. Kasinathan, Z. Hossain, H. Rosner, P. Gegenwart, C. Geibel, and F. Steglich, Phys. Rev. B **79**, 212509 (2009).

[16] Z. A. Ren, W. Lu, J. Yang, W. Yi, X. L. Shen, Z. C. Li, G. C. Che, X. L. Dong, L. L. Sun, F. Zhou, and Z. X. Zhao, Chin. Phys. Lett. **25**, 2215 (2008).

[17] S. Matsuishi, Y. Inoue, T. Nomura, M. Hirano, and H. Hosono, J. Phys. Soc. Jpn. **77**, 113709 (2008).

[18] J. Zhao, Q. Huang, C. de la Cruz, S. Li, J. W. Lynn, Y. Chen, M. A. Green, G. F. Chen, G. Li, Z. Li, J. L. Luo, N. L. Wang, and P. Dai, Nat. Mater. **7**, 953 (2008).

[19] H. Raffius, E. Mörsen, B. D. Mosel, W. Müller-Warmuth, W. Jeitschko, L. Terbüchte, and T. Vomhof, J. Phys. Chem. Solids **54**, 135 (1993).

[20] Z. Ren, Z. W. Zhu, S. Jiang, X. F. Xu, Q. Tao, C. Wang, C. M. Feng, G. H. Cao, and Z. A. Xu, Phys. Rev. B **78**, 052501 (2008).

[21] S. Jiang, Y. K. Luo, Z. Ren, Z. W. Zhu, C. Wang, X. F. Xu, Q. Tao, G. H. Cao, and Z. A. Xu, New J. Phys. **11**, 025007 (2009).

[22] S. Blundell, *Magnetism in Condensed Matter* (Oxford University Press, New York, 2006).

[23] Y. Xiao, Y. Su, W. Schmidt, K. Schmalzl, C. M. N. Kumar, S. Price, T. Chatterji, R. Mittal, L. J. Chang, S. Nandi, N. Kumar, S. K. Dhar, A. Thamizhavel, and Th. Brueckel, Phys. Rev. B **81**, 220406 (2010).

[24] Shuai Jiang, Hui Xing, Guofang Xuan, Zhi Ren, Cao Wang, Zhu-an Xu, and Guanghan Cao, Phys. Rev. B **80**, 184514 (2009).

[25] Y. He, T. Wu, G. Wu, Q. J. Zheng, Y. Z. Liu, H. Chen, J. J. Ying, R. H. Liu, X. F. Wang, Y. L. Xie, Y. J. Yan, J. K. Dong, S. Y. Li, and X. H. Chen, J. Phys. Condens. Matter **22**, 235701 (2010).

[26] H. S. Jeevan, Deepa Kasinathan, H. Rosner, and P. Gegenwart, Phys. Rev. B **83**, 054511 (2011).

[27] Zhi Ren, Xiao Lin, Qian Tao, Shuai Jiang, Zengwei Zhu, Cao Wang, Guanghan Cao, and Zhu'an Xu, Phys. Rev. B **79**, 094426 (2009).

[28] L. J. Li, Y. K. Luo, Q. B. Wang, H. Chen, Z. Ren, Q. Tao, Y. K. Li, X. Lin, M. He, Z. W. Zhu, G. H. Cao, and Z. A. Xu, New J. Phys. **11**, 025008 (2009).

[29] E. Dengler, J. Deisenhofer, H. A. Krug von Nidda, Seunghyun Khim, J. S. Kim, Kee Hoon Kim, F. Casper, C. Felser, and A. Loidl, Phys. Rev. B **81**, 024406 (2010).

[30] J. J. Ying, T. Wu, Q. J. Zheng, Y. He, G. Wu, Q. J. Li, Y. J. Yan, Y. L. Xie, R. H. Liu, X. F. Wang, and X. H. Chen, Phys. Rev. B **81**, 052503 (2010).

[31] Z. Guguchia, J. Roos, A. Shengelaya, S. Katrych, Z. Bukowski, S. Weyeneth, F. Murányi, S. Strässle, A. Maisuradze, J. Karpinski, and H. Keller, Phys. Rev. B **83**, 144516 (2011).

[32] I. Nowik and I. Felner, Hyperfine Interact. **28**, 959 (1986).

[33] I. Nowik and I. Felner, Physica C **469**, 485 (2009).

[34] C. Feng, Z. Ren, S. Xu, S. Jiang, Z. Xu, G. Cao, I. Nowik, I. Felner, K. Matsubayashi, and Y. Uwatoko, Phys. Rev. B **82**, 094426 (2010).

[35] I. Nowik, I. Felner, Z. Ren, G. H. Cao, and Z. A. Xu, J. Phys. Condens. Matter **23**, 065701 (2011).

[36] I. Nowik, I. Felner, Z. Ren, G. H. Cao, and Z. A. Xu, New J. Phys. **13**, 023033 (2011).

[37] S. Kohout, J. Roos, and H. Keller, Rev. Sci. Instrum. **78**, 013903 (2007).

[38] J. L. Luo, N. L. Wang, G. T. Liu, D. Wu, X. N. Jing, F. Hu, and T. Xiang, Phys. Rev. Lett. **93**, 187203 (2004).

[39] R. S. Perry, L. M. Galvin, S. A. Grigera, L. Capogna, A. J. Schofield, A. P. Mackenzie, M. Chiao, S. R. Julian, S. I. Ikeda, S. Nakatsuji, Y. Maeno, and C. Pfleiderer, Phys. Rev. Lett. **86**, 2661 (2001).

[40] T. Kimura and Y. Tokura, Ann. Rev. Mater. Sci. **30**, 451 (2000).

[41] S. Weyeneth, P. J. W. Moll, R. Puzniak, K. Ninios, F. F. Balakirev, R. D. McDonald, H. B. Chan, N. D. Zhigadlo, S. Katrych, Z. Bukowski, J. Karpinski, H. Keller, B. Batlogg, and L. Balicas, Phys. Rev. B **83**, 134503 (2011)

[42] H. Tanaka, T. Kato, K. Iio, and K. Nagata, J. Phys. Soc. Jpn. **61**, 3292 (1992).

[43] T. Sasaki, H. Uozaki, S. Endo, and N. Toyota, Synth. Metals **120**, 759 (2001).

[44] G. Blatter, M. V. Feigel'man, V. B. Geshkenbein, A. I. Larkin, and V. M. Vinokur, Rev. Mod. Phys. **66**, 1125 (1994).

4.4.3 Publication III: Muon-spin rotation and magnetization studies of chemical and hydrostatic pressure effects in $EuFe_2(As_{1-x}P_x)_2$

Z. Guguchia, A. Shengelaya, A. Maisuradze, L. Howald, Z. Bukowski, M. Chikovani, H. Luetkens, S. Katrych, J. Karpinski, and H. Keller

J. Supercond. Nov. Magn. **26**, 285 (2013).

Abstract

The magnetic phase diagram of $EuFe_2(As_{1-x}P_x)_2$ was investigated by means of magnetization and muon-spin rotation (μSR) studies as a function of chemical (isovalent substitution of As by P) and hydrostatic pressure. The magnetic phase diagrams of the magnetic ordering of the Eu and Fe spins with respect to P content and hydrostatic pressure are determined and discussed. The present investigations reveal that the magnetic coupling between the Eu and the Fe sublattices strongly depends on chemical and hydrostatic pressure. It is found that chemical and hydrostatic pressure have a similar effect on the Eu and Fe magnetic order.

DOI: 10.1007/s10948-012-1743-6
PACS numbers: 74.20.Mn, 74.25.Ha, 74.70.Xa, 76.75.+i

The original publication is electronically available at:
http://link.springer.com/article/10.1007/s10948-012-1743-6

J Supercond Nov Magn (2013) 26:285–295
DOI 10.1007/s10948-012-1743-6

ORIGINAL PAPER

Muon-Spin Rotation and Magnetization Studies of Chemical and Hydrostatic Pressure Effects in EuFe$_2$(As$_{1-x}$P$_x$)$_2$

Z. Guguchia · A. Shengelaya · A. Maisuradze · L. Howald · Z. Bukowski · M. Chikovani · H. Luetkens · S. Katrych · J. Karpinski · H. Keller

Received: 24 July 2012 / Accepted: 30 July 2012 / Published online: 25 August 2012

Abstract The magnetic phase diagram of EuFe$_2$(As$_{1-x}$P$_x$)$_2$ was investigated by means of magnetization and muon-spin rotation (μSR) studies as a function of chemical (isovalent substitution of As by P) and hydrostatic pressure. The magnetic phase diagrams of the magnetic ordering of the Eu and Fe spins with respect to P content and hydrostatic pressure are determined and discussed. The present investigations reveal that the magnetic coupling between the Eu and the Fe sublattices strongly depends on chemical and hydrostatic pressure. It is found that chemical and hydrostatic pressures have a similar effect on the Eu and Fe magnetic order.

Keywords High temperature Fe-based superconductor · Localized and band magnetism · Hydrostatic pressure · Chemical pressure

1 Introduction

The discovery of superconductivity in the iron-based pnictides [1] provided a new class of compounds to the high temperature superconductor (HTS) family. Ternary iron arsenide AFe$_2$As$_2$ (A = Sr, Ca, Ba, Eu) [2] is one of the parent compounds with ThCr$_2$Si$_2$-type structure. Similarly as LnFeAsO (Ln = La–Gd) [3], AFe$_2$As$_2$ undergoes a structural phase transition from a tetragonal to an orthorombic phase, accompanied or followed by a spin-density-wave (SDW) transition of the itinerant Fe moments. The superconducting (SC) state can be achieved either under pressure (chemical and hydrostatic) [4–6] or by appropriate charge carrier doping of the parent compounds [7–9], both accompanied by a suppression of the SDW state.

Here, we focus on EuFe$_2$As$_2$ which is a particularly interesting member of the ternary system AFe$_2$As$_2$, since the A site is occupied by a rare earth Eu^{2+} S-state (orbital moment $L = 0$) ion with a $4f^7$ electronic configuration. Eu^{2+} has a total electron spin $S = 7/2$, corresponding to a theoretical effective magnetic moment of $\mu_{\mathrm{eff}} = 7.94\,\mu_B$. In addition to the SDW ordering of the Fe moments at $T_{\mathrm{SDW}} \simeq 190$ K, an antiferromagnetic (AFM) order of the Eu^{2+} spins at $T_{\mathrm{AFM}} \simeq 19$ K was reported by Mössbauer spectroscopy [10] and later confirmed by neutron diffraction [11]. Various reports on EuFe$_{2-x}$Co$_x$As$_2$ ($x = 0$ and 0.1) suggest a strong coupling between the magnetism of the Eu^{2+} ions and the conduction electrons, which may affect or even destroy superconductiv-

---

Z. Guguchia (✉) · A. Maisuradze · L. Howald · H. Keller
Physik-Institut der Universität Zürich, Winterthurerstrasse 190, 8057 Zürich, Switzerland
e-mail: zurabgug@physik.uzh.ch

A. Shengelaya · M. Chikovani
Department of Physics, Tbilisi State University, Chavchavadze 3, 0128 Tbilisi, Georgia

Present address:
M. Chikovani
Laboratory for Developments and Methods, Paul Scherrer Institute, 5232 Villigen PSI, Switzerland

A. Maisuradze · H. Luetkens
Laboratory for Muon Spin Spectroscopy, Paul Scherrer Institute, 5232 Villigen PSI, Switzerland

Present address:
Z. Bukowski
Institute of Low Temperature and Structure Research, Polish Academy of Sciences, 50-422 Wroclaw, Poland

Z. Bukowski · S. Katrych · J. Karpinski
Laboratory for Solid State Physics, ETH Zürich, 8093 Zürich, Switzerland

Present address:
S. Katrych · J. Karpinski
Institut de Physique de la Matiére Condensée (ICMP), Ecole Polytechnique Fédérale de Lausanne (EPFL), 1015 Lausanne, Switzerland

ity [12, 13]. For example, in contrast to the other ‘122’ systems, where the substitution of Fe by Co leads to superconductivity [14, 15], the compounds containing Eu^{2+} exhibit the onset of a superconducting transition, but seem to be hindered to reach zero resistivity at ambient pressure [16]. Although Ni doping in $BaFe_2As_2$ leads to superconductivity up to 21 K [17], ferromagnetism rather than superconductivity was found in $EuFe_2As_2$ by Ni doping [18]. On the other hand, in single crystals of P substituted $EuFe_2(As_{1-x}P_x)_2$ bulk superconductivity with superconducting transition temperature $T_c \simeq 28$ K was observed by resistivity, magnetization, and specific heat measurements [19]. Isovalent P substitution on the As site in $EuFe_2As_2$ without introducing holes or electrons simulates a condition generally referred to as “chemical pressure”. Superconductivity coexisting with AFM Eu^{2+} order was only found in a very narrow range of P content x ($0.16 \le x \le 0.22$), where the SDW transition is suppressed. Superconductivity with a zero resistivity state was also observed for $EuFe_2As_2$ under applied pressure [6, 20]. Similar to the case of P substitution, superconductivity covers only a narrow pressure range of 2.5–3.0 GPa.

In this paper, we report detailed magnetization and muon spin rotation (μSR) measurements in $EuFe_2As_{2-x}P_x$ as a function of the P content x. One P substituted sample $EuFe_2(As_{0.88}P_{0.12})_2$ was also studied under applied pressure p. The μSR technique is a powerful tool to study the magnetic and superconducting properties of materials microscopically. It provides reliable measurements of T_c, T_{SDW}, the magnetic ordering temperature of Eu^{2+} spins T_{Eu} and the ordered moment size as a function of both x and p. Consequently, the phase diagrams with respect x and p are determined from these measurements. We compare the present results with previous high pressure studies on the parent compound $EuFe_2As_2$ and discuss the combined results in terms of the relation of x and p. The paper is organized as follows: Experimental details are described in Sect. 2. The results of the magnetic susceptibility and the μSR experiments at ambient and applied pressure are presented and discussed in Sects. 3.1 and 3.2, respectively. In Sect. 4, the phase diagrams are presented. The conclusions follow in Sect. 5.

2 Experimental Details

In the present work, the system $EuFe_2(As_{1-x}P_x)_2$ with $x = 0$, 0.12, 0.2, and 1 is investigated. Note that the sample with $x = 0$ is single crystalline, and all the P substituted compounds are pollycrystalline. The concentrations $x = 0.12$ and 0.2 were studied due to their proximity to the SC phase reported in [19]. A single crystal of $EuFe_2As_2$ was grown out of Sn flux [21]. Polycrystalline samples were synthesized by solid-state reaction between EuAs, Fe_2As, and Fe_2P. EuAs was presynthesized by heating europium grains and phosphorus powders very slowly to 1173 K followed by a tempering at this temperature for 36 h. Fe_2As was prepared by heating Fe and As powders at 973 K for 10 h and at 1173 K for 15 h. Fe_2P was presynthesized by reacting iron and phosphorus powders at 973 K for 24 h from stoichiometric amounts of the elements. All the starting materials had a purity better than 99.9 %. Powders of EuAs, Fe_2As, and Fe_2P were weighted according to the stoichiometric ratio, thoroughly ground and pressed into pellets in an argon-filled glove box. The pellets were then sealed in an evacuated quartz tube, sintered at 1273 K for 36 h, and then cooled slowly to room temperature.

Powder X-ray diffraction (XRD) studies of the $EuFe_2(As_{1-x}P_x)_2$ samples were carried out at room temperature with a STOE diffractometer ($CuK_{\alpha 1}$ radiation, $\lambda = 1.5406$ Å) equipped with a mini-phase-sensitive detector and a Ge monochromator. The structural refinements were done using the program FULLPROF [22]. The zero-field-cooled and field-cooled (ZFC and FC) magnetization measurements of the $EuFe_2(As_{1-x}P_x)_2$ samples were performed with a commercial SQUID magnetometer (*Quantum Design* MPMS-XL). The samples with $x = 0.2$ and 1 were studied only at ambient pressure. For $x = 0.12$, the investigations were also carried out under applied pressures up to $p = 5.9$ GPa by using a diamond anvil cell (DAC) filled with Daphne oil which served as a pressure-transmitting medium. The pressure at low temperatures was determined by the pressure dependence of the SC transition temperature of Pb.

Zero-field (ZF) μSR experiments were performed at the μE1 and πM3 beamlines of the Paul Scherrer Institute (Villigen, Switzerland). The general purpose instrument (GPS) was used to study the system $EuFe_2(As_{1-x}P_x)_2$ ($x = 0$, 0.12, 0.2, and 1) at ambient pressure. The samples were mounted inside of a gas-flow ^{4}He cryostat on a sample holder with a standard veto setup providing a low-background μSR signal. In addition, the sample with $x = 0.12$ was studied under pressure using the GPD instrument. Pressures up to 2.0 GPa were generated in a double wall piston-cylinder type of cell made of MP35N [23] material especially designed to perform μSR experiments under pressure. As a pressure transmitting medium Daphne oil was used. The pressure was measured by tracking the SC transition of a very small indium plate by AC susceptibility. The μSR time spectra were analyzed using the free software package MUSRFIT [24].

3 Results and Discussion

3.1 Crystal Structure and Magnetic Properties of $EuFe_2(As_{1-x}P_x)_2$

3.1.1 X-Ray Powder Diffraction

The crystal structure for all $EuFe_2(As_{1-x}P_x)_2$ samples at room temperature was refined with the tetragonal $ThCr_2Si_2$

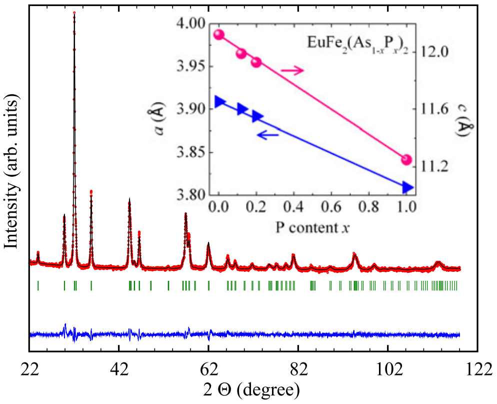

Fig. 1 X-ray powder diffraction pattern at room temperature for the sample EuFe$_2$(As$_{0.88}$P$_{0.12}$)$_2$. *The solid line* represents a Ritveld refinement profile. The residuals are plotted at *the bottom* of *the figure*. In *the inset*, refined lattice parameters are plotted as a function of P content x

structure. An example of the refinement profile for EuFe$_2$(As$_{0.88}$P$_{0.12}$)$_2$ is shown in Fig. 1. No obvious secondary phase can be detected. The weighted pattern factor and goodness of fit are Rwp ~ 11.2 % and $S \sim 1.6$, respectively, indicating a fairly good refinement. In addition, the refined occupancies are close to the nominal values. The lattice constants for the tetragonal unit cell based upon the Rietveld refinements are $a = 3.9095(2)$ Å and $c = 11.979(1)$ Å for $x = 0.12$, $a = 3.9006(2)$ Å and $c = 11.9312(1)$ Å for $x = 0.2$, $a = 3.8152(2)$ Å and $c = 11.2401(1)$ Å for $x = 1$. The values for $x = 1$ are in agreement with the literature values [$a = 3.8178(1)$ Å and $c = 11.2372(3)$ Å] [25]. The lattice constants a and c as a function of x are plotted in the inset of Fig. 1. A decrease of both a and c with increasing x is observed. The decrease of the lattice constant c as a result of P substitution implies an increase of the coupling between the Eu and the Fe$_2$(As$_{1-x}$P$_x$)$_2$ layers. This might also be important for the evolution of the magnetic order in the Eu-sublattice, since the Ruderman–Kittel–Kasuya–Yosida (RKKY) coupling strongly depends on the distance between the magnetic ions [13, 18, 25].

3.1.2 *Magnetization Measurements*

The temperature dependence of the zero-field-cooled (ZFC) and field-cooled (FC) magnetic susceptibility $\chi = M/H$ for EuFe$_2$(As$_{1-x}$P$_x$)$_2$ ($x = 0.12$, 0.2, and 1) in a magnetic field of $\mu_0 H = 2$ mT is shown in Fig. 2. The results for $x = 0$ were already discussed in detail in our previous work [21], and hence, are not shown here. The magnetic susceptibility at high temperatures (i.e., far above the magnetic ordering temperature of the Eu^{2+} moments T_{Eu}) is well described by

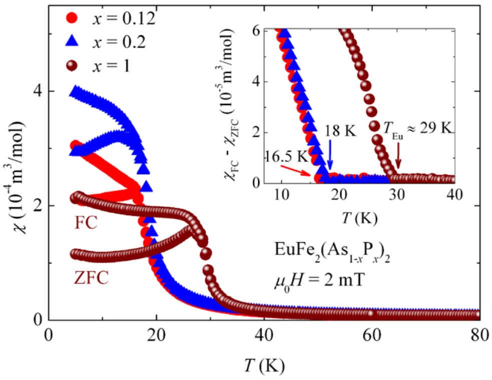

Fig. 2 Temperature dependence of the ZFC and FC magnetic susceptibility for the samples EuFe$_2$(As$_{1-x}$P$_x$)$_2$ ($x = 0.12$, 0.2, 1) measured in a magnetic field of $\mu_0 H = 2$ mT. *The inset* illustrates the temperature dependence of the difference of both susceptibilities ($\chi_{\mathrm{FC}} - \chi_{\mathrm{ZFC}}$). *The arrows* mark the magnetic ordering temperatures T_{Eu} of the Eu^{2+} moments

the Curie–Weiss law:

$$\chi(T) = \frac{C}{T - \theta_{\mathrm{CW}}}. \tag{1}$$

Here, C denotes the Curie constant and θ_{CW} the paramagnetic Curie–Weiss temperature. An analysis of the data in Fig. 2 with Eq. (1) yields: $\theta_{\mathrm{CW}} = 16.74(8)$ K, $\mu_{\mathrm{eff}} \simeq 8.1\ \mu_B$ for $x = 0.12$, $\theta_{\mathrm{CW}} = 18.14(7)$ K, $\mu_{\mathrm{eff}} \simeq 8.2\ \mu_B$ for $x = 0.2$, and $\theta_{\mathrm{CW}} = 29.35(9)$ K, $\mu_{\mathrm{eff}} \simeq 8.3\ \mu_B$ for $x = 1$. The obtained values of μ_{eff} are close to the theoretical value of a free Eu^{2+} ion ($\mu_{\mathrm{Eu}^{2+}} = 7.94\ \mu_B$).

As shown in Fig. 2, for all the P substituted samples an obvious deviation between χ_{ZFC} and χ_{FC} is seen at low temperatures. This is not the case for $x = 0$ [18, 21], for which AFM order of Eu^{2+} with the moments pointing along the a axis was reported. This result is consistent with previous magnetizaton studies [26], suggesting that the ground state of the coupled Eu^{2+} spins is a canted AFM state (C-AFM state) (i.e., AFM with the net ferromagnetic (FM) component along the c-axis) in EuFe$_2$(As$_{1-x}$P$_x$)$_2$ ($x = 0.12$, 0.2) and a FM state in EuFe$_2$P$_2$. Recently, neutron diffraction measurements were also performed on EuFe$_2$P$_2$ and an almost axial FM structure of the Eu^{2+} spins was established [27]. The C-AFM and FM structure of the Eu-sublattice in EuFe$_2$(As$_{1-x}$P$_x$)$_2$ ($x = 0.12$, 0.2, 1) sharply contrasts with the planar antiferromagnetism seen in the parent compound EuFe$_2$As$_2$, suggesting a delicate interplay between the Eu $4f$ and the Fe $3d$ electrons. It was concluded from different experiments [12, 13] that there is a strong coupling between the localized Eu^{2+} spins and the conduction electrons of the two-dimensional (2D) Fe$_2$As$_2$ layers in EuFe$_2$As$_2$. This revealed that the magnetic exchange interaction between the

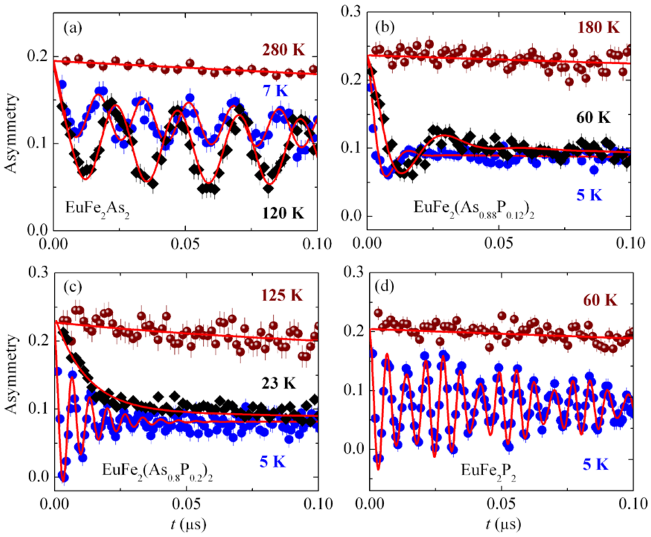

Fig. 3 ZF μSR spectra for EuFe$_2$(As$_{1-x}$P$_x$)$_2$ ($x = 0, 0.12, 0.2, 1$) recorded for three different temperatures: $T < T_{\mathrm{Eu}}$ (*circles*), $T_{\mathrm{Eu}} < T < T_{\mathrm{SDW}}$ (*diamonds*), and $T > T_{\mathrm{SDW}}$ (*spheres*). *The solid lines* represent fits to the data by means of Eq. (2)

localized Eu 4f moments is mediated by the itinerant Fe 3d electrons. However, the interaction of the Eu moments with the magnetic moments of the Fe sublattice (band magnetism) cannot be neglected. Only a combination of both interactions can further elucidate the C-AFM ground state observed in EuFe$_2$(As$_{1-x}$P$_x$)$_2$ ($x = 0.12$ and 0.2). Note that a C-AFM ground state was also found in the related compound EuFe$_{1.8}$Co$_{0.2}$As$_2$ [21].

The magnetic ordering temperature T_{Eu} of the Eu^{2+} moments was determined by the temperature at which the difference between χ_{ZFC} and χ_{FC} sets in (see the inset of Fig. 2). It was found to be $T_{\mathrm{Eu}} \simeq 16.5$, 18, and 29 K for $x = 0.12$, $x = 0.2$, and $x = 1$, respectively. The value of T_{Eu} for $x = 0.12$ is slightly reduced compared to $T_{\mathrm{Eu}} \simeq 19$ K for the parent compound $x = 0$. However, on further increasing the P concentration T_{Eu} increases and reaches a maximum for $x = 1$. The value of T_{Eu} for $x = 1$ is in agreement with those reported in literature [19, 25, 27].

3.1.3 Zero-Field μSR Measurements

In a μSR experiment, nearly 100 % spin-polarized muons μ^+ are implanted into the sample one at a time. The positively charged μ^+ thermalize at interstitial lattice sites, where they act as magnetic microprobes. In a magnetic material, the muon spin precesses in the local magnetic field B_μ at the muon site with the Larmor frequency $\nu_\mu = \gamma_\mu/(2\pi)B_\mu$ (muon gyromagnetic ratio $\gamma_\mu/(2\pi) = 135.5$ MHz T^{-1}). ZF μSR is a very powerful tool to investigate microscopic magnetic properties of solids without applying an external magnetic field.

ZF μSR time spectra for the single crystal of EuFe$_2$As$_2$ and for the polycrystalline samples EuFe$_2$(As$_{1-x}$P$_x$)$_2$ are shown in Fig. 3, recorded for three different temperatures: $T < T_{\mathrm{Eu}}$, $T_{\mathrm{Eu}} < T < T_{\mathrm{SDW}}$, and $T > T_{\mathrm{SDW}}$. For EuFe$_2$As$_2$, the ZF μSR measurements were performed with the initial muon spin polarization tilted by approximately 45° away from the crystallographic c-axis. At high temperatures (see Fig. 3), no muon spin precession and only a very weak depolarization of the μSR signal is observed. This weak depolarization and its Gaussian functional form are typical for a paramagnetic material and reflect the occurrence of a small Gaussian–Kubo–Toyabe depolarization, originating from the interaction of the muon spin with randomly oriented nuclear magnetic moments. At temperatures below T_{Eu} a well-defined spontaneous muon spin precession is observed in all compounds, indicating long-range magnetic order of the Eu^{2+} moments in the investigated compounds. For $x = 0$ and 0.12 above $T_{\mathrm{Eu}} \simeq 20.5$ and 16.5 K, respectively, muon spin precession with a lower frequency is observed which is caused by the long-range SDW order of the Fe moments. However, for $x = 0.2$, instead of the oscillatory behavior seen in the SDW state for $x = 0$ and 0.12, a fast decaying signal is observed (see Fig. 3(c)). The reason for this strongly decaying μSR signal will be discussed below. For $x = 1$, only the magnetic ordering of the Eu moments is seen in the μSR spectra (Fig. 3(d)). Note that for $x = 0$, 0.12 and 0.2 only one μSR frequency is visible. However, for $x = 1$ two distinct precession frequencies occur in the μSR spectra, corresponding to the local magnetic fields $B^1_{\mu,\mathrm{Eu}} \simeq 1.08$ T ($\simeq$70 % of the signal) and $B^2_{\mu,\mathrm{Eu}} \simeq 1.37$ T

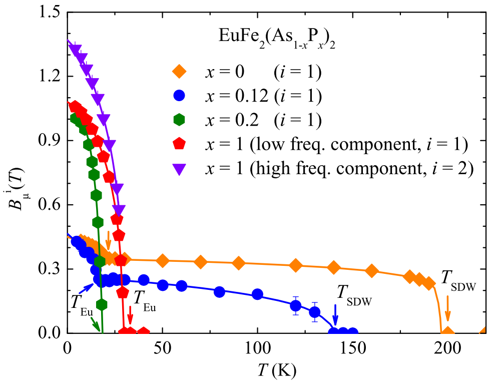

Fig. 4 The temperature dependence of the internal magnetic field B_μ^i for the samples EuFe$_2$(As$_{1-x}$P$_x$)$_2$ ($x = 0$, 0.12, 0.2, and 1). *The solid lines* represent fits to the data by means of Eq. (3). *The arrows* mark the transition temperatures for the SDW (T_{SDW}) and the Eu magnetic order (T_{Eu})

($\simeq$30 % of the signal). This indicates that two magnetically inequivalent muon stopping sites are present in EuFe$_2$P$_2$.

The ZF μSR data were analyzed using the following functional form:

$$A(t) = \sum_{i=1}^{2} A_0^i \big[\alpha_i e^{-\lambda_T^i t} \cos\big(\gamma_\mu B_\mu^i t + \varphi\big) + \beta_i e^{-\lambda_L^i t}\big]. \qquad (2)$$

α_i and $\beta_i = 1 - \alpha_i$ ($i = 1$ for $x = 0$, 0.12, 0.2, and $i = 1, 2$ for $x = 1$) are the fractions of the oscillating and nonoscillating μSR signal. For the single crystal ($x = 0$) one finds $\alpha_1 = 0.73(2)$ and $\beta_1 = 0.27(3)$. However, for the polycrystalline samples $\alpha_i = 2/3$ and $\beta_i = 1/3$. The 2/3 oscillating and the 1/3 nonoscillating μSR signal fractions originate from the spatial averaging in powder samples where only 2/3 of the magnetic field components are perpendicular to the muon spin and cause muon spin precession. A_0 denotes the initial asymmetry, and φ is the initial phase of the muon-spin ensemble. B_μ^i represents the internal magnetic field at the muon site, and the depolarization rates λ_T^i and λ_L^i characterize the damping of the oscillating and nonoscillating part of the μSR signal, respectively. The transversal relaxation rate λ_T^i is a measure of the width of the static magnetic field distribution at the muon site, and also reflects dynamical effects (spin fluctuations). The longitudinal relaxation rate λ_L^i is determined by dynamic magnetic fluctuations only [28]. The temperature dependence of the internal magnetic field B_μ^i for EuFe$_2$(As$_{1-x}$P$_x$)$_2$ is shown in Fig. 4. B_μ^i is proportional to the magnitude of the ordered moment and thus to the magnetic order parameter. The second component ($i = 2$) in the μSR signal was observed only for $x = 1$, and hence, we will discuss the x-dependence of the relevant physical parameters related to the first component ($i = 1$) only. For $x = 0$ a sharp step like increase of B_μ^1 is observed below $\simeq$195 K, which reflects the appearance of the SDW ordering of the Fe moments. The value of T_{SDW} is in good agreement with $T_{\mathrm{SDW}} \simeq 190$ K obtained from neutron diffraction [11]. A sharp increase of B_μ^1 is an indication for a first order transition. A first order transition due to SDW formation was also observed in the related compound SrFe$_2$As$_2$ [29]. Upon lowering the temperature B_μ^1 first tends to saturate, but increases again when the magnetic order of the Eu^{2+} moments occurs at T_{Eu}. To describe the temperature dependence of B_μ^i, we assumed the following phenomenological function:

$$\vec{B}_\mu^i(T) = \vec{B}_{\mu,\mathrm{Eu}}^i(0)\left[1 - \left(\frac{T}{T_{\mathrm{Eu}}}\right)^{\gamma_1}\right]^{\delta_1} + \vec{B}_{\mu,\mathrm{SDW}}^i(0)\left[1 - \left(\frac{T}{T_{\mathrm{SDW}}}\right)^{\gamma_2}\right]^{\delta_2}, \qquad (3)$$

where $B_{\mu,\mathrm{Eu}}^i(0)$ and $B_{\mu,\mathrm{SDW}}^i(0)$ represent the zero-temperature values of the internal magnetic field probed by the muons in the Eu and in the SDW ordered states, respectively. γ and δ are empirical exponents. As indicated by the solid lines in Fig. 4 the function in Eq. (3) describes the data reasonably well, yielding the parameters given in Table 1. Note that with increasing x the values of T_{SDW} and $B_{\mu,\mathrm{SDW}}^1(0)$ decrease, and for $x = 0.2$ and $x = 1$ no long-range SDW order of the Fe moments is observed. On the other hand, T_{Eu} decreases with increasing x, reaches minimum at $x = 0.12$ and then increases again, in agreement with the above susceptibility measurements. In addition, $B_{\mu,\mathrm{Eu}}^1(0)$ significantly increases with x above $x = 0.12$. Considering the magnetization results, the increase of $B_{\mu,\mathrm{Eu}}^1(0)$ may be ascribed to the appearance/growth of the ferromagnetic component as a result of P substitution. However, without microscopic modeling (i.e., calculation of the μ stopping site and the dipolar fields at the μ site) it is not possible to conclude how a change of the magnetic structure with P substitution would affect the internal field at the muon site.

The temperature dependences of the transverse and longitudinal depolarization rates λ_T^1 and λ_L^1 are presented in Fig. 5(a) and (b), respectively. Note that λ_T^1 is much smaller for the end members $x = 0$, 1 of the investigated system than for the mixed compounds $x = 0.12$, 0.2. As shown in Fig. 5(a), for $x = 0$, 0.12, and 0.2, the onset of the Fe magnetic order is accompanied by an increase of λ_T^1 that decreases with decreasing temperature. Upon reaching the magnetic ordering temperature of Eu λ_T^1 shows another maximum. For $x = 1$, the strong increase of λ_T^1 around T_{Eu} is only due the Eu order. No SDW transition is observed at higher temperatures. The magnetic ordering temperatures of Eu (T_{Eu}) and Fe (T_{SDW}) are also clearly visible in the longitudinal relaxation rate λ_L^1, which also shows a clear anomaly

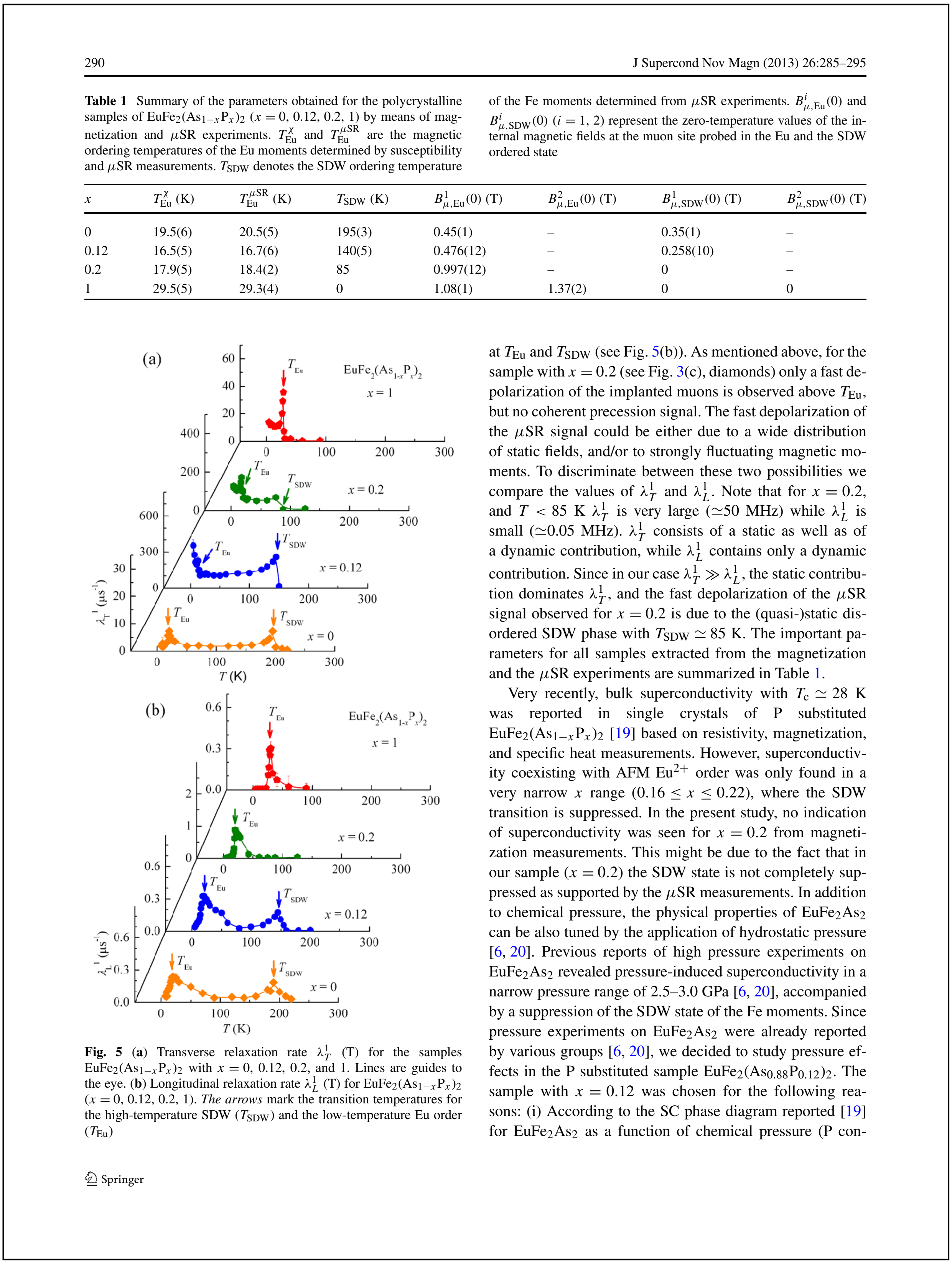

Table 1 Summary of the parameters obtained for the polycrystalline samples of $EuFe_2(As_{1-x}P_x)_2$ ($x = 0, 0.12, 0.2, 1$) by means of magnetization and μSR experiments. T_{Eu}^{χ} and $T_{Eu}^{\mu SR}$ are the magnetic ordering temperatures of the Eu moments determined by susceptibility and μSR measurements. T_{SDW} denotes the SDW ordering temperature of the Fe moments determined from μSR experiments. $B_{\mu,Eu}^{i}(0)$ and $B_{\mu,SDW}^{i}(0)$ ($i = 1, 2$) represent the zero-temperature values of the internal magnetic fields at the muon site probed in the Eu and the SDW ordered state

x	T_{Eu}^{χ} (K)	$T_{Eu}^{\mu SR}$ (K)	T_{SDW} (K)	$B_{\mu,Eu}^{1}(0)$ (T)	$B_{\mu,Eu}^{2}(0)$ (T)	$B_{\mu,SDW}^{1}(0)$ (T)	$B_{\mu,SDW}^{2}(0)$ (T)
0	19.5(6)	20.5(5)	195(3)	0.45(1)	–	0.35(1)	–
0.12	16.5(5)	16.7(6)	140(5)	0.476(12)	–	0.258(10)	–
0.2	17.9(5)	18.4(2)	85	0.997(12)	–	0	–
1	29.5(5)	29.3(4)	0	1.08(1)	1.37(2)	0	0

Fig. 5 (**a**) Transverse relaxation rate λ_T^1 (T) for the samples $EuFe_2(As_{1-x}P_x)_2$ with $x = 0, 0.12, 0.2$, and 1. Lines are guides to the eye. (**b**) Longitudinal relaxation rate λ_L^1 (T) for $EuFe_2(As_{1-x}P_x)_2$ ($x = 0, 0.12, 0.2, 1$). *The arrows* mark the transition temperatures for the high-temperature SDW (T_{SDW}) and the low-temperature Eu order (T_{Eu})

at T_{Eu} and T_{SDW} (see Fig. 5(b)). As mentioned above, for the sample with $x = 0.2$ (see Fig. 3(c), diamonds) only a fast depolarization of the implanted muons is observed above T_{Eu}, but no coherent precession signal. The fast depolarization of the μSR signal could be either due to a wide distribution of static fields, and/or to strongly fluctuating magnetic moments. To discriminate between these two possibilities we compare the values of λ_T^1 and λ_L^1. Note that for $x = 0.2$, and $T < 85$ K λ_T^1 is very large ($\simeq$50 MHz) while λ_L^1 is small ($\simeq$0.05 MHz). λ_T^1 consists of a static as well as of a dynamic contribution, while λ_L^1 contains only a dynamic contribution. Since in our case $\lambda_T^1 \gg \lambda_L^1$, the static contribution dominates λ_T^1, and the fast depolarization of the μSR signal observed for $x = 0.2$ is due to the (quasi-)static disordered SDW phase with $T_{SDW} \simeq 85$ K. The important parameters for all samples extracted from the magnetization and the μSR experiments are summarized in Table 1.

Very recently, bulk superconductivity with $T_c \simeq 28$ K was reported in single crystals of P substituted $EuFe_2(As_{1-x}P_x)_2$ [19] based on resistivity, magnetization, and specific heat measurements. However, superconductivity coexisting with AFM Eu^{2+} order was only found in a very narrow x range ($0.16 \le x \le 0.22$), where the SDW transition is suppressed. In the present study, no indication of superconductivity was seen for $x = 0.2$ from magnetization measurements. This might be due to the fact that in our sample ($x = 0.2$) the SDW state is not completely suppressed as supported by the μSR measurements. In addition to chemical pressure, the physical properties of $EuFe_2As_2$ can be also tuned by the application of hydrostatic pressure [6, 20]. Previous reports of high pressure experiments on $EuFe_2As_2$ revealed pressure-induced superconductivity in a narrow pressure range of 2.5–3.0 GPa [6, 20], accompanied by a suppression of the SDW state of the Fe moments. Since pressure experiments on $EuFe_2As_2$ were already reported by various groups [6, 20], we decided to study pressure effects in the P substituted sample $EuFe_2(As_{0.88}P_{0.12})_2$. The sample with $x = 0.12$ was chosen for the following reasons: (i) According to the SC phase diagram reported [19] for $EuFe_2As_2$ as a function of chemical pressure (P content x), the sample with $x = 0.12$ is close to the value of x at which superconductivity appears. By applying hydrostatic pressure, the SC phase might be reachable. (ii) Based on previous reports [6, 20], superconductivity was found in the vicinity of the pressure value where the SDW state is suppressed.

In the following sections, the results of the magnetization and the μSR experiments performed on $EuFe_2(As_{0.88}P_{0.12})_2$ under hydrostatic pressures are presented.

3.2 Hydrostatic Pressure Effect on $EuFe_2(As_{0.88}P_{0.12})_2$

3.2.1 High Pressure Magnetization Measurements

Magnetization measurements were carried out under hydrostatic pressures up to $p = 5.9$ GPa. The temperature dependence of the ZFC and FC magnetic susceptibilities χ for $EuFe_2(As_{0.88}P_{0.12})_2$ recorded at ambient and selected applied pressures is shown in Fig. 6(a) ($p \le 0.4$ GPa), in Fig. 6(b) (0.42 GPa $\le p \le$ 0.55 GPa), and in Fig. 6(c) (1.1 GPa $\le p \le$ 5.9 GPa). Note that Fig. 6 shows the data after subtraction of the background signal from the empty pressure cell. The magnetic ordering temperature T_{Eu} of the Eu^{2+} moments was determined as described in Sect. 3.1.2. At ambient pressure, a clear bifurcation between the ZFC and FC curves appears below $T_{Eu} \simeq 16.5$ K, which is consistent with the susceptibility data obtained for the sample without pressure cell (see Fig. 2). In addition, the magnitudes of the susceptibilities are also in fair agreement. Upon increasing the pressure, an anomaly in the ZFC susceptibility is observed at $p = 0.4$, 0.42, and 0.48 GPa as shown in Fig. 6(a) and (b). The low-temperature data for $p = 0.4$ GPa are shown in the inset of Fig. 6(a). In addition to the Eu order observed at $\simeq$18 K, a strong decrease of the ZFC susceptibility is observed at $\simeq$11 K, which is possibly due to the appearance of superconductivity. The decrease of the susceptibility corresponds to nearly 100 % diamagnetic shielding. In order to confirm superconductivity, transport measurements under pressure are necessary. Just magnetization data do not allow to conclude that the observed decrease of χ_{ZFC} is due to the appearance of superconductivity. Hence we call this phase "X". For $p = 0.42$ GPa, the susceptibility also shows a pronounced decrease at $T_X \simeq 20$ K (see Fig. 2(b), the low-temperature data are shown in the inset). Below $\simeq$18.2 K, the susceptibility starts to increase again due to the C-AFM ordering of the Eu^{2+} moments. Upon increasing the pressure to $p = 0.47$ GPa, the transition temperature T_X decreases to 8.8 K. Above $p = 0.55$ GPa, the "X" phase is no longer visible (see Fig. 6(c)). It is also absent for $p < 0.35$ GPa. Therefore, pressure-induced "X" phase in $EuFe_2(As_{0.88}P_{0.12})_2$ is very likely present in a very narrow pressure range. We observed that T_{Eu} increases upon increasing hydrostatic pressure, similar to chemical pressure. The maximum value of $T_{Eu} = 56$ K is reached at $p = 5.6$ GPa, and at higher pressures it tends to decrease (see Fig. 6(c)). For instance, $T_{Eu} = 53$ K at the maximum applied pressure $p = 5.9$ GPa. A maximum of T_{Eu} was also

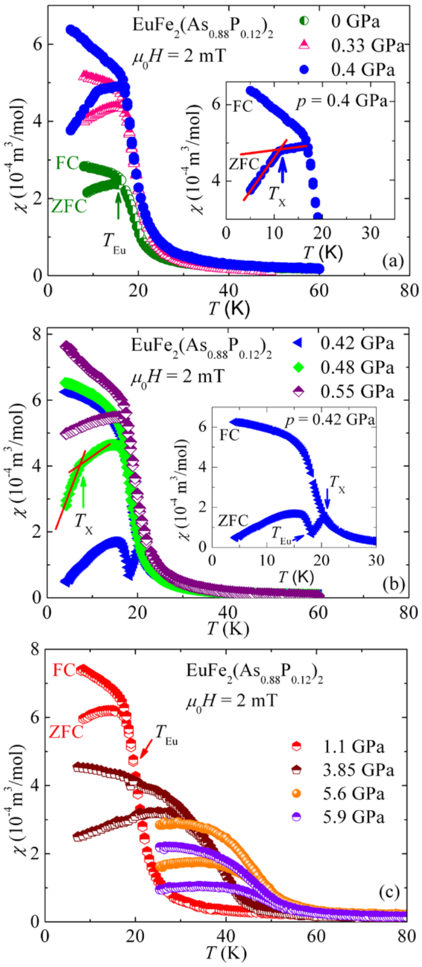

Fig. 6 Temperature dependence of the ZFC and FC magnetic susceptibility of $EuFe_2(As_{0.88}P_{0.12})_2$ in a magnetic field of $\mu_0 H = 2$ mT for $p \le 0.4$ GPa (**a**), for 0.42 GPa $\le p \le$ 0.55 GPa (**b**), and for 1.1 GPa $\le p \le$ 5.9 GPa (**c**). *The arrows* mark the ordering temperature of Eu moments (T_{Eu}) and the "X" transition temperatures (T_X). *The insets* of *panels* (**a**) and (**b**) show the low temperature data for $p = 0.4$ GPa and 0.42 GPa, respectively, illustrating the transition to the superconducting state marked by *the arrows*. *The solid lines* are guides to the eye

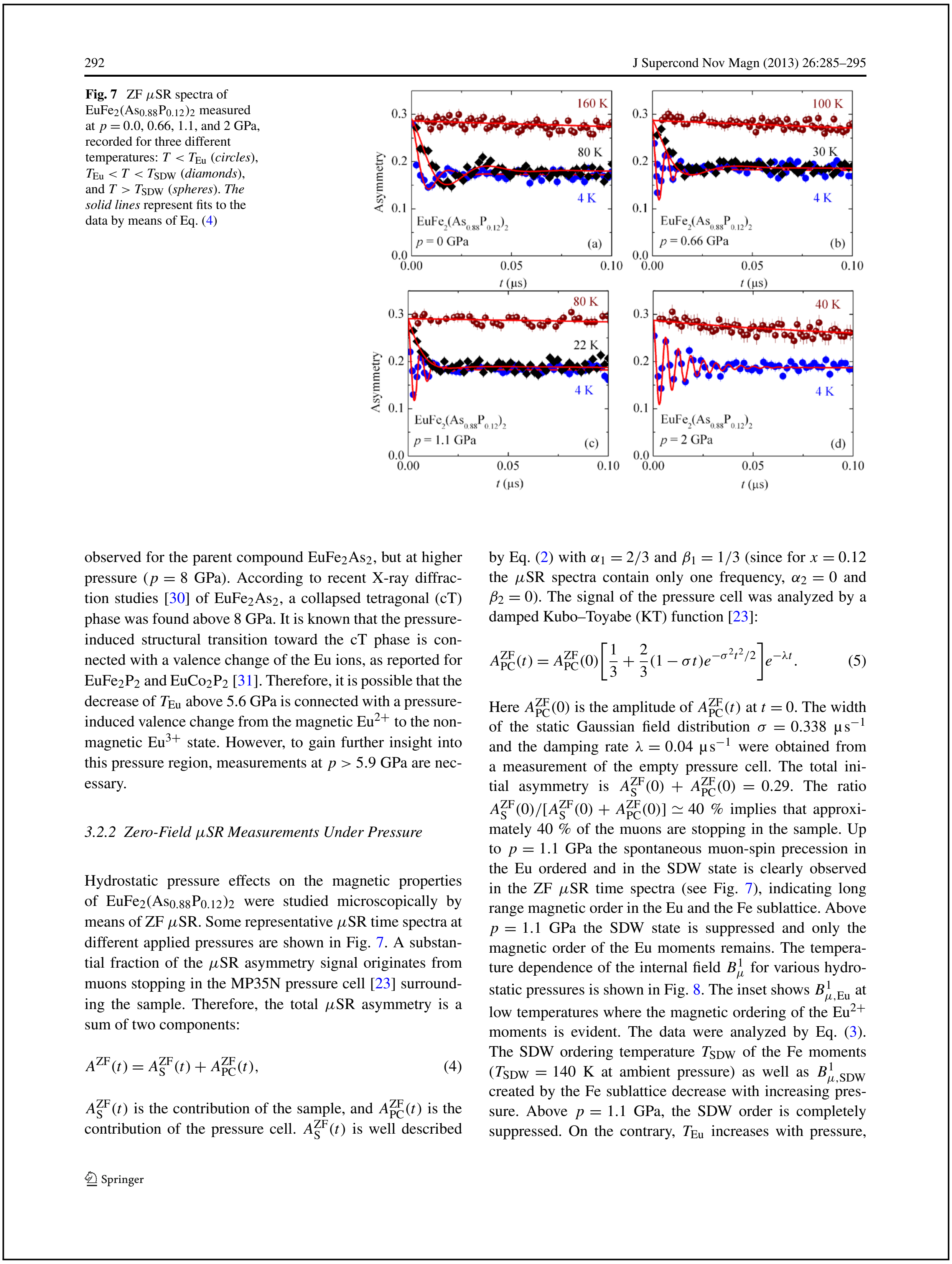

Fig. 7 ZF μSR spectra of $EuFe_2(As_{0.88}P_{0.12})_2$ measured at $p = 0.0$, 0.66, 1.1, and 2 GPa, recorded for three different temperatures: $T < T_{Eu}$ (*circles*), $T_{Eu} < T < T_{SDW}$ (*diamonds*), and $T > T_{SDW}$ (*spheres*). *The solid lines* represent fits to the data by means of Eq. (4)

observed for the parent compound $EuFe_2As_2$, but at higher pressure ($p = 8$ GPa). According to recent X-ray diffraction studies [30] of $EuFe_2As_2$, a collapsed tetragonal (cT) phase was found above 8 GPa. It is known that the pressure-induced structural transition toward the cT phase is connected with a valence change of the Eu ions, as reported for $EuFe_2P_2$ and $EuCo_2P_2$ [31]. Therefore, it is possible that the decrease of T_{Eu} above 5.6 GPa is connected with a pressure-induced valence change from the magnetic Eu^{2+} to the non-magnetic Eu^{3+} state. However, to gain further insight into this pressure region, measurements at $p > 5.9$ GPa are necessary.

3.2.2 *Zero-Field μSR Measurements Under Pressure*

Hydrostatic pressure effects on the magnetic properties of $EuFe_2(As_{0.88}P_{0.12})_2$ were studied microscopically by means of ZF μSR. Some representative μSR time spectra at different applied pressures are shown in Fig. 7. A substantial fraction of the μSR asymmetry signal originates from muons stopping in the MP35N pressure cell [23] surrounding the sample. Therefore, the total μSR asymmetry is a sum of two components:

$$A^{ZF}(t) = A^{ZF}_{S}(t) + A^{ZF}_{PC}(t), \tag{4}$$

$A^{ZF}_{S}(t)$ is the contribution of the sample, and $A^{ZF}_{PC}(t)$ is the contribution of the pressure cell. $A^{ZF}_{S}(t)$ is well described by Eq. (2) with $\alpha_1 = 2/3$ and $\beta_1 = 1/3$ (since for $x = 0.12$ the μSR spectra contain only one frequency, $\alpha_2 = 0$ and $\beta_2 = 0$). The signal of the pressure cell was analyzed by a damped Kubo–Toyabe (KT) function [23]:

$$A^{ZF}_{PC}(t) = A^{ZF}_{PC}(0)\left[\frac{1}{3} + \frac{2}{3}(1 - \sigma t)e^{-\sigma^2 t^2/2}\right]e^{-\lambda t}. \tag{5}$$

Here $A^{ZF}_{PC}(0)$ is the amplitude of $A^{ZF}_{PC}(t)$ at $t = 0$. The width of the static Gaussian field distribution $\sigma = 0.338\ \mu s^{-1}$ and the damping rate $\lambda = 0.04\ \mu s^{-1}$ were obtained from a measurement of the empty pressure cell. The total initial asymmetry is $A^{ZF}_{S}(0) + A^{ZF}_{PC}(0) = 0.29$. The ratio $A^{ZF}_{S}(0)/[A^{ZF}_{S}(0) + A^{ZF}_{PC}(0)] \simeq 40\ \%$ implies that approximately 40 % of the muons are stopping in the sample. Up to $p = 1.1$ GPa the spontaneous muon-spin precession in the Eu ordered and in the SDW state is clearly observed in the ZF μSR time spectra (see Fig. 7), indicating long range magnetic order in the Eu and the Fe sublattice. Above $p = 1.1$ GPa the SDW state is suppressed and only the magnetic order of the Eu moments remains. The temperature dependence of the internal field B^1_μ for various hydrostatic pressures is shown in Fig. 8. The inset shows $B^1_{\mu,Eu}$ at low temperatures where the magnetic ordering of the Eu^{2+} moments is evident. The data were analyzed by Eq. (3). The SDW ordering temperature T_{SDW} of the Fe moments ($T_{SDW} = 140$ K at ambient pressure) as well as $B^1_{\mu,SDW}$ created by the Fe sublattice decrease with increasing pressure. Above $p = 1.1$ GPa, the SDW order is completely suppressed. On the contrary, T_{Eu} increases with pressure, in agreement with the susceptibility measurements. In addition, $B^1_{\mu,\mathrm{Eu}}$ related to the Eu ordered state also increases with pressure. Note the sharp increase of $B^1_{\mu,\mathrm{Eu}}$ below T_{Eu} with increasing the pressure from $p = 0$ GPa to $p = 0.44$ GPa. For $p > 0.44$ GPa, a more smooth increase of $B^1_{\mu,\mathrm{Eu}}$ is observed. Relevant parameters of $\mathrm{EuFe_2(As_{0.88}P_{0.12})_2}$ extracted from the high pressure magnetization and μSR experiments are listed in Table 2.

As shown above the magnetization measurements indicate the presence of a possible SC phase in the pressure range 0.36 GPa $\leq p \leq$ 0.5 GPa. An attempt to detect it in the sample $\mathrm{EuFe_2(As_{0.88}P_{0.12})_2}$ with ZF and TF μSR, failed because of the strong intrinsic magnetism present in the sample.

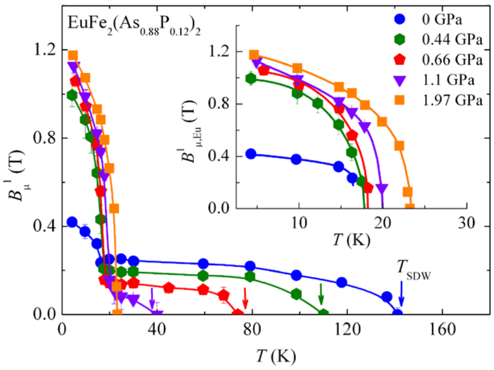

Fig. 8 Temperature dependence of the internal field B^1_μ at the muon site for the sample $\mathrm{EuFe_2(As_{0.88}P_{0.12})_2}$ recorded at various applied pressures. *The solid lines* represent fits to the data by means of Eq. (3). *The arrows* mark the ordering temperature T_{SDW}. *The inset* shows the low temperature data, illustrating the transition at T_{Eu} to the magnetically ordered state of the Eu moments

4 Phase Diagram

Figure 9(a) shows the $(x–T)$ phase diagram for the system $\mathrm{EuFe_2(As_{1-x}P_x)_2}$. The $(p–T)$ phase diagram of $\mathrm{EuFe_2(As_{0.88}P_{0.12})_2}$ is plotted in Fig. 9(b). The data for T_{Eu} represented by the triangles in Fig. 9(a) are taken from [25]. In the $(x–T)$ phase diagram, three different phases were identified: a paramagnetic phase (PM), spin-density wave order of the Fe moments (SDW), and magnetic order of $\mathrm{Eu^{2+}}$ moments (MO). Moreover, in the $(p–T)$ phase diagram, pressure-induced "X" phase was found (see the inset of Fig. 9(b)). In Fig. 10, the internal magnetic fields $B^1_{\mu,\mathrm{Eu}}$ and $B^1_{\mu,\mathrm{SDW}}$ probed by the muons in the Eu ordered and in the SDW state and the low temperature value of the magnetic susceptibility χ_{ZFC} (7 K) are plotted as a function of P content x and applied pressure p.

By combining the above phase diagrams, one obtains a coherent physical picture on the system $\mathrm{EuFe_2As_2}$ upon P substitution and on $\mathrm{EuFe_2(As_{0.88}P_{0.12})_2}$ under hydrostatic pressure. An important finding is the observation of pressure-induced "X" phase in $\mathrm{EuFe_2(As_{0.88}P_{0.12})_2}$, coexisting with magnetic order of the Eu and Fe moments. "X" phase appears in the narrow pressure region of 0.36–0.5 GPa. The presented phase diagrams in combination with the results obtained for the parent compound under pressure [6, 20] allow us to draw the following conclusion on

Table 2 Summary of the parameters obtained for the polycrystalline sample of $\mathrm{EuFe_2(As_{0.88}P_{0.12})_2}$ at different hydrostatic pressures by means of magnetization and μSR experiments. The meaning of the symbols is given in the text

p (GPa)	T^{χ}_{Eu} (K)	$T^{\mu\mathrm{SR}}_{\mathrm{Eu}}$ (K)	T_{X} (K)	$T^{\mu\mathrm{SR}}_{\mathrm{SDW}}$ (K)	$B^1_{\mu,\mathrm{Eu}}(0)$ (T)	$B^1_{\mu,\mathrm{SDW}}(0)$ (T)
0	16.5(5)	16.4(3)	–	141.2(1)	0.44(1)	0.25(1)
0.4	17.5(4)	–	11.2(3)	–	–	–
0.42	17.6(5)	–	20.3(3)	–	–	–
0.44	–	17.7(3)	-	110(1)	0.99(2)	0.19(2)
0.48	17.9(4)	–	7.3(3)	–	–	–
0.66	18.9(5)	18.4(6)	0	75(2)	1.07(5)	0.17(4)
1.1	20.5(5)	19.9(7)	0	40(3)	1.27(3)	0.12(2)
1.73	24.6(3)	–	0	–	–	–
1.97	24.4(5)	23.6(7)	0	0	1.23(2)	0
2.5	27.2(3)	–	0	–	–	–
3.85	35.8(5)	–	0	–	–	–
4.54	42.5(4)	–	0	–	–	–
5.1	49.5(3)	–	0	–	–	–
5.6	57(4)	–	0	–	–	–
5.9	53(5)	–	0	–	–	–

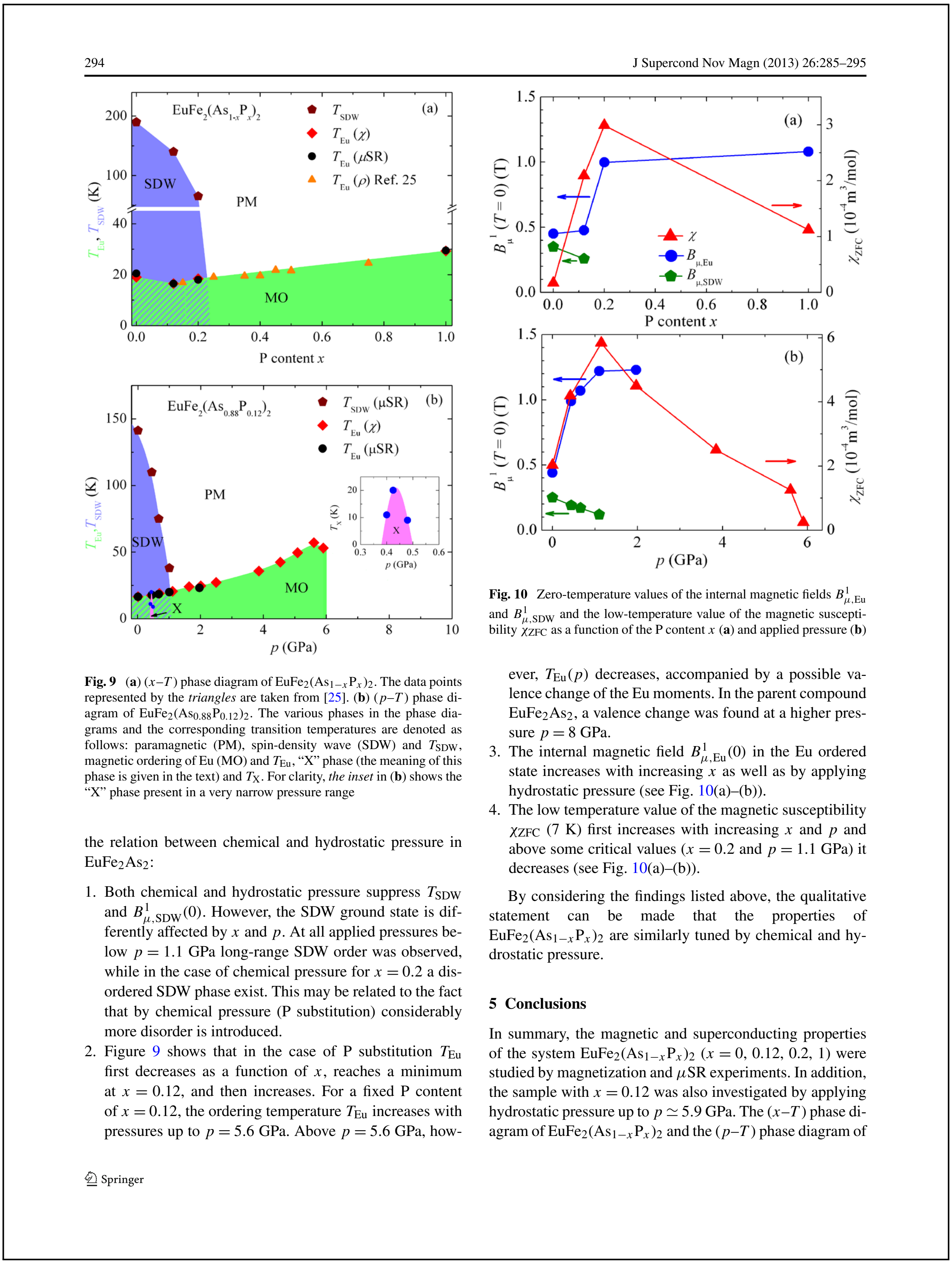

Fig. 9 (**a**) (x–T) phase diagram of EuFe$_2$(As$_{1-x}$P$_x$)$_2$. The data points represented by the *triangles* are taken from [25]. (**b**) (p–T) phase diagram of EuFe$_2$(As$_{0.88}$P$_{0.12}$)$_2$. The various phases in the phase diagrams and the corresponding transition temperatures are denoted as follows: paramagnetic (PM), spin-density wave (SDW) and T_{SDW}, magnetic ordering of Eu (MO) and T_{Eu}, "X" phase (the meaning of this phase is given in the text) and T_X. For clarity, *the inset* in (**b**) shows the "X" phase present in a very narrow pressure range

Fig. 10 Zero-temperature values of the internal magnetic fields $B^1_{\mu,Eu}$ and $B^1_{\mu,SDW}$ and the low-temperature value of the magnetic susceptibility χ_{ZFC} as a function of the P content x (**a**) and applied pressure (**b**)

the relation between chemical and hydrostatic pressure in EuFe$_2$As$_2$:

1. Both chemical and hydrostatic pressure suppress T_{SDW} and $B^1_{\mu,SDW}(0)$. However, the SDW ground state is differently affected by x and p. At all applied pressures below $p = 1.1$ GPa long-range SDW order was observed, while in the case of chemical pressure for $x = 0.2$ a disordered SDW phase exist. This may be related to the fact that by chemical pressure (P substitution) considerably more disorder is introduced.
2. Figure 9 shows that in the case of P substitution T_{Eu} first decreases as a function of x, reaches a minimum at $x = 0.12$, and then increases. For a fixed P content of $x = 0.12$, the ordering temperature T_{Eu} increases with pressures up to $p = 5.6$ GPa. Above $p = 5.6$ GPa, however, $T_{Eu}(p)$ decreases, accompanied by a possible valence change of the Eu moments. In the parent compound EuFe$_2$As$_2$, a valence change was found at a higher pressure $p = 8$ GPa.
3. The internal magnetic field $B^1_{\mu,Eu}(0)$ in the Eu ordered state increases with increasing x as well as by applying hydrostatic pressure (see Fig. 10(a)–(b)).
4. The low temperature value of the magnetic susceptibility χ_{ZFC} (7 K) first increases with increasing x and p and above some critical values ($x = 0.2$ and $p = 1.1$ GPa) it decreases (see Fig. 10(a)–(b)).

By considering the findings listed above, the qualitative statement can be made that the properties of EuFe$_2$(As$_{1-x}$P$_x$)$_2$ are similarly tuned by chemical and hydrostatic pressure.

5 Conclusions

In summary, the magnetic and superconducting properties of the system EuFe$_2$(As$_{1-x}$P$_x$)$_2$ ($x = 0$, 0.12, 0.2, 1) were studied by magnetization and μSR experiments. In addition, the sample with $x = 0.12$ was also investigated by applying hydrostatic pressure up to $p \simeq 5.9$ GPa. The (x–T) phase diagram of EuFe$_2$(As$_{1-x}$P$_x$)$_2$ and the (p–T) phase diagram of

$EuFe_2(As_{0.88}P_{0.12})_2$ were determined and discussed as well as compared to the $(p–T)$ phase diagram recently obtained for $EuFe_2As_2$ [6, 20]. The present investigations reveal that the magnetic coupling between the Eu and the Fe sublattices strongly depends on chemical and hydrostatic pressure and determines the $(x–T)$ and $(p–T)$ phase diagrams as presented in this work. According to the above discussed phase diagrams, chemical and hydrostatic pressures have qualitatively a similar effect on the Fe and Eu magnetic order.

There are still some open questions related to superconductivity and its interplay with the magnetic ground state of the system $EuFe_2As_2$. One of the most interesting aspects of this particular member of Fe-based superconductors is the possibility to observe coexistence or competition between superconductivity and rare-earth Eu magnetic order. In the present work, the so-called “X” phase induced by pressure was observed in $EuFe_2(As_{0.88}P_{0.12})_2$ in addition to the magnetic phases of the Eu and Fe sublattices. It exists in a narrow pressure range 0.36–0.5 GPa. This phase is possibly superconducting. However, transport measurements as a function of pressure are required in order to clarify this point.

Acknowledgements This work was supported by the Swiss National Science Foundation, the SCOPES grant No. IZ73Z0_128242, and the NCCR Project MaNEP. The μSR experiments were performed at the Swiss Muon Source of the Paul Scherrer Institute (PSI), Villigen, Switzerland.

References

1. Kamihara, Y., Watanabe, T., Hirano, M., Hosono, H.: J. Am. Chem. Soc. **130**, 3296 (2008)
2. Rotter, M., Tegel, M., Johrendt, D.: Phys. Rev. Lett. **101**, 107006 (2008)
3. Chen, X.H., Wu, T., Wu, G., Liu, R.H., Chen, H., Fang, D.F.: Nature (London) **453**, 761 (2008)
4. Torikachvili, M.S., Bud’ko, S.L., Ni, N., Canfield, P.C.: Phys. Rev. Lett. **101**, 057006 (2008)
5. Fukazawa, H., Takeshita, N., Yamazaki, T., Kondo, K., Hirayama, K., Kohori, Y., Miyazawa, K., Kito, H., Eisaki, H., Iyo, A.: J. Phys. Soc. Jpn. **77**, 105004 (2008)
6. Terashima, T., Kimata, M., Satsukawa, H., Harada, A., Hazama, K., Uji, S., Suzuki, H.S., Matsumoto, T., Murata, K.: J. Phys. Soc. Jpn. **78**, 083701 (2009)
7. Ren, Z.A., Lu, W., Yang, J., Yi, W., Shen, X.L., Li, Z.C., Che, G.C., Dong, X.L., Sun, L.L., Zhou, F., Zhao, Z.X.: Chin. Phys. Lett. **25**, 2215 (2008)
8. Matsuishi, S., Inoue, Y., Nomura, T., Hirano, M., Hosono, H.: J. Phys. Soc. Jpn. **77**, 113709 (2008)
9. Zhao, J., Huang, Q., de la Cruz, C., Li, S., Lynn, J.W., Chen, Y., Green, M.A., Chen, G.F., Li, G., Li, Z., Luo, J.L., Wang, N.L., Dai, P.: Nat. Mater. **7**, 953 (2008)
10. Raffius, H., Mörsen, M., Mosel, B.D., Müller-Warmuth, W., Jeitschko, W., Terbüchte, L., Vomhof, T.: J. Phys. Chem. Solids **54**, 135 (1993)
11. Xiao, Y., Su, Y., Meven, M., Mittal, R., Kumar, C.M.N., Chatterji, T., Price, S., Persson, J., Kumar, N., Dhar, S.K., Thamizhavel, A., Brueckel, T.: Phys. Rev. B **80**, 174424 (2009)
12. Jiang, S., Luo, Y.K., Ren, Z., Zhu, Z.W., Wang, C., Xu, X.F., Tao, Q., Cao, G.H., Xu, Z.A.: New J. Phys. **11**, 025007 (2009)
13. Guguchia, Z., Roos, J., Shengelaya, A., Katrych, S., Bukowski, Z., Weyeneth, S., Murányi, F., Strässle, S., Maisuradze, A., Karpinski, J., Keller, H.: Phys. Rev. B **83**, 144516 (2011)
14. Sefat, A.S., Jin, R., McGuire, M.A., Sales, B.C., Singh, D.J., Mandrus, D.: Phys. Rev. Lett. **101**, 117004 (2008)
15. Leithe-Jasper, A., Schnelle, W., Geibel, C., Rosner, H.: Phys. Rev. Lett. **101**, 207004 (2008)
16. He, Y., Wu, T., Wu, G., Zheng, Q.J., Liu, Y.Z., Chen, H., Ying, J.J., Liu, R.H., Wang, X.F., Xie, Y.L., Yan, Y.J., Dong, J.K., Li, S.Y., Chen, X.H.: J. Phys. Condens. Matter **22**, 235701 (2010)
17. Li, L.J., Luo, Y.K., Wang, Q.B., Chen, H., Ren, Z., Tao, Q., Li, Y.K., Lin, X., He, M., Zhu, Z.W., Cao, G.H., Xu, Z.A.: New J. Phys. **11**, 025008 (2008)
18. Ren, Z.: Phys. Rev. B **79**, 094426 (2009)
19. Jeevan, H.S., Kasinathan, D., Rosner, H., Gegenwart, P.: Phys. Rev. B **83**, 054511 (2011)
20. Matsubayashi, K., Munakata, K., Isobe, M., Katayama, N., Ohgushi, K., Ueda, Y., Uwatoko, Y., Kawamura, N., Mizumaki, M., Ishimatsu, N., Hedo, M., Umehara, I.: Phys. Rev. B **84**, 024502 (2011)
21. Guguchia, Z., Bosma, S., Weyeneth, S., Shengelaya, A., Puzniak, R., Bukowski, Z., Karpinski, J., Keller, H.: Phys. Rev. B **84**, 144506 (2011)
22. Rodrígues-Carvajal, J.: Physica B **192**, 55 (1993)
23. Andreica, D.: Ph.D. Thesis, IPP/ETH-Zürich (2001)
24. Suter, A., Wojek, B.M.: Phys. Procedia **30**, 69–73 (2012)
25. Cao, G., Xu, S., Ren, Z., Jiang, S., Feng, C., Xu, Z.: J. Phys. Condens. Matter **23**, 464204 (2011) (5 pp.)
26. Zapf, S., Wu, D., Bogani, L., Jeevan, H.S., Gegenwart, P., Dressel, M.: Phys. Rev. B **84**, 140503(R) (2011)
27. Ryan, D.H., Cadogan, J.M., Xu, S., Xu, Z., Cao, G.: Phys. Rev. B **83**, 132403 (2011)
28. Maeter, H., Luetkens, H., Pashkevich, Yu.G., Kwadrin, A., Khasanov, R., Amato, A., Gusev, A.A., Lamonova, K.V., Chervinskii, D.A., Klingeler, R., Hess, C., Behr, G., Büchner, B., Klauss, H.H.: Phys. Rev. B **80**, 094524 (2009)
29. Jesche, A., Caroca-Canales, N., Rosner, H., Borrmann, H., Ormeci, A., Kasinathan, D., Klauss, H.H., Luetkens, H., Khasanov, R., Amato, A., Hoser, A., Kaneko, K., Krellner, C., Geibel, C.: Phys. Rev. B **78**, 180504(R) (2008)
30. Uhoya, W., Tsoi, G., Vohra, Y.K., McGuire, M.A., Sefat, A.S., Sales, B.C., Mandrus, D., Weir, S.T.: J. Phys. Condens. Matter **22**, 292202 (2010)
31. Ni, B., Abd-Elmeguid, M.M., Micklitz, H., Sanchez, J.P., Vulliet, P., Johrendt, D.: Phys. Rev. B **63**, 100102 (2001)

4.4.4 Publication IV: Muon-spin rotation measurements of the magnetic penetration depth in the iron-based superconductor $Ba_{1-x}Rb_xFe_2As_2$

Z. Guguchia, Z. Shermadini, A. Amato, A. Maisuradze, A. Shengelaya, Z. Bukowski, H. Luetkens, R. Khasanov, J. Karpinski, and H. Keller
Phys. Rev. B **84**, 094513 (2011).

Abstract

Measurements of the magnetic penetration depth λ in the Fe-based superconductor $Ba_{1-x}Rb_x Fe_2As_2$ ($x = 0.3$, 0.35, 0.4) were carried out using the muon-spin rotation (μSR) technique. The temperature dependence of λ is well described by a two-gap s+s-wave scenario with a small gap $\Delta_1 \approx 1$ - 3 meV and a large gap $\Delta_2 \approx 7$ - 9 meV. By combining the present data with those previously obtained for $RbFe_2As_2$ a decrease of the BCS ratio $2\Delta_2/k_BT_c$ with increasing Rb content x is observed. On the other hand, the BCS ratio $2\Delta_1/k_BT_c$ is almost independent of x. In addition, the contribution of Δ_1 to the superfluid density is found to increase with x. These results are discussed in the light of the suppression of interband processes upon hole doping.

DOI: 10.1103/PhysRevB.84.094513
PACS numbers: 74.20.Mn, 74.25.Ha, 74.70.Xa, 76.75.+i

The original publication is electronically available at:
http://link.aps.org/doi/10.1103/PhysRevB.84.094513

PHYSICAL REVIEW B **84**, 094513 (2011)

Muon-spin rotation measurements of the magnetic penetration depth in the iron-based superconductor $Ba_{1-x}Rb_xFe_2As_2$

Z. Guguchia,[1,*] Z. Shermadini,[2] A. Amato,[2] A. Maisuradze,[1,2] A. Shengelaya,[3] Z. Bukowski,[4,5]
H. Luetkens,[2] R. Khasanov,[2] J. Karpinski,[4] and H. Keller[1]
[1]*Physik-Institut der Universität Zürich, Winterthurerstrasse 190, CH-8057 Zürich, Switzerland*
[2]*Laboratory for Muon Spin Spectroscopy, Paul Scherrer Institute, CH-5232 Villigen PSI, Switzerland*
[3]*Department of Physics, Tbilisi State University, Chavchavadze 3, GE-0128 Tbilisi, Georgia*
[4]*Laboratory for Solid State Physics, ETH Zürich, CH-8093 Zürich, Switzerland*
[5]*Institute of Low Temperature and Structure Research, Polish Academy of Sciences, 50-422 Wroclaw, Poland*
(Received 13 June 2011; published 14 September 2011)

Measurements of the magnetic penetration depth λ in the Fe-based superconductor $Ba_{1-x}Rb_xFe_2As_2$ ($x = 0.3$, 0.35, 0.4) were carried out using the muon-spin rotation (μSR) technique. The temperature dependence of λ is well described by a two-gap $s + s$-wave scenario with a small gap $\Delta_1 \approx$ 1–3 meV and a large gap $\Delta_2 \approx$ 7–9 meV. By combining the present data with those previously obtained for $RbFe_2As_2$ a decrease of the BCS ratio $2\Delta_2/k_BT_c$ with increasing Rb content x is observed. On the other hand, the BCS ratio $2\Delta_1/k_BT_c$ is almost independent of x. In addition, the contribution of Δ_1 to the superfluid density is found to increase with x. These results are discussed in light of the suppression of interband processes upon hole doping.

DOI: 10.1103/PhysRevB.84.094513 PACS number(s): 74.20.Mn, 74.25.Ha, 74.70.Xa, 76.75.+i

I. INTRODUCTION

The discovery[1] of superconductivity in iron oxypnictide $LaFeAsO_{1-x}F_x$ has generated great interest in the phenomenon of high temperature superconductivity. The basic units responsible for superconductivity are the fluorite type $[Fe_2Pn_2]$ layers where Pn is a pnictogen element (P, As, Sb, and Bi). These layers are separated by spacer layers which play the role of a charge reservoir. In the fluorite-type layers the Fe atoms are surrounded by four pnictogen atoms forming a tetrahedron. The first class of iron-based superconductors studied has the ZrCuSiAs structure (1111 compounds), where the spacer layer $[Ln_2O_2]$ has the "antifluoride" or Pb_2O_2 structure. With $Ln =$ Sm a critical temperature higher than 55 K was observed.[2]

Superconductivity with $T_c = 38$ K was also found in the ternary systems AFe_2As_2 (Refs. 3 and 4) (122 compounds) adopting the tetragonal $ThCr_2Si_2$ structure. In this structure the spacer layer is provided by an alkali earth element $A =$ Ca, Sr, or Ba. Doping is realized by the substitution of A by an alkali metal such as K, Cs, or Rb. Several disconnected Fermi-surface sheets contribute to superconductivity as revealed by angle-resolved photoemission spectroscopy (ARPES).[5–7] Moreover, indications of multigap superconductivity in the system $Ba_{1-x}K_xFe_2As_2$ were obtained from the temperature dependence of the magnetic penetration depth λ by means of muon-spin rotation (μSR)[8] and ARPES.[5] The magnetic penetration depth is one of the fundamental parameters of a superconductor since it is closely related to the density of the superconducting carriers n_s and their effective mass m^* via the relation $1/\lambda^2 \propto n_s/m^*$. The temperature dependence of λ reflects the topology of the superconducting gap occurring in the density of states of the superconducting ground state. The μSR technique provides a powerful tool to measure λ in type II superconductors.[9]

As demonstrated in previous works,[4,10] the value of T_c for hole-doped $Ba_{1-x}Rb_xFe_2As_2$ decreases monotonically upon increasing the Rb content x in the overdoped region. However, in contrast to the overdoped cuprates, T_c remains finite even at the highest doping level $x = 1$ with $T_c = 2.52$ K (Ref. 4). A detailed study of the doping dependence of T_c may help to clarify the origin of high-T_c superconductivity in these iron-based systems. It is thus of importance to investigate the superconducting properties of optimally doped $Ba_{1-x}Rb_xFe_2As_2$ and compare the results with those obtained for $RbFe_2As_2$ (Ref. 10).

In this paper, we report on μSR studies of the temperature and field dependence of the magnetic penetration depth of optimally doped $Ba_{1-x}Rb_xFe_2As_2$ ($x = 0.3, 0.35, 0.4$). We compare the present data with the previous results of overdoped $RbFe_2As_2$ (Ref. 10) and discuss the combined results in light of the suppression of interband processes upon hole doping.

II. EXPERIMENTAL DETAILS

Polycrystalline samples of $Ba_{1-x}Rb_xFe_2As_2$ were prepared in evacuated quartz ampoules by a solid state reaction method. Fe_2As, BaAs, and RbAs were obtained by reacting high purity As (99.999%), Fe (99.9%), Ba (99.9%), and Rb (99.95%) at 800 °C, 650 °C, and 500 °C, respectively. Using stoichiometric amounts of BaAs or RbAs and Fe_2As the terminal compounds $BaFe_2As_2$ and $RbFe_2As_2$ were synthesized at 950 °C and 650 °C, respectively. Finally, the samples of $Ba_{1-x}Rb_xFe_2As_2$ with $x = 0.3, 0.35, 0.4$ were prepared from appropriate amounts of single-phase $BaFe_2As_2$ and $RbFe_2As_2$. The components were mixed, pressed into pellets, placed into alumina crucibles, and annealed for 100 hours at 650 °C with one intermittent grinding. Powder x-ray diffraction analysis revealed that the synthesized samples are single phase materials. Zero-field (ZF) and transverse-field (TF) μSR experiments were performed at the πM3 beamline of the Paul Scherrer Institute (Villigen, Switzerland), using the general purpose instrument (GPS). The sample was mounted inside of a gas-flow ^{4}He cryostat on a sample holder with a standard veto setup providing essentially a low-background

μSR signal. All TF experiments were carried out after a field-cooling procedure.

III. RESULTS AND DISCUSSION

Figures 1(a) and 1(b) exhibit the transverse-field (TF) muon-time spectra for $Ba_{1-x}Rb_xFe_2As_2$ ($x = 0.3$, 0.4) measured in an applied magnetic field of $\mu_0 H = 0.04$ T above (45 K) and below (1.7 K) the superconducting (SC) transition temperature T_c. Above T_c the oscillations show a small relaxation due to the random local fields from the nuclear magnetic moments. Below T_c the relaxation rate strongly increases due to the presence of a nonuniform local field distribution as a result of the formation of a flux-line lattice (FLL) in the SC state. It is well known that undoped $BaFe_2As_2$ is not superconducting at ambient pressure and undergoes a spin-density wave (SDW) transition of the Fe moments far above T_c (Ref. 11). The SC state can be achieved either under pressure[12,13] or by appropriate charge carrier doping[14] of the parent compounds, leading to a suppression of the SDW state. Magnetism, if present in the samples, may enhance the muon depolarization rate and falsify the interpretation of the TF-μSR results. Therefore, we have carried out ZF-μSR experiments above and below T_c to search for magnetism (static or fluctuating) in $Ba_{1-x}Rb_xFe_2As_2$ ($x = 0.3, 0.35, 0.4$). As shown in Fig. 2(a) no sign of either static or fluctuating magnetism could be detected in ZF time spectra down to 1.7 K. Moreover, the ZF relaxation rate is small and changes very little between 45 and 1.7 K. The spectra are well described by a standard Kubo-Toyabe depolarization function,[15] reflecting the field distribution at the muon site created by the nuclear moments.

It was reported[16–18] that in some iron-based superconductors $BaFe_{2-x}Co_xAs_2$ and $SrFe_{2-x}Co_xAs_2$ field induced magnetism exists. In the present work TF-μSR spectra measured in different applied fields (see Fig. 1 for $\mu_0 H = 0.04$ T) exhibit a Gaussian-like depolarization above and below T_c that is typical of nuclear moments and the vortex lattice in polycrystalline samples, respectively. In the presence of dilute or fast fluctuating electronic moments one expects an

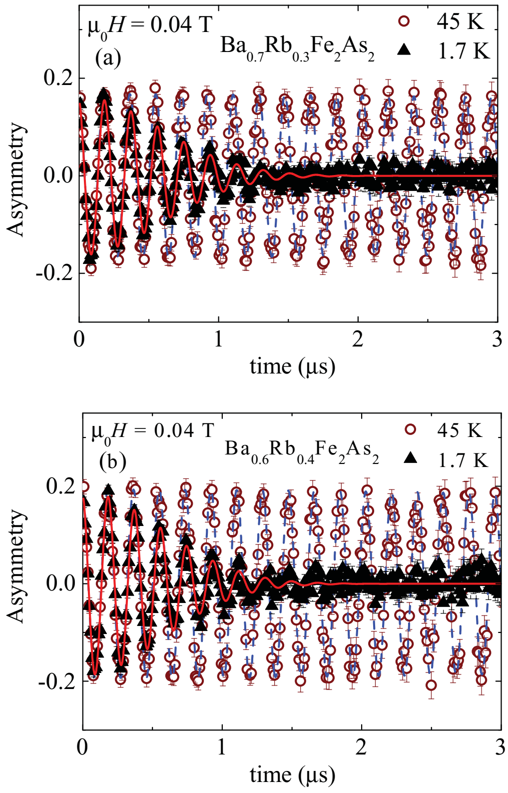

FIG. 1. (Color online) Transverse field (TF) μSR time spectra obtained in $\mu_0 H = 0.04$ T above and below T_c (after field cooling the sample from above T_c): (a) $Ba_{0.7}Rb_{0.3}Fe_2As_2$ and (b) $Ba_{0.6}Rb_{0.4}Fe_2As_2$. The solid and the dashed lines represent fits to the data by means of Eq. (1).

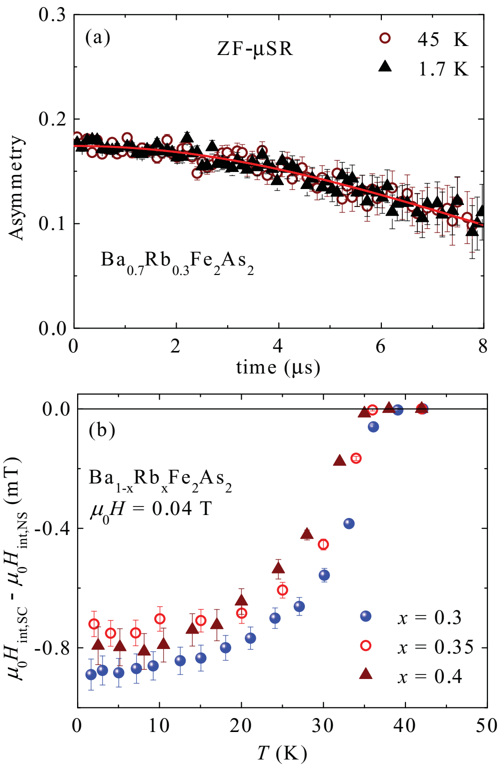

FIG. 2. (Color online) (a) ZF-μSR time spectra for $Ba_{0.7}Rb_{0.3}Fe_2As_2$ recorded above and below T_c. The line represents the fit to the data of a standard Kubo-Toyabe depolarization function (Ref. 15). (b) Temperature dependence of the difference between the internal field $\mu_0 H_{int,SC}$ measured in the SC state and the one measured in the normal state $\mu_0 H_{int,NS}$ at $T = 42$ K.

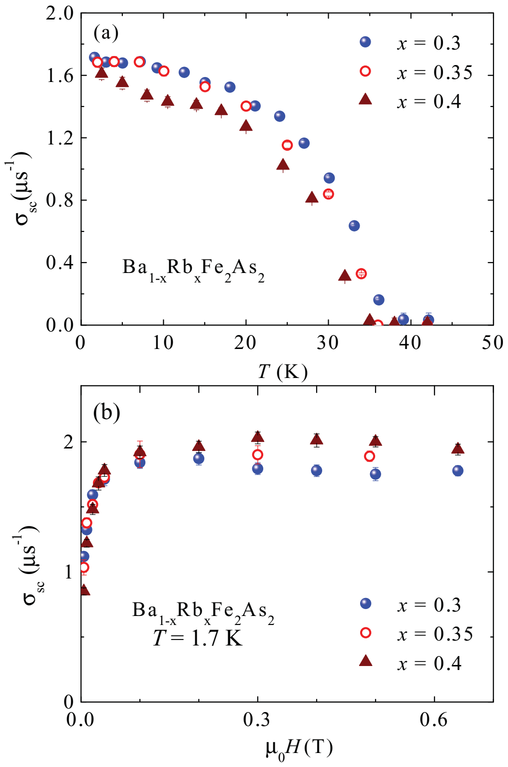

FIG. 3. (Color online) (a) Temperature dependence of the superconducting muon spin depolarization rate $\sigma_{\rm sc}$ measured in an applied magnetic field of $\mu_0 H = 0.04$ T for $\rm Ba_{1-x}Rb_xFe_2As_2$ ($x = 0.3, 0.35, 0.4$). (b) Field dependence of $\sigma_{\rm sc}$ at 1.7 K.

exponential depolarization of the TF-μSR spectrum, which is absent in the present case. Moreover, the SC muon depolarization rate $\sigma_{\rm sc}$ is constant at high fields as shown in Fig. 3(b). In addition we observed a diamagnetic shift of the internal magnetic field $\mu_0 H_{\rm int}$ sensed by the muons below $T_{\rm c}$. This is evident in Fig. 2(b), where we plot the difference between the internal field $\mu_0 H_{\rm int,SC}$ measured in the SC state and one $\mu_0 H_{\rm int,NS}$ measured in the normal state at $T = 42$ K. Note, that in the systems $\rm BaFe_{2-x}Co_xAs_2$ and $\rm SrFe_{2-x}Co_xAs_2$, where the field induced magnetism was detected, paramagnetic shift was observed[16–18] instead of the expected diamagnetic shift imposed by the SC state. All these observations indicate that there is no field induced magnetism in the system $\rm Ba_{1-x}Rb_xFe_2As_2$ down to 1.7 K. The absence of magnetism in $\rm Ba_{1-x}Rb_xFe_2As_2$ implies that the increase of the TF relaxation rate below $T_{\rm c}$ is attributed entirely to the vortex lattice.

The TF μSR data were analyzed by using the following functional form:[19]

$$P(t) = A \exp\left[-\frac{(\sigma_{\rm sc}^2 + \sigma_{\rm nm}^2)t^2}{2}\right] \cos(\gamma_\mu B_{\rm int} t + \varphi). \quad (1)$$

Here A denotes the initial asymmetry, $\gamma/(2\pi) \simeq 135.5$ MHz/T is the muon gyromagnetic ratio, and φ is the initial phase of the muon-spin ensemble. $B_{\rm int}$ represents the internal magnetic field at the muon site, and the relaxation rates $\sigma_{\rm sc}$ and $\sigma_{\rm nm}$ characterize the damping due to the formation of the FLL in the superconducting state and of the nuclear magnetic dipolar contribution, respectively. In the analysis $\sigma_{\rm nm}$ was assumed to be constant over the entire temperature range and was fixed to the value obtained above $T_{\rm c}$ where only nuclear magnetic moments contribute to the muon depolarization rate σ. As indicated by the solid lines in Fig. 1, the μSR data are well described by Eq. (1). The temperature dependence of $\sigma_{\rm sc}$ for $\rm Ba_{1-x}Rb_xFe_2As_2$ ($x = 0.3$, 0.35, and 0.4) at $\mu_0 H = 0.04$ T is shown in Fig. 3(a). Below $T_{\rm c}$ the relaxation rate $\sigma_{\rm sc}$ starts to increase from zero due to the formation of the FLL.

For polycrystalline samples the temperature dependence of the London magnetic penetration depth $\lambda(T)$ is related to the superconducting part of the Gaussian muon spin depolarization rate $\sigma_{\rm sc}(T)$ by the equation[20]

$$\frac{\sigma_{\rm sc}^2(T)}{\gamma_\mu^2} = 0.00371 \frac{\Phi_0^2}{\lambda^4(T)}, \quad (2)$$

where $\Phi_0 = 2.068 \times 10^{-15}$ Wb is the magnetic-flux quantum. Equation (2) is only valid when the separation between the vortices is smaller than λ. In this case, according to the London model $\sigma_{\rm sc}$ is field independent.[20] We measured $\sigma_{\rm sc}$ as a function of the applied field at 1.7 K (see Fig. 3(b)). Each point was obtained by field cooling the sample from above $T_{\rm c}$ to 1.7 K. First, $\sigma_{\rm sc}$ strongly increases with increasing magnetic field until reaching a maximum at $\mu_0 H \simeq 0.03$ T and then above 0.03 T stays nearly constant up to the highest field (0.64 T) investigated. Such a behavior is expected within the London model and is typical for polycrystalline high temperature superconductors (HTS's).[21] The observed field dependence of $\sigma_{\rm sc}$ implies that for a reliable determination of the penetration depth the applied field must be larger than $\mu_0 H = 0.03$ T.

$\lambda(T)$ can be calculated within the local (London) approximation ($\lambda \gg \xi$) by the following expression:[19,22]

$$\frac{\lambda^{-2}(T,\Delta_{0,i})}{\lambda^{-2}(0,\Delta_{0,i})} = 1 + \frac{1}{\pi} \int_0^{2\pi} \int_{\Delta(T,\varphi)}^{\infty} \left(\frac{\partial f}{\partial E}\right) \frac{E\,dE\,d\varphi}{\sqrt{E^2 - \Delta_i(T,\varphi)^2}}, \quad (3)$$

where $f = [1 + \exp(E/k_{\rm B}T)]^{-1}$ is the Fermi function, φ is the angle along the Fermi surface, and $\Delta_i(T,\varphi) = \Delta_{0,i}\delta(T/T_{\rm c})g(\varphi)$ ($\Delta_{0,i}$ is the maximum gap value at $T = 0$). The temperature dependence of the gap is approximated by the expression $\delta(T/T_{\rm c}) = \tanh\{1.82[1.018(T_{\rm c}/T - 1)]^{0.51}\}$ (Ref. 23), while $g(\varphi)$ describes the angular dependence of the gap and it is replaced by 1 for both an s-wave and an $s+s$-wave gap, and $|\cos(2\varphi)|$ for a d-wave gap.[24]

The temperature dependence of the penetration depth was analyzed using either a single gap or a two-gap model which is based on the so-called α model. This model was first discussed by Padamsee *et al.*[25] and later on was successfully used to analyze the magnetic penetration depth data in HTS's.[23,26] According to the α model, the superfluid density is calculated

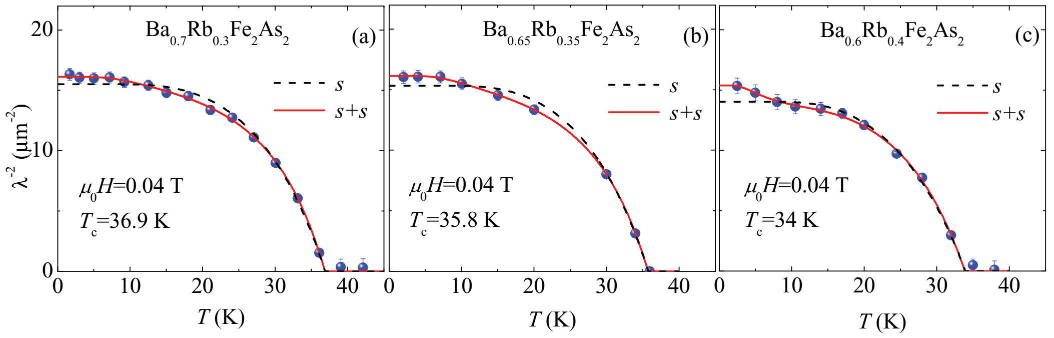

FIG. 4. (Color online) The temperature dependence of λ^{-2} for $Ba_{1-x}Rb_xFe_2As_2$, measured in an applied field of $\mu_0 H = 0.04$ T: (a) $x = 0.3$, (b) $x = 0.35$, and (c) $x = 0.4$. The dashed lines correspond to a single gap BCS s-wave model, whereas the solid ones represent a fit using a two-gap ($s + s$)-wave model.

for each component using Eq. (3) and then the contributions from the two components added together

$$\frac{\lambda^{-2}(T)}{\lambda^{-2}(0)} = \omega_1 \frac{\lambda^{-2}(T,\Delta_{0,1})}{\lambda^{-2}(0,\Delta_{0,1})} + \omega_2 \frac{\lambda^{-2}(T,\Delta_{0,2})}{\lambda^{-2}(0,\Delta_{0,2})}, \tag{4}$$

where $\lambda^{-2}(0)$ is the penetration depth at zero temperature, $\Delta_{0,i}$ is the value of the ith ($i = 1, 2$) superconducting gap at $T = 0$ K, and ω_i is a weighting factor which measures their relative contributions to λ^{-2} ($\omega_1 + \omega_2 = 1$).

The results of the analysis for $Ba_{1-x}Rb_xFe_2As_2$ ($x = 0.3$, 0.35, 0.4) are presented in Fig. 4. The dashed and the solid lines represent a fit to the data using an s-wave and a $s + s$-wave models, respectively. The analysis appears to rule out the simple s-wave model as an adequate description of $\lambda(T)$ for $Ba_{1-x}Rb_xFe_2As_2$ ($x = 0.3$, 0.35, 0.4). A d-wave gap symmetry was also tested, but was found to be inconsistent with the data. The two-gap $s + s$-wave scenario with a small gap Δ_1 and a large gap Δ_2, describes the experimental data remarkably well. The results of all samples extracted from the data analysis are summarized in Table I. A two-gap scenario is in line with the generally accepted view of multigap superconductivity in Fe-based HTS.[5,6,8,27–29] The magnitudes of the large and the small gaps for $Ba_{1-x}Rb_xFe_2As_2$ ($x = 0.3$, 0.35, 0.4) (see Table I) are in good agreement with the results of a previous report.[5] There it was pointed out that most Fe-based HTS's exhibit two-gap superconducting behavior, characterized by a large gap with $2\Delta/k_BT_c = 7(2)$ and a small one with 2.5(1.5). To reach a more complete view of the superconducting properties of $Ba_{1-x}Rb_xFe_2As_2$ as a function of the Rb composition (hole doping), we combined the present data with the previous μSR results on $RbFe_2As_2$ (Ref. 10) which presents the case of a naturally overdoped system. Figure 5 shows the small gap to T_c ratio $2\Delta_1/k_BT_c$, the large gap to T_c ratio $2\Delta_2/k_BT_c$, and the weight ω_1 of the small gap to the superfluid density as a function of Rb concentration. The data for $RbFe_2As_2$ are taken from Ref. 10. Interestingly, the ratio $2\Delta_2/k_BT_c$ decreases with increasing x. On the other hand, the ratio $2\Delta_1/k_BT_c$ for the small gap is essentially independent of x. In addition, the weighting factor ω_1 is found to increase with increasing x. We note that in the optimally doped 122-system $Ba_{1-x}K_xFe_2As_2$ several bands cross the Fermi surface (FS).[5–7] They consist of inner (α) and outer (β) hole-like bands, both centered at the zone center Γ, and an electron-like band (γ) centered at the M point. The superconducting gap opened on the β band was found to be smaller than those on the α and γ bands. It was proposed that the enhanced interband scattering between the α and γ bands might promote the kinetic process of pair scattering between these two FSs, leading to an increase of the pairing amplitude.[30] Hole doping may cause a shift of the band bottom of the electron pockets above the Fermi level E_F. As a result, the interband scattering between α and γ bands would diminish since the γ band is in the unoccupied side and concomitantly the size of the α band is increased. According to ARPES results, a decrease of interband scattering will lead to a decrease of the pairing amplitude and the ratio $2\Delta/k_BT_c$ in agreement with the results presented in Fig. 5(a). These results suggest the possible role of interband processes in optimally hole-doped iron-based 122 superconductors.[6,30]

One of the most interesting results of μSR investigations in HTS's is the observation of a remarkable proportionality between T_c and the zero-temperature relaxation rate $\sigma(0) \propto 1/\lambda^2(0)$ (Uemura relation).[31] This relation $T_c(\sigma)$, which seems to be generic for various families of cuprate HTS's, has the features that upon increasing the charge carrier doping T_c first increases linearly in the underdoped region

TABLE I. Summary of the parameters obtained for polycrystalline samples of $Ba_{1-x}Rb_xFe_2As_2$ ($x = 0.3$, 0.35, 0.4, 1) by means of μSR. The data for $x = 1.0$ are taken from Ref. 10.

	$x = 0.3$	$x = 0.35$	$x = 0.4$	$x = 1.0$
T_c (K)	36.9	35.8	34	2.52
Δ_1 (meV)	3.2(7)	2.9(8)	1.1(3)	0.15(2)
$2\Delta_1/k_BT_c$	2.0(5)	1.9(4)	0.8(6)	1.4(2)
Δ_2 (meV)	9.2(3)	8.8(3)	7.5(2)	0.49(4)
$2\Delta_2/k_BT_c$	5.8(6)	5.7(5)	5.1(4)	4.5(4)
ω_1	0.19(5)	0.21(4)	0.15(3)	0.36(3)
λ (nm)	249(15)	250 (17)	255 (9)	267(5)

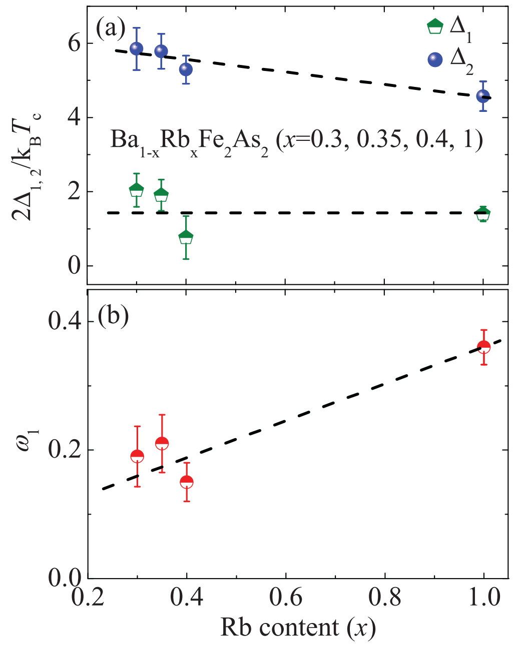

FIG. 5. (Color online) (a) Superconducting gap to T_c ratios $2\Delta_{1,2}/k_B T_c$ and (b) the contribution ω_1 of the small gap to the superfluid density as a function of the Rb composition for $Ba_{1-x}Rb_xFe_2As_2$ ($x = 0.3, 0.35, 0.4, 1.0$). The measurements were performed in an applied magnetic field of $\mu_0 H = 0.04$ T. The data for $RbFe_2As_2$ are taken from Ref. 10. The dashed lines represent guides to the eyes.

(Uemura line), then saturates, and finally is suppressed for high carrier doping. The initial linear trend of the Uemura relation indicates that for these unconventional HTS's the ratio T_c/E_F (E_F is the Fermi energy) is up to two orders of magnitude larger than for conventional BCS superconductors. Figure 6 shows T_c vs $\sigma(0)$ plot for various hole- and electron-doped high T_c Fe-based superconductors (after Ref. 28), including the present results. The solid line shows the Uemura relation in hole-doped cuprates[31] and the dashed line corresponds to electron-doped cuprates as observed by Shengelaya *et al.*[32] The Uemura relation for Fe-based superconductors was already discussed in Ref. 28. Here, we demonstrate that the data points for $Ba_{1-x}Rb_xFe_2As_2$ ($x = 0.3, 0.35, 0.4$) are located in the Uemura plot close to those of the other Fe-based superconductors. On the other hand, for naturally fully overdoped $RbFe_2As_2$, the ratio $T_c/\sigma(0)$ is strongly reduced. The small value of ratio $T_c/\sigma(0)$ is characteristic for conventional superconductors. For comparison the point for conventional BCS superconductor Nb is also shown on the Uemura plot. This suggests that superconductivity in the compound $RbFe_2As_2$ has a more conventional character. Additional experiments are in progress to clarify this point.

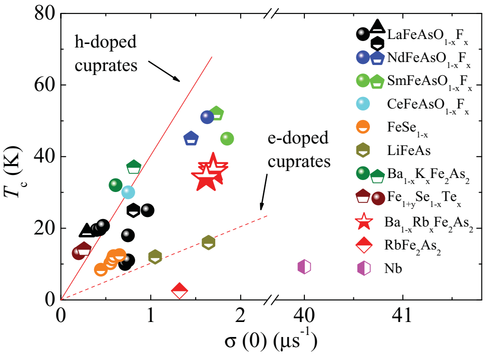

FIG. 6. (Color online) Uemura plot for hole- and electron-doped high T_c Fe-based superconductors (after Ref. 28). The Uemura relation observed for underdoped cuprates is also shown (solid line for hole doping and dashed line for electron doping) (after Ref. 32). The point for conventional BCS superconductor Nb is also shown. Data points for the pnictides are taken from Refs. 27–29, 33–39. The stars show the data for $Ba_{1-x}Rb_xFe_2As_2$ ($x = 0.3, 0.35, 0.4$) obtained in this work. The point for $RbFe_2As_2$ is taken from Ref. 10.

IV. SUMMARY AND CONCLUSION

In summary, we performed transverse-field μSR measurements of the magnetic penetration depth λ on polycrystalline samples of the iron-based HTS's $Ba_{1-x}Rb_xFe_2As_2$ ($x = 0.3, 0.35, 0.4$). The values of the superconducting transition temperature T_c and the zero temperature values of λ were estimated to be $T_c = 36.9, 35.8, 34$ K and $\lambda(0) = 249(15), 250(17), 255(9)$ nm for $x = 0.3, 0.35$, and 0.4, respectively. The temperature dependence of λ is well described by a two-gap $s + s$-wave scenario with gap values similar to $Ba_{1-x}K_xFe_2As_2$ (Refs. 5 and 8). ARPES investigations of $Ba_{1-x}K_xFe_2As_2$ revealed that the large gap opens on the inner hole-like Fermi surface (α band) centered at the Γ point and on the electron-like FS (γ band) centered at the M point (tetragonal structure notations), while the small gap opens on the outer hole-like band (β) of the Γ point.[30] We found that the large gap to T_c ratio $2\Delta_2/k_B T_c$ decreases with increasing Rb content x. On the other hand, for the small gap opening on the α and γ bands, the ratio $2\Delta_1/k_B T_c$ is practically independent of x. In addition, the contribution of the small gap ω_1 to the total superfluid density increases with increasing x. These results may be interpreted by assuming a disappearance of the electron pocket from the Fermi surface upon the high hole doping, resulting in a suppression of the scattering processes between the α and γ bands. This might cause the reduction of T_c for the overdoped $RbFe_2As_2$. We also performed zero-field μSR experiments and found no evidence of either static or fluctuating magnetism, implying that the spin-density wave ordering of the Fe moments is completely suppressed upon Rb doping. The absence of field induced magnetism in the investigated compounds is also demonstrated. Finally, the correlation between T_c and the zero-temperature relaxation rate $\sigma(0) \propto 1/\lambda^2(0)$ is discussed for the samples $Ba_{1-x}Rb_xFe_2As_2$ ($x = 0.3, 0.35, 0.4, 1$) using the Uemura classification scheme.

ACKNOWLEDGMENTS

Part of this work was performed at the Swiss Muon Source, Paul Scherrer Institut, Villigen, Switzerland. This work was supported by the Swiss National Science Foundation, the SCOPES Grant No. IZ73Z0_128242, the NCCR Project MaNEP, the EU Project CoMePhS, and the Georgian National Science Foundation Grant No. GNSF/ST08/4-416.

---

[*] zurabgug@physik.uzh.ch

[1] Y. Kamihara, T. Watanabe, M. Hirano, and H. Hosono, J. Am. Chem. Soc. **130**, 3296 (2008).

[2] Z. A. Ren, W. Lu, J. Yang, W. Yi, X. L. Shen, Z. C. Li, G. C. Che, X. L. Dong, L. L. Sun, F. Zhou, and Z. X. Zhao, Chin. Phys. Lett. **25**, 2215 (2008).

[3] M. Rotter, M. Tegel, and D. Johrendt, Phys. Rev. Lett. **101**, 107006 (2008).

[4] Z. Bukowski, S. Weyeneth, R. Puzniak, J. Karpinski, and B. Batlogg, Physica C **470**, S328 (2010).

[5] D. V. Evtushinsky, D. S. Inosov, V. B. Zabolotnyy, M. S. Viazovska, R. Khasanov, A. Amato, H.-H. Klauss, H. Luetkens, Ch. Niedermayer, G. L. Sun, V. Hinkov, C. T. Lin, A. Varykhalov, A. Koitzsch, M. Knupfer, B. Büchner, A. A. Kordyuk, and S. V. Borisenko, New J. Phys. **11**, 055069 (2009).

[6] H. Ding, P. Richard, K. Nakayama, K. Sugawara, T. Arakane, Y. Sekiba, A. Takayama, S. Souma, T. Sato, T. Takahashi, Z. Wang, X. Dai, Z. Fang, G. F. Chen, J. L. Luo, and N. L. Wang, Europhys. Lett. **83**, 47001 (2008).

[7] V. B. Zabolotnyy, D. V. Evtushinsky, A. A. Kordyuk, D. S. Inosov, A. Koitzsch, A. V. Boris, G. L. Sun, C. T. Lin, M. Knupfer, B. Büchner, A. Varykhalov, R. Follath, and S. V. Borisenko, Nature (London) **457**, 569 (2009).

[8] R. Khasanov, D. V. Evtushinsky, A. Amato, H.-H. Klauss, H. Luetkens, Ch. Niedermayer, B. Büchner, G. L. Sun, C. T. Lin, J. T. Park, D. S. Inosov, and V. Hinkov, Phys. Rev. Lett. **102**, 187005 (2009).

[9] J. E. Sonier, J. H. Brewer, and R. F. Kiefl, Rev. Mod. Phys. **72**, 769 (2000).

[10] Z. Shermadini, J. Kanter, C. Baines, M. Bendele, Z. Bukowski, R. Khasanov, H.-H. Klauss, H. Luetkens, H. Maeter, G. Pascua, B. Batlogg, and A. Amato, Phys. Rev. B **82**, 144527 (2010).

[11] Q. Huang, Y. Qiu, W. Bao, M. A. Green, J. W. Lynn, Y. C. Gasparovic, T. Wu, G. Wu, and X. H. Chen, Phys. Rev. Lett. **101**, 257003 (2008).

[12] M. S. Torikachvili, S. L. Bud'ko, N. Ni, and P. C. Canfield, Phys. Rev. Lett. **101**, 057006 (2008).

[13] C. F. Miclea, M. Nicklas, H. S. Jeevan, D. Kasinathan, Z. Hossain, H. Rosner, P. Gegenwart, C. Geibel, and F. Steglich, Phys. Rev. B **79**, 212509 (2009).

[14] J. Zhao, Q. Huang, C. de la Cruz, S. Li, J. W. Lynn, Y. Chen, M. A. Green, G. F. Chen, G. Li, Z. Li, J. L. Luo, N. L. Wang, and P. Dai, Nat. Mater. **7**, 953 (2008).

[15] R. Kubo and T. Toyabe, *Magnetic Resonance and Relaxation* (North Holland, Amsterdam, 1967).

[16] R. Khasanov, A. Maisuradze, H. Maeter, A. Kwadrin, H. Luetkens, A. Amato, W. Schnelle, H. Rosner, A. Leithe-Jasper, and H.-H. Klauss, Phys. Rev. Lett. **103**, 067010 (2009).

[17] T. J. Williams, A. A. Aczel, E. Baggio-Saitovitch, S. L. Bud'ko, P. C. Canfield, J. P. Carlo, T. Goko, H. Kageyama, A. Kitada, J. Munevar, N. Ni, S. R. Saha, K. Kirschenbaum, J. Paglione, D. R. Sanchez-Candela, Y. J. Uemura, and G. M. Luke, Phys. Rev. B **82**, 094512 (2010).

[18] J. E. Sonier, W. Huang, C. V. Kaiser, C. Cochrane, V. Pacradouni, S. A. Sabok-Sayr, M. D. Lumsden, B. C. Sales, M. A. McGuire, A. S. Sefat, and D. Mandrus, Phys. Rev. Lett. **106**, 127002 (2011).

[19] The data were analyzed with the fitting package MUSRFIT developed by A. Suter and B. Wojek (see http://lmu.web.psi.ch/facilities/software/musrfit/user/MUSR/WebHome.html). The fitting of Eq. (3) was performed using the additional library BMW developed by B. M. Wojek.

[20] E. H. Brandt, Phys. Rev. B **37**, 2349 (1988).

[21] B. Pümpin, H. Keller, W. Kündig, W. Odermatt, I. M. Savić, J. W. Schneider, H. Simmler, P. Zimmermann, E. Kaldis, S. Rusiecki, Y. Maeno, and C. Rossel, Phys. Rev. B **42**, 8019 (1990).

[22] M. Tinkham, *Introduction to Superconductivity* (Krieger, Malabar, FL, 1975).

[23] A. Carrington and F. Manzano, Physica C **385**, 205 (2003).

[24] M. H. Fang, H. M. Pham, B. Qian, T. J. Liu, E. K. Vehstedt, Y. Liu, L. Spinu, and Z. Q. Mao, Phys. Rev. B **78**, 224503 (2008).

[25] H. Padamsee, J. E. Neighbor, and C. A. Shiffman, J. Low Temp. Phys. **12**, 387 (1973).

[26] R. Khasanov, A. Shengelaya, A. Maisuradze, F. La Mattina, A. Bussmann-Holder, H. Keller, and K. A. Müller, Phys. Rev. Lett. **98**, 057007 (2007).

[27] R. Khasanov, K. Conder, E. Pomjakushina, A. Amato, C. Baines, Z. Bukowski, J. Karpinski, S. Katrych, H.-H. Klauss, H. Luetkens, A. Shengelaya, and N. D. Zhigadlo, Phys. Rev. B **78**, 220510 (2008).

[28] M. Bendele, S. Weyeneth, R. Puzniak, A. Maisuradze, E. Pomjakushina, K. Conder, V. Pomjakushin, H. Luetkens, S. Katrych, A. Wisniewski, R. Khasanov, and H. Keller, Phys. Rev. B **81**, 224520 (2010).

[29] H. Luetkens, H.-H. Klauss, R. Khasanov, A. Amato, R. Klingeler, I. Hellmann, N. Leps, A. Kondrat, C. Hess, A. Köhler, G. Behr, J. Werner, and B. Büchner, Phys. Rev. Lett. **101**, 097009 (2008).

[30] T. Sato, K. Nakayama, Y. Sekiba, P. Richard, Y.-M. Xu, S. Souma, T. Takahashi, G. F. Chen, J. L. Luo, N. L. Wang, and H. Ding, Phys. Rev. Lett. **103**, 047002 (2009).

[31] Y. J. Uemura, G. M. Luke, B. J. Sternlieb, J. H. Brewer, J. F. Carolan, W. N. Hardy, R. Kadono, J. R. Kempton, R. F. Kiefl, S. R. Kreitzman, P. Mulhern, T. M. Riseman, D. Ll. Williams, B. X. Yang, S. Uchida, H. Takagi, J. Gopalakrishnan, A. W. Sleight, M. A. Subramanian, C. L. Chien, M. Z. Cieplak, G. Xiao, V. Y. Lee, B. W. Statt, C. E. Stronach, W. J. Kossler, and X. H. Yu, Phys. Rev. Lett. **62**, 2317 (1989).

[32] A. Shengelaya, R. Khasanov, D. G. Eshchenko, D. Di Castro, I. M. Savic, M. S. Park, K. H. Kim, S. I. Lee, K. A. Müller, and H. Keller, Phys. Rev. Lett. **94**, 127001 (2005).

[33] H. Luetkens, H.-H. Klauss, M. Kraken, F. J. Litterst, T. Dellmann, R. Klingeler, C. Hess, R. Khasanov, A. Amato, C. Baines,

M. Kosmala, O. J. Schumann, M. Braden, J. Hamann-Borrero, N. Leps, A. Kondrat, G. Behr, J. Werner, and B. Büchner, Nat. Mater. **8**, 305 (2009).

[34] H. Kim, C. Martin, R. T. Gordon, M. A. Tanatar, J. Hu, B. Qian, Z. Q. Mao, Rongwei Hu, C. Petrovic, N. Salovich, R. Giannetta, and R. Prozorov, Phys. Rev. B **81**, 180503(R) (2010).

[35] S. Takeshita and R. Kadono, New J. Phys. **11**, 035006 (2009).

[36] J. P. Carlo, Y. J. Uemura, T. Goko, G. J. MacDougall, J. A. Rodriguez, W. Yu, G. M. Luke, P. Dai, N. Shannon, S. Miyasaka, S. Suzuki, S. Tajima, G. F. Chen, W. Z. Hu, J. L. Luo, and N. L. Wang, Phys. Rev. Lett. **102**, 087001 (2009).

[37] R. Khasanov, H. Luetkens, A. Amato, H.-H. Klauss, Z.-A. Ren, J. Yang, W. Lu, and Z.-X. Zhao, Phys. Rev. B **78**, 092506 (2008).

[38] R. Khasanov, M. Bendele, A. Amato, K. Conder, H. Keller, H.-H. Klauss, H. Luetkens, and E. Pomjakushina, Phys. Rev. Lett. **104**, 087004 (2010).

[39] F. L. Pratt, P. J. Baker, S. J. Blundell, T. Lancaster, H. J. Lewtas, P. Adamson, M. J. Pitcher, D. R. Parker, and S. J. Clarke, Phys. Rev. B **79**, 052508 (2009).

5 Stripe order and superconductivity in cuprate high-temperature superconductors

This chapter covers recent experimental results focussing on the interplay between the stripe order and superconductivity in cuprate HTSs. First, a basic overview of the stripe correlations in cuprates is given. Then, hydrostatic pressure effects on the stripe phase and superconductivity in $La_{2-x}Ba_xCuO_4$ with $x = 1/8$ are presented.

5.1 A brief introduction to stripe phenomena in cuprates

Since the discovery of high-T_c superconductivity in cuprates by Georg Bednorz and Alex Müller [20] in 1986, a great amount of theoretical work has been dedicated to understand the mechanism behind this phenomenon. Cuprate superconductors are formed through electrons or holes doping of the initially AFM insulating "parent compounds". La_2CuO_4 is the parent compound of the first high-T_c SC oxides $La_{2-x}Ba_xCuO_4$ (LBCO) and $La_{2-x}Sr_xCuO_4$ (LSCO) [20, 242]. They have a layered structure as shown in Fig. 5.1 [243, 244]. The key element shared by all cuprate systems is the CuO_2 plane. The CuO_2 planes are stacked in a body-centered fashion, so that the unit cell contains two layers. Each copper site has a single unpaired electron, but the copper oxide planes are insulating due to Coulomb repulsion as described by the Hubbard model. La_2CuO_4 is AFM with a Néel temperature $T_N \simeq 325$ K [245, 246, 247]. This well understood AFM state is known as a half-filled Mott insulator. Doping La_2CuO_4 by replacing a certain amount of La by Sr or Ba leads to the disappearance of the AFM order and eventually to superconductivity. Cuprate HTSs are characterized by a complex interplay between lattice, charge, and spin degrees of freedom, yielding several phases depending on doping level. One of the remarkable phases is a self-organized charge/spin structure, which is known as "stripes". The stripe phase will be briefly discussed below.

It was reported that in the prototypical HTS LBCO the superconducting transition temperature T_c has two maxima as a function of doping at $x = 0.09$ and 0.15, with a deep minimum ($T_c < 5$ K) at $x = 1/8$ [248] (see Fig. 5.2). This behavior is different from that of LSCO, where T_c shows a single maximum as a function of x [249] (see Fig. 5.2). This difference came as a surprise, especially since both compounds have the same average crystal structure. It was soon demonstrated that there is a subtle difference in the low-temperature crystal structure, associated with the tilt pattern of the CuO_6 octahedra [250]. This leads to a structural transition in LBCO from a low-temperature orthorhombic (LTO) to a low-temperature tetragonal (LTT) phase. Such a phase transition is not observed in LSCO. Investigations of other cuprate families that share the same LTT structure as LBCO, such

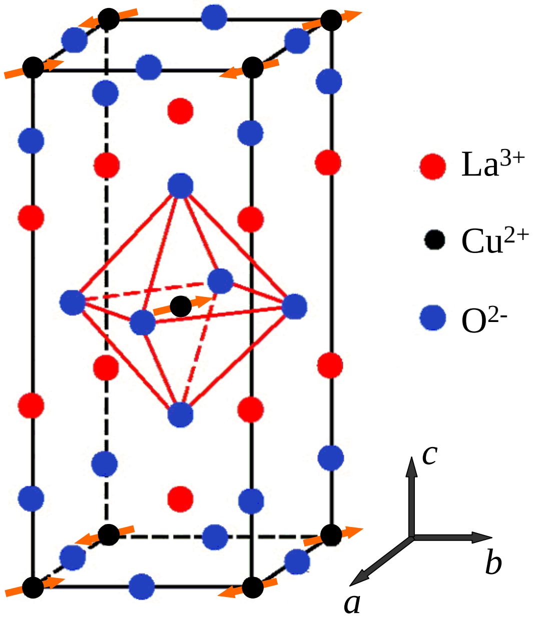

Figure 5.1: Crystal and magnetic structure of La_2CuO_4. The arrows indicate the direction of the magnetic moments.

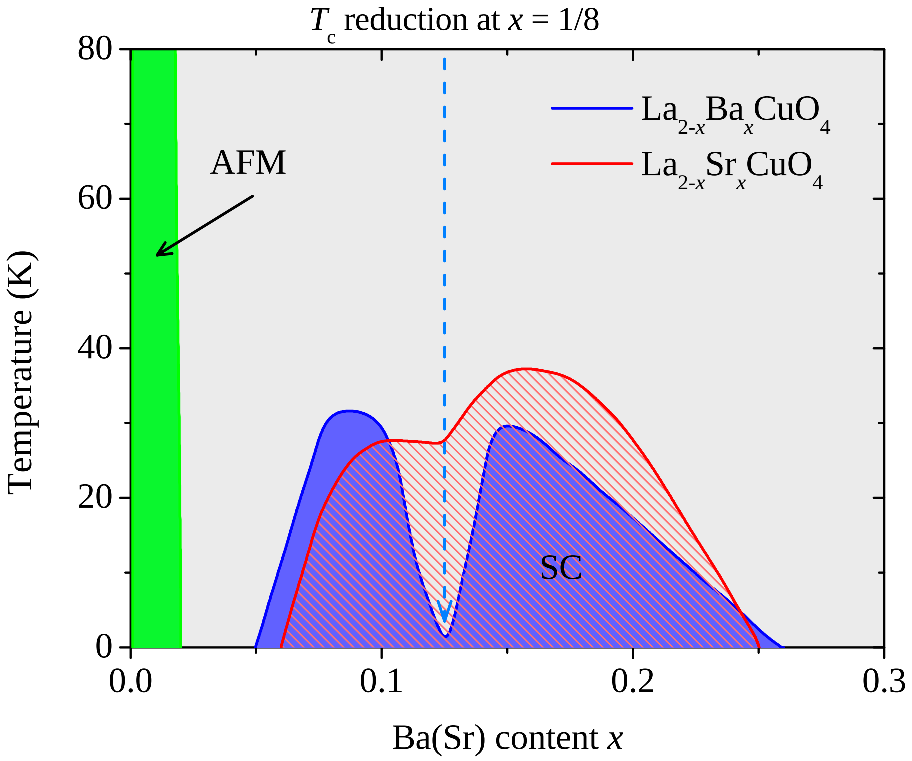

Figure 5.2: A schematic phase diagram of the hole-doped cuprates $La_{2-x}Ba_xCuO_4$ and $La_{2-x}Sr_xCuO_4$. Antiferromagnetic and superconducting phases in the phase diagram are denoted as AFM and SC. At $x = 1/8$, the T_c vs. x curve shows a dip, known as the "1/8" anomaly [248].

as Nd doped and Eu doped LSCO, revealed that they also exhibit a strong dip in T_c at $x = 1/8$ [250, 251].

A systematic study of the phase diagram in cuprates showed that not only the symmetry of the lattice modulation, but also its amplitude is correlated with the suppression of superconductivity and the appearance of local static magnetism [252]. The discovery by neutron diffraction [253, 254] of elastic superlattice peaks corresponding to two-dimensional charge and spin order in a sample of $La_{1.48}Nd_{0.4}Sr_{0.12}CuO_4$ (LNSCO) suggested a likely explanation for the anomaly: the dopant induced charge carriers, whose density is spatially modulated in a periodic fashion similar to an array of stripes, can be pinned by the lattice modulation in the LTT phase, with the pinning being strongest when the periodicity is commensurate near $x = 1/8$. With the charge stripes localized, the Cu moments in intervening regions exhibit AFM mott-like order. This remarkable phase is a self-organized charge/spin structure, known as "stripes", which is observed near the anomalous hole density of $x = 1/8$ in a few special cuprate compounds, such as $La_{2-x}Ba_xCuO_4$ [255, 256, 257, 258, 259, 260], $La_{1.6-x}Nd_{0.4}Sr_xCuO_4$ [253, 254, 261, 262], and $La_{1.8-x}Eu_{0.2}Sr_xCuO_4$ [263].

The stripe phase was first predicted in Hartree-Fock calculations of Zaanen and Gunnarsson [264], Machida [265], and Littlewood and Inui [266]. It was later discussed extensively by Kivelson and collaborators [267]. In the simplest picture stripes are a periodic pattern of one-dimensional charge and spin rivers formed in the two-dimensional CuO_2 planes. Stripe formation involves a modulation of charge density which has the translation symmetry of the lattice along one direction ($\hat{y}$) and a four unit cell repeat distance along the orthogonal direction ($\hat{x}$), as illustrated in Fig. 5.3. It was first observed by μSR that 1/8 doped LBCO exhibits static magnetic order at low temperatures [252]. Later on a detailed study of the complex nature of the magnetic phase was performed by neutron scattering in LNSCO [253, 254]. It was reported that within the stripe phase charge order appears below 70 K followed by the order of Cu spins below $T_{\mathrm{SO}} = 50$ K. It is believed that in LSCO the LTO structure of the copper oxide plane inhibits such static spin and charge stripe orders. The existence of stripes has also been demonstrated by extended x-ray absorption fine structure (EXAFS) technique which allows to probe the local structure near a selected atomic site [268, 269].

In the framework of the stripe model it is recognized that the charge/spin orders are a manifestation of dynamical spin/charge correlation and that stabilization of these orders induces an instability of the SC state. In the LTT phase stripes are favorably stabilized by the corrugated pattern of the in-plane lattice potential. Hence, T_{c} is suppressed more effectively in the LTT phase than in the LTO one. Experimental results and theoretical considerations show that the modulations of the lattice and of the charge and spin density appear to be both ubiquitous in the cuprates and intimately tied up with the physics of these materials [267, 270]. However, the role of stripes for superconductivity in cuprates is still unclear at present. Therefore, it is important to find an external control parameter which allows to tune structural and electronic properties of the cuprates and study the relation between superconductivity and stripe order. This will also give definitive hints for the debate whether stripes promote or suppress superconductivity.

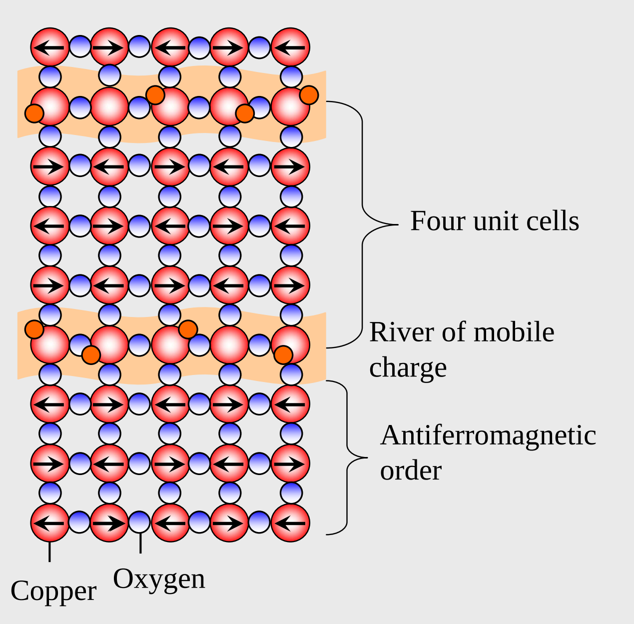

Figure 5.3: Stripe-like electronic order in the cuprates. In this form of electronic order, the material's copper oxide planes have stripes of AFM Mott-like order, separated by stripes of mobile charges.

5.2 Hydrostatic pressure effect on the static spin-stripe order and superconductivity in La$_{2-x}$Ba$_x$CuO$_4$ ($x = 1/8$)

As mentioned above, T_c is strongly suppressed for $x = 1/8$ in La$_{2-x}$Ba$_x$CuO$_4$, at which the static stripe phase appears. It is known that upon using hydrostatic pressure as a tuning parameter the LTT structural phase transition in La$_{1.875}$Ba$_{0.125}$CuO$_4$ (LBCO-1/8) is suppressed, and superconductivity is enhanced [271, 272, 273]. Though, it is not known how the magnetic order related to stripe formation changes with pressure. In order to clarify the effect of pressure on the static spin-stripe order and its relation to superconductivity in LBCO-1/8, magnetization and μSR experiments were performed on powder specimen under hydrostatic pressures up to $p \simeq 2.2$ GPa.

The temperature dependence of the FC magnetic susceptibility (χ_FC) recorded at ambient and selected applied pressures is shown in Fig. 5.4. Magnetization measurements under pressure were carried out by using a diamond anvil cell (DAC) [213, 214]. The diamagnetic susceptibility exhibits a two-step SC transition [274]. The first transition with an onset at $T_\mathrm{c1} \approx 30$ K corresponds to only about 4 % volume fraction of superconductivity estimated from ZFC susceptibility χ_ZFC at 10 K [274]. The second SC transition is observed at $T_\mathrm{c2} \approx 10$ K, with a larger diamagnetic response. However, the volume fraction of the low temperature SC phase is still small at ambient pressure and amounts to about 10 % of full shielding at 2 K. A two-step SC transition, starting at around 30 K with a weak diamagnetic response was observed previously in polycrystalline LBCO-1/8 [273, 275]. It was explained as some kind of filamentary superconductivity due to the presence of a very small fraction of the

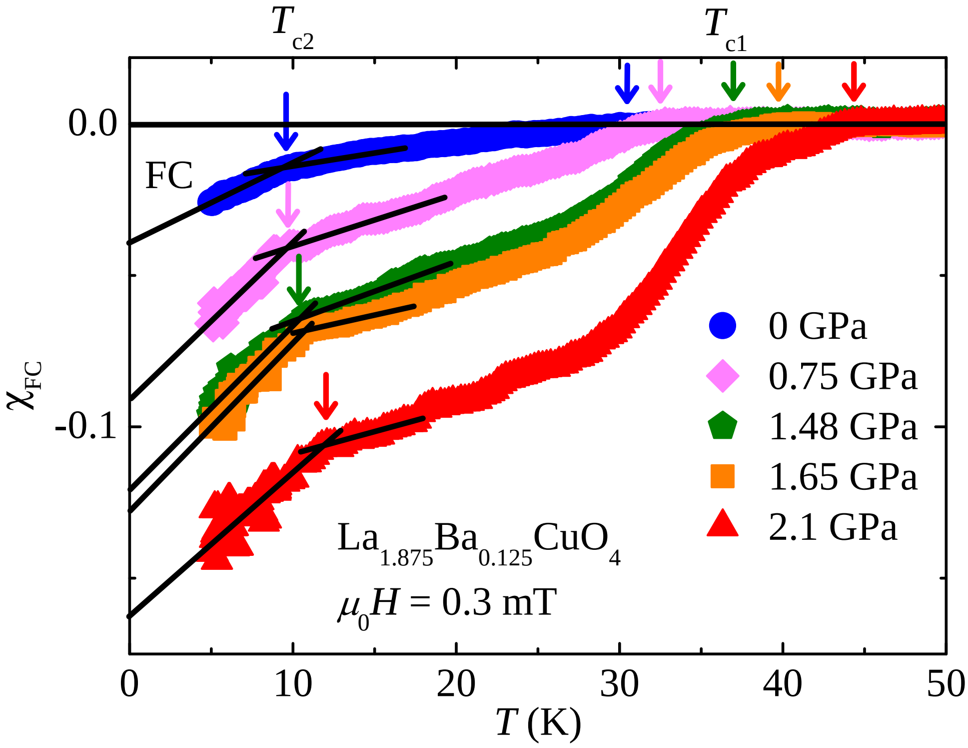

Figure 5.4: (Color online) Temperature dependence of the FC magnetic susceptibility for the sample $La_{1.875}Ba_{0.125}CuO_4$ measured at ambient and at various applied hydrostatic pressures in a magnetic field of $\mu_0 H = 0.3$ mT. The arrows denote the SC transition temperatures T_{c1} and T_{c2} (see text for an explanation). After [274].

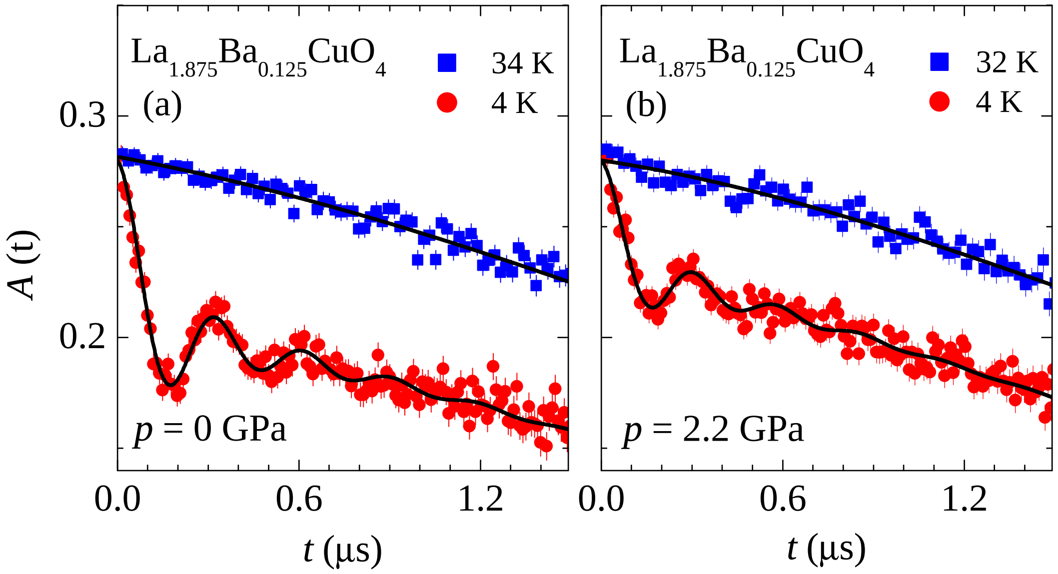

Figure 5.5: (Color online) ZF μSR signal A(t) of LBCO-1/8 measured at $p = 0$ GPa (a), and 2.2 GPa (b), recorded for two different temperatures: $T = 4$ K (circles) and $T = 32$ K (squares). The solid lines represent fits to the data by means of Eq. (1) of Ref. [274]. After [274].

LTO phase. However, recent detailed transport and susceptibility measurements in single crystal of LBCO-1/8 provided evidence of the intrinsic nature of the observed two-step SC transition [260]. We observed that T_{c2} increases only slightly with pressure from 10 K to about 12 K at the maximal pressure applied in our experiments (p = 2.1 GPa). On the other hand, $T_{\rm c1}$ shows a significant increase with a rate of 6.2 K/GPa. It is interesting that the volume fraction of the corresponding SC phase is also strongly enhanced with applied pressure (see Fig. 5.4). These results are in agreement with previous studies showing that superconductivity in LBCO-1/8 is largely enhanced by applying pressure [272, 273, 276].

In the following the results of the μSR experiments performed on LBCO-1/8 under hydrostatic pressures are presented. ZF μSR time spectra for a polycrystalline LBCO-1/8 sample at ambient and at maximum applied pressure $p = 2.2$ GPa are shown in Figs. 5.5a and b, respectively, recorded at T = 4 K and 32 K. At T = 32 K slowly relaxing non-oscillating signal signifies the paramagnetic state of the sample. Below $T_{\rm so} \simeq 30$ K a well-defined spontaneous muon spin precession is observed at all applied pressures, indicating static spin-stripe order [277, 278]. The μSR signals are analysed using the function expected for incommensurate spin density wave as described in details in Ref. [274]. Analysis of the μSR signals allows to extract important parameters such as the average internal magnetic field at the muon site B_{μ}, the relative volume $V_{\rm m}$ of the magnetic fraction in the sample as well as the transversal (λ_T) and the longitudinal (λ_L) depolarization rates. The temperature dependence of B_{μ} for LBCO-1/8 for different pressures is shown in Fig. 5.6a. The solid curves in Fig. 5.6a are fits of the data to the power law $B_{\mu}(T) = B_{\mu}(0)[1\text{-}(T/T_{\rm so})^{\gamma}]^{\delta}$, where $B_{\mu}(0)$ is the zero-temperature value of B_{μ}. γ and δ are phenomenological exponents. The values of the spin ordering temperature $T_{\rm so} \simeq 30$ K and $B_{\mu}(0) \simeq 25$ mT at ambient pressure are in good agreement with the values of a previous μSR study [278]. As evident from Fig. 5.6a the internal magnetic field $B_{\mu}(0)$ is almost pressure independent. This indicates that the ordered magnetic moment of the static stripe phase does not depend on applied pressure. Also $T_{\rm so}$ changes only slightly with pressure as shown in the inset of Fig. 5.6a. In the pressure range of p = 0 - 2.2 GPa, $T_{\rm so}(p)$ varies only between 30 and 27 K with a shallow minimum at $p \simeq$ 1.5 GPa.

It is important to note that the LTT structural phase transition is suppressed at $p_{\rm c}$ = 1.85 GPa [279]. Therefore, the present results demonstrate that the spin order due to static stripes still exists at p = 2.2 GPa, where the LTT phase is already suppressed. Recent high pressure x-ray diffraction experiments showed that also the charge order of the stripe phase survives above $p_{\rm c}$ in LBCO-1/8 [279]. Combining these results, one may conclude that both charge and spin order, and consequently the static stripe phase itself, still exist at pressures where the LTT phase is suppressed.

Here the question arises: What is the effect of pressure on the stripe order in LBCO-1/8? We found that it is the magnetic volume fraction $V_{\rm m}$ which is significantly suppressed by pressure. μSR can determine the ordered volume fraction and is thus a particularly powerful tool to study inhomogeneous magnetism in materials. Figure 5.6b shows the temperature dependence of $V_{\rm m}$ at various pressures. $V_{\rm m}$ increases progressively below $T_{\rm so}$ with decreasing temperature and acquires nearly 100 % at ambient pressure at the base temperature. An important new result is that at low temperature $V_{\rm m}$ significantly decreases with increasing pressure (see Fig. 5.6b). This means that with increasing pressure an increasingly large part of the sample remains in the nonmagnetic state down to the lowest temperatures.

In order to compare the influence of pressure on the SC and magnetic properties of LBCO-1/8, the pressure dependences of the zero-temperature limit of the magnetic volume fraction $V_{\rm m}(0)$ and the SC volume fraction $V_{\rm sc}(0) = \text{-}\chi_{\rm ZFC}(0)$ [280] are plotted in Fig. 5.7a.

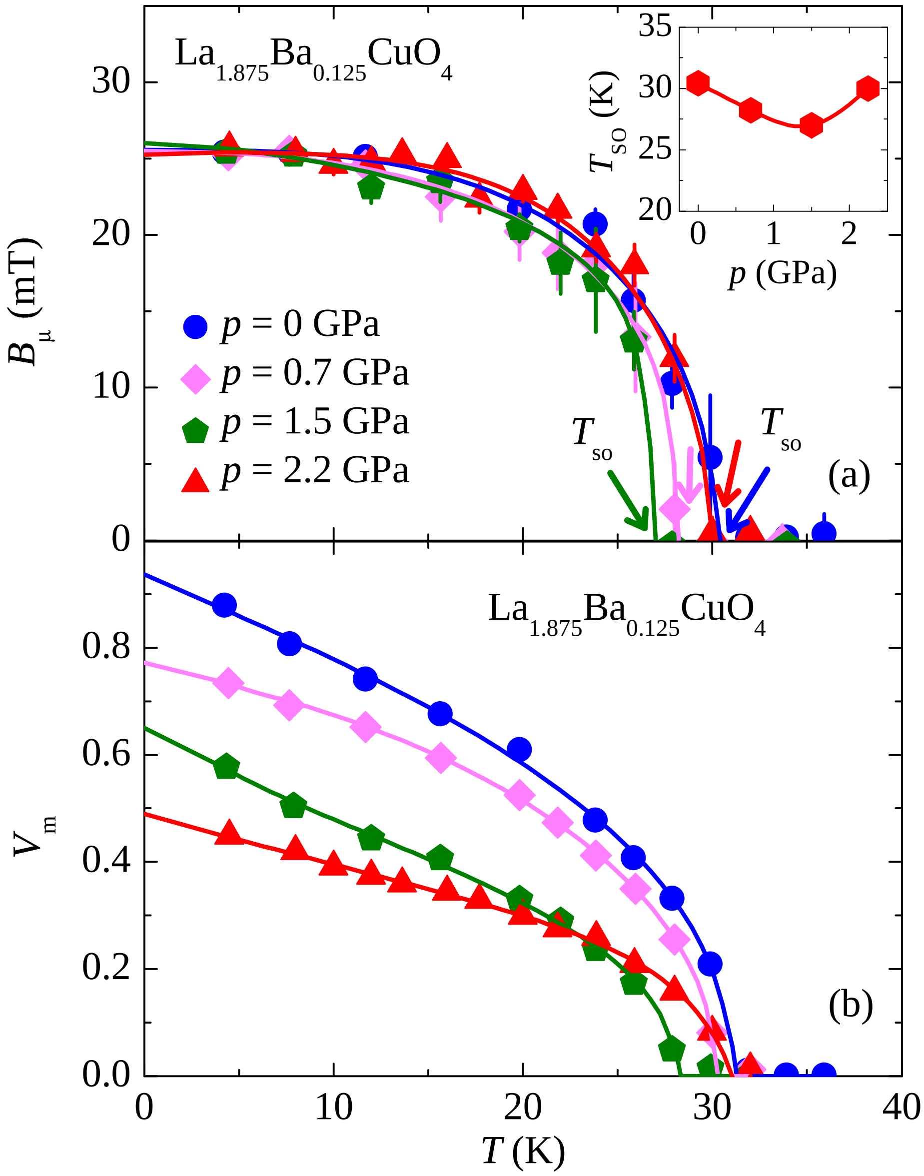

Figure 5.6: (Color online) (a) Temperature dependence of the average internal magnetic field B_μ at the muon site of LBCO-1/8 recorded at various applied pressures. The solid lines represent fits of the data to the power law described in the text. The arrows mark the transition temperatures for the static spin-stripe order $T_{\rm so}$. The inset shows $T_{\rm so}$ as a function of pressure p. (b) The temperature dependence of the magnetic volume fraction $V_{\rm m}$ in LBCO-1/8 at ambient and various hydrostatic pressures. The solid lines are fits of the data to a similar empirical power law as used for $B_\mu(T)$ in (a). After [274].

Note that $V_{\rm m}(0)$ linearly decreases with pressure to approximately 50 % at $p = 2.2$ GPa. A linear extrapolation of $V_{\rm m}(0)$ to higher pressures shows that the magnetic volume fraction should be completely suppressed at $p \approx 5$ GPa. It would be interesting to check this prediction at higher pressures by either μSR or neutron-scattering experiments. It is evident from Fig. 5.7a that the decrease of $V_{\rm m}(0)$ is followed by an increase of the SC volume fraction $V_{\rm sc}(0)$. In Fig. 5.7b we plot $V_{\rm sc}(0)$ as a function of $V_{\rm m}(0)$. The solid straight line is drawn between a hypothetical situation of a fully magnetic ($V_{\rm m}(0) = 1$) and a fully SC state ($V_{\rm sc}(0) = 1$). Remarkably, the experimental data lie on this solid straight line. Thus, the sum of the SC and magnetic volume fractions is constant and is close to one. This strongly suggests that superconductivity does not exist in those regions where static magnetism is

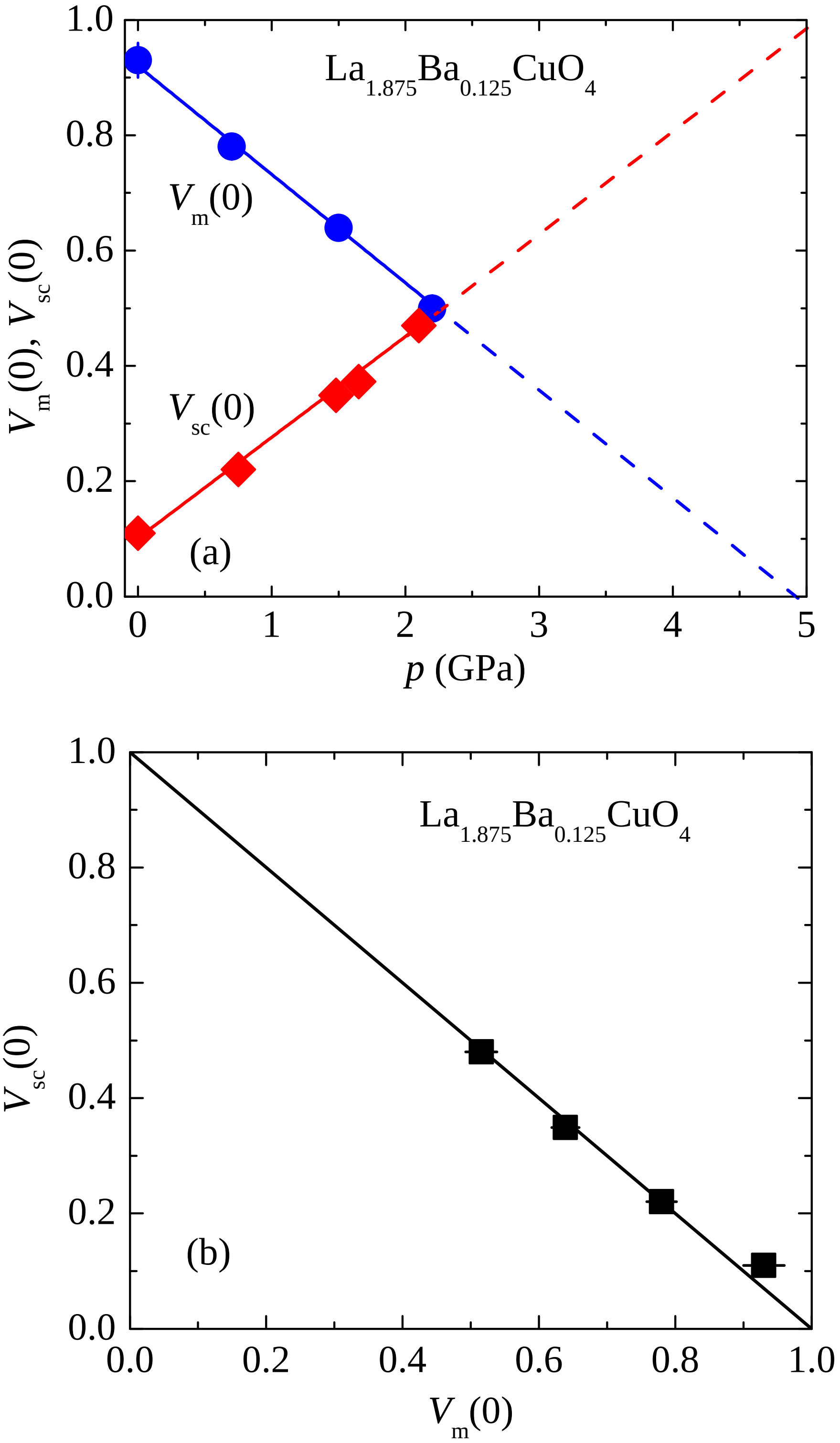

Figure 5.7: (Color online) (a) The pressure dependence of the zero-temperature limit of the magnetic and the SC volume fractions, $V_{\mathrm{m}}(0)$ and $V_{\mathrm{sc}}(0)$, respectively, of LBCO-1/8. Solid lines are linear fits to the data. (b) $V_{\mathrm{sc}}(0)$ vs. $V_{\mathrm{m}}(0)$. The solid straight line is drawn between a hypothetical situation of a fully magnetic ($V_{\mathrm{m}}(0) = 1$) and a fully SC state ($V_{\mathrm{sc}}(0) = 1$). After [274].

present. Thus, superconductivity most likely develops in those areas of the sample which are nonmagnetic down to the lowest temperatures. The latter implies that in LBCO-1/8 magnetism and superconductivity are competing order parameters.

5.3 Publication related to Chapter 5

- *Tuning the static spin-stripe phase and superconductivity in* $La_{2-x}Ba_xCuO_4$ *(*$x = 1/8$*) by hydrostatic pressure*
  Z. Guguchia, A. Maisuradze, G. Ghambashidze, R. Khasanov, A. Shengelaya, and H. Keller
  New J. Phys. **15**, 093005 (2013).

5.3.1 Publication: Tuning the static spin-stripe phase and superconductivity in La$_{2-x}$Ba$_x$CuO$_4$ (x = 1/8) by hydrostatic pressure

Z. Guguchia, A. Maisuradze, G. Ghambashidze, R. Khasanov, A. Shengelaya, and H. Keller
New J. Phys. **15**, 093005 (2013).

Abstract

Magnetization and muon spin rotation experiments were performed in La$_{2-x}$Ba$_x$CuO$_4$ (x = 1/8) as a function of hydrostatic pressure up to $p \simeq 2.2$ GPa. It was found that the magnetic volume fraction of the static stripe phase strongly decreases linearly with pressure, while the superconducting volume fraction increases by the same amount. This demonstrates competition between bulk superconductivity and static magnetic order in the stripe phase of La$_{1.875}$Ba$_{0.125}$CuO$_4$ and that these phenomena occur in mutually exclusive spatial regions. The present results also reveal that the static spin-stripe phase still exists at pressures, where the long-range low-temperature tetragonal (LTT) structure is completely suppressed. This indicates that the long-range LTT structure is not necessary for stabilizing the static spin order in La$_{1.875}$Ba$_{0.125}$CuO$_4$.

DOI: 10.1088/1367-2630/15/9/093005
PACS numbers: 74.62.Fj, 76.75.+i, 75.60.Ej, 74.25.Ha, 74.72.Dn

The original publication is electronically available at:
`http://iopscience.iop.org/1367-2630/15/9/093005/`

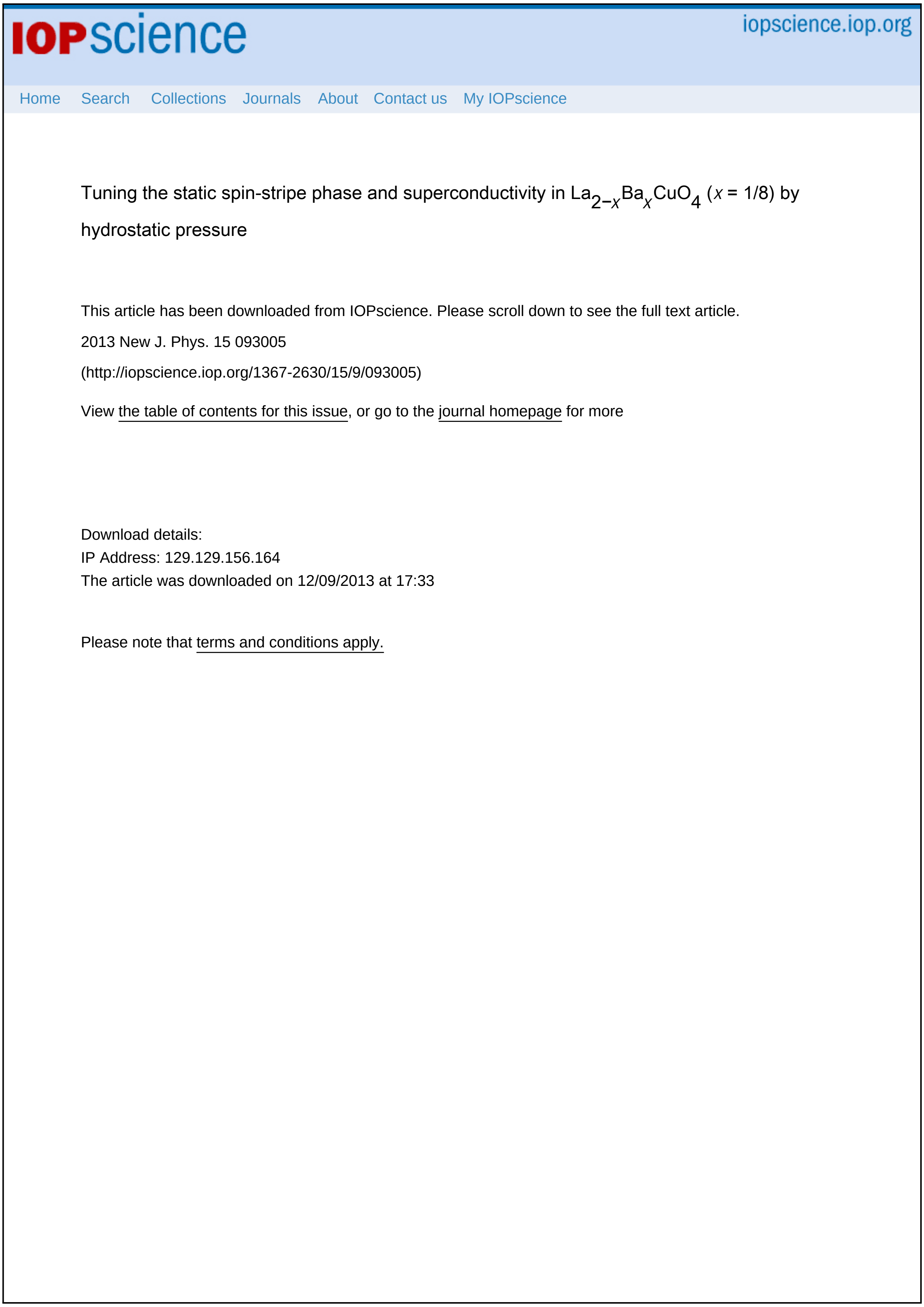

Tuning the static spin-stripe phase and superconductivity in $La_{2-x}Ba_xCuO_4$ ($x = 1/8$) by hydrostatic pressure

2013 New J. Phys. 15 093005

(http://iopscience.iop.org/1367-2630/15/9/093005)

New Journal of Physics
The open access journal for physics

Tuning the static spin-stripe phase and superconductivity in $La_{2-x}Ba_xCuO_4$ ($x = 1/8$) by hydrostatic pressure

Z Guguchia[1,4], **A Maisuradze**[1,2], **G Ghambashidze**[3],
R Khasanov[2], **A Shengelaya**[3] **and H Keller**[1]
[1] Physik-Institut der Universität Zürich, Winterthurerstrasse 190,
CH-8057 Zürich, Switzerland
[2] Laboratory for Muon Spin Spectroscopy, Paul Scherrer Institute,
CH-5232 Villigen PSI, Switzerland
[3] Department of Physics, Tbilisi State University, Chavchavadze 3,
GE-0128 Tbilisi, Georgia
E-mail: zurabgug@physik.uzh.ch

New Journal of Physics **15** (2013) 093005 (9pp)
Received 8 June 2013
Published 3 September 2013
Online at http://www.njp.org/
doi:10.1088/1367-2630/15/9/093005

Abstract. Magnetization and muon spin rotation experiments were performed in $La_{2-x}Ba_xCuO_4$ ($x = 1/8$) as a function of hydrostatic pressure up to $p \simeq 2.2$ GPa. It was found that the magnetic volume fraction of the static stripe phase strongly decreases linearly with pressure, while the superconducting volume fraction increases by the same amount. This demonstrates competition between bulk superconductivity and static magnetic order in the stripe phase of $La_{1.875}Ba_{0.125}CuO_4$ and that these phenomena occur in mutually exclusive spatial regions. The present results also reveal that the static spin-stripe phase still exists at pressures, where the long-range low-temperature tetragonal (LTT) structure is completely suppressed. This indicates that the long-range LTT structure is not necessary for stabilizing the static spin order in $La_{1.875}Ba_{0.125}CuO_4$.

---

[4] Author to whom any correspondence should be addressed.

New Journal of Physics **15** (2013) 093005
1367-2630/13/093005+09$33.00

$La_{2-x}Ba_xCuO_4$ (LBCO) was the first cuprate in which high-T_c superconductivity was discovered [1]. The undoped parent compound is an antiferromagnetic (AFM) insulator. The replacement of La^{3+} by Ba^{2+} ions, through which holes are doped into the CuO_2 planes, causes the destruction of AFM order and superconductivity appears at $x = 0.06$. Subsequent investigations showed that there exists a sharp dip in the T_c–x phase diagram, indicating that bulk superconductivity is greatly suppressed in a narrow range around a particular doping concentration $x = 1/8$ in LBCO [2]. This suppression of T_c has attracted a great deal of attention and is known in the literature as the 1/8 anomaly (see e.g. [3, 4]). Later a similar anomaly was also observed in rare earth doped $La_{2-x}Sr_xCuO_4$. Studies of the crystal structure clarified that the LBCO system undergoes at $x = 1/8$ a first-order structural phase transition from a low-temperature orthorhombic (LTO) to a low-temperature tetragonal (LTT) phase with decreasing temperature [5]. Since the structural transition to the LTT phase appears near the Ba concentration x where the strong decrease of T_c occurs, it has been suggested that there is a correlation between the appearance of the LTT phase and the suppression of superconductivity [5]. Muon spin rotation (μSR) experiments detected the appearance of static magnetic order below ~ 30 K in $La_{1.875}Ba_{0.125}CuO_4$ (LBCO-1/8) [6].

The discovery of elastic superlattice peaks in $La_{1.48}Nd_{0.4}Sr_{0.12}CuO_4$ by neutron diffraction provided evidence of two-dimensional (2D) charge and spin order, which was explained in terms of a stripe model where charge-carrier poor AFM regions are separated by one-dimensional stripes of charge carrier-rich regions [7, 8]. The presence of stripe-like charge and spin density ordering is believed to be responsible for the anomalous suppression of superconductivity around $x = 1/8$ in cuprates [7, 8]. The existence of stripes in $La_{1.85}Sr_{0.15}CuO_4$ and $Bi_2Sr_2CaCu_2O_{8+y}$ has also been demonstrated by extended x-ray absorption fine structure experiments which allow to probe the local structure near a selected atomic site [9, 10].

The fascinating issue of charge and spin stripes in cuprate superconductors has attracted a lot of attention for many years (see e.g. [3, 4]). Experimental results and theoretical considerations show that the modulations of the lattice and of the charge and spin density appear to be both ubiquitous in the cuprates and intimately tied up with the physics of these materials [3, 4]. However, the role of stripes for superconductivity in cuprates is still unclear at present. Therefore, it is important to find an external control parameter which allows to tune structural and electronic properties of the cuprates and study the relation between superconductivity and stripe order. It is known that upon applying hydrostatic pressure both the LTT and LTO structural phase transition in LBCO-1/8 are suppressed completely at the critical pressure $p_c \approx 1.85$ GPa, and superconductivity is enhanced [11–14]. The magnetic order related to stripe formation was previously studied under pressure, but only below p_c [15]. Hence, it is not known how the static spin-stripe order changes across p_c.

Here, we report studies of superconductivity and stripe magnetic order in LBCO-1/8 under hydrostatic pressure up to $p \simeq 2.2$ GPa by magnetization and μSR experiments. It was observed that the transition temperature of the stripe magnetic order and the size of the ordered moment are not significantly changed by pressure. But the volume fraction of the magnetic phase significantly decreases and simultaneously the superconducting (SC) volume fraction increases with increasing pressure. This indicates that magnetic regions in the sample are converted to SC regions with increasing pressure, providing evidence for a competition between superconductivity and static magnetic order in the stripe phase of LBCO-1/8. It was also demonstrated that the spin-stripe order still exists at pressures, where the LTT phase is suppressed.

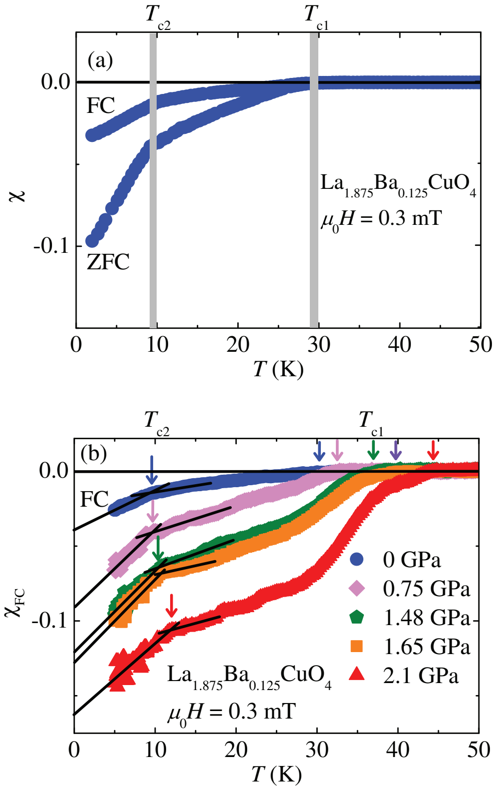

Figure 1. Temperature dependence of the magnetic susceptibility of LBCO-1/8 measured at ambient pressure without pressure cell (a) and at various applied hydrostatic pressures (b) in a magnetic field of $\mu_0 H = 0.3\,\mathrm{mT}$. The vertical grey lines and the arrows denote the SC transition temperatures T_{c1} and T_{c2} (see text for an explanation).

A polycrystalline sample of $La_{2-x}Ba_xCuO_4$ with $x = 1/8$ was prepared by the conventional solid-state method. The single-phase character of the sample was checked by powder x-ray diffraction.

The magnetic susceptibility was measured under pressures up to 2.1 GPa by a SQUID magnetometer (*Quantum Design* MPMS-XL). Pressures were generated using a diamond anvil cell (DAC) [16] filled with Daphne oil which served as a pressure-transmitting medium. The pressure at low temperatures was determined by the pressure dependence of the SC transition temperature of Pb. The temperature dependence of the zero-field-cooled (ZFC) and field-cooled (FC) magnetic susceptibility, χ_{ZFC} and χ_{FC}, respectively, for LBCO-1/8 in a magnetic field of $\mu_0 H = 0.3\,\mathrm{mT}$ is shown in figure 1(a). The diamagnetic susceptibility exhibits a two-step SC transition. The first transition with an onset at $T_{c1} \approx 30\,\mathrm{K}$ corresponds to only about 4% volume fraction of superconductivity estimated from ZFC magnetization at 10 K.

The second SC transition is observed at $T_{c2} \approx 10$ K, with a larger diamagnetic response. However, the volume fraction of the low temperature SC phase is still small at ambient pressure and amounts to about 10% of full shielding at 2 K. A two-step SC transition, starting at around 30 K with a weak diamagnetic response was observed previously in polycrystalline LBCO-1/8 [2, 11]. It was explained as some kind of filamentary superconductivity due to the presence of a very small fraction of the LTO phase. Recent detailed transport and susceptibility measurements in single crystal of LBCO-1/8 provided evidence of the intrinsic nature of the observed two-step SC transition [17]. It was found that a SC transition at higher temperature T_{c1} is present when the magnetic field is applied perpendicular to the CuO_2 planes. The SC transition at low temperature T_{c2} is more pronounced when the magnetic field is parallel to the planes ($H \parallel ab$). The authors interpreted the transition at T_{c1} as due to the development of 2D superconductivity in the CuO_2 planes, while the interlayer Josephson coupling is frustrated by static stripes. A transition to a three-dimensional SC phase takes place at much lower temperature $T_{c2} \ll T_{c1}$, reflected as a strong increase of diamagnetism below T_{c2} for $H \parallel ab$. For polycrystalline samples with random orientation of grains these two temperatures will result in two SC transitions as observed in present experiments (see figure 1(a)).

We studied the SC transition in LBCO-1/8 as a function of hydrostatic pressure. Measurements were performed in the FC mode at 0.3 mT, which was set constant during the measurements at all pressures in order to avoid a variation of the applied field during the measurements with different pressures. Figure 1(b) shows the temperature dependence of χ_{FC} for different pressures after substraction of the background signal from the empty pressure cell. A two-step SC transition is observed at all pressures, while at higher pressure ($p > 1.6$ GPa) even a three-step SC transition is visible. The reason for this is not clear at present. Further investigations, in particular on single crystals, are needed to clarify this issue. It was found that T_{c2} increases only slightly with pressure from 10 to about 12 K at the maximal pressure applied in our experiments ($p = 2.1$ GPa). On the other hand, T_{c1} shows a significant increase with a rate of 6.2 K GPa^{-1}. It is interesting that the volume fraction of the corresponding SC phase is also strongly enhanced with applied pressure (see figure 1(b)). These results are in agreement with previous studies showing that superconductivity in LBCO-1/8 is largely enhanced by applying pressure [11, 13, 18].

It is interesting to explore the pressure effect on spin order in the stripe phase and its relation to superconductivity. It is also of great interest to study the relation between static magnetism and the LTT phase in LBCO-1/8. However, to the best of our knowledge magnetism in LBCO-1/8 was studied only at low pressures [15] where the LTT phase is still present. In order to answer this question we performed zero-field (ZF) μSR experiments in LBCO-1/8 at ambient and various hydrostatic pressures, including pressures where the long-range LTT structure is suppressed. ZF μSR is a powerful tool to investigate microscopic magnetic properties of solids without applying an external magnetic field. It is especially suitable for the study of weak magnetic order, since the positive muon is an extremely sensitive local probe which is able to detect small internal magnetic fields and ordered volume fractions.

The ZF μSR experiments were carried out at the μE1 beam line at the Paul Scherrer Institute, Switzerland. Pressures up to 2.2 GPa were generated in a double wall piston-cylinder type of cell made of MP35N material, especially designed to perform μSR experiments under pressure [19]. As a pressure transmitting medium Daphne oil was used. The pressure was measured by tracking the SC transition of a very small indium plate. The μSR time spectra were analysed using the free software package MUSRFIT [20].

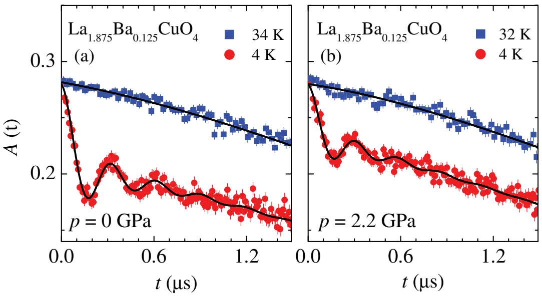

Figure 2. ZF μSR signal $A(t)$ of LBCO-1/8 measured at $p = 0\,$GPa (a), and 2.2 GPa (b), recorded for two different temperatures: $T = 4\,$K (circles) and $T = 32\,$K (squares). The solid lines represent fits to the data by means of equation (1).

Figure 2 shows representative ZF μSR time spectra for a polycrystalline LBCO-1/8 sample at ambient and at maximum applied pressure $p = 2.2\,$GPa, respectively. Below $T \approx 30\,$K damped oscillations due to muon-spin precession in local magnetic fields are observed, indicating static spin-stripe order [6, 21].

A substantial fraction of the μSR asymmetry signal originates from muons stopping in the MP35N pressure cell surrounding the sample. Therefore, the μSR data in the whole temperature range were analysed by decomposing the signal into a contribution of the sample and a contribution of the pressure cell:

$$A(t) = A_{\rm S}(0)\,P_{\rm S}(t) + A_{\rm PC}(0)\,P_{\rm PC}(t), \tag{1}$$

where $A_{\rm S}(0)$ and $A_{\rm PC}(0)$ are the initial asymmetries and $P_{\rm S}(t)$ and $P_{\rm PC}(t)$ are the muon-spin polarizations belonging to the sample and the pressure cell, respectively. The pressure cell signal was analysed by a damped Kubo–Toyabe function [19]. The response of the sample consists of a magnetic and a nonmagnetic contribution

$$P_{\rm S}(t) = V_{\rm m}\left[\frac{2}{3}\,{\rm e}^{-\lambda_{\rm T}t}\,J_0(\gamma_\mu B_\mu t) + \frac{1}{3}\,{\rm e}^{-\lambda_{\rm L}t}\right] + (1 - V_{\rm m})\,{\rm e}^{-\lambda_{\rm nm}t}. \tag{2}$$

Here, $V_{\rm m}$ denotes the relative volume of the magnetic fraction, and $\gamma_\mu/(2\pi) \simeq 135.5\,{\rm MHz\,T^{-1}}$ is the muon gyromagnetic ratio. B_μ is the average internal magnetic field at the muon site. $\lambda_{\rm T}$ and $\lambda_{\rm L}$ are the depolarization rates representing the transversal and the longitudinal relaxing components of the magnetic parts of the sample. J_0 is the zeroth-order Bessel function of the first kind. This is characteristic for an incommensurate spin density wave and has been observed in cuprates with static spin stripe order [21]. $\lambda_{\rm nm}$ is the relaxation rate of the nonmagnetic part of the sample. The total initial asymmetry $A_{\rm tot} = A_{\rm S}(0) + A_{\rm PC}(0) \simeq 0.285$ is a temperature independent constant. A typical fraction of muons stopped in the sample was $A_{\rm S}(0)/A_{\rm tot} \simeq 0.50(5)$ which was assumed to be temperature independent in the analysis.

The temperature dependence of B_μ for different pressures is shown in figure 3(a). The solid curves in figure 3(a) are fits of the data to the power law $B_\mu(T) = B_\mu(0)[1-(T/T_{\rm so})^\gamma]^\delta$, where $B_\mu(0)$ is the zero-temperature value of B_μ. γ and δ are phenomenological exponents. The values of the spin ordering temperature $T_{\rm so} \simeq 30\,$K and $B_\mu(0) \simeq 25\,$mT at ambient pressure are in good agreement with the values of a previous μSR study [15, 21]. As evident from

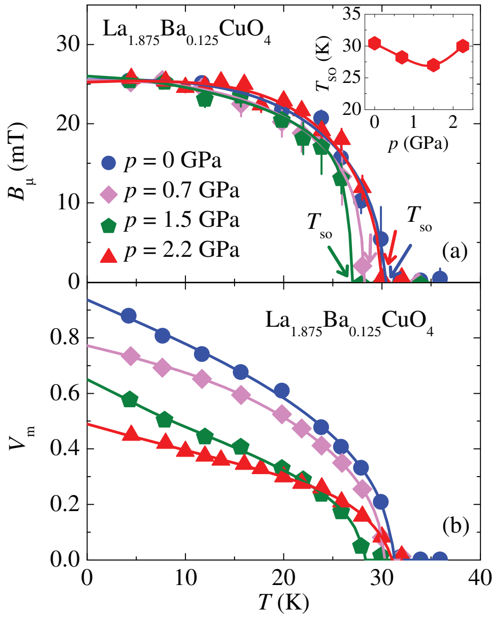

Figure 3. (a) Temperature dependence of the average internal magnetic field B_μ at the muon site of LBCO-1/8 recorded at various applied pressures. The solid lines represent fits of the data to the power law described in the text. The arrows mark the transition temperatures for the static spin-stripe order T_{so}. The inset shows T_{so} as a function of pressure p. (b) The temperature dependence of the magnetic volume fraction V_{m} in LBCO-1/8 at ambient and various hydrostatic pressures. The solid lines are fits of the data to a similar empirical power law as used for $B_\mu(T)$ in (a).

figure 3(a) the internal magnetic field $B_\mu(0)$ is almost pressure independent. This indicates that the ordered magnetic moment of the static stripe phase does not depend on applied pressure. Also T_{so} changes only slightly with pressure as shown in the inset of figure 3(a). In the pressure range of $p = 0 - 2.2$ GPa, $T_{\mathrm{so}}(p)$ varies only between 30 and 27 K with a shallow minimum at $p \simeq 1.5$ GPa.

It is important to note that both the LTT and LTO structural phase transition are suppressed at $p_{\mathrm{c}} = 1.85$ GPa [14]. Therefore, the present results demonstrate that the spin order due to static stripes still exists at $p = 2.2$ GPa, where the LTT phase is already suppressed. Recent high pressure x-ray diffraction experiments showed that also the charge order of the stripe phase survives above p_{c} in LBCO-1/8 [14]. Combining these results, one may conclude that both charge and spin order, and consequently the static stripe phase itself, still exist at pressures where the LTT phase is suppressed.

Here the question arises: What is the effect of pressure on the stripe order in LBCO-1/8? In agreement with the previous low-pressure μSR results [15], it was found that it is the

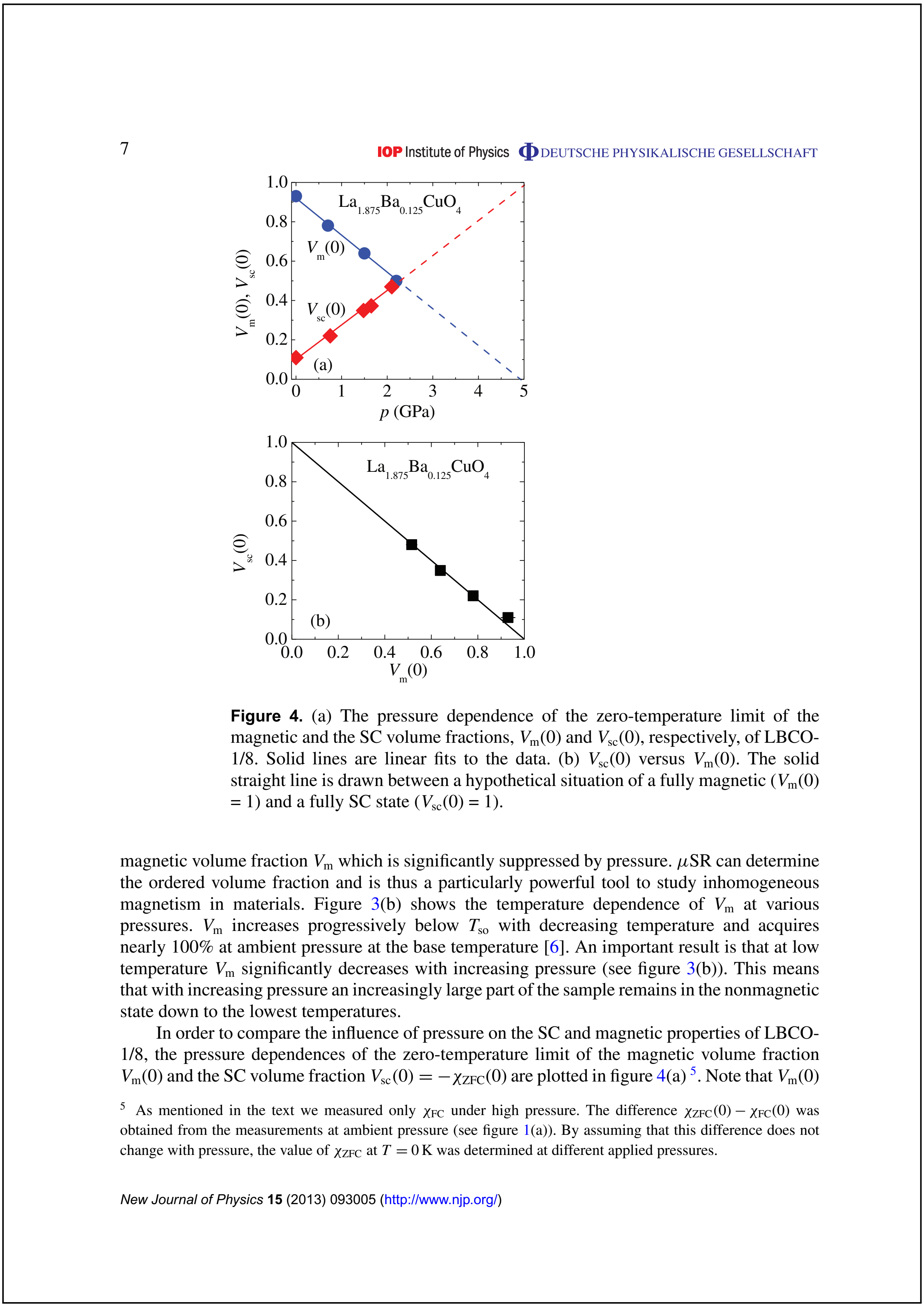

Figure 4. (a) The pressure dependence of the zero-temperature limit of the magnetic and the SC volume fractions, $V_m(0)$ and $V_{sc}(0)$, respectively, of LBCO-1/8. Solid lines are linear fits to the data. (b) $V_{sc}(0)$ versus $V_m(0)$. The solid straight line is drawn between a hypothetical situation of a fully magnetic ($V_m(0) = 1$) and a fully SC state ($V_{sc}(0) = 1$).

magnetic volume fraction V_m which is significantly suppressed by pressure. μSR can determine the ordered volume fraction and is thus a particularly powerful tool to study inhomogeneous magnetism in materials. Figure 3(b) shows the temperature dependence of V_m at various pressures. V_m increases progressively below T_{so} with decreasing temperature and acquires nearly 100% at ambient pressure at the base temperature [6]. An important result is that at low temperature V_m significantly decreases with increasing pressure (see figure 3(b)). This means that with increasing pressure an increasingly large part of the sample remains in the nonmagnetic state down to the lowest temperatures.

In order to compare the influence of pressure on the SC and magnetic properties of LBCO-1/8, the pressure dependences of the zero-temperature limit of the magnetic volume fraction $V_m(0)$ and the SC volume fraction $V_{sc}(0) = -\chi_{ZFC}(0)$ are plotted in figure 4(a) [5]. Note that $V_m(0)$

---

[5] As mentioned in the text we measured only χ_{FC} under high pressure. The difference $\chi_{ZFC}(0) - \chi_{FC}(0)$ was obtained from the measurements at ambient pressure (see figure 1(a)). By assuming that this difference does not change with pressure, the value of χ_{ZFC} at $T = 0$ K was determined at different applied pressures.

linearly decreases with pressure to approximately 50 % at $p = 2.2$ GPa. A linear extrapolation of $V_m(0)$ to higher pressures shows that the magnetic volume fraction should be completely suppressed at $p \approx 5$ GPa. It would be interesting to check this prediction at higher pressures by either μSR or neutron-scattering experiments. It is evident from figure 4(a) that the decrease of $V_m(0)$ is followed by an increase of the SC volume fraction $V_{sc}(0)$. In figure 4(b) we plot $V_{sc}(0)$ as a function of $V_m(0)$. The solid straight line is drawn between a hypothetical situation of a fully magnetic ($V_m(0) = 1$) and a fully SC state ($V_{sc}(0) = 1$). Remarkably, the experimental data lie on this solid straight line. Thus, the sum of the SC and magnetic volume fractions is constant and is close to one. This strongly suggests that superconductivity does not exist in those regions where static magnetism is present. Thus, superconductivity most likely develops in those areas of the sample which are nonmagnetic down to the lowest temperatures. The latter implies that in LBCO-1/8 magnetism and superconductivity are competing order parameters. It is interesting to note that a similar scaling was found between the superfluid density and the magnetic volume fraction in the related compound $La_{1.85-y}Eu_ySr_{0.15}CuO_4$ [22]. The tuning of the magnetic and SC properties was realized by rare-earth doping.

To summarize, magnetism and superconductivity were studied in LBCO-1/8 by means of magnetization and μSR experiments as a function of pressure up to $p \simeq 2.2$ GPa. It was demonstrated that the static spin-stripe order still exist at pressures, where the long-range LTT structure is suppressed. This suggests that the long-range LTT phase is not essential for the existence of stripe order. An unusual interplay between spin order and bulk superconductivity was also observed. With increasing pressure the spin order temperature and the size of the ordered moment are not changing significantly. However, application of hydrostatic pressure leads to a remarkable decrease of the magnetic volume fraction $V_m(0)$. Simultaneously, an increase of the SC volume fraction $V_{sc}(0)$ occurs. Furthermore, it was found that $V_m(0)$ and $V_{sc}(0)$ at all p are linearly correlated: $V_m(0) + V_{sc}(0) \simeq 1$. This is an important new result, indicating that the magnetic fraction in the sample is directly converted to the SC fraction with increasing pressure. The mechanism of this transformation, however, is not clear yet and requires further studies. The present results provide evidence for a competition between bulk superconductivity and static magnetic order in the stripe phase of LBCO-1/8, and that static stripe order and bulk superconductivity occur in mutually exclusive spatial regions. Our findings suggest that a pressure of about 5 GPa would be sufficient to completely suppress the static stripe phase and restore bulk superconductivity in LBCO-1/8.

Acknowledgments

The μSR experiments were performed at the Swiss Muon Source, Paul Scherrer Institute (PSI), Villigen, Switzerland. This work was supported by the Swiss National Science Foundation, the NCCR MaNEP, the SCOPES grant no. IZ73Z0-128242 and the Georgian National Science Foundation grant no. RNSF/AR/10-16.

References

[1] Bednorz J G and Müller K A 1986 *Z. Phys.* B **64** 189
[2] Moodenbaugh A R, Xu Y, Suenaga M, Folkerts T J and Shelton R N 1988 *Phys. Rev.* B **38** 4596
[3] Kivelson S A, Bindloss I P, Fradkin E, Oganesyan V, Tranquada J M, Kapitulnik A and Howald C 2003 *Rev. Mod. Phys.* **75** 1201

[4] Vojta M 2009 *Adv. Phys.* **58** 699
[5] Axe J D, Moudden A H, Hohlwein D, Cox D E, Mohanty K M, Moodenbaugh A R and Xu Y 1989 *Phys. Rev. Lett.* **62** 2751
[6] Luke G M, Le L P, Sternlieb B J, Wu W D, Uemura Y J, Brewer J H, Riseman T M, Ishibashi S and Uchida S 1991 *Physica* C **185–189** 1175
[7] Tranquada J M, Sternlieb B J, Axe J D, Nakamura Y and Uchida S 1995 *Nature* **375** 561
[8] Tranquada J M, Axe J D, Ichikawa N, Nakamura Y, Uchida S and Nachumi B 1996 *Phys. Rev.* B **54** 7489
[9] Bianconi A, Saini N L, Lanzara A, Missori M, Rossetti T, Oyanagi H, Yamaguchi H, Oka K and Ito T 1996 *Phys. Rev. Lett.* **76** 3412
[10] Bianconi A, Lusignoli M, Saini N L, Bordet P, Kvick Å and Radaelli P G 1996 *Phys. Rev.* B **54** 4310
[11] Katano S, Funahashi S, Môri N, Yutaka U and Fernandez-Baca Jaime A 1993 *Phys. Rev.* B **48** 6569
[12] Crawford *et al* 2005 *Phys. Rev.* B **71** 104513
[13] Zhou J S and Goodenough J B 1997 *Phys. Rev.* B **56** 6288
[14] Hücker M, Zimmermann M V, Debessai M, Schilling J S, Tranquada J M and Gu G D 2010 *Phys. Rev. Lett.* **104** 057004
[15] Satoh K H, Goko T, Takeshita S, Hayashi Y, Arai J, Higemoto W, Nishiyama K and Nagamine K 2006 *Physica* B **374** 40
[16] Giriat Gaétan, Wang Weiwei, Attfield J, Paul Huxley, Andrew D and Kamenev Konstantin V 2010 *Rev. Sci. Instrum.* **81** 073905
[17] Tranquada *et al* 2008 *Phys. Rev.* B **78** 174529
[18] Yamada Y and Ido M 1992 *Physica* C **203** 240
[19] Maisuradze A, Graneli B, Guguchia Z, Shengelaya A, Pomjakushina E, Conder K and Keller H 2013 *Phys. Rev.* B **87** 054401
[20] Suter A and Wojek B M 2012 *Phys. Procedia* **30** 69
[21] Nachumi B *et al* 1998 *Phys. Rev.* B **58** 8760
[22] Kojima K M, Uchida S, Fudamoto Y, Gat I M, Larkin M I, Uemura Y J and Luke G M 2003 *Physica* B **326** 316

6 Concluding remarks

In this thesis the magnetic and superconducting properties of the iron-based HTS systems $EuFe_2As_2$ and $Ba_{1-x}Rb_xFe_2As_2$ and the cuprate HTS system $La_{1.875}Ba_{0.125}CuO_4$ were studied by means of μSR, NMR, magnetization, and x-ray experiments.

The system $EuFe_2As_2$ was investigated as a function of charge carrier doping, as well as chemical and hydrostatic pressure. The hyperfine coupling constant between the ^{75}As nuclei and the Eu $4f$ moments in $EuFe_{1.9}Co_{0.1}As_2$ was quantitatively determined from NMR data. The observed large value of the coupling constant points to strong interaction between the localized Eu^{2+} moments and charge carriers in the $Fe_{2-x}Co_xAs_2$ layers. This may explain why it is difficult to induce superconductivity in $EuFe_{2-x}Co_xAs_2$, in contrast to the other 122 systems, where the substituion of Fe by Co leads to the appearance of an SC phase. In addition, strong interlayer coupling suggests that the RKKY interaction might play an important role in the coupling mechanism between the Eu layers, leading to a high magnetic ordering temperature of the Eu^{2+} moments in $EuFe_2As_2$. NMR experiments provide the first microscopic evidence for a possible electronic nematic phase in $EuFe_{1.9}Co_{0.1}As_2$ well above the SDW state of the Fe moments. This supports the idea that the tetragonal-orthorhombic structural transition in Fe-HTSs is of electronic origin.

The magnetic phase diagrams of the Eu and Fe spin systems in single crystals of $EuFe_{2-x}Co_xAs_2$ were determined. The magnetic ordering temperature of the Eu^{2+} moments remains nearly unchanged upon Co-doping. However, unlike the parent compound, in which the Eu^{2+} moments order antiferromagnetically at low temperatures, the Co-doped system exhibits a C-AFM state with a dominant FM component in the *ab*-plane. The magnetic anisotropy becomes smaller as a result of Co doping. This implies that the magnetic configuration of the Eu moments is strongly influenced by the Fe sublattice, where superconductivity takes place for a certain range of Co doping.

The phase diagram of pollycrystalline samples of $EuFe_2(As_{1-x}P_x)_2$ with respect to chemical (x, isovalent substitution of As by P) and hydrostatic pressures (p) were also determined. These investigations reveal that the magnetic coupling between the Eu and the Fe sublattices strongly depends on chemical and hydrostatic pressure and determines the $(x-T)$ and $(p-T)$ phase diagrams. According to the phase diagrams, both ways to apply pressure have qualitatively similar effects on the Fe and Eu magnetic order. One of the important aspects of the present results is that it confirms the presence of a SC phase in the extremely narrow pressure range in $EuFe_2(As_{1-x}P_x)_2$. This is very different from the respective phase diagram of $BaFe_2(As_{1-x}P_x)_2$, where superconductivity is observed over a large pressure range. This might be related to the complicated interplay between Eu magnetic order and superconductivity in $EuFe_2(As_{1-x}P_x)_2$.

μSR studies of another Fe-HTS $Ba_{1-x}Rb_xFe_2As_2$ with $T_c = 38$ K revealed the existence of two gaps opening below T_c, which is in line with the generally accepted view of multi-gap superconductivity in Fe-HTSs. Most probably, in the Fe-HTSs the order parameter is $s +$

s-wave like. However, some reports point towards an $s(+/-)$, or extended s-wave state.

Another interesting candidate to study the interplay between SC and magnetic ground states in HTSs is the cuprate system LBCO-1/8. It exhibits a static stripe phase at low temperatures which leads to a strong decrease of T_c. By studying this system as a function of hydrostatic pressure, an unusual interplay between spin order and superconductivity was observed. With increasing pressure the spin order temperature and the size of the ordered moment do not change significantly. However, application of hydrostatic pressure leads to a significant decrease of the magnetic volume fraction $V_\mathrm{m}(0)$. Simultaneously, an increase of the SC volume fraction $V_\mathrm{sc}(0)$ occurs. Furthermore, it was found that $V_\mathrm{m}(0)$ and $V_\mathrm{sc}(0)$ at all p are linearly correlated: $V_\mathrm{m}(0) + V_\mathrm{sc}(0) \simeq 1$. This is an important new result, indicating that the magnetic fraction in the sample is directly converted to the SC fraction with increasing pressure. The mechanism of this transformation, however, is not clear at present and requires further investigations. The present results provide evidence for a competition between superconductivity and static magnetic order in the stripe phase of LBCO-1/8, and that static stripe order and superconductivity occur in mutually exclusive spatial regions.

Combining all these observations leads to the conclusion that the Fe-based and cuprate high-T_c superconductor systems investigated in the framework of the present thesis show a substantial sensitivity of the SC and magnetic properties for small variations of various physical parameters of the system. Moreover, a complex and rather sophisticated interplay of magnetism and superconductivity in $\mathrm{EuFe_2As_2}$ and LBCO-1/8 was found. This provides new constraints for theories of superconductivity.

Bibliography

[1] H. Kamerlingh Onnes, *Further experiments with liquid helium D - On the change of the electrical resistance of pure metals at very low temperatures, etc. V The disappearance of the resistance of mercury*, Proc. K. Akad. Amsterdam **14**, 113 (1911).

[2] H. Kamerlingh Onnes, *The resistance of pure mercury at helium temperatures*, Comm. Phys. Lab. Leiden **120b** (1911).

[3] H. Kamerlingh Onnes, *The disappearance of the resistance of mercury*, Comm. Phys. Lab. Leiden **122b** (1911).

[4] H. Kamerlingh Onnes, *On the sudden change in the rate at which the resistance of mercury disappears*, Comm. Phys. Lab. Leiden **124c** (1911).

[5] W. Meissner and R. Ochsenfeld, *Short initial announcements*, Naturwissenschaften **21**, 787 (1933).

[6] F. London and H. London, *The electromagnetic equations of the supraconductor*, Proc. R. Soc. A **149**, 71 (1935).

[7] V.L. Ginzburg and L.D. Landau, *On the theory of superconductivity*, Zh. Eksp. Theor. Fiz. **20**, 1064 (1950).

[8] E. Maxwell, *Isotope effect in the superconductivity of mercury*, Phys. Rev. **78**, 477 (1950).

[9] C.A. Reynolds, B. Serin, W.H. Wright, and L.B. Nesbitt, *Superconductivity of isotopes of mercury*, Phys. Rev. **78**, 487 (1950).

[10] L.N. Cooper, *Bound electron pairs in a degenerate Fermi gas*, Phys. Rev. **104**, 1189 (1956).

[11] J. Bardeen, L. N. Cooper, and J. R. Schrieffer, *Microscopic theory of superconductivity*, Phys. Rev. **106**, 162 (1957).

[12] J. Bardeen, L. N. Cooper, and J. R. Schrieffer, *Theory of superconductivity*, Phys. Rev. **108**, 1175 (1957).

[13] A.A. Abrikosov, L.P. Gor'kov, and I.E. Dzyaloshinskii, In: *Methods of Quantum Field Theory in Statistical Mechanics*, Prentice Hall, Englewood Cliffs, NJ (1963).

[14] B.D. Josephson, *Possible new effects in superconductive tunnelling*, Phys. Lett. **1**, 251 (1962).

[15] J.R. Schrieffer, D.J. Scalapino, and J.W. Wilkins, *Effective Tunneling Density of States in Superconductors*, Phys. Rev. Lett. **10**, 336 (1963).

[16] W.L. McMillan, *Transition Temperature of Strong-Coupled Superconductors*, Phys. Rev. **167**, 331 (1968).

[17] B.T. Matthias, T.H. Geballe, R.H. Willens, E. Corenzwit, and G.W. Hull, *Superconductivity of* Nb_3Ge, Phys. Rev. **139**, A1501 (1965).

[18] J.R. Gavaler, *Superconductivity in Nb-Ge Films above 22 K*, Appl. Phys. Lett. **23**, 480 (1973).

[19] P.B. Allen, in *Dynamical Properties of Solids*, Vol. **3** (Eds G.K. Horton, A.A. Maradudin, Amsterdam: North-Holland, 1980) p. 95.

[20] J.G. Bednorz, and K.A. Müller, *Possible high-*T_c *superconductivity in the Ba-La-Cu-O system*, Z. Phys. B **64**, 189 (1986).

[21] P. Dai, B.C. Chakoumakos, G.F. Sun, K.W. Wong, Y. Xin, and D.F. Lu, *Synthesis and neutron powder diffraction study of the superconductor* $HgBa_2Ca_2Cu_3O_{8+\delta}$ *by Tl substitution*, Physica C **243**, 201 (1995).

[22] A. Schilling, M. Cantoni, J.D. Guo, and H.R. Ott, *Superconductivity above 130 K in the Hg-Ba-Ca-Cu-O system*, Nature (London) **363**, 56 (1993).

[23] L. Gao, Y.Y. Xue, F. Chen, Q. Xiong, R.L. Meng, D. Ramirez, C.W. Chu, J.H. Eggert, and H.K. Mao, *Superconductivity up to 164 K in* $HgBa_2Ca_{m-1}Cu_mO_{2m+2+\delta}$ *(m=1, 2, and 3) under quasihydrostatic pressures*, Phys. Rev. B **50**, 4260 (1994).

[24] H. Keller, A. Bussmann-Holder, and K. A. Müller, *Jahn-Teller physics and high-*T_c *superconductivity*, Materials Today **11**, 38 (2008).

[25] A. Bussmann-Holder and H. Keller, *Polaron formation as origin of unconventional isotope effects in cuprate superconductors*, Eur. Phys. J. B **44**, 487 (2005).

[26] A. Bussmann-Holder, H. Keller, A.R. Bishop, A. Simon, R. Micnas, and K. A. Müller, *Unconventional isotope effects as evidence for polaron formation in cuprates*, EPL **72**, 423 (2005).

[27] K.A. Müller, *On the superconductivity in hole doped cuprates*, J. Phys.: Condens. Matter **19**, 251002 (2007).

[28] J. Nagamatsu, N. Nakagawa, T. Muranaka, Y. Zenitani, and J. Akimitsu, *Superconductivity at 39 K in magnesium diboride*, Nature (London) **410**, 63 (2001).

[29] Y. Kamihara, H. Hiramatsu, M. Hirano, R. Kawamura, H. Yanagi, T. Kamiya, and H. Hosono, *Iron-based layered superconductor: LaOFeP*, J. Am. Chem. Soc. **128**, 10012 (2006).

[30] Y. Kamihara, T. Watanabe, M. Hirano, and H. Hosono, *Iron-based layered superconductor La[$O_{1-x}F_x$]FeAs (x = 0.05-0.12) with T_c = 26 K*, J. Am. Chem. Soc. **130**, 3296 (2008).

[31] A. Bussmann-Holder, A. Simon, H. Keller, and A. R. Bishop, *Identifying the pairing mechanism in Fe-As based superconductors: Gaps and isotope effects*, J. Supercond. Nov. Magn. **24**, 1099 (2011).

[32] I.I. Mazin, D.J. Singh, M.D. Johannes, and M.H. Du, *Unconventional superconductivity with a sign reversal in the order parameter of LaFeAs$O_{1-x}F_x$*, Phys. Rev. Lett. **101**, 057003 (2008).

[33] A.V. Chubukov, D.V. Efremov, and I. Eremin, *Magnetism, superconductivity, and pairing symmetry in iron-based superconductors*, Phys. Rev. B **78**, 134512 (2008).

[34] S. Blundell, *Magnetism in Condensed Matter*, (New York: Oxford University Press, 2006).

[35] B.D. Cullity, *Introduction to Magnetic Materials*, Addison-Wesley (1972).

[36] C.M. Hurd, *Varieties of magnetic order in solids*, Contemporary Physics **23:5**, 469493 (1982).

[37] O. Korneta, *A systematic study of transport, magnetic and thermal properties of layered iridates*, Ph.D. thesis, University of Kentucky, Lexington, KY (2012).

[38] H. Kramers, *L'interaction entre les atomes magnétogénes dans un cristal paramagnétique*, Physica **1**, 182 (1934).

[39] P.W. Anderson, *Antiferromagnetism. Theory of Superexchange Interaction*, Phys. Rev. **79**, 350 (1950).

[40] P.W. Anderson, *New Approach to the Theory of Superexchange Interactions*, Phys. Rev. **115**, 2 (1959).

[41] J.B. Goodenough and A.L. Loeb, *Theory of ionic ordering, crystal distortion, and magnetic exchange due to covalent forces in spinels*, Phys. Rev. **98**, 391 (1955).

[42] J. Kanamori, *Superexchange interaction and symmetry properties of electron orbitals*, J. Phys. Chem. Solid **10**, 87 (1959).

[43] M.A. Ruderman and C. Kittel, *Indirect exchange coupling of nuclear magnetic moments by conduction electrons*, Phys. Rev. **96**, 99 (1954).

[44] T. Kasuya, *A theory of metallic ferro- and antiferromagnetism on Zener's model*, Progress of Theoretical Physics **16**, 45 (1956).

[45] K. Yosida, *Magnetic properties of Cu-Mn alloys*, Phys. Rev. **106**, 893 (1957).

[46] D.N. Aristov, *Indirect RKKY interaction in any dimensionality*, Phys. Rev. B **55**, 8064 (1997).

[47] I. Dzyaloshinsky, *A thermodynamic theory of "weak" ferromagnetism of antiferromagnetics*, J. Phys. Chem. Solids **4**, 241 (1958).

[48] T. Moriya, *New mechanism of anisotropic superexchange interaction*, Phys. Rev. Lett. **4**, 228 (1960).

[49] T. Moriya, *Anisotropic superexchange interaction and weak ferromagnetism*, Phys. Rev. **120**, 91 (1960).

[50] A. Fert and P.M. Levy, *Role of Anisotropic Exchange Interactions in Determining the Properties of Spin-Glasses*, Phys. Rev. Lett. **44**, 1538 (1980).

[51] P.M. Levy and A. Fert, *Origin of magnetic anistropy in transition metal spin-glass alloys*, J. Appl. Phys. **52**, 1718 (1981).

[52] L.D. Landau, *The theory of phase transitions*, Nature (London) **138**, 840 (1936).

[53] M. Tinkham, *Introduction to Superconductivity*, Krieger Publishing company, Malabar, Florida (1975).

[54] K.H. Bennemann and J.B. Ketterson, *Superconductivity, Conventional and Unconventional Superconductors*, Vol **1**, Springer, Berlin (2008).

[55] A.A. Abrikosov, Zh. Eksp. Teor. Fiz. **32**, 1064 (1950).

[56] A. Abrikosov, *On the magnetic properties of superconductors of the second group*, Sov. Phys. JETP **5**, 1174 (1957).

[57] A. Schenk, *Muon Spin Rotation Spectroscopy: Principles and Applications in Solid State Physics*, Adam Hilger, Bristol, Engand (1985).

[58] G. Schatz and A. Weidinger, *Nuclear Condensed Matter Physics*, (Wiley, New York, 1996).

[59] J.H. Brewer, in *Muon Spin Rotation / Relaxation / Resonance*, Vol. **11** of *Encyclopedia of Applied Physics* (VCH Publishers, New York, 1994), pp. 2353.

[60] A. Schenck and F.N. Gygax, *Magnetic Materials studied by Muon Spin Rotation Spectroscopy*, Vol. **9** of $HandbookofMagneticMaterials$, edited by K.H.J. Buschow (Elsevier Science B.V., Amsterdam, 1995), Chap. 2, pp. 57302.

[61] A. Seeger and L. Schimmele, *μ^+SR in Magnetically Ordered Metals, Perspectives of Meson Science*, edited by T. Yamazaki, K. Nakai, and K. Nagamine (North- Holland, Amsterdam, 1992), pp. 293382.

[62] P. Dalmas de Réotier and A. Yaouanc, *Muon Spin Rotation in Magnetic Materials*, J.Phys.: Cond. Matt. **9**, 9113 (1997).

[63] K. Hagiwara *et al.* (Particle Data Group), *Review of Particle Physics*, Phys. Rev. D **66**, 010001 (2002).

[64] A.E. Pifer, T. Brown, and K.R.K enadall, *A high stopping density μ^+ beam*, Nucl. Instr. Meth. **135**, 39 (1976).

[65] G.W. Ford and C.J. Mullin, *Scattering of Polarized Dirac Particles on Electrons*, Phys. Rev. **108**, 477 (1957).

[66] S.J. Blundell, *Spin-polarized muons in condensed matter physics*, Contemporary Physics **40**, 175 (1999).

[67] R. Kubo and T. Toyabe, *A stochastic model for low field resonance and relaxation*, in *Magnetic Resonance and relaxation*, pages **810-823**, North-Holland, Amsterdam, 1967.

[68] J. Major, J. Mundy, M. Schmolz, A. Seeger, K. Döring, K. Fürderer, M. Gladisch, D. Herlach, and G. Majer, *Zero-field muon spin rotation in monocrystalline chromium*, Hyperfine Interactions **31**, 259 (1986).

[69] A. Amato, *Heavy-fermion systems studied by μSR technique*, Rev. Mod. Phys. **69**, 1119 (1997).

[70] E.H. Brandt, *Flux distribution and penetration depth measured by muon spin rotation in high-T_c superconductors*, Phys. Rev. B **37**, 2349 (1988).

[71] E.H. Brandt, *Properties of the ideal Ginzburg-Landau vortex lattice*, Phys. Rev. B **68**, 054506 (2003).

[72] I.L. Landau and H. Keller, *On the interpretation of muon-spin-rotation experiments in the mixed state of type-II superconductors*, Physica C **466**, 131 (2007).

[73] M. Weber, A. Amato, F.N. Gygax, A. Schenk, H. Maletta, V.N. Duginov, V.G. Grebinnik, A.B. Lazarev, V.G. Olshevsky, V.Yu. Pomjakushin, S.N. Shilov, B.F. Kirillov, A.V. Pirogov, A.N. Ponomarev, V.G. Storchak, S. Kapusta, and J. Bock, *Magnetic-flux distribution and the magnetic penetration depth in superconducting polycrystalline $Bi_2Sr_2Ca_{1-x}Y_xCu_2O_{8+\delta}$ and $Bi_{2-x}Pb_xSr_2CaCu_2O_{8+\delta}$*, Phys. Rev. B **48**, 13022 (1993).

[74] R. Khasanov, A. Shengelaya, A. Maisuradze, F. La Mattina, A. Bussman-Holder, H.Keller, and K.A. Müller, *Experimental Evidence for Two Gaps in the High-Temperature $La_{1.83}Sr_{0.17}CuO_4$ Superconductor*, Phys. Rev. Lett. **98**, 057007 (2007).

[75] A. Maisuradze, R. Khasanov, A. Shengelaya, and H. Keller, *Comparison of different methods for analyzing μSR line shapes in the vortex state of type-II superconductors*, J. Phys.: Condens. Matter **21**, 075701 (2009).

[76] Z. Hao, J.R. Clem, M.W. McElfresh, L. Civale, A.P. Malozemoff, and F. Holtzberg, *Model for the reversible magnetization of high-κ type-II superconductors: Application to high-T_c superconductors*, Phys. Rev. B **43**, 2844 (1991).

[77] A. Yaouanc, P. Dalmas de Réotier, and E. H. Brandt, *Effect of the vortex core on the magnetic field in hard superconductors*, Phys. Rev. B **55**, 11107 (1997).

[78] S.L. Lee, P. Zimmermann, H. Keller, M. Warden, I.M. Savić, R. Schauwecker, D. Zech, R. Cubitt, E.M. Forgan, P.H. Kes, T.W. Li, A.A. Menovsky, and Z. Tarnawski, *Evidence for flux-lattice melting and a dimensional crossover in single-crystal* $Bi_{2.15}Sr_{1.85}CaCu_2O_{8+\delta}$ *from muon spin rotation studies*, Phys. Rev. Lett. **71**, 3862 (1993).

[79] S.L. Lee, M. Warden, H. Keller, J.W. Schneider, D. Zech, P. Zimmermann, R. Cubitt, E.M. Forgan, M.T. Wylie, P.H. Kes, T.W. Li, A.A. Menovsky, and Z. Tarnawski, *Evidence for Two-Dimensional Thermal Fluctuations of the Vortex Structure in* $Bi_{2.15}Sr_{1.85}CaCu_2O_{8+\delta}$ *from Muon Spin Rotation Experiments*, Phys. Rev. Lett. **75**, 922 (1995).

[80] C.M. Aegerter, S.L. Lee, H. Keller, E.M. Forgan, and S.H. Lloyd, *Dimensional crossover in the magnetic phase diagram of* $Bi_{2.15}Sr_{1.85}CaCu_2O_{8+\delta}$ *crystals with different oxygen stoichiometry*, Phys. Rev. B **54**, R15661 (1996).

[81] C.M. Aegerter, J. Hofer, I.M. Savić, H. Keller, S.L. Lee, C. Ager, S.H. Lloyd, and E.M. Forgan, *Angular dependence of the disorder crossover in the vortex lattice of* $Bi_{2.15}Sr_{1.85}CaCu_2O_{8+\delta}$ *by muon spin rotation and torque magnetometry*, Phys. Rev. B **57**, 1253 (1998).

[82] E. Morenzoni, Th. Prokscha, A. Hofer, B. Matthias, M. Meyberg, Th. Wutzke, H. Glückler, M. Birke, J. Litterst, Ch. Neidermayer, and G. Schatz, *Characteristics of condensed gas moderators for the generation of very slow polarized muons*, J. Appl. Phys. **81**, 3340 (1997).

[83] A. Abragam, *Principles of Nuclear Magnetism*, Clarendon, Oxford, 1961.

[84] C. Slichter, *Principles of Magnetic Resonance*, Springer, Berlin, 1990.

[85] V. Johnson and W. Jeitschko, *ZrCiSiAs-Filled PbFCl-type*, J. Solid State Chem. **11**, 161 (1974).

[86] M. Reehuis and W. Jeitschko, *Structure and magnetic-properties of the phosphides* $CaCo_2P_2$ *and* LnT_2P_2 *with* $ThCr_2Si_2$ *structure and lanthanoids FeP, lanthanoids CoP, lanthanoids NiP with PbFCl structure*, J. Phys. Chem. Solids **51**, 961 (1990).

[87] B.I. Zimmer, W. Jeitschko, J.H. Albering, R. Glaum, and M. Reehuis, *The rare earth transition metal phosphide oxides LnFePO, LnRuPO and LnCoPO with ZrCuSiAs type structure*, J. Alloys Comp. **229**, 238 (1995).

[88] S. Weyeneth, *Anisotropic properties and critical behavior of high-temperature superconductors*, Ph.D. thesis, University of Zürich, 2009.

[89] Z.-A. Ren, G.-C. Che, X.-L. Dong, J. Yang, W. Lu, W. Yi, X.-L. Shen, Z.-C. Li, L.-L. Sun, F. Zhou, and Z.-X. Zhao, *Superconductivity and phase diagram in iron-based arsenic-oxides* $ReFeAsO_{1-\delta}$ *(Re = rare-earth metal) without fluorine doping*, EPL **83**, 17002 (2008).

[90] T.M. McQueen, M. Regulacio, A.J. Williams, Q. Huang, J.W. Lynn, Y.S. Hor, D.V. West, M.A. Green, and R.J. Cava, *Intrinsic properties of stoichiometric LaFePO*, Phys. Rev. B **78**, 024521 (2008).

[91] R.C. Che, R.J. Xiao, C.Y. Liang, H.X. Yang, C. Ma, H. Shi, and J.Q. Li, *Electron energy-loss spectroscopy and ab initio electronic structure of the LaOFeP superconductor*, Phys. Rev. B **77**, 184518 (2008).

[92] H. Takahashi, K. Igawa, K. Arii, Y. Kamihara, M. Hirano, and H. Hosono, *Superconductivity at 43 K in an iron-based layered compound* $LaO_{1-x}F_xFeAs$, Nature (London) **453**, 376 (2008).

[93] X.H. Chen, T. Wu, G. Wu, R.H. Liu, H. Chen, D.F. Fang, *Superconductivity at 43 K in* $SmFeAsO_{1-x}F_x$, Nature (London) **453**, 761 (2008).

[94] G.F. Chen, Z. Li, D. Wu, G. Li, W.Z. Hu, J. Dong, P. Zheng, J.L. Luo, and N.L. Wang, *Superconductivity at 41 K and its competition with spin-density-wave instability in layered* $CeO_{1-x}F_xFeAs$, Phys. Rev. Lett. **100**, 247002 (2008).

[95] Z.-A. Ren, J. Yang, W. Lu, W. Yi, X.-L. Shen, Z.-C. Li, G.-C. Che, X.-L. Dong, L.-L. Sun, F. Zhou, and Z.-X. Zhao, *Superconductivity in the iron-based F-doped layered quaternary compound* $Nd[O_{1-x}F_x]FeAs$, EPL **82**, 57002 (2008).

[96] P. Cheng, L. Fang, H. Yang, X. Y. Zhu, G. Mu, H. Q. Luo, Z. S. Wang, and H.-H. Wen, *Superconductivity at 36 K in gadolinium-arsenide oxides* $GdO_{1-x}F_xFeAs$, Sci. China, Ser. G **51**, 719 (2008).

[97] Z.-A. Ren, J. Yang, W. Lu, W. Yi, G.-C. Che, X.-L. Dong, L.-L. Sun, and Z.-X. Zhao, *Superconductivity at 52 K in iron based F doped layered quaternary compound* $Pr[O_{1-x}F_x]FeAs$, Mat. Res. Inn. **12**, 105 (2008).

[98] J.-W.G. Bos, G.B.S. Penny, J.A. Rodgers, D.A. Sokolov, A.D. Huxley, and J.P. Attfield, *High pressure synthesis of late rare earth RFeAs(O,F) superconductors; R = Tb and Dy*, Chem. Comm. **31**, 3634 (2008).

[99] W. Yi, C. Zhang, L.-L. Sun, Z.-A. Ren, W. Lu, X.-L. Dong, Z.-C. Li, G.-C. Che, J. Yang, X.-L. Shen, X. Dai, Z. Fang, F. Zhou, and Z.-X. Zhao, *High-pressure study on* $LaFeAs(O_{1-x}F_x)$ *and LaFeAsO with different* T_c, EPL **84**, 67009 (2008).

[100] H. Kito, H. Eisaki, and A. Iyo, *Superconductivity at 54 K in F-free* $NdFeAsO_{1-y}$, J. Phys. Soc. Jap. **77**, 063707 (2008).

[101] Y. Kamihara, M. Hirano, H. Yanagi, T. Kamiya, Y. Saitoh, E. Ikenaga, K. Kobayashi, and H. Hosono, *Electromagnetic properties and electronic structure of the iron-based layered superconductor LaFePO*, Phys. Rev. B **77**, 214515 (2008).

[102] J.J. Hamlin, R.E. Baumbach, D.A. Zocco, T.A. Sayles, and M. B. Maple, *Superconductivity in single crystals of LaFePO*, J. Phys.: Condens. Matter **20**, 365220 (2008).

[103] R.E. Baumbach, J.J. Hamlin, L. Shu, D.A. Zocco, N.M. Crisosto, and M.B. Maple, *Superconductivity in LnFePO (Ln = La, Pr and Nd) single crystals*, New J. Phys. **11**, 025019 (2009).

[104] Y.-P. Qi, L. Wang, Z.-S. Gao, D.-L. Wang, X.-P. Zhang, Z.-Y. Zhang, and Y.-W. Ma, *Superconductivity in Ir-doped* $LaFe_{1-x}Ir_xAsO$, Phys. Rev. B **80**, 054502 (2009).

[105] Y.-P. Qi, L. Wang, Z.-S. Gao, D.-L. Wang, X.-P. Zhang, Z.-Y. Zhang, and Y.-W. Ma, *Superconductivity in* $SmFe_{1-x}M_xAsO$ *(M = Co, Rh, Ir)*, EPL **89**, 67007 (2010).

[106] X.-Y. Zhu, F. Han, P. Cheng, G. Mu, B. Shen, and H.-H. Wen, *Superconductivity in fluorine-arsenide* $Sr_{1-x}La_xFeAsF$, EPL **85**, 17011 (2009).

[107] M. Rotter, M. Tegel, and D. Johrendt, *Superconductivity at 38 K in the iron arsenide* $(Ba_{1-x}K_x)Fe_2As_2$, Phys. Rev. Lett. **101**, 107006 (2008).

[108] K. Sasmal, B. Lv, B. Lorenz, A.M. Guloy, F. Chen, Y.-Y. Xue, and C.-W. Chu, *Superconducting Fe-based compounds* $(A_{1-x}Sr_x)Fe_2As_2$ *with A = K and Cs with transition temperatures up to 37 K*, Phys. Rev. Lett. **101**, 107007 (2008).

[109] G. Wu, H. Chen, T. Wu, Y.L. Xie, Y.J. Yan, R.H. Liu, X.F. Wang, J.J. Ying, and X.H. Chen, *Different resistivity response to spin-density wave and superconductivity at 20 K in* $Ca_{1-x}Na_xFe_2As_2$, J. Phys.: Condens. Matter **20**, 422201 (2008).

[110] H.S. Jeevan, Z. Hossain, D. Kasinathan, H. Rosner, C. Geibel, and P. Gegenwart, *High-temperature superconductivity in* $Eu_{0.5}K_{0.5}Fe_2As_2$, Phys. Rev. B **78**, 092406 (2008).

[111] Y. Qi, Z. Gao, L. Wang, D. Wang, X. Zhang, and Y. Ma, *Superconductivity at 34.7 K in the iron arsenide* $Eu_{0.7}Na_{0.3}Fe_2As_2$, New J. Phys. **10**, 123003 (2008).

[112] Z. Bukowski, S. Weyeneth, R. Puzniak, P. Moll, S. Katrych, N.D. Zhigadlo, J. Karpinski, H. Keller, and B. Batlogg, *Superconductivity at 23 K and low anisotropy in Rb-substituted* $BaFe_2As_2$ *single crystals*, Phys. Rev. B **79**, 104521 (2009).

[113] J. Karpinski, N.D. Zhigadlo, S. Katrych, Z. Bukowski, P. Moll, S. Weyeneth, H. Keller, R. Puzniak, M. Tortello, D. Daghero, R. Gonnelli, I. Maggio-Aprile, Y. Fasano, Ø. Fischer, K. Rogacki, and B. Batlogg, *Single crystals of* $LnFeAsO_{1-x}F_x$ *(Ln = La, Pr, Nd, Sm, Gd) and* $Ba_{1-x}Rb_xFe_2As_2$*: Growth, structure and superconducting properties*, Physica C **469**, 370 (2009).

[114] A.S. Sefat, R. Jin, M.A. McGuire, B.C. Sales, D.J. Singh, and D. Mandrus, *Superconductivity at 22 K in Co-doped* $BaFe_2As_2$ *crystals*, Phys. Rev. Lett. **101**, 117004 (2008).

[115] A. Leithe-Jasper, W. Schnelle, C. Geibel, and H. Rosner, *Superconducting state in* $SrFe_{2-x}Co_xAs_2$ *by internal doping of the iron arsenide layers*, Phys. Rev. Lett. **101**, 207004 (2008).

[116] L.J. Li, Y.K. Luo, Q.B. Wang, H. Chen, Z. Ren, Q. Tao, Y. K. Li, X. Lin, M. He, Z.W. Zhu, G.H. Cao, and Z.A. Xu, *Superconductivity induced by Ni doping in* $BaFe_2As_2$ *single crystals*, New J. Phys. **11**, 025008 (2009).

[117] X.C. Wang, Q.Q. Liu, Y.X. Lv, W.B. Gao, L.X. Yang, R.C. Yu, F.Y. Li, and C.Q. Jin, *The superconductivity at 18 K in LiFeAs system*, Solid State Comm. **148**, 538 (2008).

[118] D.R. Parker, M.J. Pitcher, P.J. Baker, I. Franke, T. Lancaster, S.J. Blundell, and S.J. Clarke, *Structure, antiferromagnetism and superconductivity of the layered iron arsenide NaFeAs*, Chem. Comm. **16**, 2189 (2009).

[119] F.-C. Hsu, J.-Y. Luo, K.-W. Yeh, T.-K. Chen, T.-W. Huang, P.M. Wu, Y.-C. Lee, Y.-L. Huang, Y.-Y. Chu, D.-C. Yan, and M.-K. Wu, *Superconductivity in the PbO-type structure* α*-FeSe*, Proc. Nat. Acad. Sci. USA **105**, 14262 (2008).

[120] R. Khasanov, M. Bendele, A. Amato, P. Babkevich, A.T. Boothroyd, A. Cervellino, K. Conder, S.N. Gvasaliya, H. Keller, H.-H. Klauss, H. Luetkens, E. Pomjakushina, and B. Roessli, *Coexistence of incommensurate magnetism and superconductivity in* $Fe_{1+y}Se_xTe_{1-x}$, Phys. Rev. B **80**, 140511(R) (2009).

[121] H. Ogino, Y. Matsumura, Y. Katsura, K. Ushiyama, S. Horii, K. Kishio, and J. Shimoyama, *Superconductivity at 17 K in* $(Fe_2P_2)(Sr_4Sc_2O_6)$*: A new superconducting layered pnictide oxide with a thick perovskite oxide layer*, Supercond. Sci. Technol. **22**, 075008 (2009).

[122] H. Ogino, Y. Katsura, S. Horii, K. Kishio, and J.-I Shimoyama, *New iron-based arsenide oxides* $(Fe_2As_2)(Sr_4M_2O_6)(M = Sc, Cr)$, Supercond. Sci. Technol. **22**, 085001 (2009).

[123] G.F. Chen, T.L. Xia, H.X. Yang, J.Q. Li, P. Zheng, J.L. Luo, and N.L. Wang, *Possible high temperature superconductivity in a Ti-doped A-Sc-Fe-As-O (A = Ca, Sr) system*, Supercond. Sci. Technol. **22**, 072001 (2009).

[124] Ying Jia, Peng Cheng, Lei Fang, Huiqian Luo, Huan Yang, Cong Ren, Lei Shan, Changzhi Gu, and Hai-Hu Wen, *Critical fields and anisotropy of* $NdFeAsO_{0.82}F_{0.18}$ *single crystals*, Appl. Phys. Lett. **93**, 032503 (2008).

[125] F. Hunte, J. Jaroszynski, A. Gurevich, D.C. Larbalestier, R. Jin, A.S Sefat, M.A. McGuire, B.C. Sales, D.K. Christen, and D. Mandrus, *Two-band superconductivity in* $LaFeAsO_{0.89}F_{0.11}$ *at very high magnetic fields*, Nature **453**, 903 (2008).

[126] Huan Yang, Cong Ren, Lei Shan, and Hai-Hu Wen, *Magnetization relaxation and collective vortex pinning in the Fe-based superconductor* $SmFeAsO_{0.9}F_{0.1}$, Phys. Rev. B **78**, 092504 (2008).

[127] D. Parker, O.V. Dolgov, M.M. Korshunov, A.A. Golubov, and I.I. Mazin, *Extended s(+/-) scenario for the nuclear spin-lattice relaxation rate in superconducting pnictides*, Phys. Rev. B **78**, 134524 (2008).

[128] J. Zhang, R. Sknepnek, R.M. Fernandes, and J. Schmalian, *Orbital coupling and superconductivity in the iron pnictides*, Phys. Rev. B **79**, 220502 (2009).

[129] D.C. Johnston, *The puzzle of high temperature superconductivity in layered iron pnictides and chalcogenides*, Advances In Physics **59**, 803 (2010).

[130] H. Liu, T. Wu, H. Chen, X.F. Wang, Y.L. Xie, J.J. Ying, Y.J. Yan, Q.J. Li, B.C. Shi, W.S. Chu, Z.Y. Wu, and X.H. Chen, *A large iron isotope effect in* $SmFeAsO_{1-x}F_x$ *and* $Ba_{1-x}K_xFe_2As_2$, Nature (London) **459**, 64 (2008).

[131] P.M. Shirage, K. Miyazawa, K. Kihou, H. Kito, Y. Yoshida, Y. Tanaka, H. Eisaki, and A. Iyo, *Absence of an Appreciable Iron Isotope Effect on the Transition Temperature of the Optimally Doped* $SmFeAsO_{1-y}$ *Superconductor*, Phys. Rev. Lett. **105**, 037004 (2010).

[132] P.M. Shirage, K. Kihou, K. Miyazawa, C.-H. Lee, H. Kito, H. Eisaki, T. Yanagisawa, Y. Tanaka, and A. Iyo, *Inverse Iron Isotope Effect on the Transition Temperature of the* $(Ba,K)Fe_2As_2$ *Superconductor*, Phys. Rev. Lett. **103**, 257003 (2009).

[133] R. Khasanov, M. Bendele, K. Conder, H. Keller, E. Pomjakushina, and V. Pomjakushin, *Iron isotope effect on the superconducting transition temperature and the crystal structure of* $FeSe_{1-x}$, New J. Phys. **12**, 073024 (2010).

[134] R. Khasanov, M. Bendele, A. Bussmann-Holder, and H. Keller, *Intrinsic and structural isotope effects in Fe-based superconductors*, Phys. Rev. B **82**, 212505 (2010).

[135] R. Khasanov, A. Shengelaya, A. Maisuradze, F. La Mattina, A. Bussmann-Holder, H. Keller and K.A. Müller, *Experimental evidence for two gaps in the high-temperature* $La_{1.83}Sr_{0.17}CuO_4$ *superconductor*, Phys. Rev. Lett. **98**, 057007 (2007).

[136] R. Khasanov, S. Strässle, D. Di Castro, T. Masui, S. Miyasaka, S. Tajima, A. Bussmann-Holder, and H. Keller, *Multiple gap symmetries for the order parameter of cuprate superconductors from penetration depth measurements*, Phys. Rev. Lett. **99**, 237601 (2007).

[137] A. Bussmann-Holder, R. Khasanov, A. Shengelaya, A. Maisuradze, F. La Mattina, H. Keller, and K. A. Müller, *Mixed order parameter symmetries in cuprate superconductors*, EPL **77**, 27002 (2007).

[138] R. Khasanov, A. Shengelaya, J. Karpinski, A. Bussmann-Holder, H. Keller, and K.A. Müller, *s-wave symmetry along the c-axis and* $s + d$ *in-plane superconductivity in bulk* $YBa_2Cu_4O_8$, J. Supercond. Nov. Magn. **21**, 81 (2008).

[139] H. Raffius, M. Mörsen, B.D. Mosel, W. Müller-Warmuth, W. Jeitschko, L. Terbüchte, and T. Vomhof, *Magnetic properties of ternary lanthanoid transition metal arsenides studied by Mössbauer and susceptibility measurements*, J. Phys. Chem. Solids **54**, 135 (1993).

[140] Z. Ren, Z.W. Zhu, S. Jiang, X.F. Xu, Q. Tao, C. Wang, C.M. Feng, G.H. Cao, and Z.A. Xu, *Antiferromagnetic transition in* $EuFe_2As_2$*: A possible parent compound for superconductors*, Phys. Rev. B **78**, 052501 (2008).

[141] Y. Xiao, Y. Su, M. Meven, R. Mittal, C.M.N. Kumar, T. Chatterji, S. Price, J. Persson, N. Kumar, S.K. Dhar, A. Thamizhavel, and Th. Brueckel, *Magnetic structure of* $EuFe_2As_2$ *determined by single-crystal neutron diffraction*, Phys. Rev. B **80**, 174424 (2009).

[142] Javier Herrero-Martín, Valerio Scagnoli, Claudio Mazzoli, Yixi Su, Ranjan Mittal, Yinguo Xiao, Thomas Brueckel, Neeraj Kumar, S.K. Dhar, A. Thamizhavel, and Luigi Paolasini, *Magnetic structure of* $EuFe_2As_2$ *as determined by resonant x-ray scattering*, Phys. Rev. B **80**, 134411 (2009).

[143] A.S. Sefat, R. Jin, M.A. McGuire, B.C. Sales, D.J. Singh, and D. Mandrus, *Superconductivity at 22 K in Co-Doped* $BaFe_2As_2$ *Crystals*, Phys. Rev. Lett. **101**, 117004 (2008).

[144] A. Leithe-Jasper, W. Schnelle, C. Geibel, and H. Rosner, *Superconducting State in* $SrFe_{2-x}Co_xAs_2$ *by Internal Doping of the Iron Arsenide Layers*, Phys. Rev. Lett. **101**, 207004 (2008).

[145] Y. He, T. Wu, G. Wu, Q.J. Zheng, Y.Z. Liu, H. Chen, J.J. Ying, R.H. Liu, X.F. Wang, Y.L. Xie, Y.J. Yan, J.K. Dong, S.Y. Li, and X.H. Chen, *Evidence for competing magnetic and superconducting phases in superconducting* $Eu_{1-x}Sr_xFe_{2-y}Co_yAs_2$ *single crystals*, J. Phys.: Condens. Matter **22**, 235701 (2010).

[146] C.F. Miclea, M. Nicklas, H.S. Jeevan, D. Kasinathan, Z. Hossain, H. Rosner, P. Gegenwart, C. Geibel, and F. Steglich, *Evidence for a reentrant superconducting state in* $EuFe_2As_2$ *under pressure*, Phys. Rev. B **79**, 212509 (2009).

[147] T. Terashima, M. Tomita, M. Kimata, H. Satsukawa, A. Harada, K. Hazama, S. Uji, H.S. Suzuki, T. Matsumoto, and K. Murata, $EuFe_2As_2$ *under High Pressure: An Antiferromagnetic Bulk Superconductor*, J. Phys. Soc. Jpn. **78**, 083701 (2009).

[148] Liling Sun, Jing Guo, Genfu Chen, Xianhui Chen, Xiaoli Dong, Wei Lu, Chao Zhang, Zheng Jiang, Yang Zou, Suo Zhang, Yuying Huang, Qi Wu, Xi Dai, Yuanchun Li, Jing Liu, and Zhongxian Zhao, *Valence change of europium in* $EuFe_2As_{1.4}P_{0.6}$ *and compressed* $EuFe_2As_2$ *and its relation to superconductivity*, Phys. Rev. B **82**, 134509 (2010).

[149] H.S. Jeevan, Deepa Kasinathan, H. Rosner, and P. Gegenwart, *Interplay of antiferromagnetism, ferromagnetism, and superconductivity in* $EuFe_2(As_{1-x}P_x)_2$ *single crystals*, Phys. Rev. B **83**, 054511 (2011).

[150] Zhi Ren, Xiao Lin, Qian Tao, Shuai Jiang, Zengwei Zhu, Cao Wang, Guanghan Cao, and Zhu'an Xu, *Suppression of spin-density-wave transition and emergence of ferromagnetic ordering of* Eu^{2+} *moments in* $EuFe_{2-x}Ni_xAs_2$, Phys. Rev. B **79**, 094426 (2009).

[151] L.J. Li, Y.K. Luo, Q.B. Wang, H. Chen, Z. Ren, Q. Tao, Y.K. Li, X. Lin, M. He, Z.W. Zhu, G.H. Cao, and Z.A. Xu, *Superconductivity induced by Ni doping in* $BaFe_2As_2$ *single crystals*, New J. Phys. **11**, 025008 (2008).

[152] S. Jiang, Y.K. Luo, Z. Ren, Z.W. Zhu, C. Wang, X.F. Xu, Q. Tao, G.H. Cao, and Z.A. Xu, *Metamagnetic transition in* $EuFe_2As_2$ *single crystals*, New J. Phys. **11**, 025007 (2009).

[153] E. Dengler, J. Deisenhofer, H.A. Krug von Nidda, Seunghyun Khim, J.S. Kim, Kee Hoon Kim, F. Casper, C. Felser, and A. Loidl, *Strong reduction of the Korringa relaxation in the spin-density wave regime of* $EuFe_2As_2$ *observed by electron spin resonance*, Phys. Rev. B **81**, 024406 (2010).

[154] J.J. Ying, T. Wu, Q.J. Zheng, Y. He, G. Wu, Q.J. Li, Y.J. Yan, Y.L. Xie, R.H. Liu, X.F. Wang, and X.H. Chen, *Electron spin resonance in* $EuFe_{2-x}Co_xAs_2$ *single crystals*, Phys. Rev. B **81**, 052503 (2010).

[155] Z. Guguchia, S. Bosma, S. Weyeneth, A. Shengelaya, R. Puzniak, Z. Bukowski, J. Karpinski, and H. Keller, *Anisotropic magnetic order of the Eu sublattice in single crystals of* $EuFe_{2-x}Co_xAs_2$ *($x = 0, 0.2$) studied by means of magnetization and magnetic torque*, Phys. Rev. B **84**, 144506 (2011).

[156] X.F. Wang, T. Wu, G. Wu, R.H. Liu, H. Chen, Y.L. Xie, and X.H. Chen, *The peculiar physical properties and phase diagram of* $BaFe_{2-x}Co_xAs_2$ *single crystals*, New J. Phys. **11**, 045003 (2009).

[157] Z. Guguchia, J. Roos, A. Shengelaya, S. Katrych, Z. Bukowski, S. Weyeneth, F. Murányi, S. Strässle, A. Maisuradze, J. Karpinski, and H. Keller, *Strong coupling between* Eu^{2+} *spins and* Fe_2As_2 *layers in* $EuFe_{1.9}Co_{0.1}As_2$ *observed with NMR*, Phys. Rev. B **83**, 144516 (2011).

[158] M. Rotter, M. Tegel, D. Johrendt, I. Schellenberg, W. Hermes, and R. Pöttgen, *Spin-density-wave anomaly at 140 K in the ternary iron arsenide* $BaFe_2As_2$, Phys. Rev. B **78**, 020503(R) (2008).

[159] Kentaro Kitagawa, Naoyuki Katayama, Kenya Ohgushi, Makoto Yoshida, and Masashi Takigawa, *Commensurate Itinerant Antiferromagnetism in* $BaFe_2As_2$*:* ^{75}*As-NMR Studies on a Self-Flux Grown Single Crystal*, J. Phys. Soc. Jpn. **77**, 114709 (2008).

[160] Kentaro Kitagawa, Naoyuki Katayama, Kenya Ohgushi, and Masashi Takigawa, *Antiferromagnetism of* $SrFe_2As_2$ *Studied by Single-Crystal* ^{75}*As-NMR*, J. Phys. Soc. Jpn. **78**, 063706 (2009).

[161] Fanlong Ning, Kanagasingham Ahilan, Takashi Imai, Athena S. Sefat, Ronying Jin, Michael A. McGuire, Brian C. Sales, and David Mandrus, ^{59}*Co and* ^{75}*As NMR Investigation of Electron-Doped High* T_c *Superconductor* $BaFe_{1.8}Co_{0.2}As_2$ *($T_c = 22$ K)*, J. Phys. Soc. Jpn. **77**, 103705 (2008).

[162] S.-H. Baek, N.J. Curro, T. Klimczuk, E.D. Bauer, F. Ronning, and J.D. Thompson, *First-order magnetic transition in single-crystalline* $CaFe_2As_2$ *detected by* ^{75}As *nuclear magnetic resonance*, Phys. Rev. B **79**, 052504 (2009).

[163] P. Jeglič, J.-W. G. Bos, A. Zorko, M. Brunelli, K. Koch, H. Rosner, S. Margadonna, and D. Arčon, *Influence of the Nd 4f states on the magnetic behavior and the electric field gradient of the oxypnictides superconductors* $NdFeAsO_{1-x}F_x$, Phys. Rev. B **79**, 094515 (2009).

[164] Fengjie Ma, Zhong-Yi Lu, and Tao Xiang, *Electronic structures of ternary iron arsenides* AFe_2As_2 *(A = Ba, Ca, or Sr)*, Front. Phys. China, **5(2)**, 150 (2010).

[165] A.A. Abrikosov and L.P. Gor'kov, *Contribution to the theory of superconducting alloys with paramagnetic impurities*, Zh. Eksp. Teor. Fiz. **39**, 1781 (1960) [Sov. Phys. JETP **12**, 1243 (1961)].

[166] Q. Huang, Y. Qiu, W. Bao, M.A. Green, J.W. Lynn, Y.C. Gasparovic, T. Wu, G. Wu, and X.H. Chen, *Neutron-Diffraction Measurements of Magnetic Order and a Structural Transition in the Parent* $BaFe_2As_2$ *Compound of FeAs-Based High-Temperature Superconductors*, Phys. Rev. Lett. **101**, 257003 (2008).

[167] N. Ni, S.L. Bud'ko, A. Kreyssig, S. Nandi, G.E. Rustan, A.I. Goldman, S. Gupta, J.D. Corbett, A. Kracher, and P.C. Canfield, *Anisotropic thermodynamic and transport properties of single-crystalline* $Ba_{1-x}K_xFe_2As_2$ *(x = 0 and 0.45)*, Phys. Rev. B **78**, 014507 (2008).

[168] C. Lester, Jiun-Haw Chu, J.G. Analytis, S. Capelli, A.S. Erickson, C.L. Condron, M.F. Toney, I.R. Fisher, and S.M. Hayden, *Neutron scattering study of the interplay between structure and magnetism in* $Ba(Fe_{1-x}Co_x)_2As_2$, Phys. Rev. B **79**, 144523 (2009).

[169] D.K. Pratt, W. Tian, A. Kreyssig, J.L. Zarestky, S. Nandi, N. Ni, S.L. Bud'ko, P.C. Canfield, A.I. Goldman, and R.J. McQueeney, *Coexistence of Competing Antiferromagnetic and Superconducting Phases in the Underdoped* $Ba(Fe_{0.953}Co_{0.047})_2As_2$ *Compound using X-ray and Neutron Scattering Techniques*, Phys. Rev. Lett. **103**, 087001 (2009).

[170] M.A. Tanatar, A. Kreyssig, S. Nandi, N. Ni, S.L. Bud'ko, P.C. Canfield, A.I. Goldman, and R. Prozorov, *Direct imaging of the structural domains in the iron pnictides* AFe_2As_2 *(A = Ca,Sr,Ba)*, Phys. Rev. B **79**, 180508(R) (2009).

[171] J.Q. Yan, A. Kreyssig, S. Nandi, N. Ni, S.L. Bud'ko, A. Kracher, R.J. McQueeney, R.W. McCallum, T.A. Lograsso, A.I. Goldman, and P.C. Canfield, *Structural transition and anisotropic properties of single-crystalline* $SrFe_2As_2$, Phys. Rev. B **78**, 024516 (2008).

[172] A. Jesche, N. Caroca-Canales, H. Rosner, H. Borrmann, A. Ormeci, D. Kasinathan, H.H. Klauss, H. Luetkens, R. Khasanov, A. Amato, A. Hoser, K. Kaneko, C. Krellner, and C. Geibel, *Strong coupling between magnetic and structural order parameters in* $SrFe_2As_2$, Phys. Rev. B **78**, 180504(R) (2008).

[173] M. Tegel, M. Rotter, V. Weiss, F.M. Schappacher, R. Pöttgen, and Dirk Johrendt, *Structural and magnetic phase transitions in the ternary iron arsenides* $SrFe_2As_2$ *and* $EuFe_2As_2$, J. Phys. Cond. Mat. **20**, 452201 (2008).

[174] Haifeng Li, Wei Tian, Jerel L. Zarestky, Andreas Kreyssig, Ni Ni, Sergey L. Bud'ko, Paul C. Canfield, Alan I. Goldman, Robert J. McQueeney, and David Vaknin, *Magnetic and lattice coupling in single-crystal* $SrFe_2As_2$*: A neutron scattering study*, Phys. Rev. B **80**, 054407 (2009).

[175] Jack Gillet, Sitikantha D. Das, Paul Syers, Alison K. T. Ming, Jose I. Espeso, Chiara M. Petrone, and Suchitra E. Sebastian, *Dimensional Tuning of the Magnetic-Structural Transition in* $A(Fe_{1-x}Co_x)_2As_2$ *(A = Sr, Ba)*, arXiv:1005.1330v1 (2010).

[176] N. Ni, S. Nandi, A. Kreyssig, A.I. Goldman, E.D. Mun, S.L. Bud'ko, and P.C. Canfield, *First-order structural phase transition in* $CaFe_2As_2$, Phys. Rev. B **78**, 014523 (2008).

[177] Stephen D. Wilson, C.R. Rotundu, Z. Yamani, P.N. Valdivia, B. Freelon, E. Bourret-Courchesne, and R.J. Birgeneau, *Universal magnetic and structural behaviors in the iron arsenides*, Phys. Rev. B **81**, 014501 (2010).

[178] J.C. Loudon, C.J. Bowell, J. Gillett, S.E. Sebastian, and P.A. Midgley, *Determination of the nature of the tetragonal to orthorhombic phase transition in* $SrFe_2As_2$ *by measurement of the local order parameter*, Phys. Rev. B **81**, 214111 (2010).

[179] C. de la Cruz, Q. Huang, J.W. Lynn, J. Li, W. Ratcliff II, H.A. Mook, G.F. Chen, J.L. Luo, N.L. Wang, and Pengcheng Dai, *Magnetic Order versus superconductivity in the Iron-based layered* $La(O_{1-x}F_x)FeAs$ *systems*, Nature (London) **453**, 899 (2008).

[180] Q. Huang, J. Zhao, J.W. Lynn, G.F. Chen, J.L. Luo, N.L. Wang, and P. Dai, *Doping evolution of antiferromagnetic order and structural distortion in* $LaFeAsO_{1-x}F_x$, Phys. Rev. B **78**, 054529 (2008).

[181] J. Zhao, W. Ratcliff II, J.W. Lynn, G.F. Chen, J.L. Luo, N.L. Wang, J. Hu, and P. Dai, *Spin and lattice structures of single-crystalline* $SrFe_2As_2$, Phys. Rev. B **78**, 140504 (2008).

[182] H. Luetkens, H.-H. Klauss, M. Kraken, F.J. Litterst, T. Dellmann, R. Klingeler, C. Hess, R. Khasanov, A. Amato, C. Baines, M. Kosmala, O.J. Schumann, M. Braden, J. Hamann-Borrero, N. Leps, A. Kondrat, G. Behr, J. Werner, and B. Büchner, *The electronic phase diagram of the* $LaO_{1-x}F_xFeAs$ *superconductor*, Nature Mater. **8**, 305 (2009).

[183] Chen Fang, Hong Yao, Wei-Feng Tsai, Jiang Ping Hu, and Steven A. Kivelson, *Theory of electron nematic order in LaFeAsO*, Phys. Rev. B **77**, 224509 (2008).

[184] T. Yildirim, *Strong Coupling of the Fe-Spin State and the As-As Hybridization in Iron-Pnictide Superconductors from First-Principle Calculations*, Phys. Rev. Lett. **102**, 037003 (2009).

[185] C. Xu, M. Müller, and S. Sachdev, *Ising and spin orders in the iron-based superconductors*, Phys. Rev. B **78**, 020501 (2008).

[186] M. Johannes and I. Mazin, *Microscopic origin of magnetism and magnetic interactions in ferropnictides*, Phys. Rev. B **79**, 220510 (2009).

[187] Frank Krüger, Sanjeev Kumar, Jan Zaanen, and Jeroen van den Brink, *Spin-orbital frustrations and anomalous metallic state in iron-pnictide superconductors*, Phys. Rev. B **79**, 054504 (2009).

[188] C.-C. Chen, B. Moritz, J. van den Brink, T. P. Devereaux, and R.R.P. Singh, *Finite-temperature spin dynamics and phase transitions in spin-orbital models*, Phys. Rev. B **80**, 180418(R) (2009).

[189] Weicheng Lv, Jiansheng Wu, and Philip Phillips, *Orbital ordering induces structural phase transition and the resistivity anomaly in iron pnictides*, Phys. Rev. B **80**, 224506 (2009).

[190] James G. Analytis, Ross D. McDonald, Jiun-Haw Chu, Scott C. Riggs, Alimamy F. Bangura, Chris Kucharczyk, Michelle Johannes, and I.R. Fisher, *Quantum oscillations in the parent pnictide* $BaFe_2As_2$*: Itinerant electrons in the reconstructed state*, Phys. Rev. B **80**, 064507 (2009).

[191] D.A. Tompsett, and G.G. Lonzarich, *Dimensionality and magnetic interactions in* $CaFe_2As_2$*: An ab initio study*, Physica B **405**, 2440 (2010).

[192] D. Kasinathan, A. Ormeci, K. Koch, U. Burkhardt, W.Schnelle, A. Leithe-Jasper, and H. Rosner, AFe_2As_2 *(A = Ca, Sr, Ba, Eu) and* $SrFe_{2-x}TM_xAs_2$ *(*TM *= Mn, Co, Ni): crystal structure, charge doping, magnetism and superconductivity*, New J. Phys. **11**, 025023 (2009).

[193] A.F. Kemper, C. Cao, P.J. Hirschfeld, and H-P. Cheng, *Effects of cobalt doping and three-dimensionality in* $BaFe_2As_2$, Phys. Rev. B **80**, 104511 (2009).

[194] T.-M. Chuang, M.P. Allan, Jinho Lee, Yang Xie, Ni Ni, S.L. Bud'ko, G.S. Boebinger, P.C. Canfield, and J.C. Davis, *Nematic Electronic Structure in the ”Parent” State of the Iron-Based Superconductor* $Ca(Fe_{1x}Co_x)_2As_2$, Science **327**, 181 (2010).

[195] I.I. Mazin, and J. Schmalian, *Pairing symmetry and pairing state in ferropnictides: Theoretical overview*, Physica C **469**, 614 (2009).

[196] M.A. Tanatar, E.C. Blomberg, A. Kreyssig, M.G. Kim, N. Ni, A. Thaler, S.L. Bud'ko, P.C. Canfield, A.I. Goldman, I.I. Mazin, and R. Prozorov, *Uniaxial-strain mechanical detwinning of* $CaFe_2As_2$ *and* $BaFe_2As_2$ *crystals: Optical and transport study*, Phys. Rev. B **81**, 184508 (2010).

[197] Jiun-Haw Chu, James G. Analytis, Kristiaan De Greve, Peter L. McMahon, Zahirul Islam, Yoshihisa Yamamoto, and Ian R. Fisher, *In-Plane Resistivity Anisotropy in an Underdoped Iron Arsenide Superconductor*, Science **329**, 824 (2010).

[198] I. Nowik and I. Felner, *Intermediate valence of europium in* $Eu_xLa_{1-x}Be_{13}$, Hyperfine Interact. **28**, 959 (1986).

[199] I. Nowik and I. Felner, *Mössbauer spectroscopy studies of oxypnictides superconductors*, Physica C **469**, 485 (2009).

[200] C. Feng, Z. Ren, S. Xu, S. Jiang, Z. Xu, G. Cao, I. Nowik, I. Felner, K. Matsubayashi, and Y. Uwatoko, *Magnetic ordering and dense Kondo behavior in* $EuFe_2P_2$, Phys. Rev. B **82**, 094426 (2010).

[201] I. Nowik, I. Felner, Z. Ren, G.H. Cao, and Z.A. Xu, *Coexistence of ferromagnetism and superconductivity: magnetization and Mössbauer studies of* $EuFe_2(As_{1-x}P_x)_2$, J. Phys.: Condens. Matter **23**, 065701 (2011).

[202] I. Nowik, I. Felner, Z. Ren, G.H. Cao, and Z.A. Xu, ^{57}*Fe and* ^{151}*Eu Mössbauer spectroscopy and magnetization studies of* $Eu(Fe_{0.89}Co_{0.11})_2As_2$ *and* $Eu(Fe_{0.9}Ni_{0.1})_2As_2$, New J. Phys. **13**, 023033 (2011).

[203] S. Kohout, J. Roos, and H. Keller, *Novel sensor design for torque magnetometry*, Rev. Sci. Instrum. **78**, 013903 (2007).

[204] Vinh Hung Tran, Tomasz A. Zaleski, Zbigniew Bukowski, Lan Maria Tran, and Andrzej J. Zaleski, *Tuning superconductivity in* $Eu(Fe_{0.81}Co_{0.19})_2As_2$ *with magnetic fields*, Phys. Rev. B **85**, 052502 (2012).

[205] Vinh Hung Tran, Zbigniew Bukowski, Lan Maria Tran, and Andrzej J. Zaleski, *The electronic phase diagrams of the* $Eu(Fe_{0.81}Co_{0.19})_2As_2$ *superconductor*, New J. Phys. **14**, 073052 (2012).

[206] S. Thirupathaiah, E.D.L. Rienks, H.S. Jeevan, R. Ovsyannikov, E. Slooten, J. Kaas, E. van Heumen, S. de Jong, H.A. Dürr, K. Siemensmeyer, R. Follath, P. Gegenwart, M.S. Golden, and J. Fink, *Dissimilarities between the electronic structure of chemically doped and chemically pressurized iron pnictides from an angle-resolved photoemission spectroscopy study*, Phys. Rev. B **84**, 014531 (2011).

[207] Zhi Ren, Qian Tao, Shuai Jiang, Chunmu Feng, Cao Wang, Jianhui Dai, Guanghan Cao, and Zhu'an Xu, *Superconductivity Induced by Phosphorus Doping and Its Coexistence with Ferromagnetism in* $EuFe_2(As_{0.7}P_{0.3})_2$, Phys. Rev. Lett. **102**, 137002 (2009).

[208] Aamir Ahmed, M. Itou, Shenggao Xu, Zhu'an Xu, Guanghan Cao, Y. Sakurai, James Penner-Hahn, and Aniruddha Deb, *Competing Ferromagnetism and Superconductivity on FeAs Layers in* $EuFe_2(As_{0.73}P_{0.27})_2$, Phys. Rev. Lett. **105**, 207003 (2010).

[209] K. Matsubayashi, K. Munakata, N. Katayama, M. Isobe, K. Ohgushi, Y. Ueda, N. Kawamura, M. Mizumaki, N. Ishimatsu, M. Hedo, I. Umehara, and Y. Uwatoko, *Pressure-induced changes in the magnetic and valence state of* $EuFe_2As_2$, Phys. Rev. B **84**, 024502 (2011).

[210] Z. Guguchia, A. Shengelaya, A. Maisuradze, L. Howald, Z. Bukowski, M. Chikovani, H. Luetkens, S. Katrych, J. Karpinski, and H. Keller, *Muon-Spin Rotation and Magnetization Studies of Chemical and Hydrostatic Pressure Effects in* $EuFe_2(As_{1-x}P_x)_2$, J. Supercond. Nov. Magn. **26**, 285 (2013).

[211] J. Rodrigues-Carvajal, *Recent advances in magnetic structure determination by neutron powder diffraction*, Physica B **192**, 55 (1993).

[212] S. Zapf, D. Wu, L. Bogani, H.S. Jeevan, P. Gegenwart, and M. Dressel, *Varying* Eu^{2+} *magnetic order by chemical pressure in* $EuFe_2(As_{1-x}P_x)_2$, Phys. Rev. B **84**, 140503(R) (2011).

[213] M. Mito, M. Hitaka, T. Kawae, K. Takeda, T. Kitai, and N. Toyoshima, *Development of Miniature Diamond Anvil Cell for the Superconducting Quantum Interference Device Magnetometer*, Jpn. J. Appl. Phys., Part 1 **40**, 6641 (2001).

[214] Gaétan Giriat, Weiwei Wang, J. Paul Attfield, Andrew D. Huxley, and Konstantin V. Kamenev, *Turnbuckle diamond anvil cell for high-pressure measurements in a superconducting quantum interference device magnetometer*, Review of scientific instruments **81**, 073905 (2010).

[215] A. Maisuradze, B. Graneli, Z. Guguchia, A. Shengelaya, E. Pomjakushina, K. Conder, and H. Keller, *Effect of pressure on the Cu and Pr magnetism in* $Nd_{1-x}Pr_xBa_2Cu_3O_{7-\delta}$ *investigated by muon spin rotation*, Phys. Rev. B **87**, 054401 (2013).

[216] W. Uhoya, G. Tsoi, Y.K. Vohra, M.A. McGuire, A.S. Sefat, B.C. Sales, D. Mandrus, and S.T. Weir, *Anomalous compressibility effects and superconductivity of* $EuFe_2As_2$ *under high pressures*, J. Phys.:Condens. Matter **22**, 292202 (2010).

[217] B. Ni, M.M. Abd-Elmeguid, H. Micklitz, J.P. Sanchez, P. Vulliet, and D. Johrendt, *Interplay between structural, electronic, and magnetic instabilities in* EuT_2P_2 *(T = Fe, Co) under high pressure*, Phys. Rev. B **63**, 100102 (2001).

[218] Guanghan Cao, Shenggao Xu, Zhi Ren, Shuai Jiang, Chunmu Feng, and Zhu'an Xu, *Superconductivity and ferromagnetism in* $EuFe_2(As_{1-x}P_x)_2$, J. Phys.: Condens. Matter **23**, 464204(5pp) (2011).

[219] Y. Tokiwa, S.-H. Hübner, O. Beck, H.S. Jeevan, and P. Gegenwart, *Unique phase diagram with narrow superconducting dome in* $EuFe_2(As_{1-x}P_x)_2$ *due to* Eu^{2+} *local magnetic moments*, Phys. Rev. B **86**, 220505(R) (2012).

[220] Alireza Akbari, Ilya Eremin, and Peter Thalmeier, *RKKY interaction in the spin-density-wave phase of iron-based superconductors*, Phys. Rev. B **84**, 134513 (2011).

[221] Z. Guguchia, Z. Shermadini, A. Amato, A. Maisuradze, A. Shengelaya, Z. Bukowski, H. Luetkens, R. Khasanov, J. Karpinski, and H. Keller, *Muon-spin rotation measurements of the magnetic penetration depth in the iron-based superconductor* $Ba_{1-x}Rb_xFe_2As_2$, Phys. Rev. B **84**, 094513 (2011).

[222] Q. Huang, Y. Qiu, W. Bao, M.A. Green, J.W. Lynn, Y.C. Gasparovic, T. Wu, G. Wu, and X.H. Chen, *Neutron-Diffraction Measurements of Magnetic Order and a Structural Transition in the Parent* $BaFe_2As_2$ *Compound of FeAs-Based High-Temperature Superconductors*, Phys. Rev. Lett. **101**, 257003 (2008).

[223] J. Zhao, Q. Huang, C. de la Cruz, S. Li, J.W. Lynn, Y. Chen, M.A. Green, G.F. Chen, G. Li, Z. Li, J.L. Luo, N.L. Wang, and P. Dai, *Structural and magnetic phase diagram of* $CeFeAsO_{1-x}F_x$ *and its relation to high-temperature superconductivity*, Nature Materials **7**, 953 (2008).

[224] D.V. Evtushinsky, D.S. Inosov, V.B. Zabolotnyy, M.S. Viazovska, R. Khasanov, A. Amato, H.-H. Klauss, H. Luetkens, Ch. Niedermayer, G.L. Sun, V. Hinkov, C.T. Lin, A. Varykhalov, A. Koitzsch, M. Knupfer, B. Büchner, A.A. Kordyuk, and S.V. Borisenko, *Momentum-resolved superconducting gap in the bulk of* $Ba_{1-x}K_xFe_2As_2$ *from combined ARPES and μSR measurements*, New J. Phys. **11**, 055069 (2009).

[225] H. Ding, P. Richard, K. Nakayama, K. Sugawara, T. Arakane, Y. Sekiba, A. Takayama, S. Souma, T. Sato, T. Takahashi, Z. Wang, X. Dai, Z. Fang, G.F. Chen, J.L. Luo, and N.L. Wang, *Observation of Fermi-surface-dependent nodeless superconducting gaps in* $Ba_{0.6}K_{0.4}Fe_2As_2$, Europhys. Lett. **83**, 47001 (2008).

[226] V.B. Zabolotnyy, D.S. Inosov, D.V. Evtushinsky, A. Koitzsch, A.A. Kordyuk, G.L. Sun, J.T. Park, D. Haug, V. Hinkov, A.N. Yaresko, A.V. Boris, C.T. Lin, M. Knupfer, B. Büchner, A. Varykhalov, R. Follath, and S.V. Borisenko, *(π,π) electronic order in iron arsenide superconductors*, Nature **457**, 569 (2009).

[227] R. Khasanov, D.V. Evtushinsky, A. Amato, H.-H. Klauss, H. Luetkens, Ch. Niedermayer, B. Büchner, G.L. Sun, C.T. Lin, J.T. Park, D.S. Inosov, and V. Hinkov, *Two-Gap Superconductivity in* $Ba_{1-x}K_xFe_2As_2$*: A Complementary Study of the Magnetic Penetration Depth by Muon-Spin Rotation and Angle-Resolved Photoemission*, Phys. Rev. Lett. **102**, 187005 (2009).

[228] J.E. Sonier, J.H. Brewer, and R.F. Kiefl, *μSR studies of the vortex state in type-II superconductors*, Rev. Mod. Phys. **72**, 769 (2000).

[229] R. Khasanov, A. Maisuradze, H. Maeter, A. Kwadrin, H. Luetkens, A. Amato, W. Schnelle, H. Rosner, A. Leithe-Jasper, and H.-H. Klauss, *Superconductivity and Field-Induced Magnetism in* $SrFe_{1.75}Co_{0.25}As_2$, Phys. Rev. Lett. **103**, 067010 (2009).

[230] T.J. Williams, A.A. Aczel, E. Baggio-Saitovitch, S.L. Bud'ko, P.C. Canfield, J.P. Carlo, T. Goko, H. Kageyama, A. Kitada, J. Munevar, N. Ni, S.R. Saha, K. Kirschenbaum, J. Paglione, D.R. Sanchez-Candela, Y.J. Uemura, and G. M. Luke, *Superfluid density and field-induced magnetism in* $Ba(Fe_{1-x}Co_x)_2As_2$ *and* $Sr(Fe_{1-x}Co_x)_2As_2$ *measured with muon spin relaxation*, Phys. Rev. B **82**, 094512 (2010).

[231] J.E. Sonier, W. Huang, C.V. Kaiser, C. Cochrane, V. Pacradouni, S.A. Sabok-Sayr, M.D. Lumsden, B.C. Sales, M.A. McGuire, A.S. Sefat, and D. Mandrus, *Magnetism and Disorder Effects on Muon Spin Rotation Measurements of the Magnetic Penetration Depth in Iron-Arsenic Superconductors*, Phys. Rev. Lett. **106**, 127002 (2011).

[232] The data were analyzed with the fitting package musrfit developed by A. Suter and B. Wojek: Phys. Procedia **30**, 6973 (2012). (see also http://lmu.web.psi.ch/facilities/software/musrfit/user/M- USR/WebHome.html). The fitting of Eq. 3 was performed using the additional library BMW developped by B. Wojek.

[233] E.H. Brandt, *Flux distribution and penetration depth measured by muon spin rotation in high-T_c superconductors*, Phys. Rev. B **37**, 2349 (1988).

[234] B. Pümpin, H. Keller, W. Kündig, W. Odermatt, I.M. Savić, J.W. Schneider, H. Simmler, P. Zimmermann, E. Kaldis, S. Rusiecki, Y. Maeno, and C. Rossel, *Muon-spin-rotation measurements of the London penetration depths in $YBa_2Cu_3O_{6.97}$*, Phys. Rev. B **42**, 8019 (1990).

[235] A. Carrington and F. Manzano, *Magnetic penetration depth of MgB_2*, Physica C **385**, 205 (2003).

[236] M.H. Fang, H.M. Pham, B. Qian, T.J. Liu, E.K. Vehstedt, Y. Liu, L. Spinu, and Z.Q. Mao, *Superconductivity close to magnetic instability in $Fe(Se_{1-x}Te_x)_{0.82}$*, Phys. Rev. B **78**, 224503 (2008).

[237] H. Padamsee, J.E. Neighbor, and C.A. Shiffman, *Quasiparticle phenomenology for thermodynamics of strong-coupling superconductors*, J. Low Temp. Phys. **12**, 387 (1973).

[238] R. Khasanov, A. Shengelaya, A. Maisuradze, F. La Mattina, A. Bussmann-Holder, H. Keller, and K. A. Müller, *Experimental Evidence for Two Gaps in the High-Temperature $La_{1.83}Sr_{0.17}CuO_4$ Superconductor*, Phys. Rev. Lett. **98**, 057007 (2007).

[239] R. Khasanov, K. Conder, E. Pomjakushina, A. Amato, C. Baines, Z. Bukowski, J. Karpinski, S. Katrych, H.-H. Klauss, H. Luetkens, A. Shengelaya, and N. D. Zhigadlo, *Evidence of nodeless superconductivity in $FeSe_{0.85}$ from a muon-spin-rotation study of the in-plane magnetic penetration depth*, Phys. Rev. B **78**, 220510 (2008).

[240] M. Bendele, S. Weyeneth, R. Puzniak, A. Maisuradze, E. Pomjakushina, K. Conder, V. Pomjakushin, H. Luetkens, S. Katrych, A. Wisniewski, R. Khasanov, and H. Keller, *Anisotropic superconducting properties of single-crystalline $FeSe_{0.5}Te_{0.5}$*, Phys. Rev. B **81**, 224520 (2010).

[241] H. Luetkens, H.-H. Klauss, R. Khasanov, A. Amato, R. Klingeler, I. Hellmann, N. Leps, A. Kondrat, C. Hess, A. Köhler, G. Behr, J.Werner, and B. Büchner, *Field and Temperature Dependence of the Superfluid Density in $LaFeAsO_{1-x}F_x$ Superconductors: A Muon Spin Relaxation Study*, Phys. Rev. Lett. **101**, 097009 (2008).

[242] H. Takagi, S. Uchida, K. Kitazawa, and S. Tanaka, *High-T_c Superconductivity of La-Ba-Cu Oxides. II. Specification of the Superconducting Phase*, Jpn. J. Appl. Phys. **26**, L123 (1987).

[243] J.M. Tranquada, *Neutron scattering in Layered Copper-Oxide Superconductors*, (Kluwer, Dordrecht, The Netherlands, 1998).

[244] Y.S. Lee, R.J. Birgeneau, M.A. Kastner, Y. Endoh, S. Wakimoto, K. Yamada, R.W. Erwin, S.-H. Lee, and G. Shirane, *Neutron-scattering study of spin-density wave order in the superconducting state of excess-oxygen-doped* La_2CuO_{4+y}, Phys. Rev. B **60**, 3643 (1999).

[245] D. Vaknin, S.K. Sinha, D.E. Moncton, D.C. Johnston, J.M. Newsam, C.R. Safinya, and H.E. King, *Antiferromagnetism in* La_2CuO_{4-y}, Phys. Rev. Lett. **58**, 2802 (1987).

[246] T. Freltoft, J.P. Remeika, D.E. Moncton, A.S. Cooper, J.E. Fischer, D. Harshman, G. Shirane, S.K. Sinha, and D. Vaknin, *Antiferromagnetism and oxygen deficiency in single-crystal* $La_2CuO_{4-\delta}$, Phys. Rev. B **36**, 826 (1987).

[247] R. Coldea, S.M. Hayden, G. Aeppli, T.G. Perring, C.D. Frost, T.E. Mason, S.-W. Cheong, and Z. Fisk, *Spin Waves and Electronic Interactions in* La_2CuO_4, Phys. Rev. Lett. **86**, 5377 (2001).

[248] A.R. Moodenbaugh, Y. Xu, M. Suenaga, T.J. Folkerts, and R.N. Shelton, *Superconducting properties of* $La_{2-x}Ba_xCuO_4$, Phys. Rev. B **38**, 4596 (1988).

[249] H. Takagi, T. Ido, S. Ishibashi, M. Uota, S. Uchida, and Y. Tokura, *Superconductor-to-nonsuperconductor transition in* $(La_{1-x}Sr_x)_2CuO_4$ *as investigated by transport and magnetic measurements*, Phys. Rev. B **40**, 2254 (1989).

[250] J.D. Axe, A.H. Moudden, D. Hohlwein, D.E. Cox, K.M. Mohanty, A.R. Moodenbaugh, and Y. Xu, *Structural phase transformations and superconductivity in* $La_{2-x}Ba_xCuO_4$, Phys. Rev. Lett. **62**, 2751 (1989).

[251] M.K. Crawford, R.L. Harlow, E.M. McCarron, W.E. Farneth, J.D. Axe, H. Chou, and Q. Huang, *Lattice instabilities and the effect of copper-oxygen-sheet distortions on superconductivity in doped* La_2CuO_4, Phys. Rev. B **44**, 7749 (1991).

[252] G.M. Luke, L.P. Le, B.J. Sternlieb, W.D. Wu, Y.J. Uemura, J.H. Brewer, T.M. Riseman, S. Ishibashi, and S. Uchida, *Static magnetic order in* $La_{1.875}Ba_{0.125}CuO_4$, Physica C **185-189**, 1175 (1991).

[253] J.M. Tranquada, B.J. Sternlieb, J.D. Axe, Y. Nakamura, and S. Uchida, *Evidence for stripe correlations of spins and holes in copper oxide superconductors*, Nature (London) **375**, 561 (1995).

[254] J.M. Tranquada, J.D. Axe, N. Ichikawa, Y. Nakamura, S. Uchida, and B. Nachumi, *Neutron-scattering study of stripe-phase order of holes and spins in* $La_{1.48}Nd_{0.4}Sr_{0.12}CuO_4$, Phys. Rev. B **54**, 7489 (1996).

[255] M. Fujita, H. Goka, K. Yamada, J.M. Tranquada, and L.P. Regnault, *Stripe order, depinning, and fluctuations in* $La_{1.875}Ba_{0.125}CuO_4$ *and* $La_{1.875}Ba_{0.075}Sr_{0.050}CuO_4$, Phys. Rev. B **70**, 104517 (2004).

[256] P. Abbamonte, A. Rusydi, S. Smadici, G.D. Gu, G.A. Sawatzky, and D.L. Feng, *Spatially modulated 'Mottness' in* $La_{2-x}Ba_xCuO_4$, Nat. Phys. **1**, 155 (2005).

[257] Y.-J. Kim, G.D. Gu, T. Gog, and D. Casa, *X-ray scattering study of charge density waves in* $La_{2-x}Ba_xCuO_4$, Phys. Rev. B **77**, 064520 (2008).

[258] S.R. Dunsiger, Y. Zhao, Z. Yamani, W.J.L. Buyers, H.A. Dabkowska, and B.D. Gaulin, *Incommensurate spin ordering and fluctuations in underdoped* $La_{2-x}Ba_xCuO_4$, Phys. Rev. B **77**, 224410 (2008).

[259] M. Hücker, M.v. Zimmermann, G.D. Gu, Z.J. Xu, J.S. Wen, Guangyong Xu, H.J. Kang, A. Zheludev, and J.M. Tranquada, *Stripe order in superconducting* $La_{2-x}Ba_xCuO_4$ *(*$0.095 \leq x \leq 0.155$*)*, Phys. Rev. B **83**, 104506 (2011).

[260] J.M. Tranquada, G.D. Gu, M. Hücker, Q. Jie, H.-J. Kang, R. Klingeler, Q. Li, N. Tristan, J.S. Wen, G.Y. Xu, Z.J. Xu, J. Zhou, and M.v. Zimmermann, *Evidence for unusual superconducting correlations coexisting with stripe order in* $La_{1.875}Ba_{0.125}CuO_4$, Phys. Rev. B **78**, 174529 (2008).

[261] N. Ichikawa, S. Uchida, J.M. Tranquada, T. Niemöller, P.M. Gehring, S.-H. Lee, and J.R. Schneider, *Local Magnetic Order vs Superconductivity in a Layered Cuprate*, Phys. Rev. Lett. **85**, 1738 (2000).

[262] N.B. Christensen, H. M. Rønnow, J. Mesot, R.A. Ewings, N. Momono, M. Oda, M. Ido, M. Enderle, D.F. McMorrow, and A.T. Boothroyd, *Nature of the Magnetic Order in the Charge-Ordered Cuprate* $La_{1.48}Nd_{0.4}Sr_{0.12}CuO_4$, Phys. Rev. Lett. **98**, 197003 (2007).

[263] M. Hücker, G.D. Gu, J.M. Tranquada, M.v. Zimmermann, H.-H. Klauss, N.J. Curro, M. Braden, and B. Büchner, *Coupling of stripes to lattice distortions in cuprates and nickelates*, Physica C **460-462**, 170 (2007).

[264] J. Zaanen and O. Gunnarsson, *Charged magnetic domain lines and the magnetism of high-*T_c *oxides*, Phys. Rev. B **40**, 7391 (1989).

[265] K. Machida, *Magnetism in* La_2CuO_4 *based compounds*, Physica C **158**, 192 (1989).

[266] M. Inui and P.B. Littlewood, *Hartree-Fock study of the magnetism in the single-band Hubbard model*, Phys. Rev. B **44**, 4415 (1991).

[267] S.A. Kivelson, I.P. Bindloss, E. Fradkin, V. Oganesyan, J.M. Tranquada, A. Kapitulnik, and C. Howald, *How to detect fluctuating stripes in the high-temperature superconductors*, Rev. Mod. Phys. **75**, 1201 (2003).

[268] A. Bianconi, N.L. Saini, A. Lanzara, M. Missori, T. Rossetti, H. Oyanagi, H. Yamaguchi, K. Oka, and T. Ito, *Determination of the Local Lattice Distortions in the* CuO_2 *Plane of* $La_{1.85}Sr_{0.15}CuO_4$, Phys. Rev. Lett. **76**, 3412 (1996).

[269] A. Bianconi, M. Lusignoli, N.L. Saini, P. Bordet, A. Kvick, and P.G. Radaelli, *Stripe structure of the* CuO_2 *plane in* $Bi_2Sr_2CaCu_2O_{8+y}$ *by anomalous x-ray diffraction*, Phys. Rev. B **54**, 4310 (1996).

[270] M. Vojta, *Lattice symmetry breaking in cuprate superconductors: stripes, nematics, and superconductivity*, Adv. Phys. **58**, 699 (2009).

[271] M.K. Crawford, R.L. Harlow, S. Deemyad, V. Tissen, J.S. Schilling, E.M. McCarron, S.W. Tozer, D.E. Cox, N. Ichikawa, S. Uchida, and Q. Huang, *High-pressure study of structural phase transitions and superconductivity in* $La_{1.48}Nd_{0.4}Sr_{0.12}CuO_4$, Phys. Rev. B **71**, 104513 (2005).

[272] J.-S. Zhou and J.B. Goodenough, *Electron-lattice coupling and stripe formation in* $La_{2-x}Ba_xCuO_4$, Phys. Rev. B **56**, 6288 (1997).

[273] S. Katano, S. Funahashi, N. Môri, Yutaka Ueda, and Jaime A. Fernandez-Baca, *Pressure effects on the structural phase transitions and superconductivity of* $La_{2-x}Ba_xCuO_4$ *(*$x = 0.125$*)*, Phys. Rev. B **48**, 6569 (1993).

[274] Z. Guguchia, A. Maisuradze, G. Ghambashidze, R. Khasanov, A. Shengelaya, and H. Keller, *Tuning the static spin-stripe phase and superconductivity in* $La_{2-x}Ba_xCuO_4$ *(*$x = 1/8$*) by hydrostatic pressure*, arXiv:1303.3865v1 (2013).

[275] A.R. Moodenbaugh, Youwen Xu, M. Suenaga, T.J. Folkerts, and R.N. Shelton, *Superconducting properties of* $La_{2-x}Ba_xCuO_4$, Phys. Rev. B **38**, 4596 (1988).

[276] M. Ido, N. Yamada, M. Oda, Y. Segawa, N. Momono, A. Onodera, Y. Okajima, and K. Yamaya, *Pressure effect on superconductivity and low-temperature phase transition in Ba-doped* La_2CuO_4, Physica C **185-189**, 911 (1991).

[277] G.M. Luke, L.P. Le, B.J. Sternlieb, W.D. Wu, Y.J. Uemura, J.H. Brewer, T.M. Riseman, S. Ishibashi, and S. Uchida, *Static magnetic order in* $La_{1.875}Ba_{0.125}CuO_4$, Physica C **185-9**, 1175 (1991).

[278] B. Nachumi, Y. Fudamoto, A. Keren, K. M. Kojima, M. Larkin, G. M. Luke, J. Merrin, O. Tchernyshyov, Y.J. Uemura, N. Ichikawa, M. Goto, H. Takagi, S. Uchida, M.K. Crawford, E.M. McCarron, D.E. MacLaughlin, and R.H. Heffner, *Muon spin relaxation study of the stripe phase order in* $La_{1.6-x}Nd_{0.4}Sr_xCuO_4$ *and related 214 cuprates*, Phys. Rev. B **58**, 8760-8772 (1998).

[279] M. Hücker, M.v. Zimmermann, M. Debessai, J.S. Schilling, J.M. Tranquada, and G.D. Gu, *Spontaneous Symmetry Breaking by Charge Stripes in the High Pressure Phase of Superconducting* $La_{1.875}Ba_{0.125}CuO_4$, Phys. Rev. Lett. **104**, 057004 (2010).

[280] As it was mentioned in the text at applied pressures we measured only $\chi_{\rm FC}$. However, the zero-temperature limit of the difference $\chi_{\rm ZFC}$-$\chi_{\rm FC}$ was obtained from the measurements at ambient pressure. By assuming that this difference does not change with pressure the value of $\chi_{\rm ZFC}$ at $T = 0$ K was determined at different applied pressures.

Acknowledgements

I would like to acknowledge all those who contributed to the success of this thesis.

It was a great honor for me to work in the group where one of its members, Em. Prof. Dr. phil. Dr. phil. h.c. mult. Karl Alexander Müller, was one of the discoverer of high-temperature superconductivity in the cuprates and who received the Nobel prize for this discovery.

My foremost thank goes to my advisors Prof. Dr. Hugo Keller, and Prof. Dr. Alexander Shengelaya. Without them, this dissertation would not have been possible. I thank them for their patience and encouragement that carried me on through difficult times, and for their insightful ideas and suggestions that greatly helped me shape my research skills. During my work in the group of Prof. Keller, I obtained very valuable experience in experimental condensed matter physics.

Prof. Dr. Alexander Shengelaya is effectively my mentor who rendered me knowledge on the physics of HTSs and the application of the different experimental techniques (μSR, Electron Paramagnetic Resonance and SQUID magnetometer) to this subject. His interesting ideas concerning HTS and enthusiasm is really catching to me.

I appreciated more for my advisors to teach me how to think, and telling me what behaviors a good researcher should have. They have set the models for excellent researchers, and I will try my best to follow this. During the course of preparing this dissertation, they provided a lot of feedback that turned out to be critical. These years of working with them were very pleasant, interesting and fruitful in science as well as in our personal relationships.

The measurements would not have been possible without well characterized samples with excellent quality, provided by Dr. Zbigniew Bukowski and Prof. Dr. Janusz Karpinski at ETHZ. It was a great pleasure to work with them. Furthermore, I would like to thank Dr. Ekaterina Pomjakushina and Prof. Dr. Kazimierz Conder for the samples prepared at PSI.

I would also like to express my sincere thank to Dr. Joseph Roos for introducing me into the details of working with the NMR technique and for all the fruitful discussions we had.

I am very grateful to our group member Dr. Alexander Maisuradze for his important contributions in some of my projects. Diamond anvil pressure cell for magnetization measurements, used in this work was developed by him at the University of Zürich.

I am very grateful to Dr. Stephen Weyeneth for fruitfull collaboration, wonderfull discussions, teamwork and friendship.

I also benefit from other group members such as Dr. Ludovic Howald, whom I worked on cuprate thin films, Saskia Bosma with whom I collaborated on a particular member of Fe-based superconductors, and Dr. Markus Bendele.

My collaborations with other researchers and groups have been very fruitful and joyful. These include those wonderful people from Max Planck Institute for Solid State Research, Germany: Prof. Dr. Annette Bussmann-Holder and Prof. Dr. Jürgen Köhler. Prof. Dr Roman Puzniak at the Institute of Physics, Polish Academy of Sciences. Dr. Rustem Khasanov, Zurab Shermadini, Dr. Alex Amato, and Dr. Hubertus Luetkens at PSI, Switzerland. Dr. Sergiy Katrych at ETHZ, Switzerland.

I would like to thank my colleagues from our group for the friendly working atmosphere: Saskia Bosma, Dr. Stephen Weyeneth, Dr. Alexander Maisuradze, Dr. Markus Bendele, Dr. Simon Strässle, Dr. Ferenc Muranyi, Dr. Ludovic Howald, Evelyin Stilp, Stefan Sigrist, and Dr. Bastian Wojek. I am grateful to all these people for the pleasant years we spent together.

I am grateful to Peter Soland, Dr. Vollhardt Achim, Ticiano Crudelli, Dr. Roland Bernet, Lucien Pauli, and the whole workshop team of Kurt Bösiger for their help in solving various technical problems.

I would like to thank Dr. Aaron Manalaysay for his help in correcting the English of my thesis.

I am grateful to Evelyn Stilp for her help in translating the abstract of my thesis to German.

I would like to acknowledge the funding support from the Swiss National Science Foundation and the Physik-Institut.

Last but not least, I thank all my family members. They are the people where I obtain my strength, hope, and happiness. I will always appreciate their past, on-going and never ending supports. To appreciate them, I know the best way is to work harder, and live better. My last and most special thank goes to my dear wife, Magda and daughter, Mariami who was born during my Ph.D. studies. Importantly, Mariami brought me tremendous motivation that I have never had before. My wife has taken good care of me and punched me ever since we met. If there is any chance that I would be able to succeed, 50 % of the credit goes to her.

Curriculum Vitae

Name	Guguchia
Prename	Zurab
Date of birth	September 27th, 1987
Place of birth	Gulriphshi (Georgia)
Citizenship	Georgia

Education

1993 – 2003	- Studied at the Apkhazeti Secondary School N1, Zugdidi, Georgia
2003 – 2007	- Bachelor studies of Physics, Tbilisi State University, Georgia
2007	**Degree of Bachelor of Physics**
2007 – 2009	- Master studies of Physics, Tbilisi State University, Georgia
2009	**"Degree of Master of Physics in Experimental Physics"**
	- Title of Master thesis *Magnetic ordering and Superconductivity in* $R_{1-x}Pr_xBa_2Cu_3O_{7-y}$ *high temperature superconductors* - Supervisor: Prof. Dr. Alexander Shengelaya
2010 – 2013	- Ph.D. student in the *Superconductivity and Magnetism* group of Prof. Dr. H. Keller, University of Zürich

Awards

2006 - Second degree diploma on the student 66-th scientific conference, Tbilisi State University, Georgia.

2007 - First degree diploma on the student 67-th scientific conference, Tbilisi State University, Georgia.

2009 - First degree diploma on the student 69-th scientific conference, Tbilisi State University, Georgia.

2009 - Best oral presentation at the International Workshop "Material Science Days", Tbilisi State University, Georgia.

Scholarships

2004/2005 - Scholarship of publishing house ‘Intellect‘ for outstanding students, Georgia.

2006/2007 - Scholarship named after Shota Rustaveli for outstanding students,
Ministry of Education and Science, Tbilisi, Georgia.

2008 - Scholarship named after President of Georgia Mikheil Saakashvili for outstanding students,
Ministry of Education and Science, Tbilisi, Georgia.

Publication list (work performed in the framework of this PhD thesis)

issued 07.05.2013

- *Strong coupling between* Eu^{2+} *spins and* Fe_2As_2 *layers in* $EuFe_{1.9}Co_{0.1}As_2$ *observed with NMR*
  Z. Guguchia, J. Roos, A. Shengelaya, S. Katrych, Z. Bukowski, S. Weyeneth, F. Murányi, S. Strässle, A. Maisuradze, J. Karpinski, and H. Keller
  Phys. Rev. B **83**, 144516 (2011).

- *Muon-spin rotation measurements of the magnetic penetration depth in the iron-based superconductor* $Ba_{1-x}Rb_xFe_2As_2$
  Z. Guguchia, Z. Shermadini, A. Amato, A. Maisuradze, A. Shengelaya, Z. Bukowski, H. Luetkens, R. Khasanov, J. Karpinski, and H. Keller
  Phys. Rev. B **84**, 094513 (2011).

- μSR *investigation of magnetism and magnetoelectric coupling in* Cu_2OSeO_3
  A. Maisuradze, **Z. Guguchia**, B. Graneli, H.M. Rønnow, H. Berger, and H. Keller
  Phys. Rev. B **84**, 064433 (2011).

- *Anisotropic magnetic order of the Eu sublattice in single crystals of* $EuFe_{2-x}Co_xAs_2$ *(x = 0, 0.2) studied by means of magnetization and magnetic torque*
  Z. Guguchia, S. Bosma, S. Weyeneth, A. Shengelaya, R. Puzniak, Z. Bukowski, J. Karpinski, and H. Keller
  Phys. Rev. B **84**, 144506 (2011).

- *Muon Spin Rotation Study of the Intercalated Graphite Superconductor* CaC_6 *at Low Temperatures*
  F. Murányii, M. Bendele, R. Khasanov, **Z. Guguchia**, A. Shengelaya, C. Baines, and H. Keller
  J. Supercond. Nov. Magn. **25**, 159 (2012).

- *Tuning the structural instability of* $SrTiO_3$ *by Eu doping: The phase diagram of* $Sr_{1-x}Eu_xTiO_3$
  Z. Guguchia, A. Shengelaya, H. Keller, J. Köhler, and A. Bussmann-Holder
  Phys. Rev. B **85**, 134113 (2012).

- *Hybrid paramagnon phonon modes at elevated temperatures in* $EuTiO_3$
  A. Bussmann-Holder, **Z. Guguchia**, J. Köhler, H. Keller, A. Shengelaya, and A.R. Bishop
  New Journal of Physics **14**, 093013 (2012).

- *Superconductivity and magnetism in $Rb_xFe_{2-y}Se_2$: Impact of thermal treatment on mesoscopic phase separation*
  S. Weyeneth, M. Bendele, F. von Rohr, P. Dluzewski, R. Puzniak, A. Krzton-Maziopa, S. Bosma, **Z. Guguchia**, R. Khasanov, Z. Shermadini, A. Amato, E. Pomjakushina, K. Conder, A. Schilling, and H. Keller
  Phys. Rev. B **86**, 134530 (2012).

- *Magnetic field enhanced structural instability in $EuTiO_3$*
  Z. Guguchia, H. Keller, J. Köhler, and A. Bussmann-Holder
  J. Phys.: Condens. Matter **24**, 492201 (2012).
  Paper was selected by IOP as "IOPSELECT".

- *Muon-Spin Rotation and Magnetization Studies of Chemical and Hydrostatic Pressure Effects in $EuFe_2(As_{1-x}P_x)_2$*
  Z. Guguchia, A. Shengelaya, A. Maisuradze, L. Howald, Z. Bukowski, M. Chikovani, H. Luetkens, S. Katrych, J. Karpinski, and H. Keller
  J. Supercond. Nov. Magn. **26**, 285 (2013).

- *Effect of pressure on the Cu and Pr magnetism in $Nd_{1-x}Pr_xBa_2Cu_3O_{7-\delta}$ investigated by muon spin rotation*
  A. Maisuradze, B. Graneli, **Z. Guguchia**, A. Shengelaya, E. Pomjakushina, K. Conder, and H. Keller
  Phys. Rev. B **87**, 054401 (2013).

- *Tuning the static spin-stripe phase and superconductivity in $La_{2-x}Ba_xCuO_4$ ($x = 1/8$) by hydrostatic pressure*
  Z. Guguchia, A. Maisuradze, G. Ghambashidze, R. Khasanov, A. Shengelaya, and H. Keller
  New J. Phys. **15**, 093005 (2013).

- *Nonlinear pressure dependence of T_N in almost multiferroic $EuTiO_3$*
  Z. Guguchia, K. Caslin, R.K. Kremer, H. Keller, A. Shengelaya, A. Maisuradze, J.L. Bettis Jr, J. Köhler, A. Bussmann-Holder, and M.-H. Whangbo
  J. Phys.: Condens. Matter **25**, 376002 (2013).
  Paper was selected by IOP as "IOPSELECT".

Other publications

issued 07.05.2013

- *Amplification and energy transformation of the magnetized Rossby waves in the ionosphere with an inhomogeneous zonal wind. II. Analysis of numerical solution*
  G. Aburjania, **Z. Guguchia**, A. Khantadze, and O. Kharshiladze
  GEOMAGNETISM AND AERONOMY **47**, 452 (2007).
- *Amplification and energy transformation of the magnetized Rossby waves in the ionosphere with an inhomogeneous zonal wind. I. A theory*
  G. Aburjania, **Z. Guguchia**, A. Khantadze, and O. Kharshiladze
  GEOMAGNETISM AND AERONOMY **47**, 442 (2007).
- *Lattice dynamics and anomalous softening in the* $YbFe_4Sb_{12}$ *skutterudite*
  A. Möchel, I. Sergueev, H.-C. Wille, J. Voigt, M. Prager, M.B. Stone, B.C. Sales, **Z. Guguchia**, A. Shengelaya, V. Keppens, and R.P. Hermann
  Phys. Rev. B **84**, 184306 (2011).